UNIVERSITY OF SOUTHAMPTON

**FACULTY OF ENGINEERING
AND THE ENVIRONMENT**

Energy Technology Research Group

E-*J* Characteristics, Current Sharing and Quench Behaviour of YBCO Coated Conductor Tapes at Different Temperatures

by

Iole Falorio

Thesis for the degree of Doctor of Engineering

27 November 2014

Academic Thesis: Declaration of Authorship

I, Iole Falorio, declare that this thesis, and the work presented in it, are my own and has been generated by me as the result of my own original research.

E-J characteristics, Current Sharing and Quench Behaviour of YBCO Coated Conductor Tapes at Different Temperatures

I confirm that:

1. This work was done wholly or mainly while in candidature for a research degree at this University;

2. Where any part of this thesis has previously been submitted for a degree or any other qualification at this University or any other institution, this has been clearly stated;

3. Where I have consulted the published work of others, this is always clearly attributed;

4. Where I have quoted from the work of others, the source is always given. With the exception of such quotations, this thesis is entirely my own work;

5. I have acknowledged all main sources of help;

6. Where the thesis is based on work done by myself jointly with others, I have made clear exactly what was done by others and what I have contributed myself;

7. Either none of this work has been published before submission, or parts of this work have been published as: [please list references below]:

Signed:

Date:

Hoc unum scio, me nihil scire.

Socrate.

Acknowledgements

My biggest thanks go to my supervisor Prof. Yifeng Yang for the inspirational, supporting and patient role he played during the years of my PhD. Without him this work could not have been possible. I will continue to treasure his lessons and his dedication to research in all my future work and my career.

I would also like to thank Dr. Edward Young for teaching me how to work successfully and independently in the laboratory. I have learnt from him the importance of being methodical and precise and how 'slowing down' can help to achieve much better results, even in my everyday life.

Prof. Carlo Beduz has imparted to me his enthusiasm for research since the first time we met. He has continually given me encouraging suggestions and positive advice throughout the years and for this I owe him my most sincere gratitude.

I would like to acknowledge all of the other members of the cryogenic group: Mike Webb for his expertise, ideas and invaluable help which made the magic in the lab possible; Dr. Wendell Bailey for his precious help and support in any circumstance; Dr. Jorge Pelegrín and Jessica Spurrell for contributing reviewing my thesis, providing positive feedback and for sharing a good laugh with me at the end of the working day. I deeply feel that it has been a privilege to be part of this team and you have all contributed to make the time of my PhD productive and stimulating.

Prof. Marco Breschi was the one who first believed in me and encouraged me to follow the road of scientific research, so I would like to thank him for the contribution he made to the progress of my studies.

Finally, a big thanks goes to all the people who helped me to persevere during the stressful moments and contributed to my everyday life happiness: my family and in particular my brother Emanuele; my best friends of all-time thanks to whom I know I will never be alone, Pieranna, Alice, Michela and Fiamma; all those who shared part of their life with me in Omdurman Road: Coralie, Sarah, Nuria, Thomas, Kirsten, Laetitia, Lyndsay, Mark, Tristan, Stanislav, Zohra and Francesco; and a special thanks to Jaime for the sensitivity and comprehension demonstrated in the very last weeks before my exam and for his contagious positive approach to life.

Contents

Abstract **1**

1 Fundamental on superconductivity for practical applications **3**

1.1 Superconducting properties 3

1.1.1 Basic phenomena 3

1.1.2 Type I and Type II superconductors 6

1.1.3 Flux motion, flux pinning and critical current density 10

1.1.4 The critical state model 11

1.2 High Temperature Superconductors 15

1.2.1 YBCO structure 16

1.2.2 Thallium, mercury and bismuth compounds structure 17

1.2.3 Phenomenological phase diagram of HTS superconductors in presence of thermal fluctuations 19

1.2.4 Vortices dynamics in presence of thermal fluctuations 22

1.2.5 Experimental evidences of the melting transition 24

1.2.6 Effects of correlated and uncorrelated defects in Type II superconductors 26

1.3 Non linear E-J characteristic and current sharing 32

1.3.1 Stabilisation of conductors 34

1.4 Quench and disturbances 36

1.4.1 Current sharing in LTS and HTS superconductors 37

1.4.2 Thermal stability 39

1.4.3 Minimum propagation zone 40

1.4.4 Minimum quench energy, MQE 43

1.4.5 Normal zone propagation velocity, $NZPV$ 43

2 Apparatus and measurements methodology **45**
2.1 Tape description 46
2.2 Quench measurements set-up 47
2.2.1 Sample instrumentation for quench measurements 47
2.3 *E-J* characteristic measurements set-up 48
2.3.1 Reduction of the sample section 48
2.3.2 Sample holder and and cross-section reduction 49
2.4 Experimental flow cryostat designed for quasi-adiabatic measurements . 49
2.4.1 Cryostat operational mode 52
2.4.2 Sample platform 53
2.4.3 Electrical and thermal links 55
2.4.4 Operations for adiabatic measurement 57
2.5 Experimental cryostat for *E-J* characteristics measurements in liquid nitrogen pool 57

3 The *E-J* Characteristics of 2G YBCO Conductors: experimental results **61**
3.1 Motivation and Objectives 61
3.2 Experimental Set-up 62
3.2.1 Transport measurement in liquid nitrogen and mitigation of self heating 62
3.2.2 Cryogen-free transport measurement at variable temperatures . . 66
3.2.3 Sample preparation and validation 66
3.3 Measurement protocol 69
3.3.1 Transport current: DC, semi-transient steps and pulses 69
3.3.2 Voltage acquisition: resolution, noise and inductive component . 70
3.3.3 Magnetization measurements 72
3.4 Results 74
3.4.1 Samples 74
3.4.2 DC *E-J* characteristics at liquid nitrogen temperatures 76
3.4.3 *E-J* characteristics at different temperatures 79
3.4.4 *E-J* characteristics in low fields 85
3.4.5 Magnetization measurements at different sweep rate 91

3.4.6 Power law exponent n-calculated from magnetization measurements 92
3.5 Conclusion 93

4 HTS pinning models and E-J characteristics of 2G YBCO Tapes 95
4.1 Objectives 95
4.2 Dynamic pinning properties of HTS and E-J characteristics 95
4.2.1 HTS pinning models 95
4.2.2 E-J characteristics of HTS pinning models 96
4.2.3 Determination of the dynamic parameters of HTS pinning models 99
4.3 Experimental results analysed with the HTS pinning models 104
4.3.1 E-J characteristics at different temperatures 104
4.4 The dynamic parameters and pinning of a single vortex and of vortex bundles 109
4.4.1 Static properties of the HTS pinning models 111
4.4.2 Single vortex in Boson-glass model 112
4.4.3 Small bundles in Boson-glass model 113
4.4.4 Single vortex in classic collective pinning model 115
4.4.5 Small bundles in classic collective pinning model 115
4.4.6 E-J characteristics in applied low fields 119
4.4.7 Magnetization measurements and HTS pinning models 121
4.5 Conclusions 123

5 Flux pinning distribution and E-J characteristics of 2G YBCO Tapes 125
5.1 Motivation 125
5.2 Theory of the distribution model 126
5.2.1 Analytical expression of the global E-J characteristic 127
5.2.2 E-J characteristic parameters obtained by a given distribution . 130
5.2.3 Distribution parameters obtained by a given E-J characteristic . 130
5.3 Distribution model parameters 131
5.3.1 Scenario I: reduced I_{C0} and wider distribution 132
5.3.2 Scenario II: increased I_{C0} and same distribution 133
5.3.3 Scenario III: increased I_{C0} and narrower distribution 134
5.4 Applicability and methodology of pinning distribution analysis 136

5.4.1 Non-power law E-J characteristics of 2G YBCO can be described by the distribution model . . . 136
5.4.2 Deduction of the pinning distribution . . . 138
5.5 Experimental results analysed with the distribution model . . . 143
5.5.1 E-J characteristics in self field, at different temperatures. . . . 143
5.5.2 Distribution parameters as a function of temperature . . . 148
5.5.3 Underlying distribution of 2G YBCO tape as a function of temperature . . . 149
5.5.4 E-J characteristic in applied field . . . 151
5.5.5 Pinning distribution dependence on field . . . 153
5.6 Discussion . . . 155
5.6.1 Pinning distribution at different temperatures . . . 155
5.6.2 Pinning distribution at different fields . . . 156
5.7 Conclusion . . . 158

6 Quench investigation **161**
6.1 Introduction . . . 161
6.2 Thermal-electrical properties . . . 162
6.3 Critical current . . . 163
6.4 Quench measurement protocol . . . 164
6.5 Quench initiation . . . 164
6.5.1 Typical recovery and quench event . . . 164
6.6 MQE, $NZPV$ and l_{MPZ} . . . 169
6.7 Results and discussion . . . 171
6.7.1 MQE temperature dependence . . . 171
6.7.2 MQE dependence on current . . . 172
6.7.3 MQE for Critical State Superconductors . . . 173
6.7.4 MQE in Power Law Superconductors . . . 176
6.7.5 Application of the Critical State model and Power-law approximated model to data . . . 179

7 Conclusion and further work **183**
7.1 Conclusion . . . 183
7.2 Further work . . . 186

References **189**

List of Figures **197**

List of Tables **209**

Abstract

Superconductivity is widely regarded as one of the great scientific discoveries of the 20th century. The property of superconducting material, to lose all the resistance to the flow of current at low enough temperature, enables the development of a range of innovative technology applications. Large magnets like accelerators, detectors, MRI (Magnetic Resonance Imaging), NMR (Nuclear Magnetic Resonance) and SMES (Superconducting Magnetic Energy Storage) systems are some of the applications that already take advantage from low temperature superconducting materials.

The discovery of ceramic superconductors such as $YBa_2Cu_3O_{7-x}$ (critical temperature $T_C \sim 93$ K), $Bi_2Sr_2CaCu_2O_x$ ($T_c \sim 110$ K), $HgBa_2Ca_2Cu_3O_x$ ($T_C \sim 135$ K) and $TlBa_2CaCu_2O_x$ ($T_C \sim 118$ K) made superconducting applications more attractive since it is possible to substitute liquid helium with nitrogen as a coolant. Because of this feature, they are known as High Temperature Superconductors (HTS). HTS are also good candidates to replace copper based technology such as motors, generators and transformers, and their use would allow to obtain more compact devices and to save huge amounts on energy.

The progress in the performance and commercial availability of second generation (2G) YBCO tapes has resulted in a marked increase in the research activities on their applications to a wide range of magnet components and power devices. Unlike 1G counterpart, 2G conductors bring an enhanced flux pinning in medium to high magnetic fields at intermediate temperatures between 4.2 K and 77 K. Most new applications are designed for cryogen-free operation at 20-50 K depending on the magnetic field required.

The voltage-current (E-J) relation is a crucial characteristic of superconducting materials, relevant to the fundamental understanding of flux pinning, the optimization of

material performances and several aspects of magnet applications including the quench dynamics/protection and the persistent mode stability. Although the *E-J* characteristics of YBCO materials have been the subject of intense research focus 15-20 years ago when the understanding of flux dynamics at higher temperatures and very short coherence length was developed. A collective pinning mechanism in a vortex glass was shown to be predominant in YBCO materials. However, most published *E-J* data were at high temperatures where the melting of the vortex glass was the main focus and measurements could be made reliably on high quality single crystals and films at relative small current. A systematic study of the *E-J* characteristics of 2G conductors is necessary and the availability of stabilized 2G tapes presents an opportunity for extending the YBCO *E-J* data to a wider temperature range.

The work presented in this thesis was carried out in the practical and fundamental context outline above and focuses on a systematic study of *E-J* characteristics and quench propagation and characterization of the state-of the art 2G $YBa_2Cu_3O_{7-x}$ of Super Power. *E-J* characteristics have been measured at different temperatures (15 K and 80 K) and fields (0 - 300 mT).

1

Fundamental on superconductivity for practical applications

1.1 Superconducting properties

1.1.1 Basic phenomena

Superconducting state is characterized by two distinctive properties: *perfect electrical conductivity* ($\rho = 0$) and *perfect diamagnetism* ($B = 0$).

- **Zero resistance** is one of the peculiar properties of superconductors. It was observed for the first time in 1911 by Onnes, who was measuring the electrical resistance of solid mercury in liquid helium. He found that the resistance of mercury abruptly drops to zero in a very narrow range of temperature $4.19\,\mathrm{K} - 4.22\,\mathrm{K}$. The phenomena occurs independently from the crystal lattice structure and describes a phase transition of the material. The zero resistance is a characteristic property of superconductivity but it is not enough to describe this state of matter: any conductor in fact, when cooled to temperature close to 0 Kelvin, shows resistivity close to zero. The macroscopic characteristic that distinguishes a superconductor from an ideal conductor is the magnetic behaviour.

- **Perfect diamagnetism** is shown in presence of an external applied field of magnitude smaller than a critical field B_C: material in superconducting state

have the ability of totally expel from its interior the magnetic field they are exposed to. In order to highlight the difference between a superconductor and a perfect conductor, a schematic representation is presented in fig.(1.1).

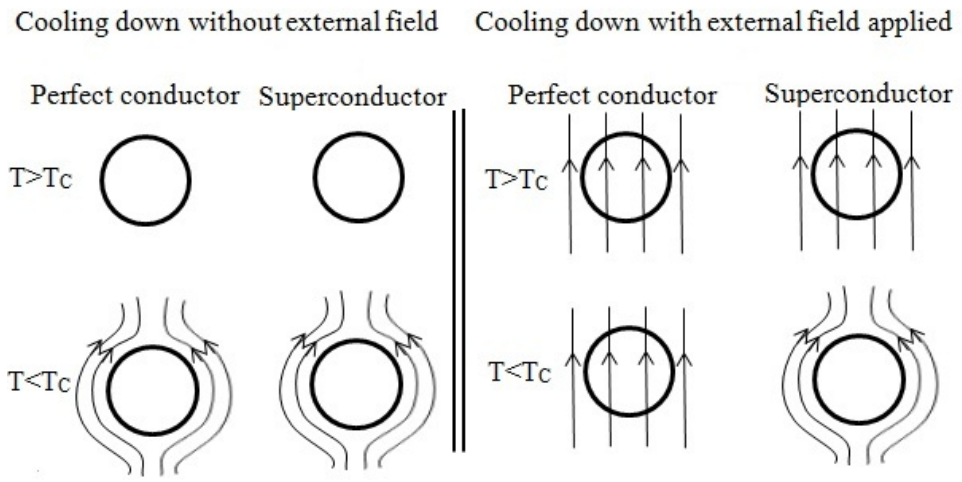

Figure 1.1: Schematic representation of the magnetic behaviour of a perfect conductor and of a superconductor once cooled down when applying field before and after cooling.

Let's consider a material cooled down until obtaining a perfect conductor, characterised by $\rho = 0$. Once the perfect conductor is cooled down and exposed to an external field, current loops are generated to cancel the change in field as predicted by Lenz's law, and the field does not penetrate the conductor. On the other hand, if the field is applied before cooling, the current induced dies rapidly out because of the resistance, and the conductor remains magnetised when cooled down in field.

Differently from a perfect conductor, the expulsion of the magnetic field in a superconductor occurs independently if the field has been applied before or after cooling the material. Hence, the magnetization state of a superconductor depends only from the external conditions and not from the sequence in which the conditions have been reached.

A first phenomenological approach to explain the superconducting phenomena was provided by Gunzburg-Landau (G-L) theory in 1950, according to which in the superconducting state, the current is carried by superconducting electrons which begin to form at the transition temperature and become more numerous as the temperature is further lowered. The G-L theory introduces two characteristic lengths of the superconducting state:

- *Penetration depth.* According to London's equation, in presence of an applied external field, superficial currents start circulating on the skin of the material and induce an internal field equal in strength but opposite in direction to the external one. The external field partially penetrates the material and decays to zero inside the superconductor where the field is fully shielded. This phenomena has a length decay constant called London penetration depth λ_L, and its typical value lies in the range 0.1μm -0.8μm.

- *Coherence length.* The superconducting electron density cannot vary abruptly at the interface between the superconductor and the normal material, therefore, when the superconductor is shielded, the number of superconducting electrons changes from 0 at the surface to its full bulk value at the interior of the material. The length scale required to set a full superconducting state is known as coherence length ξ.

A microscopic theory able to explain the origin of superconductivity, was formulated in 1957 by John Bardeen, Leon Cooper and Robert Schrieffer, and it is known as BCS theory. Cooper demonstrated the presence, in the superconducting state, of pairs of electrons with same velocity but which move in opposite directions and with opposite spin. Despite their common negative electric charge, these electron pairs feel a net attraction due to the mediation of the lattice. According to the BCS theory Cooper pairs are scattered as a single object and electrical resistance is not produced as long as there is not available energy to brake the pair apart. The scale of the spatial correlation in a superconductor is given by the coherence length ξ which, in the BCS theory, correspond to the size of the cooper pair [1].

1.1.2 Type I and Type II superconductors

Superconductors can be classified in Type I and Type II depending on their magnetic behaviour in response to an external magnetic field. For a superconductor immersed in an external field eq.(1.1) is valid :

$$B = \mu_0(H + M) \tag{1.1}$$

Considering a cylindrical geometry with the field applied parallel to the longitudinal dimension and appling eq.(1.1) inside the superconductor where the internal magnetization is zero, it can be obtained eq.(1.2):

$$\mu_0 M = -B_{app} \tag{1.2}$$

where the field applied is $H_{app} = B_{app}/\mu_0$.

The magnetization diagrams of Type I and Type II superconductors are shown respectively in fig.(1.2a) and in fig.(1.2b).

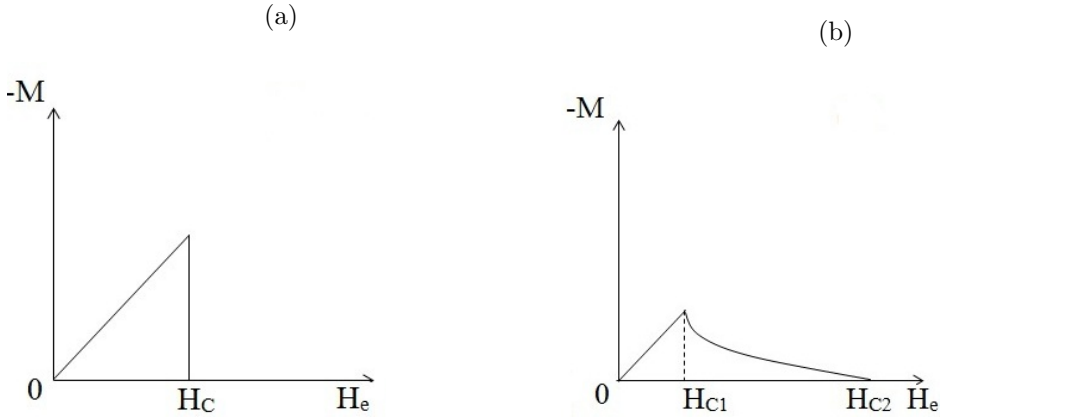

Figure 1.2: Schematic phase diagram of a superconductor (a) Type I and (b) Type II.

Type I superconductors are able to expel the external applied magnetic field if below the critical field H_C. At H_C, the material abruptly transits to the normal state, the internal magnetization drops to zero, as shown in fig.(1.2a), and the field fully penetrates the material.

Type II superconductors are characterised by a more gradual transition from superconducting to normal state. As the field is increased, Type II superconductors show perfect diamagnetism for field below the critical lower field H_{C1}. For field greater than H_{C1}, the magnetic flux penetrates the material turning small regions to normal. The internal magnetization changes continuously until reaching zero at the upper critical field H_{C2}, as shown in fig.(1.2b). Because of the presence of small normal regions, the material is described to be in the *mixed state*.

Criterion for Type I and Type II superconductivity

The distinction between Type I and Type II is not just empirical but depends on the conditions at the interface between the normal and the superconducting region. In terms of characteristic lengths, the number of superconducting electrons n_s at the interface increases from zero to a constant value in a length scale ξ. On the other hand, the external applied field B decays exponentially in a length scale λ. Depending on which one of the two length scales is greater than the other, Type I and Type II superconductors can be distinguished.

Type I superconductors are characterised by coherence length larger than the penetration depth ($\xi >> \lambda$), which corresponds to admit the presence of superconducting electrons only in regions where the field has already decayed, as shown in fig.(1.3a). Materials which are instead characterised by penetration depth larger than the the coherence length ($\lambda >> \xi$), are Type II superconductors. These type of conductors presents regions where the magnetic field penetrates the material and, in these regions, penetrated flux lines coexist with high concentration of superconducting electrons, as shown in fig.(1.3b). Hence, it is favourable for Type II superconductors to spontaneously develop small normal regions in order to obtain the greatest saving in free energy. The G-L theory introduces the parameter κ, defined as $\kappa = \lambda/\xi$ and Type I and Type II superconductors are classified depending whether $\kappa < 1/\sqrt{2}$ or $\kappa > 1/\sqrt{2}$, respectively.

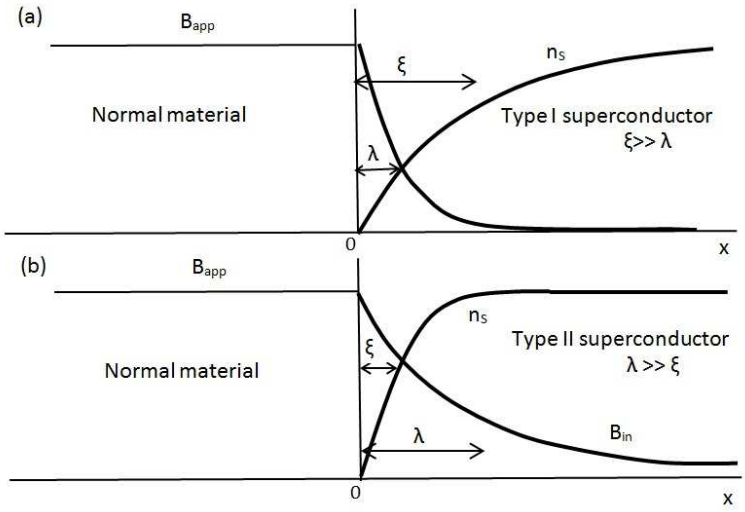

Figure 1.3: Increment of the number of superconducting electrons n_s and decay of the magnetic field from the surface of the superconductor and respective characteristic lengths λ_L and ξ for (a) Type I superconductors and (b) Type II superconductors [2].

Magnetic field penetrates Type II superconductors in a mixed state in form of flux lines, each one carrying precisely one unit of magnetic flux. The flux quantum carried by each flux line is expressed by equation (1.3):

$$\phi_0 = h\,c\,/2\,e \tag{1.3}$$

which h is the Plank constant and e the electron charge.

Quantized flux occurs in vortices which have a core at very high magnetic field and are supported by a vortex of supercurrents which separate the normal zone from the superconducting one, as it is schematically represented in fig.(1.4). Out of the core the field decreases with distance almost exponentially [3] .

Superconducting electrons flow in the vortex core and their density increases from 0 at the boundary with the normal material, to a constant value in a length scale of ξ. The shielding current screens the magnetic field which decays exponentially to zero inside the superconductor in a distance λ_L from the vortex centre line. Therefore coherence length and penetration depth characterise the radius of the core and the radius of the field outside the core, respectively.

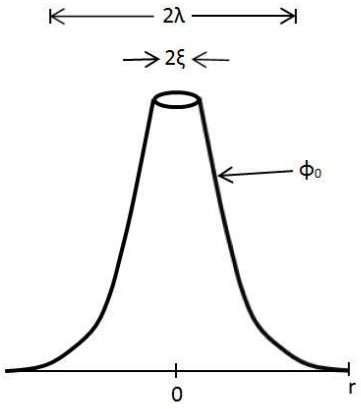

Figure 1.4: Schematic representation of the magnetic field around an individual vortex [2].

Abrikosov elucidated the nature of vortices and predicted that, because of the mutual repulsive Lorentz force involved, vortices dispose in a regular periodic hexagonal configuration, as the one schematically illustrated in fig.(1.5), so that to minimise the energy of the system [4]. The interflux line spacing between vortices is defined as $a_0 = \left(2\,\Phi_0/\sqrt{3}\,B\right)^{1/2}$

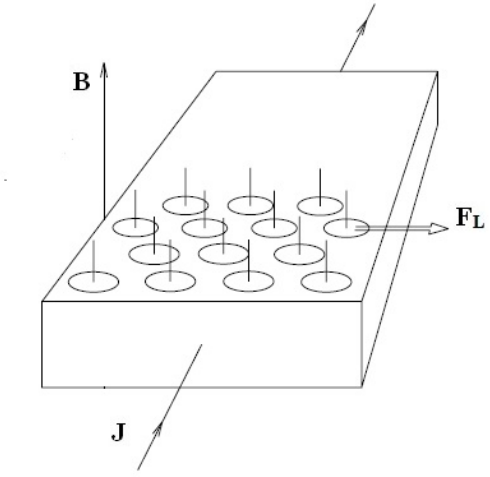

Figure 1.5: Arrangement of vortex of super-currents penetrated in the material. Lorentz force direction in presence of current.

As the field is further increased, vortices get closer to each other and start overlapping till covering the all body of the material and the transition to the normal state takes place.

Practical Type I and Type II superconductors

Type I superconductors, such as mercury and lead, were the first superconductors to be discovered. The critical field of Type I conductors is very low (the highest is B_C=0.206 T for Nb), thus they cannot be used in high field magnet applications. Type II superconductors are usually alloys or compounds and can remain superconducting at higher field (B_{C2}=35 T for Nb_3Sn). However Type I superconductors are not useful for high current and high field technologies because of their low operative critical temperatures [2].

1.1.3 Flux motion, flux pinning and critical current density

In the mixed state, the flux lines penetrate the material and, in absence of anchoring, collective motion of flux lines is induced by the flow of current. The Lorentz force $F_L = J \times B$ acts on vortices perpendicularly to both current and flux lines as shown in fig.(1.5). If the state is maintained steady and the system is homogeneous, the Lorentz force is counteracted by the friction force, and hence an electrical resistance appears, leading to dissipation [5].

To maintain the superconducting state, flux motion needs to be stopped. The presence of solid-state defects (such as impurities, vacancies, interstitial atoms, dislocations, grain boundaries, precipitates), allows to stop the free vortices movement. This effect of immobilization is known as *flux pinning* and is the mechanism which allows the material to sustain the Lorentz force between the flux and the current. A pinned flux line can be thought to be hold by pinning in a potential well of pinning energy U, which is the energy needed to overcome the barrier.

When the Lorentz force dominates on the pinning force, the vortices are free to move and the dissipation starts. The phenomena is known as *flux flow* and the current density at which the flow voltage clearly appears is called *critical current density*, J_C. The critical current density is given by the transport current divided by the cross sectional area of

the superconducting region $J_C = I_C/A_S$.

Hence, in a real superconductor, the dissipation does not occur till the Lorentz force is small enough to be counteracted by the pinning force. Before the depinning of vortices starts, the Lorentz force is perfectly balanced by the pinning force. From a practical point of view, pinning is an essential property of superconductors because allows to raise significantly the resistive temperature transition of the material.

1.1.4 The critical state model

The behaviour of Type II superconductor in presence of an applied external field has been theoretically explained by Bean's [6] and Kim's [7] models. These models assume that, when a magnetic field is switched on beyond H_{C1}, a current flows into the sample to prevent the field penetration and the outer region of the conductor, where the shielding current is circulating, is said to be in *critical state*. Magnetic field and current density present in the superconductor are related through Maxwell's law, given in eq.(1.4) for one dimensional case.

$$\frac{\mathrm{d}B_z(x)}{\mathrm{d}x} = \mu_0 \, J_y(x) \tag{1.4}$$

- **Bean's model.** According to Bean's model, the current that flows at any point in the superconductor, without flux motion appearance, is either zero or the maximum possible value J_C. When the superconductor is carrying J_C, is told to be in *critical state*. Assuming an infinite slab geometry of width $2a$, exposed to an applied field B_0, eq.(1.4) assumes the form of eq.(1.5)

$$B_z(x) = -\mu_0 J_C x + B_0 \tag{1.5}$$

  The field penetration profile of eq.(1.5) is represented in fig.(1.6a) and the corresponding distribution of J_C is schematically plot in fig.(1.6b) with the plain lines. The flux front penetrates the slab to a penetration depth δ.

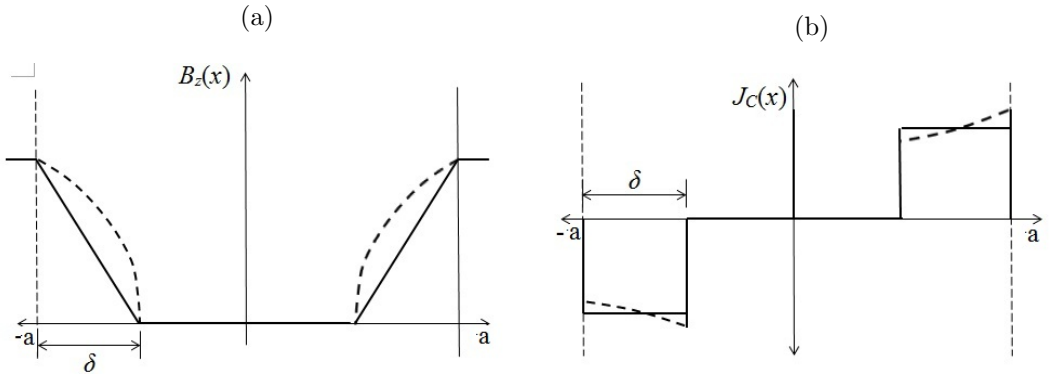

Figure 1.6: Distribution of (a) $B(x)$ and of (b) $J_C(x)$ within an infinite slab superconductor according to Bean's model (plain lines) and to Kim's model (dashed lines).

- **Kim's model.** According to Kim's model, the critical state is characterised by a constant pinning force. The assumption of constant pinning gives the relation between current density and field as in eq.(1.6).

$$J_y(B_z) = \frac{F_P}{B_z(x)} \tag{1.6}$$

In this model for the magnetic field within the superconductor can be expressed as in eq.(1.7).

$$B_z(x) = B_0\sqrt{x} + \mathrm{A} \tag{1.7}$$

where A is a constant.

This field penetration profile is represented in fig.(1.6a) with the corresponding distribution of J_C in fig.(1.6b) with dashed lines.

Bean's and Kim's model provide a qualitatively good description of how the field penetrate a superconductors. Bean's model is the most commonly used one to estimate the critical current density from magnetization measurements, where the sample is exposed to field cycles.

The magnetic field and the current profile inside a superconductor exposed to an increasing field are shown in fig.(1.7) in the top and bottom graphs, respectively.

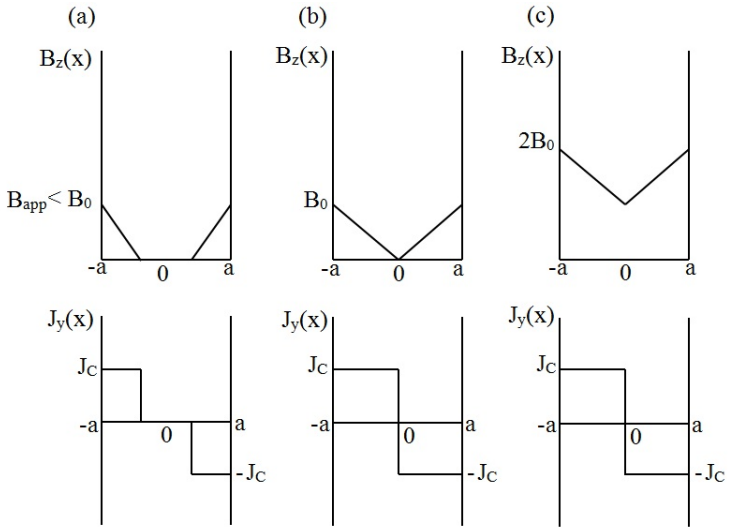

Figure 1.7: Magnetic field (top graphs) and current profile (bottom graphs) with increasing field applied according to Bean's model [2].

When the applied field is $B_{app} < B_0$, field starts penetrating the material but there is still a field-free region inside the slab, as in fig.(1.7a). Complete penetration takes place for $B_{app} = B_0$ (fig.(1.7b)) and for $B_{app} > B_0$ (fig.(1.7c)) producing consequent critical state in the material.

The magnetic field and the current profile inside a superconductor exposed to a decreasing field is shown in fig.(1.8). When the field starts being reduced, the critical current flows in the opposite direction (fig.(1.8a)) to prevent the flux (pinned into defects) to leave the sample. The amount of trapped field reaches a maximum value when field is decreased of a range $2B_0$ (fig.(1.8b)). With further decrement in field, the trapped flux inside the material remains constant (fig.(1.8c)). Considerable hysteresis are produced when the field is decreased, and field remains trapped inside even when the external applied field is $B_{app} = 0$. Since the applied field is smaller than the internal trapped field, the internal magnetization becomes positive. Therefore, when $B_{app} < 0$, a critical state in opposite direction to the one observed in the increasing field case, is produced as can be observed in the current profiles shown in the bottom graphs of fig.(1.8).

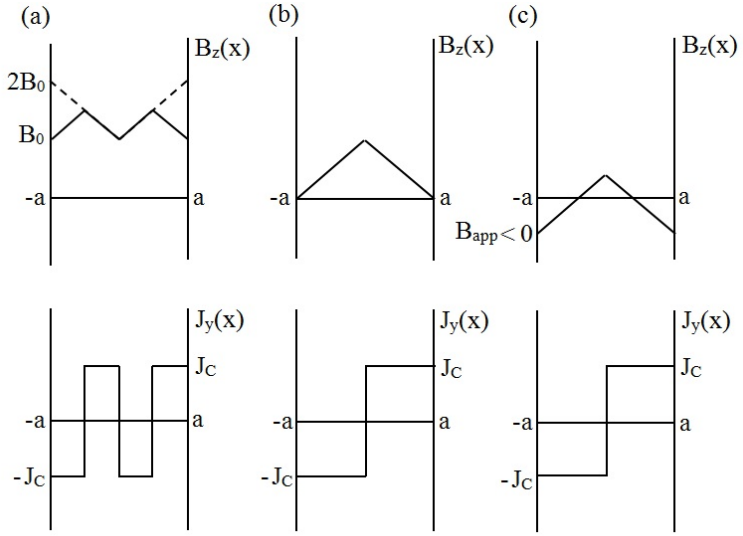

Figure 1.8: Magnetic field (top graphs) and current profile (bottom graphs) with decreasing field applied according to Bean's model [2].

The magnetization curve obtained for an entire, positive, sweep magnetization $0 \rightarrow B_{C2} \rightarrow 0$, is shown in fig.(1.9).

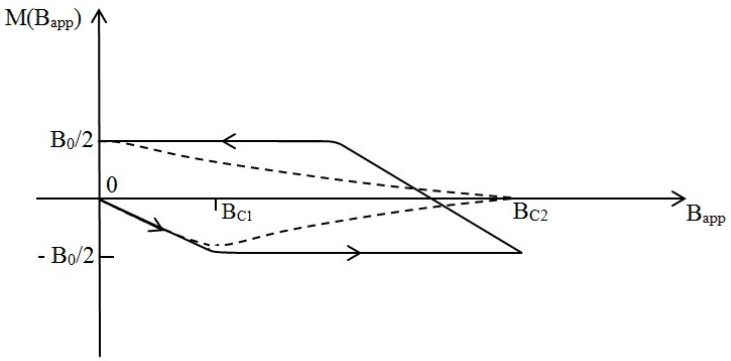

Figure 1.9: Magnetization curve obtained for an entire, positive, sweep magnetization $0 \rightarrow B_{C2} \rightarrow 0$ according to Bean's model (plain line) and in a realistic case (dashed line). [8].

As the field is increased up to B_{C1}, the superconductor shows perfect diamagnetism and the internal magnetization increases. As the field is further increased, according

to the Bean's model the magnetization remains constant (solid line), whilst, in a more realistic case, the magnetization decreases to zero (dashed line) since critical current is field dependent and in particular is zero at B_{C2}.

1.2 High Temperature Superconductors

High Temperature Superconductors (HTS), have been discovered in 1987 and, are oxygen compounds which are electrical insulators in the normal state. These compounds consists of oxygen atoms bound with other elements which are typically metals. Since the HTS are characterised by higher critical temperatures than LTS conductors, they require liquid nitrogen instead of helium as a refrigerator. Hence, their discovery raised the possibility of commercial applications of reasonable price. On the other hand, because of their ceramic nature, manufacture is rather hard. HTS are in fact, not continuous material but constituted by many small crystals, therefore the current flowing through the material is affected by:

- boundaries between grains, which act as an insulator and allow the passage of current via Josephon junctions (weak-link behaviour). The critical current density on a micro-bridge containing grain boundaries ($J_C = 2.6 \cdot 10^5 \mathrm{A/cm^2}$) has been found to be two orders of magnitude smaller when compared with the one measured intra-grain ($J_C = 1.6 \cdot 10^7$ A/cm^2) [9];
- misalignment between grains, which is required to be smaller than only a few degrees in the c-axis in order to not drastically affect the critical current [10].

High temperatures conductors can be potentially used for many electric power applications such as underground transmission cables, oil-free transformers, superconducting magnetic-energy storage, fault current limiters, current leads for LTS magnets high efficient motors and compact generators [11, 12].

First and Second generation wires and tapes

The big interest on achieving high transport currents in long cables, contributed to the optimization of materials and processing through the last years. Depending on the process used for making high temperature superconducting wires, they can be

classified in first generation wire (1G) obtained by powder in tube method (PIT) and second generation wires (2G) obtained through film deposition [13].

- First generation wires (1G): multi-filamentary Bi-2223 and Bi-2212 tapes and wires are commercially produced by PIT method because of their capacity of cleaving easily. The superconductor is firstly introduced in powder form into a silver tube, then drown in successive steps and, finally, is annealed. Individual tubes, which for two third are made in silver alloy, are produced and then bound together to obtain up to km length;
- Second generation wires (2G): YBCO and the 123 family do not cleave easily, therefore they are manufactured by etero-epitaxial growth on orientated substrates. The growth process is quite complicate since it has to provide extremely good grains alignment and it can involve up to 12 different layers.

The highest critical current value obtained for a standard wire of 4 mm width and 210 μm thickness BSCCO material at 77 K and in self-field is of about 170 A [14]. Although comparable to the current performances of 1 μm thick YBCO layer (J_C=3 MA/cm^2), a bigger engineering interest is addressed to 2G HTS because of their better in-field electrical performances at higher temperature.

1.2.1 YBCO structure

HTS superconductors are classified as perovskite because of their particular arrangement of atoms in the crystal. The YBCO unit cell is shown in fig.(1.10) and the main characteristics of this particular structure are listed below:

- Oxygen and copper are bound together in alternating layers containing chains and planes;
- The Yittrium acts only as a spacer between two CuO_2 planes and it is has been observed that it can be replaced by many of the lanthanide series of rare-earth elements without observing any appreciable change in superconducting properties;
- The Ba planes are known as intercalated planes and are surrounded by four oxygens along the edges of the unit cell;

- At the top and at the bottom of the unit cell there are copper-oxide chains with some oxygen missing. Oxygen vacancies are very important since determine changes in the critical temperature of the conductor (critical temperature results maximised to 92 K when the subscript in the formula is $x = 0.15$);

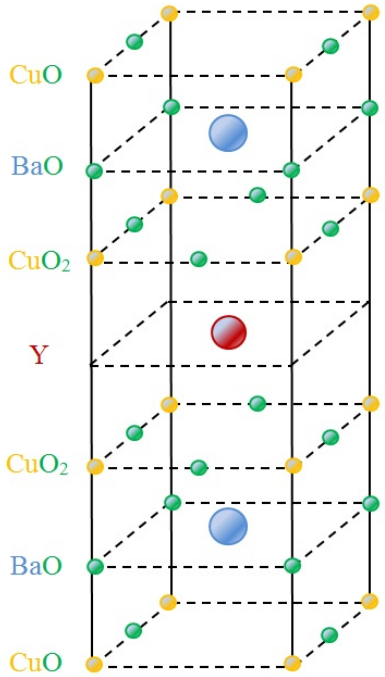

Figure 1.10: Schematic representation of $YBa_2C_3O_7$ unit cell.

Superconductivity takes place in the CuO_2 planes which are also known as conduction planes. Also, perovskite materials show strong anisotropy in many properties which differ depending if they are measured in the copper-oxygen plane or in the plane perpendicular to it [15, 16].

1.2.2 Thallium, mercury and bismuth compounds structure

The unit cell of thallium, mercury and bismuth compounds has a similar structural unit cell and layers arrangement, but some differences are observed in some specific atoms position and in the distance between CuO_2, planes, which are the ones responsible of the superconducting properties. Also, the structure of these conductors can have

different configurations, with one or more CuO_2 planes. Because of these differences, the compounds are characterised by different critical parameters T_C, I_C, B_C but generally all of them present higher transition temperature than YBCO ($T_C > 100$K). The schematic unit cell of Bi-2223 is shown in fig.(1.11)

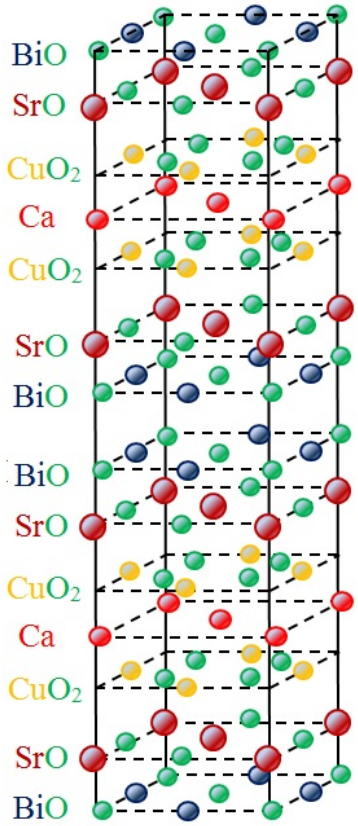

Figure 1.11: Schematic representation of Bi-2223 unit cell.

The main characteristics of the Bi-2223 unit cell are:

- Presence of CuO_2 layers, separated by a Ca layer without oxygen;
- Presence of CuO_2 grouping bounded together by middle layers of BiO and SrO;

Note that fig.(1.10) and fig.(1.11) are not in scale. BSSCO unit cell has much larger unit cell dimension along the c-axis when compared to YBCO and the inter-coupling between CuO_2 layers is of $\sim 12 \cdot 10^{-10}$ m, which is about the total size of the YBCO

unit cell, $\sim 11.68 \cdot 10^{-10}$ m. The increased space between CuO_2 layers is responsible of the increased critical temperature observed in bismuth and thallium compounds. Also, the distance between adjacent CuO_2 multilayers affects the way the flux vortices are pinned in these compounds: copper-oxygen planes along the *c*-axis are not well coupled and flux vortices arrange in array of pancakes confined in the CuO_2 planes and weakly coupled to the neighbours [15, 16].

1.2.3 Phenomenological phase diagram of HTS superconductors in presence of thermal fluctuations

The mean-field phase diagram of Type II superconductors, proposed by Abrikosov in 1957 is schematically presented in fig.(1.12) for low temperatures superconductors (black solid lines) and for high temperatures superconductors (red solid lines).

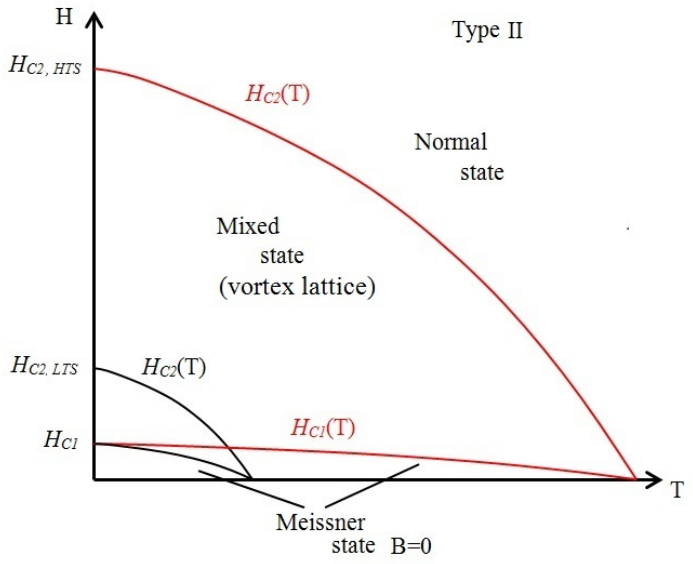

Figure 1.12: Mean field phase diagram of low temperatures (black lines) and high temperatures (red lines) Type II superconductors.

The phase diagram *H*-*T* of Type II superconductors present three regions: the Meissner phase where flux is completely expelled from the material ($H < H_{C1}(T)$), the mixed phase where flux line penetrates the superconductor ($H_{C1}(T) < H < H_{C2}(T)$), and the normal phase where the material transients to normal state ($H > H_{C2}(T)$).

The phenomenological diagram of Type II superconductors describes accurately the behaviour of conventional low temperature superconductors, but is inadequate to describe the behaviour of HTS conductors which, as clearly shown in fig.(1.12), operate in a much wider range of fields ($\mu H_{C2}(0) \sim 10^{-2}$ T in LTS and $\mu H_{C2}(0) \sim 10^{2}$ T in HTS) and temperatures ($T_C(0) << 77K$ in LTS and $T_C(0) > 77K$ in HTS) [17], and therefore are more subjected to the effect of thermal fluctuations. The effect of thermal fluctuations is also amplified by the small coherence length which characterise these conductors. The modified H-T phase diagram of a homogeneous, clean medium and of the one of a dirty one in presence of thermal fluctuations are presented in fig.(1.13a) and in fig.(1.13b) respectively.

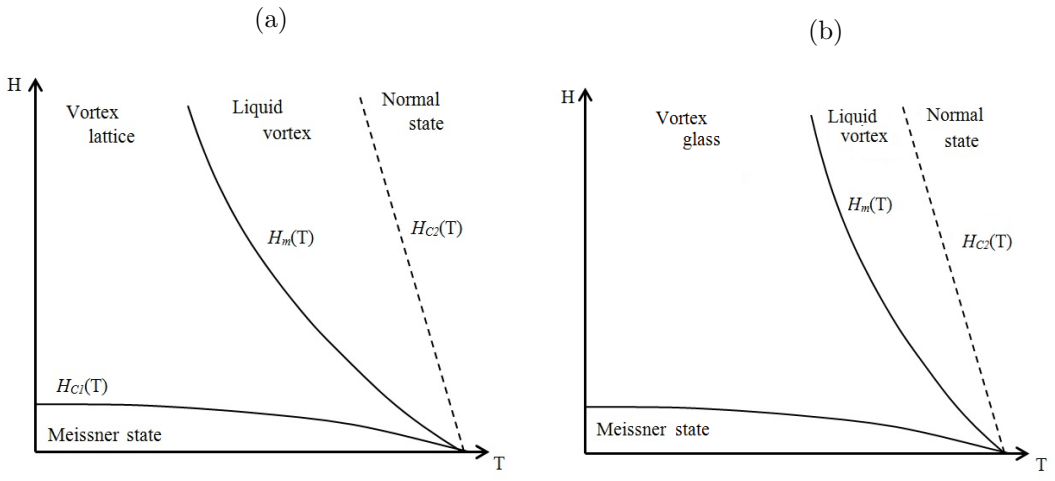

Figure 1.13: Phase diagram of (a) clean and (b) dirty high temperatures superconductors.

It can be observed that:

- A thermodynamic phase transition between a liquid phase, where vortices slowly move by thermal activation, and a solid state, takes place at $H_m(T)$;
- The Abrikosov vortex lattice is melted over a substantial part of the phase diagram;
- The vortex lattice can melt with increasing temperature (increased thermal fluctuations) as well as with decreasing field. In the latter case, in fact, flux lines are distanced apart (eventually $a_0 > \lambda$) and their interaction is exponentially

small. As a consequence, the regularity of the lattice can be lost leading to to the melting;

- H_{C2} is a crossover line between the normal and the superconducting state.

In absence of material imperfections, the phase change from liquid to solid takes place gradually and leads to the formation of a vortex lattice as shown in fig.(1.13a), where vortices are regularly distanced between each others, due to reciprocal interaction. The melting of the flux over a large region of the H-T diagram has been observed to strongly limit the current carrying capacity of an homogeneous single crystal [18].

The presence of imperfection destabilises the vortex lattice, thus the solid phase is replaced with a vortex glass phase in fig.(1.13b), where vortices lines are pinned and rigidly maintained in place but the lattice has lost its regularity. Whilst in the vortex fluid state vortices are mobile because of the thermal fluctuations (even in absence of a current), in the glassy state vortices are frozen in their position and the material has strictly zero resistivity. Note that in a perfectly clean material, the entire vortex lattice would be free to move in presence of a current, leading a non-zero resistivity (no truly superconducting state). Glass phase is instead a truly superconducting state where vortices frozen thanks to the interaction with the impurity of the material and, differently from the Meissner state, the glass phase can exist only in impure materials [19]. The position of the irreversibility line depends on the presence of disorder in the materials, and the more are the defects the higher is the melting line, as observable when comparing the phase diagram of dirty materials of fig.(1.13b) with the one of clan materials of fig.(1.13a). A dirty material is expected to be in the glassy state over a wide range of temperatures and fields, hence the importance of understanding the depinning mechanisms which take place in this state and how it is influenced by the presence in these conductors of pinning centres of different nature.

Two-Dimensional and Three-Dimensional melting .

The phase diagram presented in fig.(1.13b) is not valid for strongly anisotropic material such as BSCCO. In fact, despite their similar pronounced layered structure, YBCO is characterised by strong interaction between layers, so that the vortex lines can be thought as a single entity and the system can be considered three dimensional. BSCCO

is instead a strongly anisotropic superconductor, characterised by very weak inter-plane coupling. Thus, in BSCCO vortices can organise in two dimensional pancake structures, where each pancake lies on its CuO_2 plane and can move uncorrelated from its counterpart on the neighbour layers. Also, it has been observed that by changing temperature and field, the vortex dynamics in strongly anisotropic materials can change from 3D to 2D requiring a more complete equilibrium diagram, where several other vortex phases are included. Crossover from 3-D to 2-D melting takes place at the crossover flux density B_{cr} which has been estimated to be an unobtainable high value for YBCO ($B_{cr} \sim 10^3$ T), whilst for BSCCO is $B_{cr} \leq 1$ T [20].

1.2.4 Vortices dynamics in presence of thermal fluctuations

Thermal fluctuations and disorders strongly affect the dynamics of vortices. When a current is applied, vortices start moving under the action of the Lorentz force and the movement is obstructed by the presence of pinning centres. Thermal fluctuations can cause pinning and depinning of flux bundles as well as release and transportation of vortices even in presence of strong pinning centres.

Thermally activated flux creep

Flux lines sit at the bottom of a potential well of depth U, where U is the energy barrier which need to be win in order to move away from their pinned position. At finite temperature, thermal fluctuations can enable the flux lines to overcome the energy barrier, inducing creep-motion and leading to a measurable resistive voltage. Creep motion consist in hops of vortex segments or formation of vortex loops which cause *phase slip* as sketched in fig.(1.14a,b).

According to Anderson-Kim flux creep theory [21], the jump rate of flux bundles can be expressed as:

$$R = \omega_0 \mathrm{e}^{-\frac{U}{k_B T}} \tag{1.8}$$

where $\omega_0 = 10^5 - 10^{11}$ s^{-1} is the characteristic frequency of flux lines vibration and k_B is the Boltzman constant. In absence of current, the hopping rate is the same in both directions, therefore no net motion is observed. When instead a current is applied, the

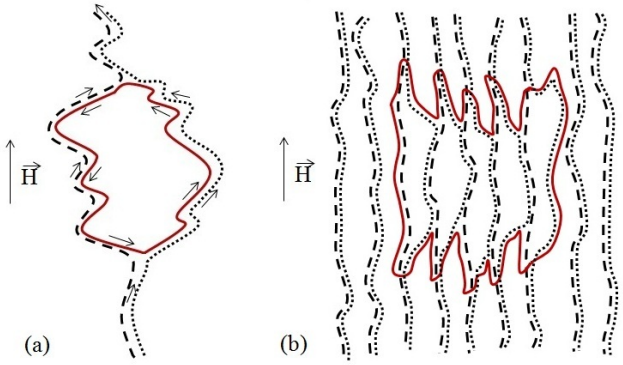

Figure 1.14: Schematic sketch of displacement of (a) a single vortex line and of (b) a vortex bundle in glass state in presence of thermal fluctuations.

motion in the forward direction is favoured to the one in the backward direction. The net jump rate in the direction of the current is expressed by eq.(1.9).

$$R_{\text{net}} = R_f - R_b = \omega_0 \left[\mathrm{e}^{\left(\frac{-(U-\Delta W)}{k_B T}\right)} - \mathrm{e}^{\left(\frac{-(U+\Delta W)}{k_B T}\right)} \right] \tag{1.9}$$

where R_f and R_b are the jump rate in the forward and backward direction respectively and ΔW is the work done by the current $\Delta W = J \times B$ to move the vortex out of its position. Thermal fluctuations are responsible of producing creep-type motion for current smaller than the critical one $J < J_C$ and the a net forward rate of

$$R_{\text{net}} = 2\,\omega_0 \mathrm{e}^{\left(\frac{-U}{k_B T}\right)} \sinh\left(\frac{\Delta W}{k_B T}\right) \tag{1.10}$$

When the flux moves, it generates an electric field $E = v\,B$, where v is the average velocity of the vortex lattice and it can be expressed as $v = R_{net}\,a_0$ where a_0 is the interflux line spacing. Since when x is small $\sinh(x) = x$, the electric field generated when $\Delta W << K_B T$ is given by eq.(1.11) and, according to flux creep model, for very small current $J \to 0$ leads $E \to 0$ [22].

$$E = 2\,\omega_0 \frac{\Delta W}{k_B T} \mathrm{e}^{\left(\frac{-U}{k_B T}\right)} \tag{1.11}$$

1.2.5 Experimental evidences of the melting transition

The effect of thermal fluctuation in HTS can be clearly appreciated by measuring the resistive transition of the conductor with increasing field. Although the resistivity is not a thermodynamic property, is however very sensitive to the drastic change in vortex dynamics which take place in presence of thermal fluctuations. Measurements on high-quality crystal (untwinned, defect-free YBCO single crystal) carried out by a different groups [23, 24, 25] revealed a remarkable broadening of the resistive transition with increasing field, as it can be seen in fig.(1.15a), where the resistive transition measured in magnetic fields of 0, 0.1, 0.5, 1, 1.5, 2, 3, 4, 5, 6, 7 and 8 T for $H \parallel c$ in an untwinned $YBa_2Cu_3O_{7-\delta}$ crystal is shown.

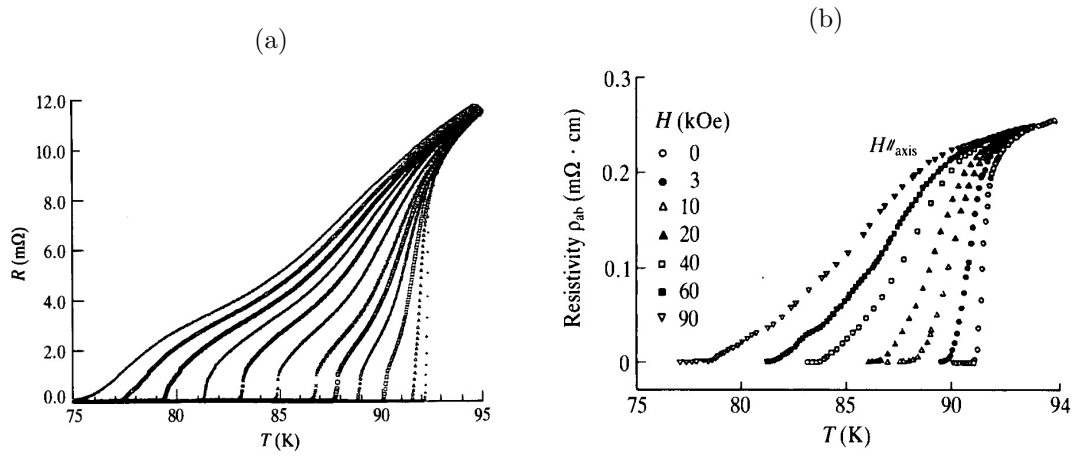

Figure 1.15: (a) Resistance of an untwinned $YBa_2Cu_3O_{7-\delta}$ crystal in magnetic fields of 0, 0.1, 0.5, 1, 1.5, 2, 3, 4, 5, 6, 7 and 8 T for $H \parallel c$ [23]. (b) Resistance dependence on temperature of a twinned YBCO crystal for several value of the magnetic field.[20].

Despite the broadening of the transition appeared to be well accounted by the thermal activated flux flow model (TAFF), the fit was quantitative good only down to $R \sim 0.1\,R_n$ where R_n is the resistance in the normal state. Below that point, the resistance drops more rapidly than the TAFF prediction indicating the possibility of either a crossover to another regime (with exponentially small resistance) or an actual phase transition (with ideally zero resistance) [20]. A sharp drop in resistance, takes place at a well defined B-T line and defines a "knee" in the transition curve.

The drop in resistance observed in YBCO crystal suggested a freezing/melting transition between a vortex liquid and a vortex glass phase. Resistivity measurement below the knee ($R \sim 0.1R_n$) revealed reproducible hysteresis when sweeping the field or the temperature, providing strong evidence of a first order transition [18]. Note that, whilst an abrupt jump of the resistance to zero is observed in clean material, as in fig.(1.15a), a more gradual, continuous transition to a glassy phase is observed in dirty materials where pinning dominates, as shown in fig.(1.15b) where measurements collected by Iye et al on a twinned YBCO crystal [26] are presented. Pinning is expected to be more effective on freezing the vortices and in fact a more rapid drop is observed in fig(1.15b) with higher onset temperature to vortex-freezing when comparing to clean material, being for example at 6 T, $T_C \sim 88$ K in the twinned YBCO crystal and $T_C \sim 79$ K in the untwinned one.

The possibility of a phase transition at a well defined melting temperature T_g between a vortex-fluid phase with linear resistance an a vortex-glass phase with truly zero resistance, was theoretically discussed by Fisher [27] who predicted an universal scaling behaviour near the vortex-glass phase transition temperature T_g.

Experimental support to this theory was provided by a number of authors [28, 29, 30, 31, 32] who observed phase transition in YBCO single crystal, polycrystalline YBCO and YBCO thin films. E-J characteristics obtained at fixed temperatures (from 72.7 K to 84.5 K with interval of 0.1 K) on a 0.4 μm thick YBCO epitaxial film in applied 4 T field by Koch et al. [28] are presented in fig.(1.16a) and show the general feature of a continuous transition. The dashed line in fig.(1.16a) indicates the transition temperature, $T_g \sim 80.8$ K.

According to the vortex-glass model predictions, the E-J characteristics of fig.(1.16a) can be universally scaled by using universal exponents and universal scaling functions. The scaling can be verified by plotting V/I scaled by $\mid T - T_g \mid^{v(z-1)}$ versus I scaled by $\mid T - T_g \mid^{2v}$ where v is the static and z is the dynamical critical exponent. As shown in fig.(1.16b), the current-voltage characteristics collapse on two master curves $T > T_g$ and $T < T_g$ obtained with v=1.7 and z= 4.8, representing the liquid and glass states of flux lines, respectively. Curves measured at H =2 T and H = 3 T also collapse on the same universal scaling functions and with the same universal exponents, as shown in the inset of fig.(1.16b) [33].

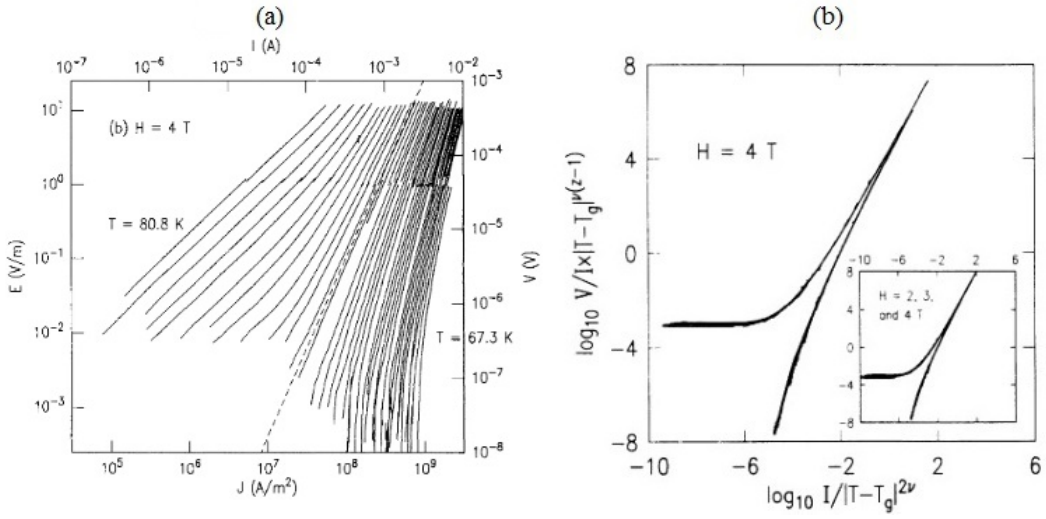

Figure 1.16: (a) E-J curves and (b) the scaling ($\nu = 1, 7, z = 4.8$) of epitaxial YBCO thin film at constant temperature (interval of 0.1 K) and magnetic field 4 T applied parallel to the c- axis [28, 33].

1.2.6 Effects of correlated and uncorrelated defects in Type II superconductors

As seen, the freezing of the flux-line liquid is modified by the presence of inhomogeneity and defects in the material. The most common pinning sites present in HTS are:

- **Point-like defects**. High temperatures superconductors are characterised by a high density of oxygen vacancies which constitute a source of weak defects randomly distributed;

- **Twin planes and extended defects**. Because of his orthorhombic structure, a and b directions in YBCO tapes are not exactly equivalent, and this strongly favours the formation of twin plains during the growth process. Point defects and impurities tend to accumulate along these plans and to attract pinning. This structure is present in the sample in a coherent way, making the pinning effective only in a range of field orientations;

- **Artificial defects**. The introduction of high density inclusion by heat treatment procedure has been demonstrated to be effective on increasing the critical current.

Impressive results have been obtained with bombardment of high energy beams of heavy ions which can penetrate through a substantial thickness of the material creating an extending set of correlated defects which lie on a same line and and are therefore called *columnar defects*. The latter are very effective once flux line are parallels to the artificial tracks created, but not for arbitrary field directions [34].

Point-like defects are uncorrelated disorders and act as weak pinning sites, whilst twin planes, grain boundaries and artificial defects act as correlated defects. Point disorders promote flux line wandering and entanglement whilst correlated disorders inhibit wandering and promote localization of flux lines.

Classical collective pinning model in a system with uncorrelated disorders.

The theory of the collective pinning model has been elaborated by Larkin and Ovchinnikon [35] and allow to describe the dynamic of vortexes in a system characterised by weak pinning centres and subjected to thermal fluctuation. According to this theory, weak random arranged pinning sites compete one another to maintain a vortex line in place and the vortex line, which is an elastic object, deforms and accommodates under the action of the exerted pinning force. Pinning forces of different sites sum up randomly and the total pinning force accumulated on a segment of length L is proportional to the square root of the segment length $F_{pin} \sim \sqrt{L}$. The total pinning force has to counteract the action of the Lorentz force, which on the other hand, increases linearly with distance $F_L \sim L$. Therefore, on long distances, the Lorentz force always wins and a stiff vortex remains unpinned. As a consequence, lattice deforms and breaks up in segments of length L_C, defined as collective pinning length, where each segment is pinned independently from the others and compete individually with the Lorentz force. The deformation takes place so that to achieve a new equilibrium configuration which is the one that minimize the sum of the elastic energy, spent in deforming the lattice, and of the pinning energy that has been gained with the displacement [35].

The net free energy change per unit volume between the elastic and pinning energies can be expressed as

$$\delta \mathrm{F} = \mathrm{E}_{elast} - \mathrm{E}_{pin} = C_{66} \left(\xi / R_C\right)^2 + C_{44} \left(\xi / L_C\right)^2 - f\xi \cdot n^{1/2} \cdot V_C^{1/2} \tag{1.12}$$

where f is the elementary force interaction, n is the number of pinning centres per unit volume, ξ is the core radius . The first two terms express the energy expense on distorting the lattice, whilst the last term represented the energy gained on pinning the line in that particular configuration. Because of the deformation, long range order of the flux line lattice is lost but the periodicity of the vortex configuration is maintained in a small coherence volume V_C defined by R_C and L_C, respectively the transverse and longitudinal volume dimensions. Inside each correlation volume, the flux lines lattice can thus be considered reasonably undistorted [35].

By minimising eq.(1.12) with respect of R_C and L_C, it can be obtained:

$$L_C = \frac{2C_{44}C_{66}\xi^2}{nf^2} \qquad R_C = \frac{2^{1/2}C_{44}^{1/2}C_{66}^{3/2}\xi^2}{nf^2} \qquad V_C = \frac{4C_{44}^2C_{66}^4\xi^6}{n^3f^6} \tag{1.13}$$

Small correlation volumes correspond to a lattice more distorted, and from eq.(1.13) it can be observed that this condition is verified in case of either increased presence of pinning centres (which in turn correspond to bigger interaction force $f(n/V_C)^{1/2}$ per unit volume) or smaller elastic moduli (big deformation under the action of small stresses) [20].

The collective pinning model provides an empirical formula which allows to predict E-J characteristic in material characterised by the presence of weak pinning defects. The model predicts that the voltage developed when the current is applied, is related to the pinning energy according to eq.(1.14):

$$E \sim \mathrm{e}^{-U(J)} \tag{1.14}$$

Accordig to the collective pinning model, the activation energy $U(J)$ dependence on current for $J << J_C$ at given temperature T can be expressed as:

$$U(J) \propto \frac{U}{k_BT}\left(\frac{J_C}{J}\right)^{\mu} \tag{1.15}$$

where k_B is the Boltzman constant, T the operative temperature, U is the pinning potential below the critical current and μ the glass exponent which characterises the vortex system in the vortex glass state.

The relation between voltage and current can be easily obtained by substituting eq.(1.15) into eq.(1.14) and by imposing the condition $E = E_C$ at $J = J_C$, which leads to:

$$\frac{E}{E_C} = \exp\left[\frac{U}{k_B T}\left[1 - \left(\frac{J_C}{J}\right)^{\mu}\right]\right] = \exp\left[u_0\left[1 - \left(\frac{J_C}{J}\right)^{\mu}\right]\right] \tag{1.16}$$

where u_0 is defined as $u_0 = U/(k_B \cdot T)$.

In presence of other vortices, the tilt energy accumulated on a single vortex line has to compete with the interaction energy between vortices in the neighbourhood, therefore is possible to pass from the collective pinning of a single vortex to the collective pinning of flux bundles. By balancing these two forces it can be found that the interaction between vortices takes place when the condition $L > a_0$ is verified [5]. The schematic H-T phase diagram of a medium characterised by uncorrelated disorder in presence of thermal fluctuations predicted by the collective pinning model, is presented in fig.(1.17). In each region is reported the glass exponent which characterise the specific vortex state.

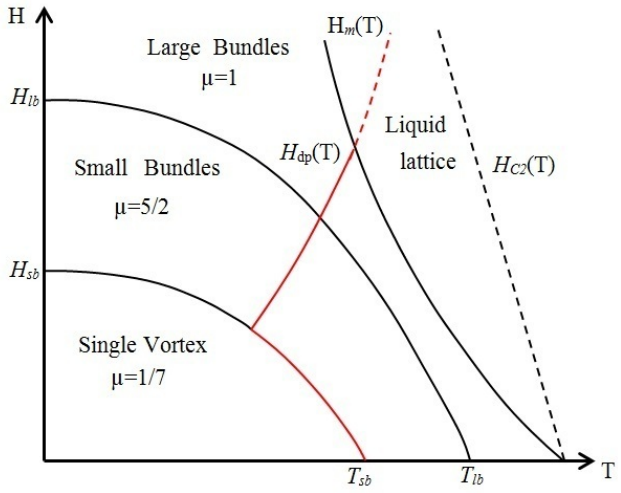

Figure 1.17: Phase diagram of High Temperatures Superconductors in presence of thermal fluctuation and weak pinning centres according to classical collective pinning model.

The different regions which can be distinguished in fig.(1.17) are:

- Single vortex region. Single vortex lines are pinned under the collective action of weak pinning centres at low temperatures and fields ($\mu_0 H_{sb} \sim 6$ T and $T_{sb} \sim 60$K for YBCO [5]);

- Small bundles region. Group of flux lines of small dimension ($a_0 < R_\perp$ and $R_\parallel < \lambda$, where $R_\perp$ and $R_\parallel$ are the flux bundles dimension in the ab plane and in the c-axis respectively) are collectively pinned in the region $H_{sb}(T) < H(T) < H_{lb}(T)$ ($\mu_0 H_{lb} \sim 10$ T and $T_{lb} \sim 70$K for YBCO [5]);

- Large bundles region. Large flux bundles ($\lambda < R_\perp$ and $R_\parallel \sim L_C$), are pinned in the region $H(T) > H_{lb}(T)$.

Note that the melting line $H_m(T)$ lies in the large bundles region and is only weakly perturbed by defects. The crossover red line $H_{dp}(T)$ of fig.(1.17) separates the area (below the red curve) where the different regimes are strongly influenced by thermal fluctuations from the area (above the red line) where the vortex-vortex interactions dominate..

Boson-glass model in system with correlated disorder.

Although all real materials are characterised by the presence of weak pinning sites, their contribution to pinning is reduced in presence of correlated defects which provide forces which add coherently, rather than randomly, over the extended pinning structure. Nelson and Vinokur [36] proposed a model for materials characterised by strong pinning centres such as columnar defect artificially added to the material. The model leads to prediction similar to the one obtained from classic collective pinning theory in presence of uncorrelated disorder. At sufficiently low temperatures, and in presence of field parallel to the axis of defects, vortices are strongly attracted by strong pinning centres, and lie in them or remain localised in the vicinity of the columnar pins, leading a zero linear resistance. The regime is called Boson-glass phase. The current-voltage characteristic relation provided by the Boson-glass model has the same current dependence of the one predicted by the classic collective pinning model and follows the relation:

$$E \sim \exp\left[-\left(\frac{J_C}{J}\right)^{\mu}\right] \tag{1.17}$$

The schematic H-T phase diagram of a medium characterised by uncorrelated disorder in presence of thermal fluctuation is presented in fig.(1.18).

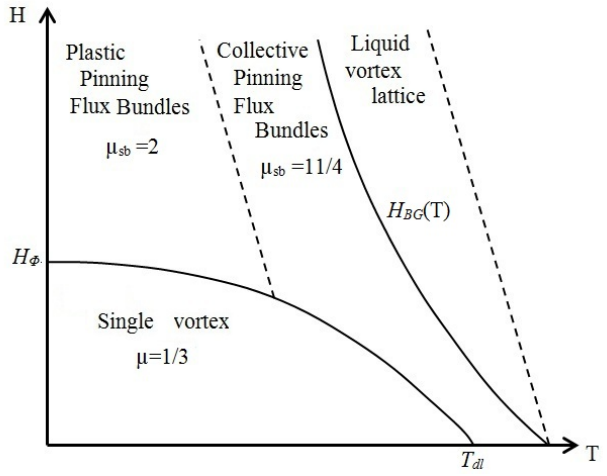

Figure 1.18: Phase diagram of High Temperatures superconductors in presence of thermal fluctuation and strong pinning centres (Boson-glass model).

Similarly to the uncorrelated disorder case, the phase diagram is characterised by crossover lines which separate regions where interaction of vortices is or not dominant, and in particular the following regions can be distinguished:

- Single vortex region. Single vortex lines are pinned by single rods at low temperatures and fields region ($\mu_0 B < \mu_0 B_\phi \sim 1$ T and $T < T_{dl} \sim 85$ K for YBCO [5]);

- Plastic pinning region. Plastic collective pinning takes place in a region at high field and low temperatures. In this region, a fraction of vortices is pinned by columnar defects and the rest is fixed by the shear force between the lattice;

- Collective pinning region. Collective pinning of flux bundles takes place in a region at high temperatures and fields.

Both plastic and collective pinning regions can act on flux bundles of different dimensions and in particular bundles are classified as small bundles when $a_0 < R_\perp < (a_0^2\lambda)^{1/3}$, intermediate bundles when $(a_0^2\lambda)^{1/3} < R_\perp < \lambda$ and large bundles when $\lambda < R_\perp$. On increasing temperature at given field, the system can pass through the three phases: from collective pinning of single vortex to plastic pinning of flux bundles, to collective

pinning of flux bundles. The glass exponent μ_{sb} associated to a change of phase in presence of small flux bundles is reported in the graph for each region.

1.3 Non linear E-J characteristic and current sharing

The investigation of the voltage-current characteristics of HTS conductors is important not only for understanding the superconductors vortex dynamics, but it is also crucial to correctly design and improve the performances of superconducting applications, such as superconducting coils and magnets. Different models have been suggested in literature in order to predict the E-J characteristic behaviour experimentally observed.

According to the critical state model, as the current is increased, the system undergoes an abruptive change from zero flow to flux flow regime when the Lorentz force is strong enough to win the pinning force which maintains the flux lines in place. The E-J characteristic predicted by critical state is the one represented in fig.(1.19).

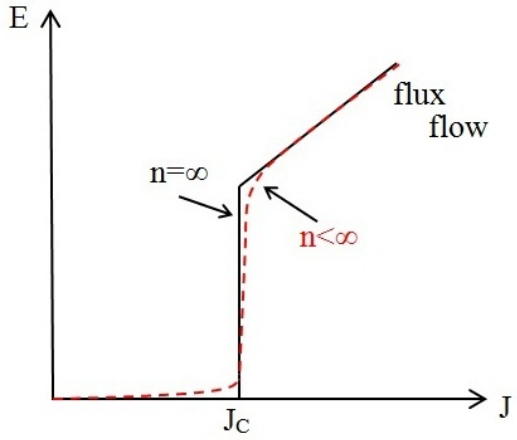

Figure 1.19: E-J characteristic predicted by critical state model (black plain line) and by power law model (red dashed line).

According to the critical state, depinning takes place only when the current reaches the value J_C and the Lorentz force is strong enough to overcome the energy barrier U.

HTS, non critical state

Because of the thermal fluctuations effect previously discussed, the current-voltage characteristics of practical superconductors do not appear as presented in fig.(1.19), instead voltage rises gradually near J_C as the transport current increases. The observed non-linearity of the transition characteristic, is due to different causes, both microscopic (such as flux creep and non linearity of flux motion) and macroscopic ones (such as spatial non uniformity of critical current).

The resistive transition of HTS is commonly accepted to be described by an empirical power relation. The model holds for:

- HTS characterised by a broad melted region, such as BSCCO;
- HTS in single vortex pinning regime (μ very small);

The power law commonly used is given by eq.(1.18).

$$E = E_0 \cdot \left(\frac{J}{J_C}\right)^n \tag{1.18}$$

where the critical current J_C is engineering critical current density and the respective inverse function of the simple power law is simply given by eq.(1.19).

$$J_S(E) = J_C \cdot \left(\frac{E}{E_0}\right)^{\frac{1}{n}} \tag{1.19}$$

The exponent n is a parameter indicating the strength of the non-linearity of the current-voltage characteristics. For an ideal homogeneous superconductor the n-number is expected to be $n = \infty$, whilst practical superconductors are characterised by $n < \infty$. Note the the case $n = \infty$ coincides with the critical state model. Since only ideal superconductors have $n = \infty$, for the real ones, which have finite n-number, the appearance of finite voltage below J_C is expected. Hence, the power law given by eq.(1.18) predicts $E \neq 0$ for any $J \neq 0$, implying that truly superconducting state does not exist [8]. The exponent n, is a useful indication of the sharpness of the transition. Also, it has been observed that the n-number is related at the macro and microstructural homogeneity of the superconductor. Measurements performed on different quality BSCCO-2223 tapes at 0.25 T, showed a decrement in n-number from 35 for an homogeneous sample to 25

for an inhomogeneous one [37, 38]. Thus an high n-number indicates a good homogeneity of the sample and hence a good distribution of the critical current. The exponent n is therefore used as a comparison criteria to qualify the goodness of the conductor.

1.3.1 Stabilisation of conductors

Current sharing. A disturbance of the system can cause a local increment in temperature. As a consequence, the operative current current can become locally greater than the critical current at that local temperature. In these circumstances, a local zone develops a resistance and the electrical field increases steeply. Practical superconductor must be stabilised with a low resistive matrix in order to prevent burn-out in the event of sudden lost of superconductivity. For currents above J_C and temperatures below T_C, current sharing takes place between the superconductor and the stability matrix. Stabilisation is achieved by using pure metal (usually copper and sometimes aluminium), which offers a small resistance at low temperatures and therefore presents a less resistive path when the superconductor locally turn to normal [39, 40]. In modern conductor copper is joined to the superconductor at an early stage of the manufacturing process and then the two metals are drowned down together [41].

The current sharing model predicts that, if the operative current is above the critical current, the superconductor carries the critical current whilst the excess in current diverts into the matrix. Current sharing can be schematically represented as two resistors in parallel as shown in fig.(1.20).

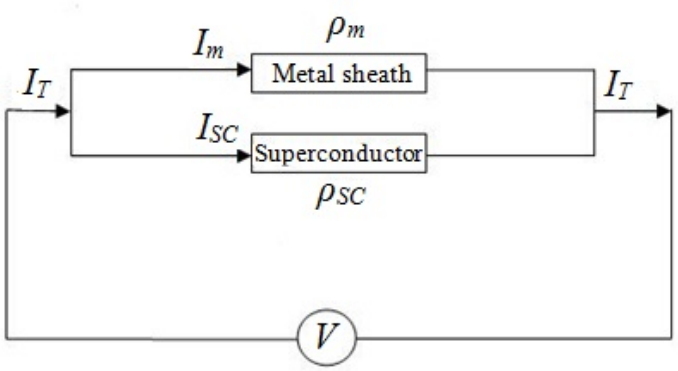

Figure 1.20: Current sharing model for HTS superconductors.

Extraction and underlying E-J from measurements of practical superconductors

According to the current sharing model, the total current density can be expressed as in eq.(1.20)

$$I_T = I_S(T) + I_M(T) = I_S(T) + \frac{V}{R_M} \tag{1.20}$$

which, if scaled with the area occupied by the superconductor A_S as in eq.(1.21),

$$\frac{I_T}{A_S} = \frac{I_S(T)}{A_S} + \frac{I_M(T)}{A_S} = \frac{I_S(T)}{A_S} + \frac{V}{R_M\, A_S} \tag{1.21}$$

it can be expressed in terms of critical current density as in eq.(1.22)

$$J_T = J_S(T) + \frac{E}{\rho_M(T)} \cdot \frac{1-\lambda}{\lambda} \tag{1.22}$$

where λ is the filling factor and it is defined as the ratio between the area occupied by the superconductor and the total area of the conductor inclusive of the matrix.

As a result of current sharing, the intrinsic E-J characteristics are superimposed with the contribution of the normal resistive sheath which corresponds to additional further curvature of the transition curve at high voltage and current. To extract the underline E-J characteristics, an accurate knowledge of the sheath resistance $R_M(T)$ is required. The resistance of the sheath $R_M(T)$ expressed per unit length of the conductor, is typically temperature dependent and is calculated as the resistivity of the superconductor $\rho(T)$ divided by the conductor cross section area A.

As mentioned in section (1.3.1), it has been observed that in practical conductors non critical behaviour takes place and the dissipation in the superconductors can be described according to the power-law of eq.(1.18), with $n \neq \infty$. Extensive study of power law behaviour on HTS have been done by different authors and a good agreement with experimental data of Bi-2223 and Bi-2212 has been found [42] [43]. As an example, the E-J characteristic of Bi-2223 high strength reinforced tape, measured in liquid nitrogen bath at 77 K and in self field scenario, is presented in a log$E$-log$I$ graph in fig.(1.21).

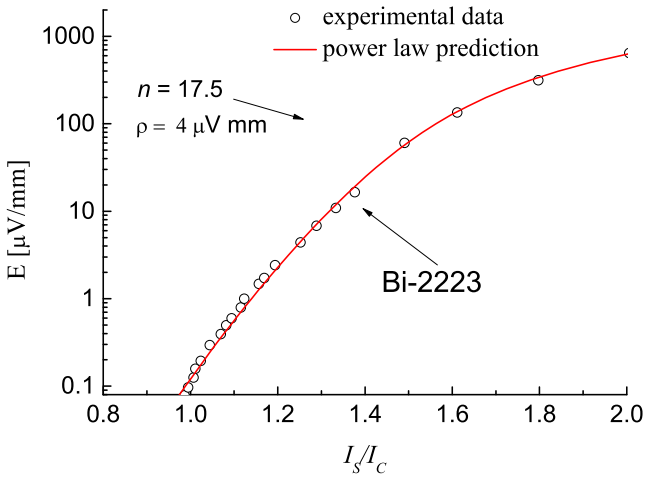

Figure 1.21: *E-J* characteristic of Bi-2223 high strength reinforced tape in liquid nitrogen bath at 77 K and in self field scenario.

E-J characteristic of Bi-2223 can be satisfactorily described by a constant power law exponent n=17.5, with I_C=150 A, as highlighted in fig.(1.21), where the exponent n has been calculated in the range 0.1-10 μV/cm.

1.4 Quench and disturbances

If during operations, a region of the superconductor is suddenly subjected to a release of energy, the temperature rises locally turning the region to normal. Since the current is flowing, ohmic generation takes place in the region interested by the hot spot. When the provided cooling power is not enough to contrast the heat locally generated, the normal zone spreads over a larger area by a process of ohmic heating and thermal conduction, with consequently further increment in temperature. The phenomena is known as *thermal quench*. A quench can cause overheating, overstressing and arcing in the conductor, and this phenomenon is more accentuated when the propagation of the heat is confined in a small zone. In this case active protective measures must be taken [41]. Quench process in a composite superconductor is governed by the following one dimension differential equation:

$$C_p(T)\,\frac{\partial T}{\partial t} = \frac{\partial}{\partial x}\left(k(T)\,\frac{\partial T}{\partial x}\right) + G(T,I) + P(x,t) - \frac{h(T)\,P}{A}(T - T_{\text{ref}}) \tag{1.23}$$

where T is the temperature, t is time, x is the spatial coordinate $C_p(T)$ is the volumetrically averaged heat capacity, k is the volumetrically averaged thermal conductivity, $G(T,I)$ is the average Joule power dissipation per unit volume, $h(T)$ is the heat transfer coefficient, P is the conductor perimeter of exposed to the coolant and T_{ref} is the system temperature. The left hand of the eq.(1.23) represents the rate of internal energy change in the section of the superconductor, the first term of the right-hand side represents the thermal conduction along the superconductor, the second one represents the heat generation, the term $P(x,t)$ is the power per unit volume deposited in the superconductor by en external perturbation and the last term on the right-hand side represents the convective cooling.

1.4.1 Current sharing in LTS and HTS superconductors

A significant difference between LTS and HTS can be observed in the slope of the critical current density $J_C(T)$ versus T as shown in fig.(1.22).

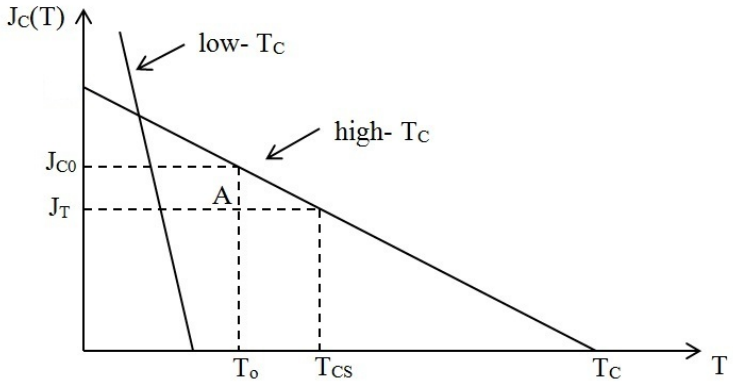

Figure 1.22: Critical current versus temperature. General slope for LTS and HTS.

The slope of $J_C(T)$ in high temperature superconductors is much smaller when compared to the low temperature superconductors one. This results in a greater difference in temperature $(T_C - T_{CS})$, where T_{CS} is the temperature at which the current

sharing occurs. For LTS, $(T_C - T_{CS})$ is in the range of few Kelvin, whilst for HTS superconductors the current share range is extended to potentially to 100 K at helium temperature. Therefore, current sharing in HTS cannot be neglected as normally done for low temperature superconductors, which are normally considered to jump from fully superconducting state to fully normal conductor state [44].

Superconductors are normally operated in safe conditions by carrying an operative current J_T smaller that the critical current at the operative temperature T_o $(J_T < J_{Co} = J_C(T_o))$, as indicated in point A of fig.(1.22). If the temperature is increased at the current sharing temperature T_{CS}, ohmic generation starts . Assuming a linear dependence of the critical current with temperature, $J_C(T)$ can be express as in eq.(1.24).

$$J_C(T) = J_T \frac{(T - T_C)}{(T_{CS} - T_C)} \tag{1.24}$$

According to the critical state model, when current sharing takes place, the conductor is able to carry the critical current density $J_C(T)$, whilst the matrix carries the excess in current $(J_T - J_C(T))$. The power generation per unit volume given by eq.(1.25) is the results of the current sharing between the superconductor and the composite metals, where $\lambda = A_{sc}/A$ is the filling factor between the superconductor cross section A_{sc} and the total conductor cross section A. Note that the generation term is also affected by the resistivity of the matrix and its dependence of temperature.

$$G = \lambda J_T E = \frac{\lambda^2}{1 - \lambda} J_T \, \rho \, (J_T - J_C(T)) \tag{1.25}$$

By substituting eq.(1.24) into eq.(1.25), it is possible to express the heat generation as a function of temperature, as in eq.(1.26).

$$G = \frac{\rho \, \lambda^2 J_T^2}{(1 - \lambda)} \frac{T - T_{CS}}{T_C - T_{CS}} = G_C \frac{T - T_{CS}}{T_C - T_{CS}} \tag{1.26}$$

The heat generation rises linearly between T_{CS} and T_C until reaching its critical value $G_C = \rho \, \lambda^2 J_T^2/(1 - \lambda)$ at T_C, as shown in fig.(1.23) by the plain line [41].

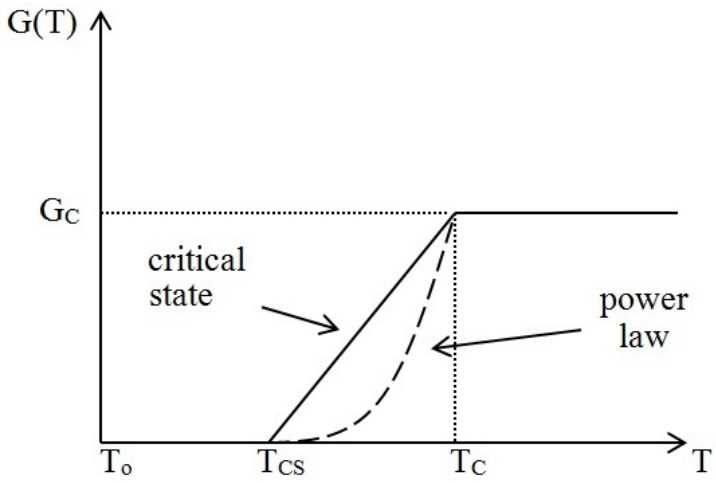

Figure 1.23: Schematic representation of heat generation in a normal zone according to (a) critical state model and (b) power law model.

Although eq.(1.25) well describes heat generation in LTS, is not accurate on describing heat generation in HTS superconductors where dissipation is a complex non-linear function of temperature. The critical current model does not hold anymore, and the superconductor is able to carry a current above the critical value and to develop a voltage, as flux flow starts, without turning to normal. Therefore, when current sharing starts, less current is diverted to the matrix and contribution to dissipation is given from both the superconductor and the matrix, resulting in a reduced heat generation as schematically shown in fig.(1.23) by the dashed line.

The heat generation strongly affects the thermal behaviour during quench.

1.4.2 Thermal stability

Thermal stability analysis is based on the determination of the normal zone and its propagation. Stability in HTS is much more complex to achieve than in LTS, mainly because of the following reasons:

- the extended current sharing window;
- the complex non linear heat generation;

- the strong dependence on temperature of the relevant thermal-electrical properties such as resistivity, specific heat and thermal conductivity.

Numerous quench studies on both HTS and LTS conductors show that HTS superconductors tolerate considerably larger disturbances than LTS materials do their large temperature margins and to the higher heat capacity at their working temperatures [45, 46, 47, 48, 49].

1.4.3 Minimum propagation zone

As previously explained, a disturbance causes a local increment in temperature and a formation of a normal zone where the current is shared between the metal sheath and the superconductor. The minimum propagation zone, is the minimum area of the tape of length l_{MPZ} that is able to originate a quench. A normal zone longer than l_{MPZ} grows irreversibly triggering a quench, whilst a normal zone smaller than l_{MPZ} collapses and fully superconductivity is recovered. Considering a superconducting wire as the one schematically represented in fig.(1.24), the l_{MPZ} can be roughly estimated for the one dimensional case.

A normal zone of length L generated by the hot spot is assumed to be at temperature T_C. The heat generated in the normal zone is given by $J_C^2 \rho A\, L$, where ρ is the resistivity of the normal state, A the cross-sectional area of the wire, and L the length of the normal zone. The boundary temperature of the wire is set to be T_{op} and a gradient of roughly $(\frac{T_C - T_{op}}{L})$ is observed along the sample.

The generated heat is conducted away under balanced conditions, therefore the minimum propagation zone length l_{MPZ} is obtained when the heat generated equals the heat dissipated by conduction, as shown in eq.(1.27):

$$2kA\frac{(T_C - T_{op})}{l_{MPZ}} = J_C^2 \rho A\, l_{MPZ} \tag{1.27}$$

where k is the thermal conductivity. The length of the minimum propagation zone can be obtained from eq.(1.28) and expressed as follow:

$$l_{MPZ} = \left\{ 2k\frac{(T_C - T_{op})}{J_C^2 \rho} \right\}^{\frac{1}{2}} \tag{1.28}$$

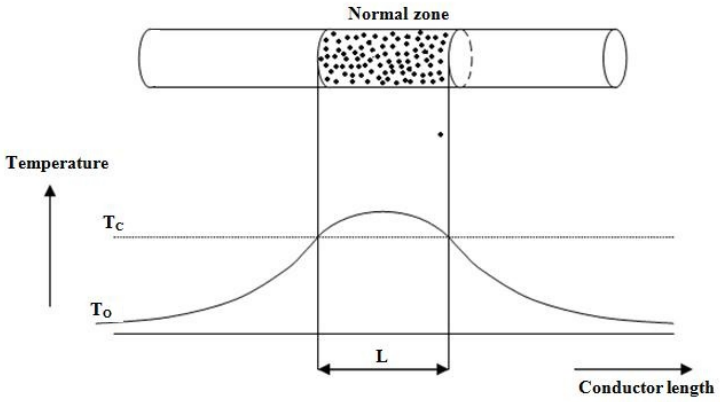

Figure 1.24: One dimensional distribution of the normal zone.

Note that in order to obtain a long minimum propagation zone, materials with high k and small ρ are required. The thermal conductivity can be expressed as function of temperature and of the electrical resistivity of the material according to Weidermann-Franz law of eq.(1.29), which is valid for most alloys and metals [41].

$$k(T)\,\rho(T) = L_0\,T \tag{1.29}$$

where L_0 is the Lorentz number $L_0 = 2.45 \cdot 10^{-8}$ W Ω K^{-2}. By substituting eq.(1.26) into eq.(1.28), the l_{MPZ} can be express as follow:

$$l_{MPZ} = \left\{ 2\frac{L_0\,T \cdot (T_C - T_0)}{J_C^2 \rho^2} \right\}^{\frac{1}{2}} \tag{1.30}$$

The l_{MPZ} can be estimated for LTS and HTS superconductors and the typical characteristic parameters for LTS (NbTi) and HTS (YBCO) [50, 51], are presented in table(1.1).

Parameters	NbTi (LTS)	YBCO (HTS)		
	4K	4K	20K	77K
k [$\mathrm{Wm^{-1}K^{-1}}$]	~ 1200	~ 700	~ 1600	~ 260
ρ[Ω m]	$\sim 0.1 \cdot 10^{-9}$	$\sim 0.2 \cdot 10^{-9}$	$\sim 0.25 \cdot 10^{-9}$	$\sim 5 \cdot 10^{-9}$
ΔT=$(T_C - T_{op})$[K]	~ 5	~ 88	~ 72	~ 15
c_P[J $\mathrm{Kg^{-1}K^{-1}}$]	~ 0.1	~ 0.36	~ 6.78	~ 97.94
l_{MPZ} [mm]	~ 11	~ 25	~ 30	~ 1.2
$NZPV$ [m/sec]	$\sim$194	~ 13.8	~ 1.37	~ 0.38

Table 1.1: Comparison between LTS and HTS characteristic parameters.

Comparison has been done between an LTS conductor which operates at 4 K and a HTS conductors which operates at 77 K, assuming that the critical current density of the conductor is $J_C = 10^9\,\mathrm{A/m^2}$, reasonable for both materials.

By looking at the HTS, the l_{MPZ} is observed to increase when these materials are operated at temperature well below 77 K, due to both the effect of the increased ΔT and the of the decreased ρ, and the l_{MPZ} becomes comparable with the value obtained for LTS at 77 K, if assumed the same critical current density for both LTS and HTS, operating in different field region. By using the values listed in table(1.1), it can be observed that at 77 K the ratio $kabi \cdot \Delta T/\rho$ of eq.(1.30) , similarly to LTS at 4 K, is of about $\sim 2 \times 10^{11}$ $\mathrm{K^2/\Omega}$ m. Thus the difference in l_{MPZ} between these two conductors operating one at 77 K and the other at 4 K, is mostly dominated by the square root of the resistivity of the normal material $\rho^{1/2}$, which differs by a factor of $\sim$7 between the two cases.

Concerning the electrical resistivity, it can be observed that is strongly non-linear with temperature being 50 times smaller at helium temperature than at 77 K. For more accuracy in calculation, its value should be averaged for large temperature gradient.

The size of l_{MPZ} is a propriety of the specific superconductor and it can be used as a distinguishing feature of the stability properties of the superconducting magnets. Note that the size of the disturbance are essential on determining the l_{MPZ}. If the disturbance cover a region much larger than L, in fact the quench initiation is determined by the energy deposited rather than the energy locally generated, and the effect

of conduction are negligible [41].

1.4.4 Minimum quench energy, MQE

The energy to initiate a quench is the one required to set up a minimum propagation zone . The MQE can be calculated by using equation (1.31).

$$\Delta E_h = V_{MZ} \int_{T_C}^{T_{op}} C_{WD}(T) dT \tag{1.31}$$

where V_{MZ} is the volume of the MPZ, C_{WD}(T) is the volumetric heat capacity at a given temperature, T_{op} is the operating temperature of the superconductor and T_C is the critical temperature of the superconductor.

Comparing the LTS at 4K with the HTS at 77 K according to the data listed in table(1.1) it can be found that $E_{\mathrm{LTS}} \sim 0.002$ J and $E_{\mathrm{HTS}} \sim 0.2$. The increased heat capacity is in fact partially cancelled by the factor L^3_{MPZ}. Thus, the energy to quench a HTS at 77K is about 100 times bigger than the one required to quench a LTS, therefore HTS are more stable.

1.4.5 Normal zone propagation velocity, $NZPV$

Once a quench has been initiated the boundary between the normal region and the superconducting one starts to propagate. The speed at which the normal/superconducting boundary propagates further into the superconducting region is defined as normal zone propagation velocity, ($NZPV$). $NZPV$ is the measure of the speed at which a travelling temperature wave carries the heat generation forward in the conductor. The general approach to calculate the boundary propagation velocity is to assume that the velocity of the normal state-superconducting boundary has reached the steady state and by using a translating coordinate system. The longitudinal normal zone propagation is given by eq.(1.32).

$$u_L = \frac{J}{C_p} \sqrt{\frac{\rho_m \; k_m}{(T_C - T_o)}} \tag{1.32}$$

where J is the current density, C_p is the average volumetric capacity of the conductor over the temperature range, ρ_m is the resistivity and k_m the thermal conductivity of the matrix, T_C the critical temperature, and T_o the operative temperature. The measure of the $NZPV$ is useful in magnet designs since it is an indication of the ability of the

magnet of protecting in case of quench. In general, a high NPZV implies a quick growth of the quench volume, which enable the stored electromagnetic energy to be dissipated over a larger volume reducing the risk of burn-out.

The NPZV has been estimated for LTS and HTS according to the parameters listed in table(1.1) and once again assuming the same current capacity. As it can be noticed from the value obtained, the $NZPV$ in HTS operating at 77 K more than 500 times smaller than the one of LTS. The propagation of the normal zone is slower compared with LTS, even at lower temperature than 77 K and it is known to become comparable to the one of LTS only at 4 K (in the table the current density has not been carried with temperature). The difference observed is mostly due to the higher heat capacity at high temperature (factor > 1000).

The quenching process is extremely slower in HTS rather than LTS: it takes almost an hour to spread a normal zone developed at 77 K over a km, whilst only few seconds (~ 5 sec) are needed for a LTS conductor. The energy stored is dissipated in a much smaller volume, increasing the local heating and the risk of damaging the conductor. Despite the low $NZPV$, HTS are still promising material for application thanks to their high critical current density, elevated magnetic field and increased thermal stability.

2

Apparatus and measurements methodology

Quench initiation and propagation tests as well as E-J characteristic measurements have been performed on short HTS 2G YBCO Cu stabilised samples. Measurements have been carried out in both cryogen and cryogen-free facilities and opportune modifications have been done where the system presented limits in the design for performing the tests.

The cryogen facility allowed measurements in nitrogen in a narrow range of temperatures (67 K-77 K) achieved by reducing the internal pressure of the system. The cryogen-free facility allowed to perform measurements in a wide range of temperatures (15 K-86 K).

This chapter focuses on:

- Description of the samples measured;
- Procedure for instrumenting the sample with thermocouples and voltage taps for quench and E-J characteristics measurements;
- Description of cryogen and cryogen-free facilities;
- Description of the experimental procedure developed in order to ensure the reproducibility of the test conditions for similar runs.

2.1 Tape description

The YBCO tape supplied by SuperPower [52] and produced by Ion-beam-assisted deposition method (IBAD), has the structure shown in fig.(2.1).

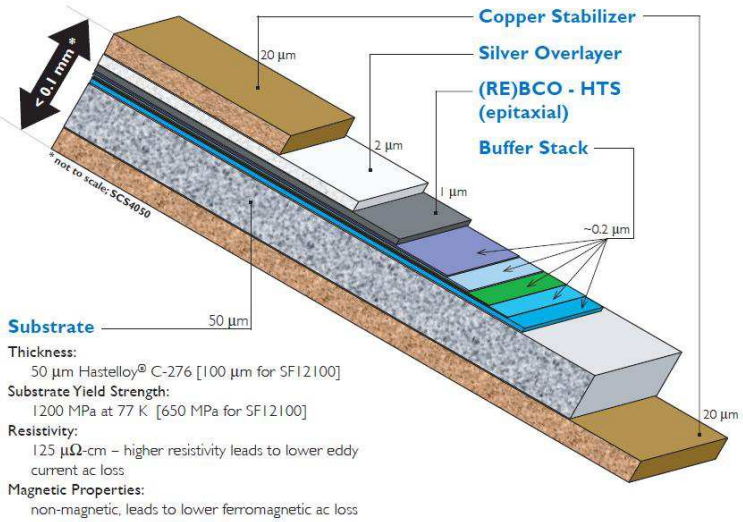

Figure 2.1: Layers structure of the YBCO tape produced by Superpower [52].

During the process the buffer layers, the ceramic-based superconductor material and the protective over layers are added on top of an inexpensive high strength metal alloy tape. The IBAD buffer stack of fig.(2.1) include the following layers:

- The superconducting layer of YBCO of about 1 μm thick;
- The Hastelloy layer of about 50 μm which provides mechanical stability to the tape;
- The external copper protective layers 20 μm thick, which function as thermal stabiliser and provide protection in case of overcurrent.

The total thickness of the sample, is 100 μm and the tape as supplied measures 4 mm width as indicated in fig.(2.1). SuperPower has successfully produced single piece YBCO tape with over 1000 m length with uniform critical current of $I_C(77\text{K}, \text{sf}) = 110-145$ A [53, 54, 55].

2.2 Quench measurements set-up

2.2.1 Sample instrumentation for quench measurements

In order to monitor the quench initiation and propagation, a set of spatially distributed voltage taps and of miniature differential thermocouples have been soldered directly to the sample as shown in fig.(2.2).

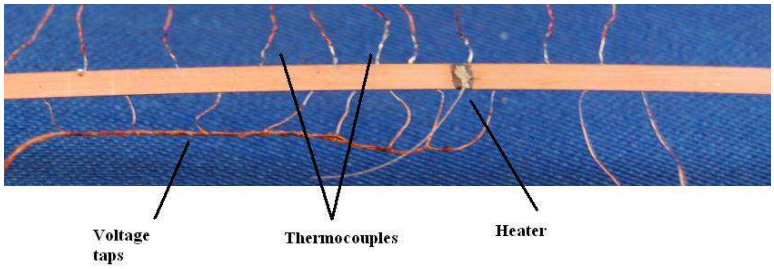

Figure 2.2: Instrumentation of 2G YBCO sample for quench measurements.

The mean features of the set-up of fig.(2.2), which it would be refereed to as *quench set-up*, are:

- The voltage taps and the thermocouples are soldered on the Hastelloy side of the tape, in order to reduce the chance of damaging the superconducting layer;
- The differential thermocouples have been realised by twisting a constantan wire between two copper wires to form two junctions. One of the two junction allows to measure the temperature of the tape, the other one is used as a temperature reference;
- The wires used for the both voltage taps and thermocouples are about 70 μm in diameter and, in order to reduce heat losses through the connections, they have been thermally anchored to the first stage;
- The miniature heater needed to initiate a quench event has been made by depositing in the middle of the sample a layer of conductive silver-loaded epoxy on top of a layer of carbon loaded epoxy. One of the electrode is connected to the heater and the other one on the sample in order to ensure the deposition of the energy on the sample. The heater is mounted on the sample, opposite to the

voltage taps side and is used to discharge a short heat pulse (10 100 msec), so that to initiate a hot spot in the conductor which gradually increases until an irreversible quench is detected. Increasing amount of energy has been deposited on the tape by varying the level and the duration of the electric pulse. The final resistance of the heater depends on the contact made with the sample and it is required to be of the order of Ohms so that to generate sufficient heat to quench the conductor.

Sample instrumentation for in-field quench measurements

For in-field measurements, the sample has been mounted between two Neodymium Iron Boron magnets. A clearance of ∼1 mm has been maintained between the magnet faces and the sensors on the sample surface. A 100 μm thick, 2 mm wide strip of G10 fiber glass was bounded with epoxy to the tape surface to stiffen the tape so that a constant distance could be maintained from the magnets surface.

2.3 *E*-*J* characteristic measurements set-up

E-*J* curves have been measured in a nitrogen liquid pool and in cryogen-free conditions. The transition characteristics measurement require the tape to carry a current up to about 1.5 times the critical current value of the tape at the operative temperature, $I_{\rm op} > I_C(T_0)$. The projected current of the 2G tape at 10 K in presence of self-field is of $\sim$ 1000 A, which is of course too high for the available measurement facility. In order to overcome the current leads limitations in current, which would have become an issue for measurements on lowering the operative temperature, the cross section of the tape has been reduced. A novel procedure to reduce the cross section without damaging the tape has been developed and allowed measurements in a range of temperatures still unexplored.

2.3.1 Reduction of the sample section

By assuming an uniform distribution of current along the sample at given operative conditions, the critical current can be expressed as in eq.(2.1)

$$I_C = \int J_C \, \widehat{n} \, dS \sim J_C \, S \tag{2.1}$$

where S is the cross section of the conductor, $\widehat{n}$ is the unit vector normal to the surface dS and J_C is the critical current density. Note that the critical current density is independent on the sample geometry $J_C = f(B, T)$.

Thus, a reduction in the cross section of the sample enables a reduction of the critical current I_C. However reducing the cross-section without bending or damaging the tape is a challenging.

2.3.2 Sample holder and and cross-section reduction

The sample has been soldered on two large current contacts (each 35 mm long) separated by a short length (1.2 mm) in between for voltage measurement, as shown in fig.(2.3). A pair of voltage taps is soldered on the tape at the extremities of the gap, where a reassessment of few microns has been included and filled with cigarette paper, in order to measure the actual voltage of the superconductor without including the transverse resistance at the current injections.

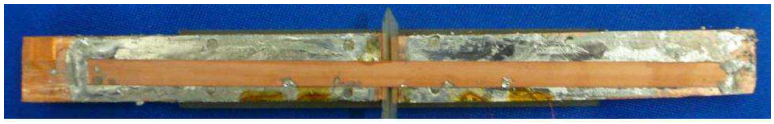

Figure 2.3: Sample set-up for transient characteristic measurements.

In order to provide mechanical strength to the tape, the gap of fig.(2.3) is filled with Stycast, then the cross section is reduced by milling. In this particular set-up with reduced cross-section, less accuracy on the voltage taps location is required since the operative current applied is critical only for the narrowed section.

2.4 Experimental flow cryostat designed for quasi-adiabatic measurements

A dual operational refrigerator/flow cryostat able to carry 1200 A transport current and to work in the range 4.2 K - 77 K, was designed and built. A picture of the test apparatus is shown in fig.(2.4) where the main components are labelled by numbers.

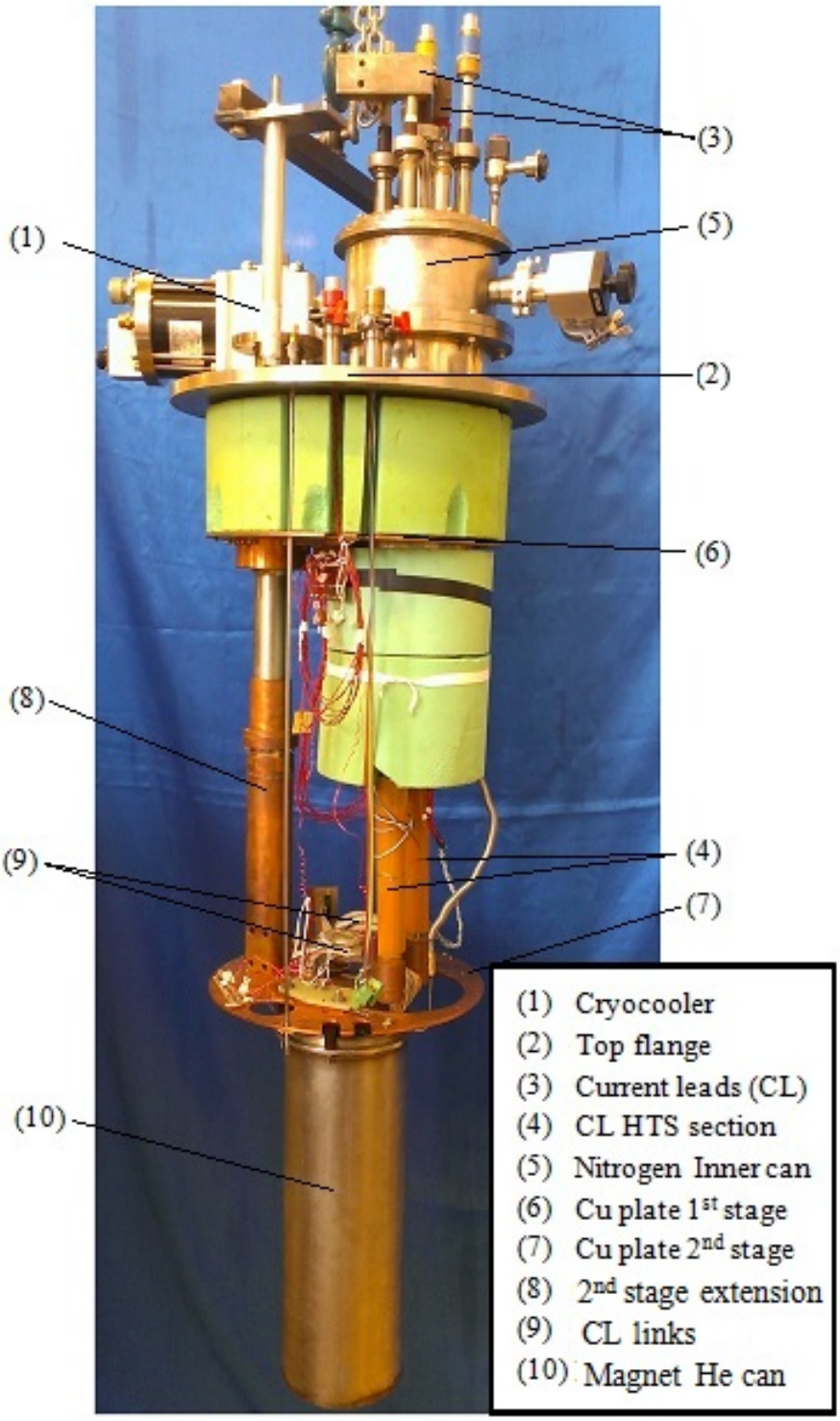

Figure 2.4: Picture of the experimental apparatus for quasi-adiabatic measurement.

The main components of the cryostat and their features are listed below.

- The facility is equipped with a cryo-refrigerator Sumitomo RDK-415D 4K 2 stage GM cycle (1) with 1.5 W at 4.2 K and 45 W at 50 K [56] ;
- The top flange (2) of the nitrogen vessel contains a fill and a vent path, instrumentation connectors and a pair of isolated current leads (CL) (3);
- The current leads are constructed in two parts: an upper copper section which delivers the current from outside the cryostat at room temperature into the cryostat (3) and a lower CL section made by HTS tapes (4). Each HTS section is made from a stack of five Ag-Au 4% HTS tapes. The lower HTS section of the current leads allows to minimise the heat leaks and to provide stability during measurements. Minimization of losses is of great importance, in particular at low temperatures where the heat capacity C_P is small and few watts can lead great difference in temperature to the system;
- The long upper copper section of the current leads passes through the nitrogen inner can (5) where it is submerged in liquid;
- The double wall stainless steel inner can (5) allows to store $\sim$ 10 litre of liquid nitrogen. The liquid nitrogen not only intercepts the heat leaks but also guarantees a 77 K upper temperature boundary on the top of the current leads HTS section (4) which is placed below the can;
- The HTS section of the current leads, is about 200 mm long and has been made from two stacks of ten AMSC thin tapes which are soldered inside a groove. The grove has been milled in a thick stainless steel wall for support.
- The 1^{st} stage copper plate (6) is thermally anchored to the first stage of the cryocooler, providing a shield from the top flange environment;
- The 2^{nd} stage copper plate (7) is thermally anchored to the cold finger (second stage of the cryocooler) through a copper extension (8);
- The ends of the HTS sections are clamped to two flexible electrical links which end on the other side in a two square copper sections (9) which in turn are bolted to the 2^{nd} stage Cu plate (7). The link to the cryocooler coldfinger provides

thermal anchor to the bottom of the current leads which are maintained at a stable temperature below < 77 K;

- The rig has been designed to be compact with a footprint of 0.5 m^2 and can be integrated with wide bore, 180 mm, 5 T magnet to test tapes and coils in field [57];
- The double wall He can (10) is used only in liquid helium operation, and allows to isolate the sample environment from the helium bath in which the magnet is immersed, extending the measurable range of temperatures;
- The rig is inserted in a double wall staleness container and further protection from radiation during measurement in vacuum, is provided by the insertion of the super-insulation layers. The vessel allow measurements in high vacuum environment ($10^{-5} - 10^{-6}$ mbar) achieved by connecting a diffusion pump to the cryostat at the top flange.

2.4.1 Cryostat operational mode

The cryostat shown in fig.(2.4) can operate with different configurations such as without helium, with helium in quasi-adiabatic conditions (vacuum measurements) and with a static helium gas. All the possible working temperature and field configurations are listed in fig.(2.1). The helium gas option allows to use the full current of the HTS leads but implies a higher base temperature due to the added heat leak impinging on the available cooling power.

Mode	Cooling	Temperature Range [K]	Maximum Current[A]	Magnetic field [T]
Vacuum	Conduction	10 - 87	600	0
He gas	Vapour	15 - 87	1200	0
He liquid (no magnet)	Liquid	4.2	1200	0
He liquid (magnet)	Vapour flow	4.2 - 87	1200	0 to 5 $\pm$ 0.3

Table 2.1: Data for different operative configurations of the measurement facility [57].

As shown in table(2.1), depending on the working configuration, the cryostat can operate in a wide range of temperatures, the widest between 4.2 K-87 K when it operates with liquid helium. The wide range of temperatures achievable allows different measurement possibilities on 2G HTS such as:

- Possibility of investigate the critical current dependence on temperature and field up to 5 T;
- Possibility of exploring the dependence of critical current on the orientation of the external field;
- Possibility of investigation of the thermal stability of HTS tape and coils by conducting quench propagation measurements in self field scenario and in-field scenario.

2.4.2 Sample platform

In order to conduct measurements a special platform, as the on schematically presented in fig.(2.5), has been designed.

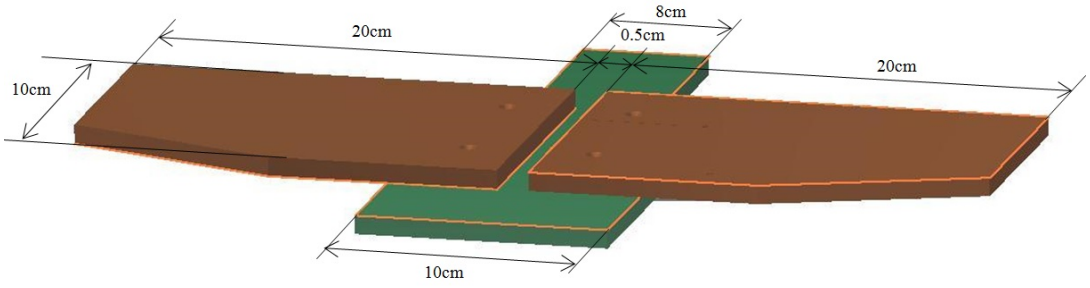

Figure 2.5: Schematic representation of the platform for dry operational mode measurement.

Two pieces of copper separated by few millimetres gap, were bolted on a piece of G10 to provide easy handling and ensuring electrical isolation between the two parts. The sample sits on across two pieces of copper ensuring the flow of current through it. To ensure the smallest temperature gradient possible across the sample, the platform is equipped with two heaters and two Cernox sensors (one on each side), to

allow the automatized PID control of temperature. Two veroboards provide electrical connection to the logger. The copper platform is also supplied with small holes to sit the thermocouple references during measurements.

The platform can be fixed directly to the second stage copper plate through copper bars. The design of the copper platforms in dry and wet operational mode is conceptually similar and differ only in dimensions. The platform for measurements in liquid helium has, in fact, a circular shape in order to fit the magnet He can (10) shown in fig.(2.4), used for measurements in field. A picture of the platform used in wet operational mode is presented in fig.(2.6).

Figure 2.6: Platform for wet operational mode measurements.

Once the sample set-up has been done and the sample is soldered into the platform, the two Copper bars can be soldered in situ on the bottom side of the square copper sections (9) of fig.(2.4), where electrical connection with the current leads and thermal anchoring to the coldfinger of the cryocooler is provided.

2.4.3 Electrical and thermal links

The electrical links between the current leads and the platform have been designed. A good contact surface area is needed in order to allow the current injection without affecting the platform temperature. It is also important to make the two electrical contact links as symmetrical as possible.

The temperature of the platform is influenced by a number of different contributions to heat within the system (mainly the heat leak contribution due to the current leads and the radiation background). However the temperature on the platform is largely controlled by the temperature of the 2nd stage cryocooler after the background heating has been removed. A good thermal contact between the cryocooler and the sample platform is required. Also, the low current leads section needs to be thermally linked to the second stage temperature.

From a transient energy balance to the platform is possible to work out the surface of copper joint needed to heat up the contact surface of 0.1 K in 10 seconds. The balance is given by eq.(2.2).

$$\rho_{Cu}\, V\, C_P\, \Delta T = R\, I^2\, t \tag{2.2}$$

where ρ_{Cu} is the density of copper and $_{Cp}$ the heat capacity.

By expressing both the volume V and the resistance R in eq.(2.2), as a function of the surface area A, the cross section can be obtained by eq.(2.3).

$$A = I \sqrt{\frac{\rho\, t}{\rho_C\, C_P\, \Delta T}} \tag{2.3}$$

Assuming the maximum operative current $I_{\mathrm{op}} = 600$ A and taking the value of density, of the heat capacity and of the resistivity of copper at 30 K, $\rho_C = 8$ g/cm^3, $C_p = 0.1$ J/(kg K) and $\rho \sim 0.2\ 10^{-6}\ \Omega$ cm respectively, the surface required for each contact joint results to be $A \sim 3$ cm^2. Note from eq.(2.3), that the cross section is not a function of the length of the contacts.

Two copper braids as the one shown in fig.(2.7) have been designed. One end of the braid was soldered to a copper block and clamped to the lower copper section of current leads whilst the other was electrically connected to the squared copper sections.

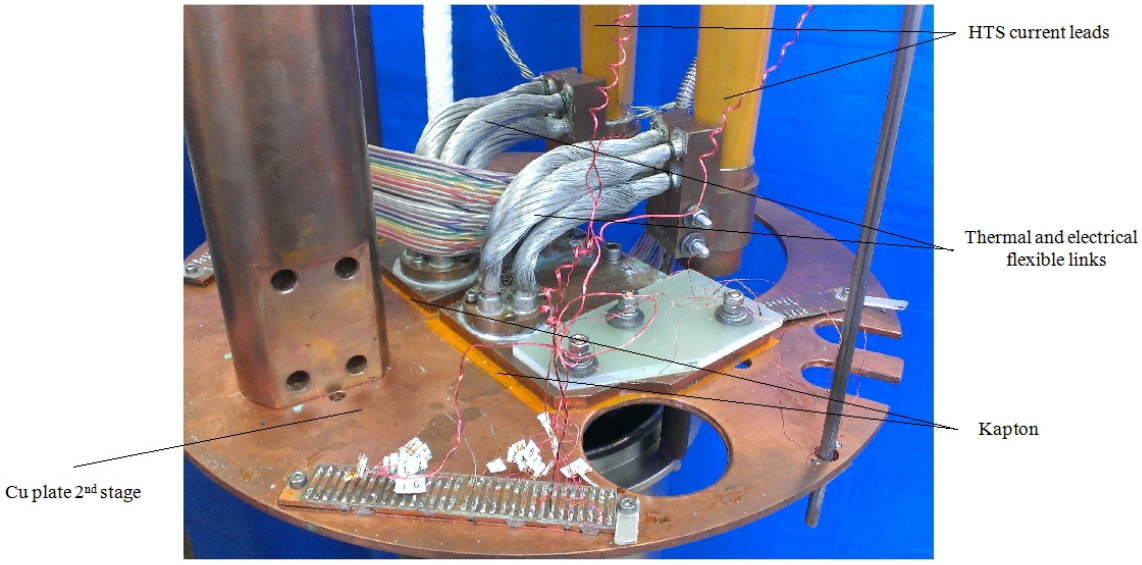

Figure 2.7: Thermal and electrical flexible links.

Thus, the squared copper sections at the end of the flexible electric links (9) of fig.(2.7) have been designed with the double function of providing not just electrical but also thermal connection to the platform:

- Thermal contact: the square sections are bolted into the 2^{nd} stage Copper plate (7) separated by a thin layer of Kapton to avoid electrical contact. The bolts were electrically isolated using tufnol bushes;
- Electrical contact: a hole trough the 2^{nd} stage copper plate allow access to the copper plate from underneath, where the two copper bars connected to the sample platform can be soldered.

2.4.4 Operations for adiabatic measurement

Before starting any measurement, the following experimental steps have been followed to ensure the environment inside the cryogen-free test rig was reproducible for all experiments:

- The vacuum of the system has to be pulled down to $\sim 10^{-5}$ mbar;
- The cryostat is switched in order to cool the system down;
- The top of the current leads is maintained at 77 K by filling the nitrogen can with liquid nitrogen;
- The operating temperature of the sample is controlled by adjusting the power of two heaters located on both sides of the platform. Two PID controllers fine tune the balance of the heaters.

Once the sample temperature has been stabilised at the desired operating temperature, the E-J measurement and the quench measurement can begin.

2.5 Experimental cryostat for E-J characteristics measurements in liquid nitrogen pool

A glass Dewar has been used to investigate the E-J characteristics of YBCO coated conductors tape immersed in liquid nitrogen pool. A schematic diagram of the test rig is shown in fig.(2.8).

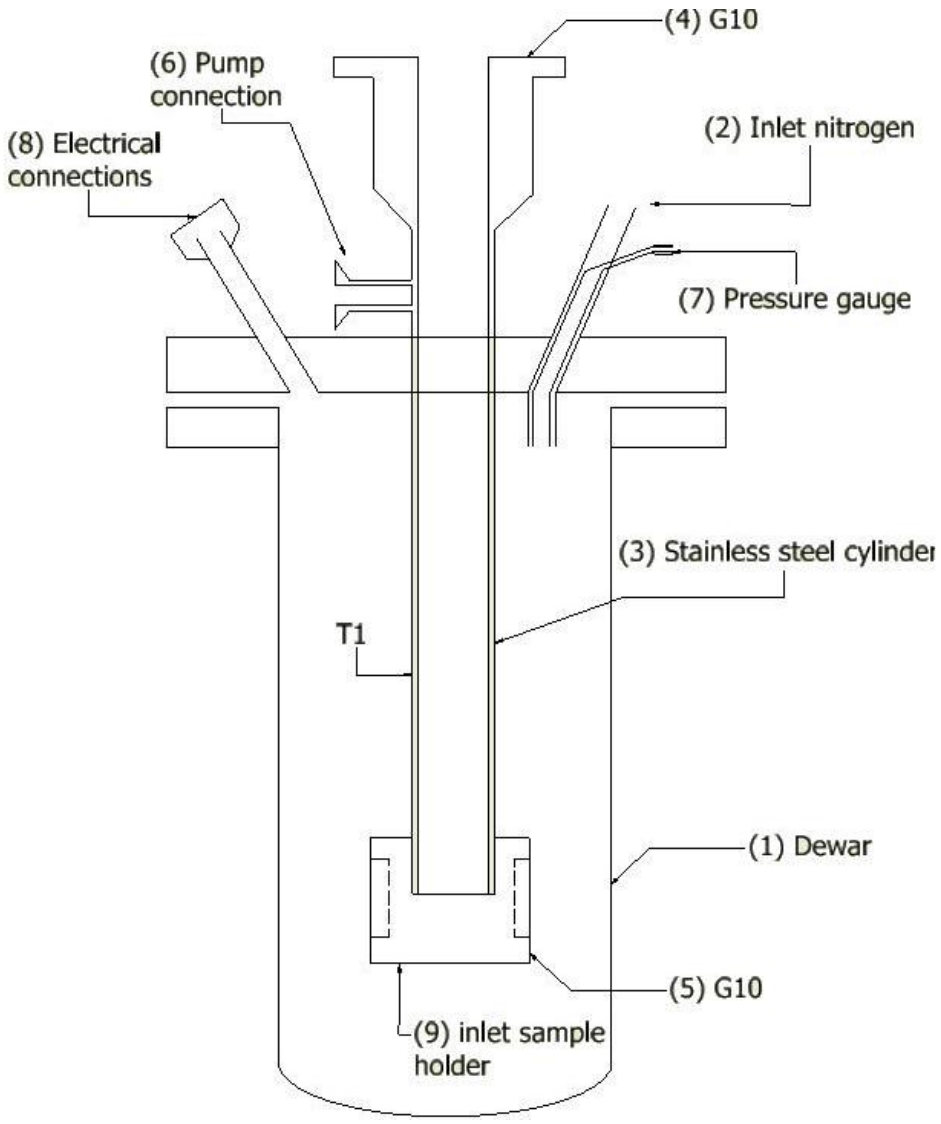

Figure 2.8: Schematic design of the cryostat used for measurement in liquid nitrogen pool

The Dewar (1) is a glass vessel with double wall vacuum. The nitrogen is constantly refilled through the entry line (2). A shut off valve is located at the beginning of the nitrogen line to seal the system during the measurements at low pressure. The rig allows a number of measurement in a liquid nitrogen at atmospheric pressure and below atmospheric pressure.

The current leads run down the centre of the Dewar and deliver current from the current source to the bottom of the Dewar, where the sample is located. The current leads are maintained fixed in place into a G10 tube through which the nitrogen gas exhaust is forced to flow providing cooling during the operation. The G10 tube also provides electrical insulation from the top flange of the Dewar. The pressure of the Dewar is monitored with a vacuum pressure gauge (7) and accordingly adjusted by using the inlet valve. The measurement of the pressure allows to determine the temperature of the liquid surface in equilibrium with the nitrogen vapour by using the saturation curve. Saturation pressure versus temperature table is available on-line. [58].

Measurements have been taken by varying the operating pressure, the field intensity and the field orientation. The temperature of the liquid nitrogen bath inside the Dewar has been reduced by varying the pressure inside the dewar. The temperature has been measured in two different locations inside the sample space using platinum resistance thermometers. The first thermometer is located on top of the sample holder and operates as a level indicator. The second thermometer is positioned close to the centre of the tape and measures the local temperature of the sample. An electromagnet produces field up to 0.5 T and the Dewar can be rotated around its axis so that the field orientation with respect of the sample can be changed.

3

The E-J Characteristics of 2G YBCO Conductors: experimental results

3.1 Motivation and Objectives

The recent enhancement in the performance of the 2G HTS tape has led to the availability of practical conductors suitable for medium/high field applications at intermediate temperature range. Most of the new applications, are designed for cryogen free operation at $20\,\mathrm{K} - 50\,\mathrm{K}$ depending on the the magnetic field required. The E-J characteristics of these materials are essential to magnet design and safe operation since they provide useful information to understand the flux dynamics and the flux pinning as well as the quench dynamic and protection. Due to the difficulties on carrying transient measurements without liquid cooling, experimental data in the temperature range of interest are not yet available in literature and there is an insufficient understanding of the dissipation mechanism for high field scenario at low temperature.

The objectives of this chapter are:

- Design and optimisation of specific sample holder set-up to allow measurements in liquid nitrogen pool as well as in cryogen-free scenario;
- Acquisition of experimental data over a wider range of temperature and field not yet available in literature;

- Investigation of the transition in self field and of the transition dependence on the applied external field;

- Comparison of the power law prediction with the experimental results.

3.2 Experimental Set-up

3.2.1 Transport measurement in liquid nitrogen and mitigation of self heating

Because of the critical temperatures well above the saturation temperature of nitrogen at ambient pressure, the basic J_C characterisation of HTS conductors are conveniently and routinely conducted in liquid nitrogen bath. Most basic measurements have been conducted likewise in other laboratories. The test facility used in this work for measurement in liquid is the one described in section(2.5) and the temperature of the sample has been changed by adjusting the vapour pressure [58]. Although the saturation temperature is given by the vapour pressure, a thermometer located next to the sample allowed monitoring and eliminate the effect of stratification in the nitrogen column. Typical samples are usually up to 10 cm long with the voltage taps separated by few centimetres to ensure the voltage resolution for the J_C criterion of 1μV/cm. As the performance of the conductors continues to improve, such a rudimentary method becomes difficult for E-J characteristics measurements when the critical current is so high that pool boiling cooling is insufficient to maintain a isothermal condition in the samples [59].

Self-heating is indeed a problem with the state-of-the-art of YBCO 2G conductors as it can be observed on E-J characteristics measurements carried out on an YBCO tape 4 mm wide as provided (Sample AS), with the set-up of fig.(3.1). Long current contacts are made at the extremities so that to leave the central part of the sample exposed to nitrogen. Voltage taps are soldered in the centre and distanced 1 mm. The set-up of fig.(3.1) would be referred to as "long sample set-up" (LSS).

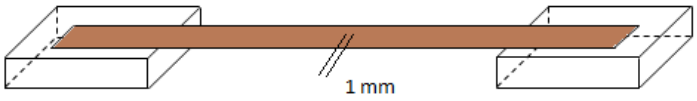

Figure 3.1: Schematic experimental set-up for E-J characteristic of YBCO in liquid nitrogen pool scenario.

The current voltage characteristic plotted as a function of the total operative current is shown in fig.(3.2a). The transition curve so obtained appears to agree with power law behaviour, and a good fitting has been obtained with n=35 and I_C = 105.5A.

In order to better appreciate the effect that heating has on measurements, the E-J characteristic is also plotted as a function of the current carried by the superconductor in fig.(3.2b). The latter has been obtained by subtracting from eq.(1.20), the current carried from the matrix.

(a) (b)

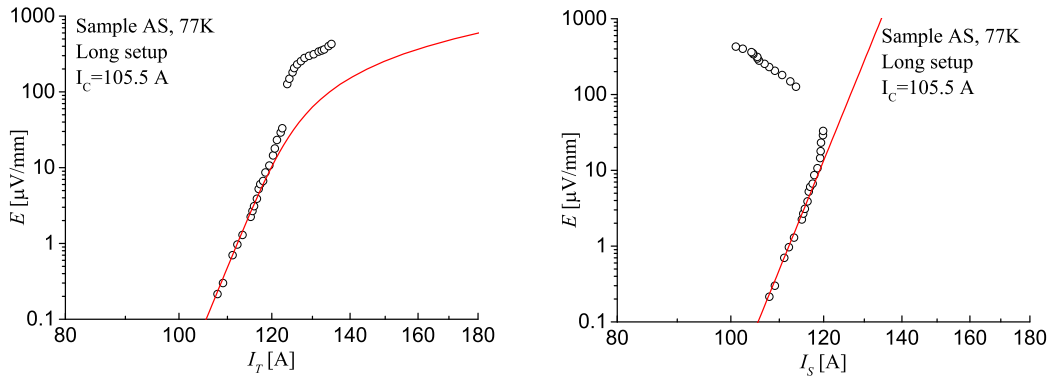

Figure 3.2: E-J characteristics of long length sample measured in liquid nitrogen bath, presented as a function of (a) the total operative current and (b) as a function of the superconducting current (plain line). Comparison with power law fitting.

Current sharing analysis in fig.(3.2b) reveals an increasing n-number with increased

current I_S and an excessive current sharing for $I_S > 1.1\ I_C$, consistent with non-negligible heating above I_C. As a further indication of the self-heating effect on measurements, a drastic jump in voltage is observed at about 1.1 I_C, where the voltage jumps from 30 μV/mm to 130 μV/mm in less that 1 A. The jump is due to a local drastic reduction of the heat transfer which occurs when the nitrogen at the superconductor surface goes from nucleate to film boiling regime, due to the local increment in temperature.

A solution to the problem should be a combination of an enhanced heat transfer and a compromise on the voltage sensitivity, with a reduced sample length for a reduced temperature gradient. In order to satisfy these requirements a new sample set-up, as the one presented in fig.(3.3), has been realised. Such a set-up will be referred to as "short sample set-up" (SSS).

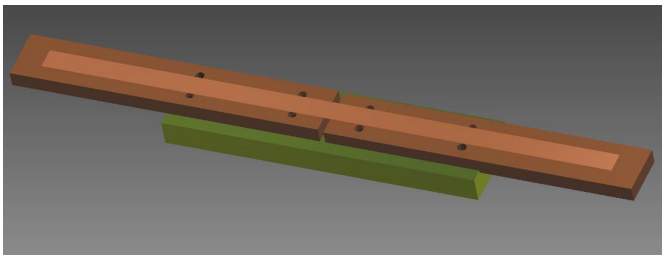

Figure 3.3: Short sample experimental set up for E-J characteristics of YBCO tape in liquid nitrogen pool scenario.

Two large current contacts (35 mm long), separated by a short length (1.2 mm) for voltage measurements, allowed an extension of the current range in the obtained E-J characteristics. Voltage taps distanced 1 mm, have been observed to be sufficient for useful E-J measurements and therefore they have been located in the centre of the tape. The short distance between the current contacts was essential to reduce the temperature gradient along the measured distance, which would have otherwise affected measurements. Self heating is in fact minimised as the boiling lateral heat transfer is assisted by longitudinal heat conduction for the copper pads in the vicinity of the gap. The size of the current contacts should be sufficiently large to allow minimal contact dissipation.

The *E-J* characteristics measured on the superconducting tape with the set-up of fig.(3.3) are compared with the transition curves measured on the long sample set-up. Comparison is shown as a function of the operative current in fig.(3.4a). The two transition curves measured on samples with different set-up, are characterised by the same critical current, but show very different behaviour as the current is increased, and in particular the transition curve measured on the short sample set-up presents increased curvature. In order to obtain the contribution to the voltage given by the only superconductor, the current carried by the matrix has been removed according to the current sharing phenomena described in section (1.3.1) and the transition characteristics have been plotted as a function of the current carried by the superconductor, as shown in fig.(3.4b).

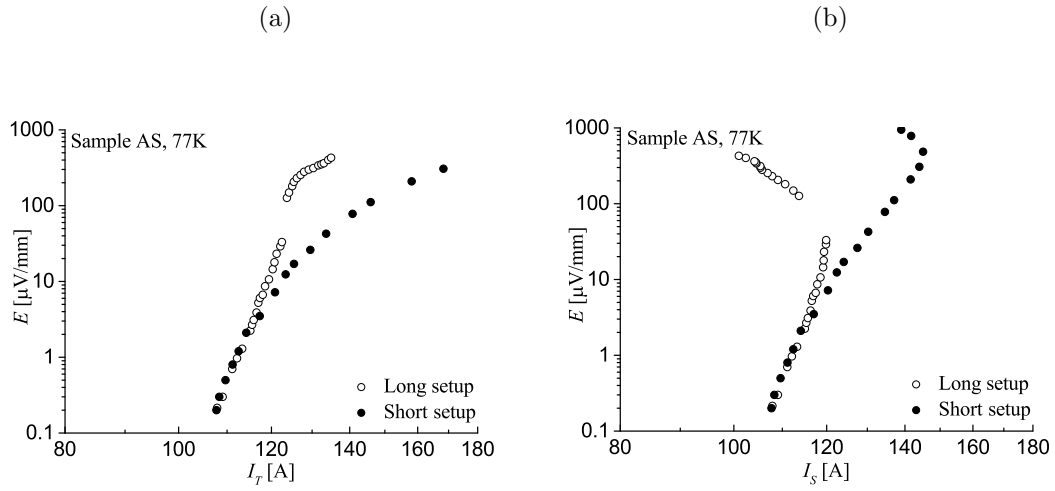

Figure 3.4: *E-J* characteristics of short sample set-up with taps distanced 1 mm measured in liquid nitrogen bath and presented as a function of (a) the operative current and (b) of the superconducting current.

The *E-J* characteristic measured on the short length markedly differs from the one obtained on the long length sample, and the slope is observed to no longer increase with current, as evidenced in both fig.(3.4a) and fig.(3.4b). Moreover, at about 1.3 I_C, self heating in the short set-up sample occurs.

3.2.2 Cryogen-free transport measurement at variable temperatures

As self-heating is already a significant factor for measuring the E-J in a liquid nitrogen pool, the problem will be intensified at lower temperatures in a cryogen-free set-up. In order to limit the self-heating effect on measurements, a few precautions have to be taken in designing the sample holder for cryogen-free set-up.

- Cooling is essentially longitudinal therefore the measured length has been limited to 1 mm;
- Large current contacts for low contact dissipation and large thermal mass are required;
- The projected $I_C \sim 1000$ A at 10 K requires a reduction of sample width from 4 mm to 1-2 mm due to system constraints as well as thermal considerations;

3.2.3 Sample preparation and validation

Samples with a narrow bridge cross-section.

A schematic drawing of the sample holder realised to overcome the problems discussed in section (3.2.2), is shown in fig.(3.5).

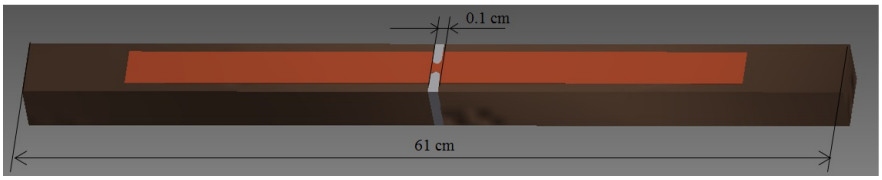

Figure 3.5: Experimental set-up for E-J characteristics of YBCO tape in free-cryogen scenario.

Samples with a narrow bridge cross-section proposed above were prepared in the following steps:

- Preparation of a sample holder of two large copper contacts glued together with a 2 mm thick G10 spacer;
- Soldering of the sample to the current contacts;

- Strengthen of the top surface of the measured region by gluing a copper shim via a thin insulation. The copper shim also adds additional longitudinal thermal conduction to the current contacts;

- Milling material away symmetrically from both side of the tape to form a narrow bridge;

- Filling the gap with epoxy to seal the sample and strengthen the assembly.

An enlargement of the tape after milling is shown in fig.(3.6). Tape with reduced cross section of respectively 3 mm, 2 mm and 1 mm, have been realised and measured.

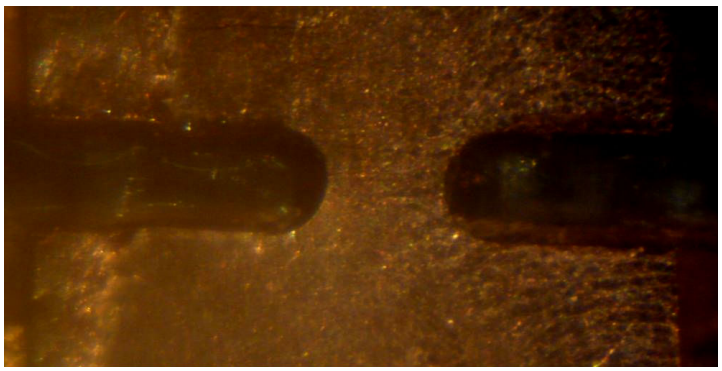

Figure 3.6: Enlargement of a milled narrow bridge of YBCO tape.

Validation of the narrow bridge preparation, is required in order to verify that the sample is not damaged during milling and that the set-up process is reproducible. The validation is based on the comparison of I_C and E-J between as-supplied and sectioned samples.

The critical current of narrow bridge samples characterised by bridges of different width, has been measured at 77 K in liquid nitrogen bath and the results obtained are presented in fig.(3.7). It can be observed as the critical current proportionally decreases with decreasing the cross section of the tape as shown in fig.(3.7).

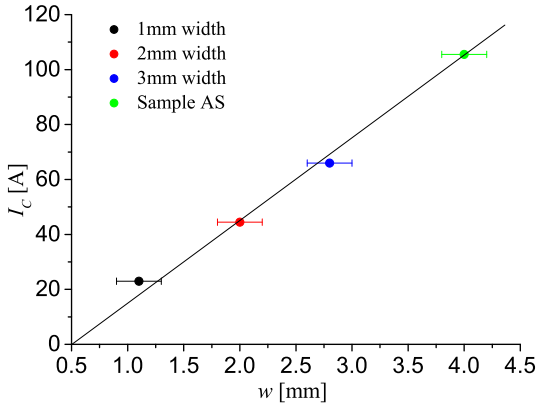

Figure 3.7: Critical current dependence on the tape cross section, measured at 77 K in liquid nitrogen bath.

The E-J characteristics of Sample I, with reduced cross section, have been measured and compared with the one of the unbridged tape (Sample AS). The current voltage characteristics of the two samples, plotted in fig.(3.8) against the scaled current I_T/I_C, appear to overlap. Therefore, measurement show that Sample I has not been degraded by milling, and is hence representative of the original uncut 4 mm width sample.

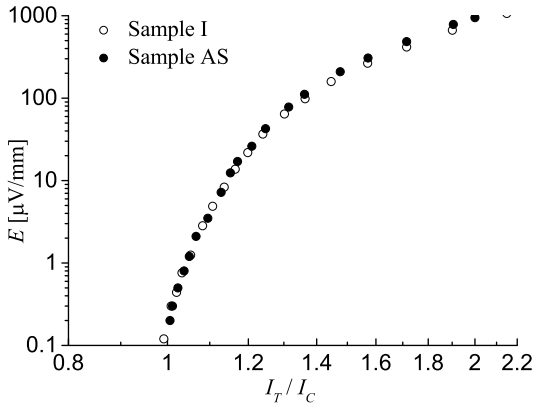

Figure 3.8: Current-voltage characteristic of 4 mm width sample (Sample AS) and 1 mm bridged sample (Sample I) at 77 K.

Summarising, it has been observed that:

- Critical current of tapes with reduced cross section showed that I_C reduces linearly with the bridge width;
- E-J characteristics of as-supplied tape and sectioned tape are not affected by the bridge width.

Therefore, the reduction in the cross section has been proved to be a good strategy for measuring at low temperatures with reduced operative current.

3.3 Measurement protocol

3.3.1 Transport current: DC, semi-transient steps and pulses

The use of samples with a narrow bridge alone was insufficient to ensure reliable E-J measurements of 2G YBCO tapes at temperatures well below T_C due to the self heating of the tape. Heating during measurements was further reduced by using a sequence of short current steps or a single fast ramp. It should be noticed that, in practice, all current modes have their pros and cons:

- DC current allows best resolution for voltage measurement but is most susceptible to heating;
- A single fast pulse/ramp has the least heating and allows E-J to be acquired in a single step. However voltage must be measurement in transient mode at a lower sensitivity and may contain a large inductive component;
- A train of short current steps with small increments can reduce the induction pick-up substantially but the number and duration of steps are limited by the cumulative heating.

As an example, two different current pulses injected on the bridged tape at 77 K, are shown in fig.(3.9a). One of the pulse is at $\sim 1.2\, I_C$, whilst the other at $\sim 3.0\, I_C$. As it can be observed, the two current pulses ramp up at different rate, and in particular, as highlighted in fig.(3.9a), the low current pulse ramps up at I_C at lower rate than the high current one.

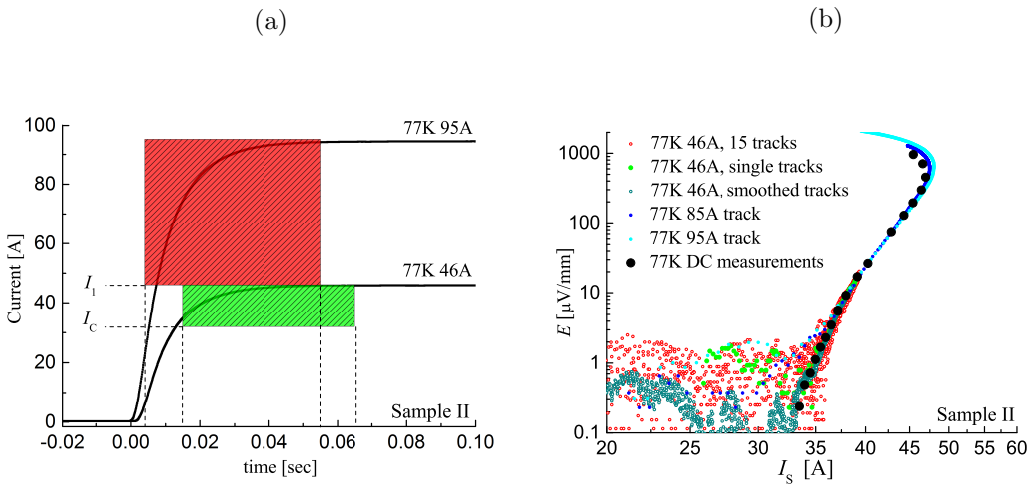

Figure 3.9: (a) Current ramp up at 1.2 I_C and at 3.0 I_C at 77 K. (b) Transient characteristics correspondent to different current ramp up at 77 K.

3.3.2 Voltage acquisition: resolution, noise and inductive component

A combination of three different transport current modes were used for the present work:

- A limited number of DC currents have been taken to mark out the envelope of the E-J range at $I \sim I_C$ where heating is relatively low and at $V < 0.1mV$ where short voltage reading time constant is possible. DC data are shown by the black dots in fig.(3.9b);
- One current pulse at typically $I_{peak} < 1.2I_C$ for $V_{peak} < 10 - 20\,\mu V$ shown by the green dots in in fig.(3.9b);
- One current pulse at typically I_{peak} $1.5 - 2.5\,I_C$ for V_{peak} up to 1 mV shown by the blue and light blue dots in fig.(3.9b). The latter does not yield useful results at low voltages due to the inductance.

The voltage resolution at the low current pulse was improved by averaging over repetitive pulses at $I_{peak} < 1.2\,I_C$. The overall inductive transient was usually reduced by a preconditioning pulse at $I < 0.8\,I_C$ and a sufficiently resistive load in series with the sample.

Current pulse with $I_{\mathbf{peak}} < 1.2\, I_C$.

The current-voltage characteristics obtained from low current pulses and shown in fig.(3.9b) by the red dots, corresponds to the voltage data measured in the green area of fig.(3.9a). The 46 A current pulse ramps up at lower rate than the 95 A as it can be observed in fig.(3.9a). As a result, a higher number of low voltage data points can be measured by ramping the current to a small percentage of the critical current, as can be appreciated in fig.(3.9b). DC measurements are also plotted in fig.(3.9b) and show good agreement with the data obtained with low current pulses. On the other hand, the transient measurements appear to be accurate on describing the transition characteristic only above 1 μV/mm. Repetitive pulses at low I_{peak} current pulse have been taken (about 15 tracks) as shown in fig.(3.9b) by the red dots, and then smoothed until obtaining a single track with better resolution at low current (dark green dots).

Current pulse with $I_{\mathbf{peak}}$ $1.5 - 2.5\, I_C$.

When collecting high voltage data, a faster ramp rate is desired to reduce the heat generation . On recording the high current pulse, the voltage limit is set up to a value higher than the one required by the power supply, so that to reduce the time needed to reach the desired operative currents. As an example, two high-current tracks collected at 77 K, one ramped up to 85 A and the other up to 95 A, are shown in fig.(3.9b) in blue dots and light blue dots respectively, and compared with the experimental data. The high voltage data points, obtained by ramping the current at high percentage of I_C, are less affected by heating than the ones obtained with DC measurements. On the other hand, the voltage data point obtained at the beginning of the current pulse, are strongly affected by inductance, thus points recorded below a minimum current, indicated in fig.(3.9a) as I_1, have to be removed from the voltage current characteristic obtained. Also, just above I_1, the sharp increment in current does not allow to measure a substantial number of data points. The data of interest for measurements with high pulse track are the one which correspond to the current range highlighted in the red area of fig.(3.9a).

The final transient characteristic at given temperature has been therefore obtained by joining the low voltage data measured with the low current pulses and the high

voltage data obtained with the high current pulse. Because of the high current involved, precaution from sample burn-out has to be taken and, since the current protection available appeared to be too slow on cutting the current, a cut-off switch has been introduced in parallel with the protection system. The latter is manually activated as soon as the current is injected, so that the protection system sees the open parallel circuit and cuts out the current quickly enough, independently of whether or not a quench event occurs. The cut-off switch allows to obtain time pulses in the range of 300-400 msec.

Removal of inductive pick up.

Inducting pick up can be reduced by adding a resistive load in series with the current line, so that the resistance offered by the load, allows to slow down the ramp up in current and the inductance effect days away when the current is still too low to produce any voltage. Furthermore, the ramp up in current is influenced by the voltage limit set up on the power supply. For low current pulses, a small voltage limit on the power supply is required, so that the current does not initially overshoot. By changing the load and the voltage limit set up, it is possible to obtain data not affected by inductance.

3.3.3 Magnetization measurements

In order to extend the measurement to lower voltage level than the one obtained with the semi-transient method, magnetization measurements using a Vibrating Sample Magnetometer (VSM) technique, have been performed.

Sample preparation.

An YBCO sample of rectangular shape with dimensions 1mm x 4mm x 0.001 mm has been glued on a purpose rod sample holder with negligible magnetic moment (below the instrument noise's floor). The sample is mounted so that the plane a-b is perpendicular to the external applied field as schematically shown in fig.(3.10).

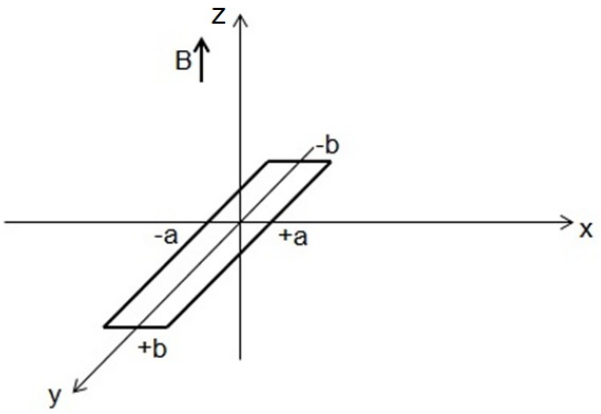

Figure 3.10: Schematic representation of the sample geometry for magnetization measurements.

Measurements have been carried at out 77 K applying field up to 4 T with different sweep rates: 195 Oe/sec, 45 Oe/sec and 11 Oe/sec respectively. The data acquisition time was increased to 0.2 sec for 195 Oe/sec sweep rate, whilst kept to 0.1 sec for the other two cases.

- Current

  According to Bean's model, the magnetization of a dipole m characterised by $b >> a$ can be expressed as:

  $$m = 2 \cdot 2b \int_0^a \sigma(x) \cdot x \cdot \mathrm{d}x = 4b \cdot \sigma \cdot \frac{a^2}{2} = a \cdot b \cdot I \tag{3.1}$$

  where σ is the linear current assumed uniform $\sigma = I/2a$ and a and b are half of the width and the length of the sample respectively [60]. Magnetization is measured in emu, therefore a more convenient unit measurement conversion can be done, taking into account that 1 emu= 10^{-3} A m^2;

- Voltage

  According to Faraday's law, the induced voltage due to a change in the magnetic field is given by

  $$V = -\frac{\mathrm{d}\Phi}{\mathrm{d}t} \tag{3.2}$$

which can be re-expressed as:

$$E\,b = -a\,b\,\frac{\mathrm{d}B}{\mathrm{d}t} \tag{3.3}$$

Because of the observed proportionality between the magnetic flux and the voltage as well as between the magnetization and the current, the E-J characteristics are equivalent to $\frac{\mathrm{d}B}{\mathrm{d}t}$-$\frac{m}{ab}$ characteristics and the magnetization measurements can be used to obtain further data point in the low voltage range.

Because of the equivalence observed between E-J and the equivalent relation expected between E-J has to be valid also for $\mathrm{d}B/\mathrm{d}t$ and m/ab, therefore the common power law of eq.(1.18) can be rewritten as in eq.(3.4). The latter expression provides a further approach to calculate the power exponent at different temperatures.

$$\frac{(\mathrm{d}B/dt)_1}{(\mathrm{d}B/dt)_2} = \left(\frac{m_1}{m_2}\right)^n \tag{3.4}$$

Important achievements have been reached thanks to the experimental set-up and to the methods proposed in this chapter. It is relevant to highlight that:

- The heating problem that affects the E-J characteristic measurements has been successfully overcome by a reproducible small sample cross section and by a reduced distance between voltage taps;
- E-J characteristics have been measured in a wider electrical field range which goes from 5 nV/cm up to $\sim$ 10 mV/mm by a combination of DC, semi-transient steps and pulses and magnetization measurements at different sweep rate.

3.4 Results

3.4.1 Samples

In order to verify both the reproducibility of the observed phenomena and the homogeneity of the tape, the investigation of the E-J characteristics at different temperatures and fields, has been carried out on the uncut tape, Sample AS, as well as on four different cut samples, which it will be refereed to as Sample I and Sample II (cuts belonging to the same wheel as Sample AS, Tape I), and as Sample III and Sample IV (cuts belonging to a different wheel, Tape II).

The superconducting transition measured on the different samples, has been recorded during the cooling down by imposing a constant transport current of $I = 1\,\mathrm{A}$. The recorded transition are shown in fig.(3.11a).

(a) (b)

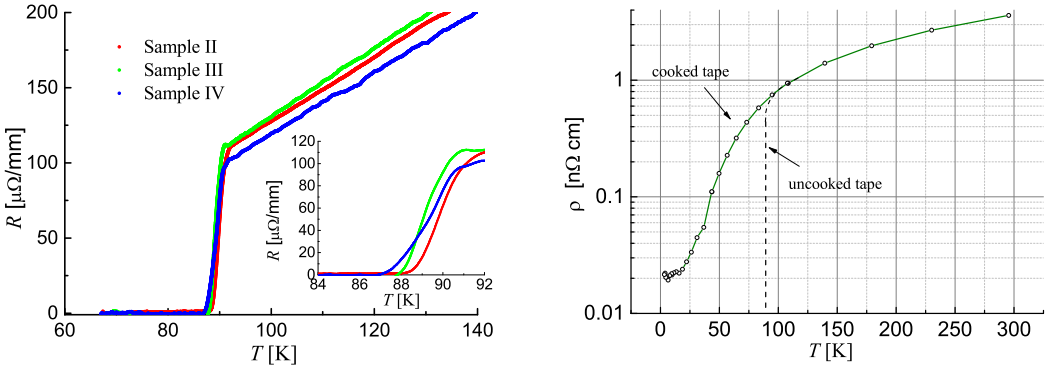

Figure 3.11: (a) Superconducting transition measured on Sample II, Sample III and Sample IV, recorded during cooling down by imposing a constant transport current of $I = 1\,\mathrm{A}$. (b) Resistivity dependence on temperature of a cooked YBCO tape at 600°.

All measured samples show the typical superconducting behaviour with a drop in resistance at the critical temperature of ~ 92 K. The trend observed is a further demonstration that no damage has been induced on the tape during milling. Note that Sample II presents the best T_C onset, Sample III presents the sharper transition and then finishes as Sample II, and Sample IV shows a broader transition, when compared with Sample II and Sample III. These differences might be attributed to differences in oxygen content since, as known, the critical temperature is observed to be higher when $O_2 \sim 7$ and to decrease in case of oxygen deficiency. According to this picture, measurements suggest that Sample II has the best stoichiometric oxygen content $O_2 \sim 7$, whilst Sample III appears to be slightly over doped and Sample IV is characterised by low oxygen content or less homogeneity.

The sheath resistance dependence on temperature is shown in fig.(3.11b). Measurement of the sheath resistance is needed in order to extract the underlying E-J

characteristic from the actual measured characteristic which include the matrix contribution. The normal resistivity below T_C, labelled in fig.(3.11b) as cooked tape, has been obtained on a sample specially processed at 600° in vacuum so that to disable the superconducting transition. The dashed line in fig.(3.11b) shows the expected resistivity dependence on temperature of an uncooked tape. The conductor resistivity $\rho(T)$ dependence on temperature has been used in this work for the current share analysis of the 2G conductors. According to the data, the R(77 K) and R(45 K) of the standard 4 mm tape are 12.6 $\mu\ \Omega$ /mm and 3.12 $\mu\ \Omega$ /mm respectively.

Critical current dependence on temperature measured for the analysed samples are compared one another in fig.(3.12).

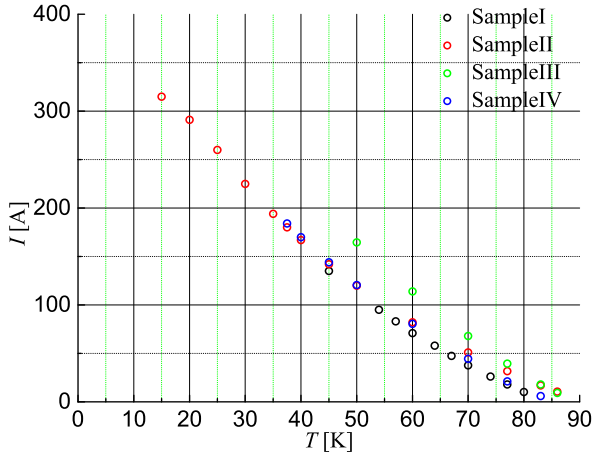

Figure 3.12: Critical current dependence on temperature, measured on Sample I, Sample II, Sample III and Sample IV.

The data presented in fig.(3.12) are extrapolated data from the measured E-J curves. Measurements show that different samples such as Sample I, Sample II and Sample IV have the same critical current dependence on temperature whilst Sample III appears to be steeper as the temperature is lowered.

3.4.2 DC E-J characteristics at liquid nitrogen temperatures

E-J characteristics of the uncut sample (Sample AS) have been measured in liquid nitrogen bath at 77 K in a range of temperature (67 K-74 K), with the set-up described

in section (3.2.1). The set of current-voltage characteristics obtained at different temperatures is presented in fig.(3.13a) as a function of the total operative current. Experimental data are compared with the respective transition characteristics predicted by the power law equation, plotted in red lines.

(a) (b)

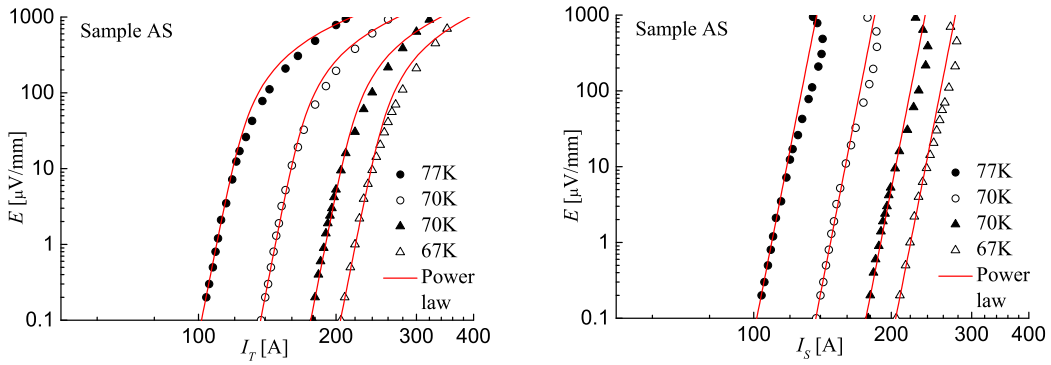

Figure 3.13: *E-J* characteristics at 77 K, 74 K, 70 K and 67 K of Sample AS in self field measured in liquid nitrogen bath, and relative power law predictions, presented as a function of (a) the operative current current and (b) of the current carried by the superconductor.

On observing the *E-J* characteristics presented in fig.(3.13a) it can be noticed that:

- Curves show an unexpected non-linear behaviour in disagreement with thermal activated flux flow predictions presented in section (1.3);
- As a result of current sharing, described in section (1.3.1), the intrinsic *E-J* characteristics are superimposed with the contribution of the normal resistive sheath, which is expected to give additional further curvature in the ln$E$-ln$I$ plot at high voltage and current;
- Curves present noticeable deviation from power law behaviour. The power law fittings presented fig.(3.13a) are obtained to impose a better fit to the lower part of the curve and the correspondent n-values have been calculated in the range of voltage 0.1 - 1 μV/mm. The exponent n is found to be almost constant, in fact

$n = 30.8 \pm 0.3$. Critical current and n-number obtained at different temperatures are listed in tab.(3.1);

- A slower rate for voltage increase can be noticed at high current and such a lower E-J voltage is considered significant as it could not be the result of heating.

T [K]	I_C **[A]**	**R [μV/mm]**	$\mathbf{n_{I_C}}$
77	101.5	12.6	30.5
74	136.7	11.2	31.0
70	176.0	9.8	30.8
67	204.5	8.7	30.5

Table 3.1: Critical current and n-number values as a function of temperature, obtained according to power law model.

Note that the deviation from power law cannot be accounted with increasing current sharing by a reduced sheath resistance, which would result in increasing the curvature initially but undershooting the experimental data as the current is further increased.

As a further prove of the observed deviation from power law behaviour, data are presented in fig.(3.13b), as a function of the scaled current carried by the superconductor. This set of data has been obtained by taking into account the current sharing and by using the resistivity dependence on temperature plotted in fig.(3.11b). The scaled plot allows also to highlight the current at which the heating starts affecting the measurements. The effect of heating is characterised by a sharp onset, noticeable because the transition curves start bending backwards when the superconductor current capability is reduced by the increased local temperature. The onset takes place to happen at about 1.4 I_C. Change of slope and deviation from power law of the E-J characteristics are also highlighted in the scaled graph where the bending observed clearly appears not to be consequence of current sharing.

Transition curves are also plotted with respect of the normalised superconducting current in fig.(3.14) and compared with data obtained on Sample AS. E-J characteristics in a normalised current scaled graph, appear to overlap confirming that they can be all fit by a single scaled power law characteristic with $n \sim 30.8$.

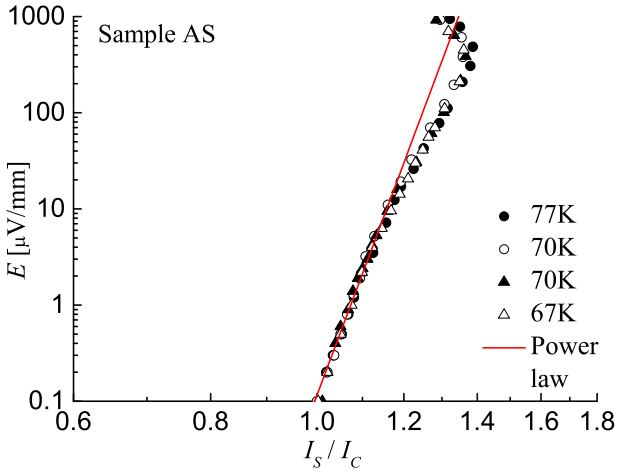

Figure 3.14: *E-J* characteristics at 77 K, 74 K, 70 K and 67 K of Sample AS in self field measured in nitrogen bath, and relative power law predictions, presented as a function of the normalised superconducting current.

The observed power exponent calculated at I_C gives un unexpected result, since it has being found to be almost constant, rather than changing with temperature as expected. Results obtained raised two questions: firstly if the deviation is confirmed in a wider temperature range and therefore how the power exponent would behave with a further reduction of temperature, and secondly if there is a common scaling law which can describe the deviation observed. As discussed, measurements at lower temperatures require a cryocooler and transient measurements as described in section(3.3.1).

3.4.3 *E-J* characteristics at different temperatures

The *E-J* characteristics measured at different temperatures in the range of $15\,\mathrm{K} - 86\,\mathrm{K}$, in quasi-adiabatic conditions and self field, on Sample I, Sample II, Sample III and Sample IV are presented in fig.s(3.15a-d) respectively as a function of the operative current and in fig.s(3.16a-d) respectively as a function of the current carried by the superconductor. Deviation from power law, highlighted in dashed lines, is consistent in the all temperature range and for all samples measured.

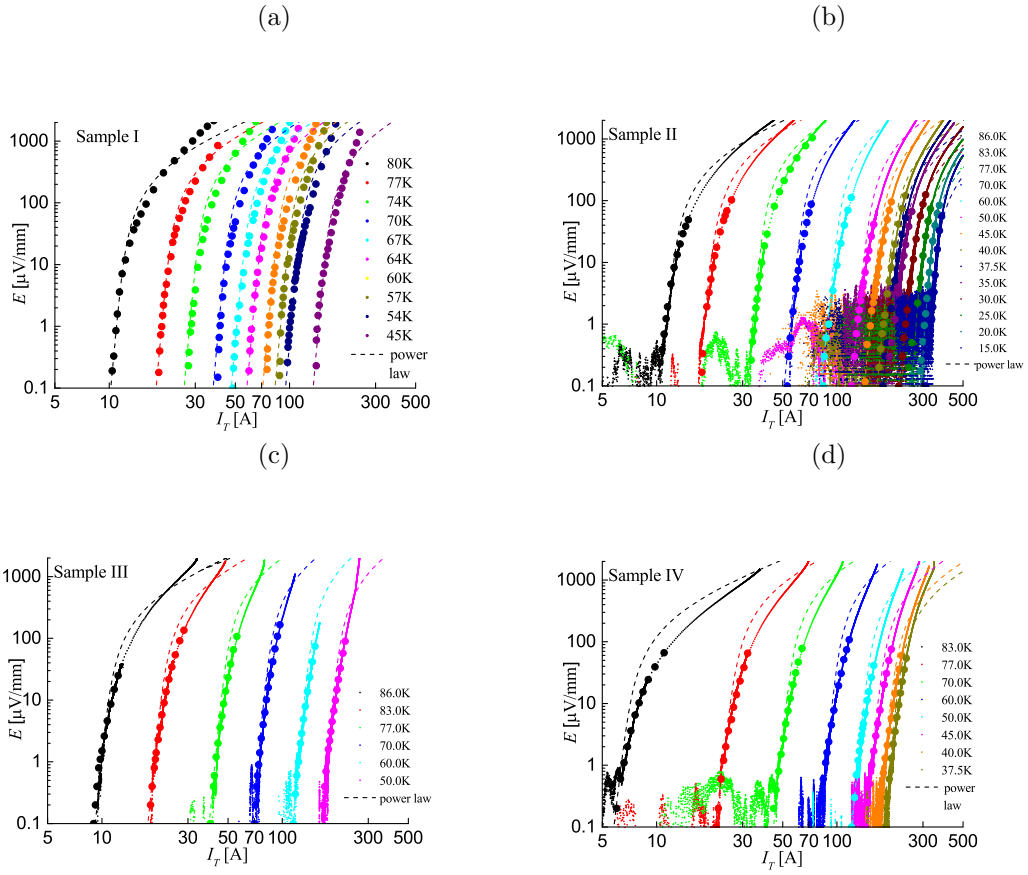

Figure 3.15: *E-J* characteristics measured on (a) Sample I in the range of temperatures 45 K - 80 K, (b) on Sample II in the range of temperatures 15 K - 80 K, (c) on Sample III in the range of temperatures 50 K - 86 K (c) and (d) on Sample IV in the range of temperatures 37.5 K - 83 K plotted as a function of the operative current. Deviation from power law is confirmed for all samples, across the all range of temperature.

The measured data covers consistently four decades of electrical field. The differences in the measured range of temperatures between samples are due to premature burn out. The level of noise in fig.(3.15b) is higher than in other cases and increases at low temperature due to the change of the power supply which has been made to satisfy the current requirement at low temperatures. The global level of noise has been successfully reduced when measuring Sample III and Sample IV.

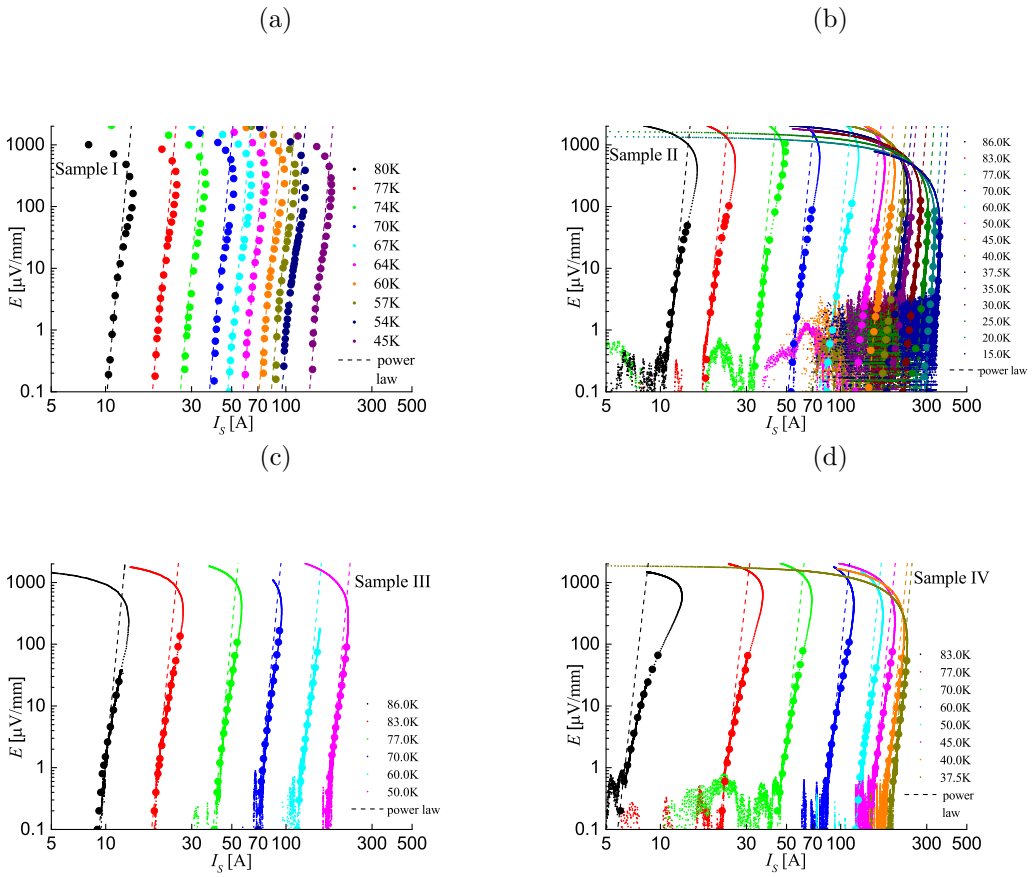

Figure 3.16: Scaled E-J characteristics of (a) Sample I, (b) Sample II, (c) Sample III and (d) Sample IV plotted as a function of the superconducting current. Deviation from power law is highlighted with the dashed lines.

The dashed lines, corresponding to a power-law fit using the n-number calculated at I_C, consistently fail to match the data for all the temperatures. E-J characteristics at different temperatures are also presented as a function of the current carried by the superconductor in fig.s(3.17a-d) respectively for Sample I, Sample II, Sample III and Sample IV, where the non-power behaviour is better highlighted.

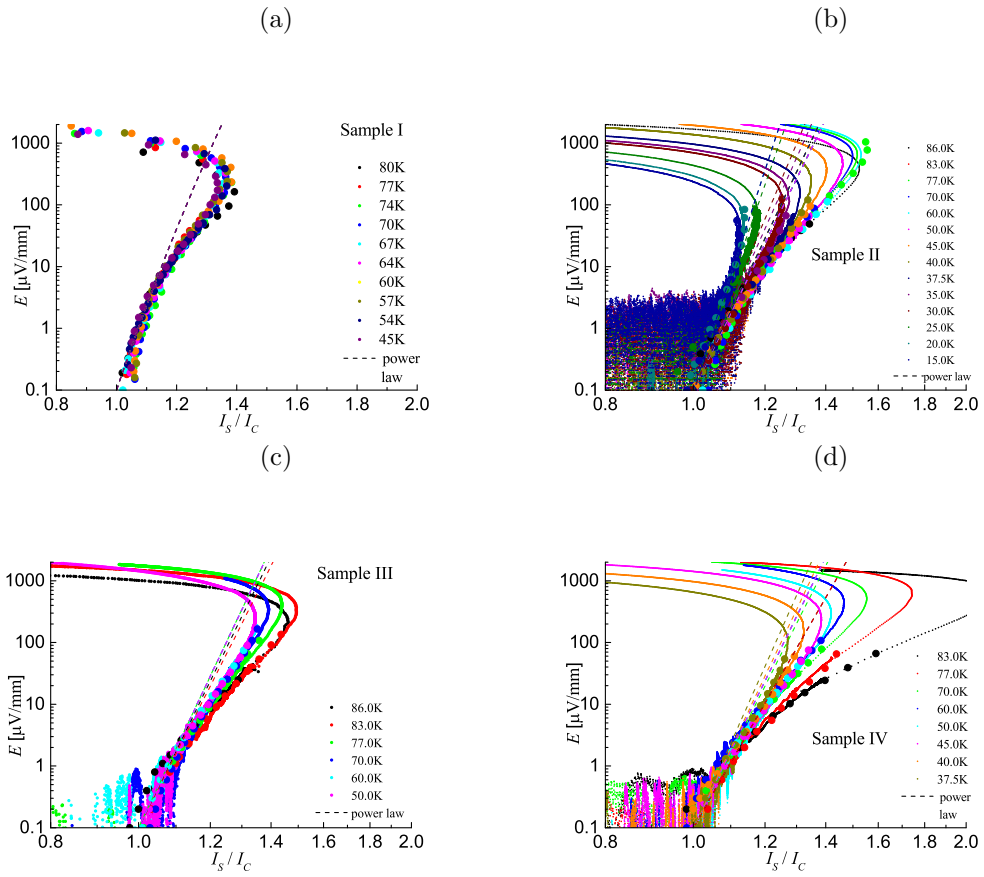

Figure 3.17: Scaled *E-J* characteristics of (a) Sample I, (b) Sample II, (c) Sample III and (d) Sample IV plotted as a function of the normalised superconducting current. Deviation from power law is highlighted with the dashed lines.

Looking at fig.s(3.16a-d) and fig.s(3.17a-d) it can be noticed that:

- The *E-J* characteristics of Sample I measured in the range 45 K - 80 K (only DC measurements available) present similar behaviour as Sample AS;
- The *E-J* characteristics of Sample III and Sample IV are measured in the same range as Sample I and both DC and transient measurements are available;
- The *E-J* characteristics of Sample IV show a different bending from Sample I, Sample II and Sample III ones;
- Sample II, which has been measured in a wider range of temperature $15\,\mathrm{K} - 80\,\mathrm{K}$ with both DC and transient measurements, presents *E-J* characteristics which

spread below 45 K with consequent increment of the power exponent n with temperature.

In order to further highlight how the transition curves of different tapes show the same qualitative behaviour in the range of temperature 45 K - 77 K, the data collected on Sample I, Sample II and Sample III, are plotted together in fig.(3.18a).

(a) (b)

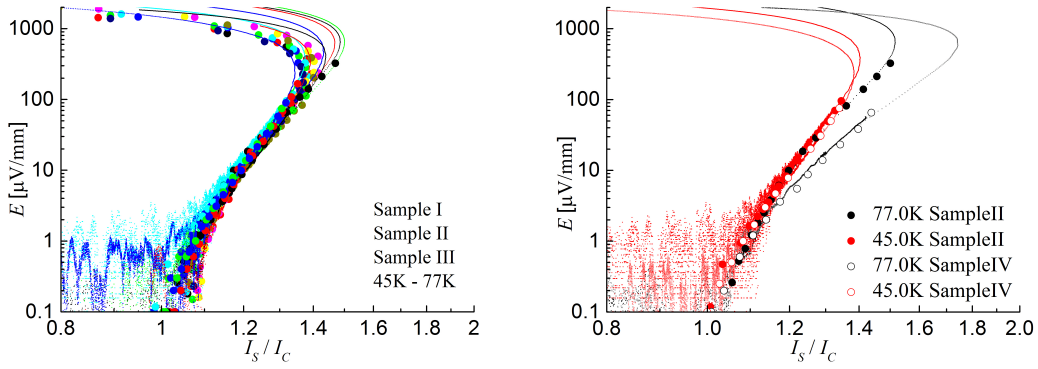

Figure 3.18: (a) Scaled E-J characteristics plotted as a function of the scaled superconducting current of Sample I, Sample II, Sample II and Sample III in the range $45\,\mathrm{K} - 77\,\mathrm{K}$. (b) E-J characteristics comparison of Sample II and Sample IV at $45\,\mathrm{K}$ and $77\,\mathrm{K}$.

As expected, the E-J characteristics of different samples collected in the range $45\,\mathrm{K} - 77\,\mathrm{K}$, collapse on the same curve confirming to have similar slope at the same temperature and to behave qualitatively similarly in this temperature range. On the other hand, Sample IV shows a different behaviour at high temperatures as it is shown in fig.(3.18b) where E-J characteristics at temperature 77 K and 45 K are compared with data obtained on Sample II for which also transient measurement are available. A similar trend of the E-J characteristics of Sample II and of Sample IV can be observed at 45 K whilst at 77 K the E-J characteristic of Sample IV shows strong deviation from the common behaviour observed in the other samples. The current voltage characteristics shows in fact an increased bending which in turns indicate an increased sharing with the matrix.

Measurements on Sample II have been carried out in a wider temperature range and

the current-voltage characteristics below 45 K appear to have a different behaviour. Deviation from power law, is confirmed down to 15 K, but a new feature has been observed: the power exponent n gradually increases at temperatures below 40 K until reaching the value of 40 at 15 K. The set of curves for which the n number appears to increase is presented in fig.(3.17b).The critical current, the resistance and the n-value obtained from measurements on Sample II below 45 K are listed in table.(3.2).

T [K]	$\mathbf{I_C}$ **[A]**	**R [μV/mm]**	$\mathbf{n_{I_C}}$
40.0	169	8.18	32
37.5	180	6.12	33
35.0	193	5.18	33
30.0	221	4.23	33
25.0	250	3.18	35
20.0	282	2.54	38
15.0	310	2.24	40

Table 3.2: Critical current and n-number values as a function of temperature, obtained according to power law model for Sample II at temperatures below 45 K.

Note as the self heating plays a dominant effect at low temperatures, in fact, whilst at 86 K the self heating starts affecting measurements when the current is 150% of I_C, at 30 K the E-J characteristics are strongly affected by self heat heat at about 115% of I_C. The latter is due to the increased transport current carried by the superconductor as the temperature is lowered. Curves at low temperatures appear also to be more spread one with respect of the other, because of the smaller resistance offered by the matrix at low temperature, which makes the matrix a more attractive path for the current once the dissipation in the superconductor has started. The latter can be further proved by looking at eq.(1.20), where it is observed that, on scaling all terms with the critical current I_C and by assuming the same ratio I_{TOT}/I_C, the term on the right representing the current carried by the matrix, becomes more and more important as the resistivity reduces as the temperature is lowered.

The n-number dependence on temperature for all the measured samples is presented in fig.(3.19) where it can be observed that the power law exponent dependence on

temperature is very similar for all samples, presenting a plateaux between $45\,\mathrm{K} - 77\,\mathrm{K}$, but that Sample I and Sample III are characterised by higher n-number.

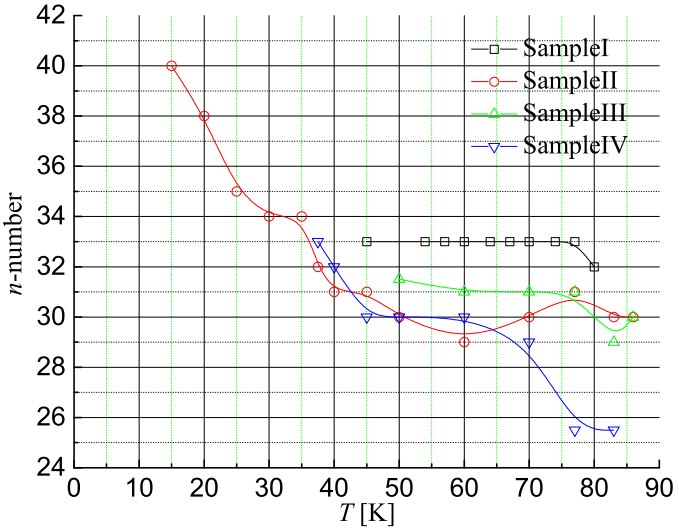

Figure 3.19: Exponent n dependence on temperature for Sample I, Sample II, Sample III and Sample IV.

3.4.4 E-J characteristics in low fields

In the self field scenario the flux structure is rather complex and not uniform, therefore it is of interest to investigate the transition characteristic behaviour when an external field is applied.

Measurements have been performed on Sample AS by using a cryostat exposed to an external field generated by an electromagnet described in section (2.5), and by preparing the tape according to the set-up described in section (3.2.1).

The cryostat used for measurements has a support which allows rotation, so that the field orientation can be changed. The rotation of the angle has been read with a resolution of 0.1 degree. The rotation was allowed along the longitudinal direction of the tape, and thus along the current axis, implying a constant Lorentz force for all the tape orientations. Measurements in field confirm the strongly anisotropic behaviour of YBCO tapes, already observed in literature for single crystalline material [61] as well as epitaxial films [62]. In order to define the position of the sample, the cryostat has

been rotated under a constant transport current applied until finding the position corresponding to having the field perpendicular to the a-b plane. The highest peak in voltage defines the "perpendicular" configuration, whilst data, collected rotating the cryostat of 90° anticlockwise, are here refereed to as "parallel" configuration. "Perpendicular" and "parallel" reefer to the relative angle between the field and the a-b plane of the tape, whilst, as mentioned, in both configurations the field is perpendicular to the current and corresponds to a constant Lorentz force scenario.

The critical current dependence on field, evaluated according to the engineering critical current criteria, has been measured for different imposed fields both in perpendicular and parallel configuration and is presented in fig.(3.20).

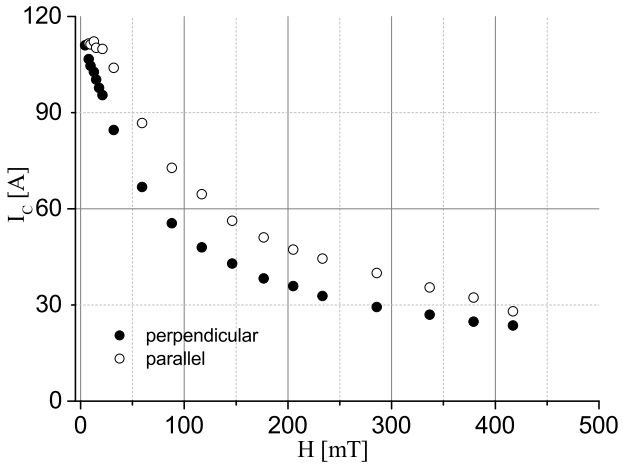

Figure 3.20: Critical current dependence on field in perpendicular and parallel configurations.

The critical current dependence on field results to be qualitatively similar in both perpendicular and parallel configurations in the measured range of field, whilst the two curves are expected to have a different slope for field above 1 T as observed by Safar [63]. Both curves present an initial slow dependence on field (from self field up to 20 mT) followed by a faster drop as the field is further increased. The critical current in the perpendicular configuration lies below the parallel configuration as expected. The

complete set of E-J characteristics measured at 77 K in low fields in the range $0 - 0.3$ T in perpendicular and parallel configurations respectively is presented as a function of the total current in fig.s(3.21a and c) and of the current carried by the superconductor in in fig.(3.21b and d).

(a) (b)

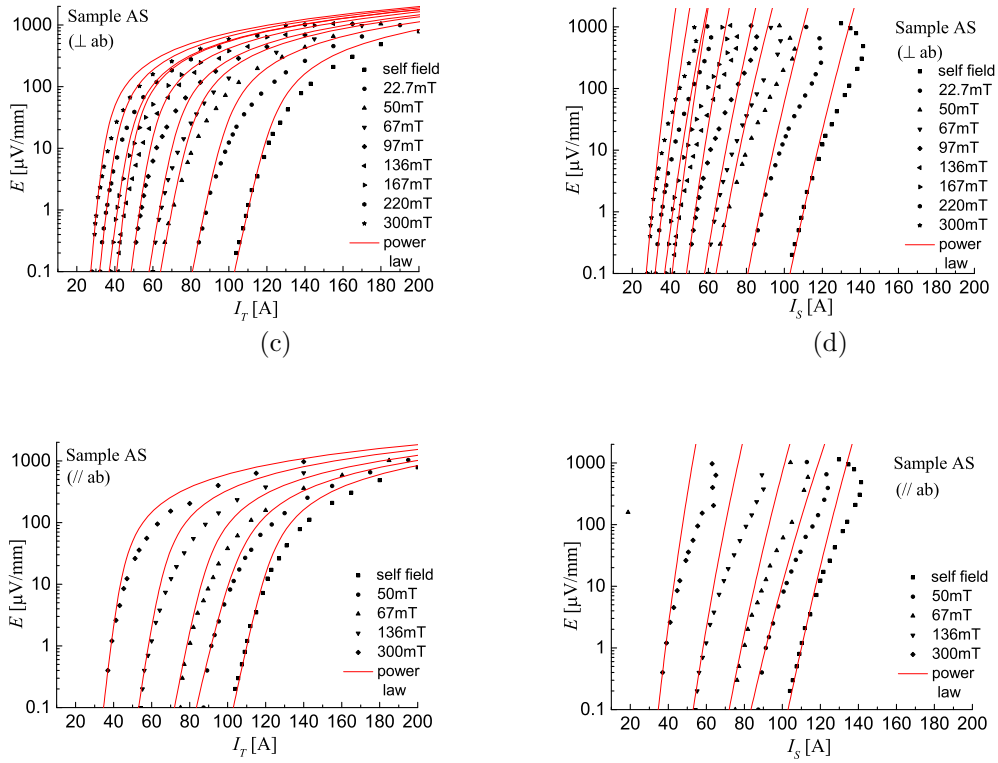

Figure 3.21: E-J characteristics of YBCO 4 mm wide measured in low fields in the range 0 - 0.3 T in perpendicular and parallel configurations respectively, plotted as a function of (a and c) the total current and (b-d) of the current carried by the superconductor.

The E-J characteristics, as it can be observed in fig.(3.21a) and fig.(3.21c), lie on the left as the field is increased, as a result of the reduction of the critical current with field. It can be noticed that a faster current dependence on field takes place for low external applied field, whilst for further increment in field the current increment tends to flatter. It can also be noticed a change in shape with increasing field and, in particular, current sharing appears to start at lower current value as the field is

increased. The change in shape of the current voltage characteristics has been already observed in several measurements on YBCO and BSCCO at 77 K [38] and 4.2 K [64]. The E-J characteristics appear to be less sharp as the field is increased and this can be attributed to a weaker pinning strength of the pinning centres, which makes vortices more easily to be depinned compared to the self field scenario. Once dissipation starts the superconductor is able to carry a lower percentage of the critical current, part of which diverts into the matrix (at about 130% of I_C in self field compared to about 110% of I_C at 130 mT), resulting in a earlier bending of the characteristic. Deviation from power law is confirmed in low fields in both parallel and perpendicular configuration and deviation from experimental data appears to be more important as field in increased.

The E-J characteristics are also presented in a scaled graph for both perpendicular and parallel configurations in fig.(3.22a) and fig.(3.22b), where the change in slope at low voltage with increased field can be better appreciated.

(a) (b)

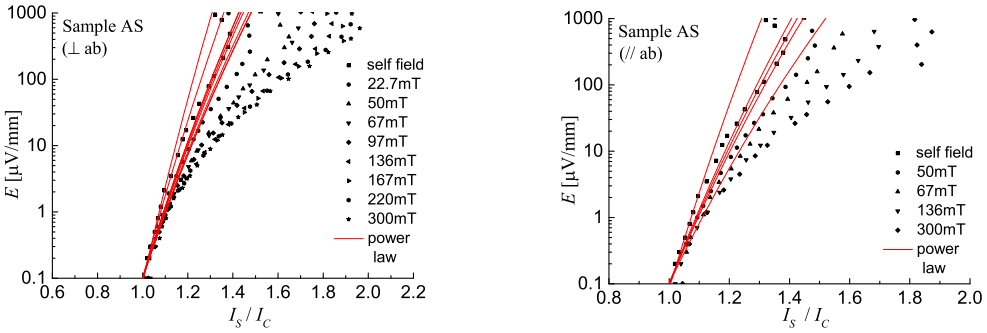

Figure 3.22: E-J characteristics of YBCO 4 mm wide measured in low fields in the range 0 - 0.3 T in (a) perpendicular and (b) parallel configurations, presented as a function of the scaled current carried by the superconductor.

On comparing the E-J characteristics obtained in parallel and perpendicular configuration, the shape of the transition characteristic seems to not be influenced by the field orientation, in the range of fields applied. As an example, the comparison of E-J characteristics at 67 mT for the two different configurations is showed in fig.(3.23). In this particular case, the calculated n-number is ~ 27 for both configurations.

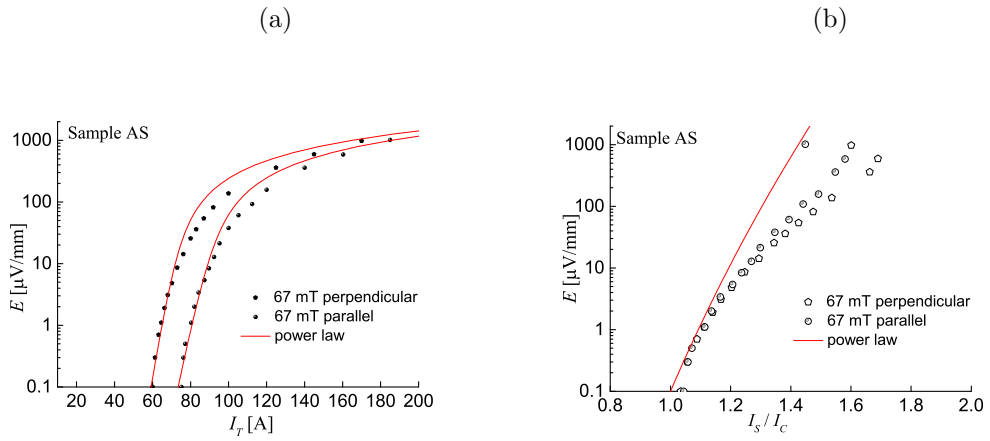

Figure 3.23: *E-J* characteristics of YBCO 4 mm wide measured in low fields in the range 0-0.3 mT in (a) perpendicular and (b) parallel configurations, presented as a function of the scaled current carried by the superconductor.

As for the self field measurements, the power law has been used to predict the *E-J* characteristics experimentally measured in field by imposing fitting in the low voltage part of the transition curve. As highlighted in fig.(3.24a), the power exponent linearly decreases with increasing field, going from 30 at zero external applied field to about 22 when a field of 0.3 T is applied. Similar results on the power law exponent, have been obtained from measurements on YBCO tapes with different cross sections, of 1 mm, 2 mm and 3 mm width, under the same external applied fields, as shown in fig.(3.24a). The dependence of the power exponent on field appears to be qualitatively similar for samples with different cross sections.

The critical current per unit width dependence on field, measured on samples of different cross section width and on the "as provided" sample (Sample AS), is shown in fig.(3.24b). Critical current is observed to decrease with field and, in particular, a greater decrement (about 30%) is observed at very small applied field (0 - 20 mT). The critical current shows a qualitatively similar dependence on field, in tapes with different cross sections, suggesting a good uniformity of the tape structure. Therefore it can be claimed that the deviation from the power law is independent from both field and geometry.

(a) (b)

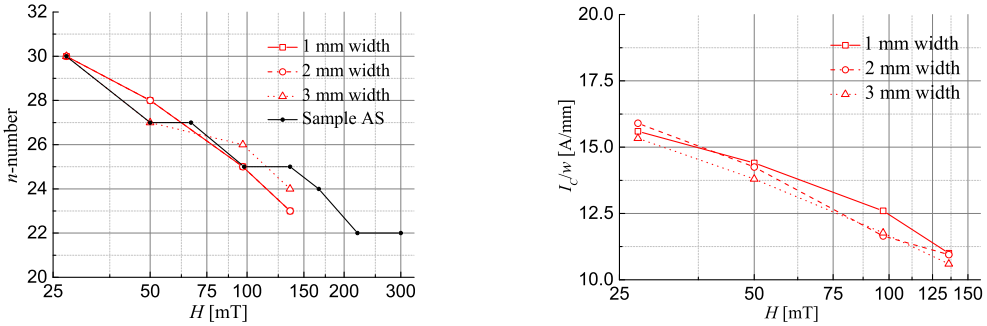

Figure 3.24: (a) Power exponent n and (b) critical current per unit width dependence on the applied perpendicular field for "as provided" sample (Sample AS), and samples with reduced cross section respectively of 1 mm, 2 mm and 3 mm.

As an example, a set of *E-J* curves measured on a sample with a reduced cross section to 1 mm (called Sample V) and collected with increasing perpendicular applied field (27.5 mT, 50.0 mT, 97.0 mT and 136.0 mT) at 77 K, are presented in fig.(3.25).

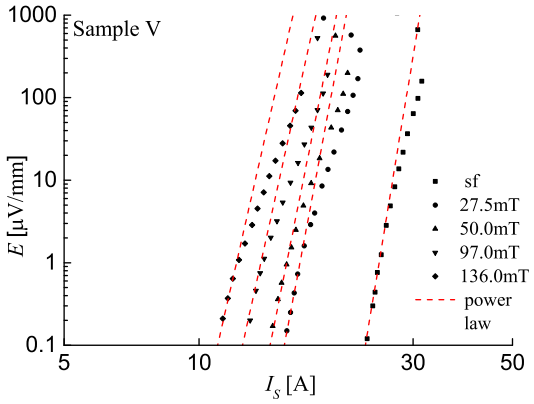

Figure 3.25: *E-J* characteristics measured in low perpendicular fields on Sample V, at 77 K.

The external field was imposed by placing two neodymium iron boron magnets on a support and by distancing them opportunely so that to obtain the desired field.

3.4.5 Magnetization measurements at different sweep rate

By performing the field cycle $-H_0 \rightarrow 0 \rightarrow H_0 \rightarrow 0 \rightarrow -H_0$ with H_0 =40000 Oe, and by imposing a field increment sweep rate of 195 Oe/sec, 45 Oe/sec and 11 Oe/sec, three magnetization curves are obtained. The magnetization curves are presented in fig.(3.26) and indicated in the enlargement respectively as 1, 2 and 3. Critical current in high T_C superconductors decays exponentially with field, and as observable in the magnetization curve presented in fig.(3.26), on increasing the field, the magnetization decreases [65].

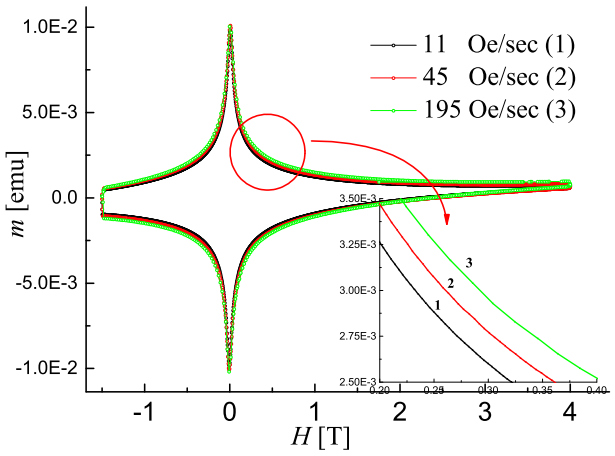

Figure 3.26: Magnetization curves at 77 K up to 4 T for three different sweep rates: 195 Oe/sec, 45 Oe/sec and 11Oe/sec.

When the cycle is started from zero, measurements present an initial linear behaviour due to a shielding critical current-induced. In order to obtain measurements in the quadrants on the right not affected by the linear response, it has been chosen to start the cycle from a negative field value. Curves with different sweep rate correspond to different magnetic flux, thus to a different voltage level. As a result, curves with different sweep rate do not perfectly overlap but they appear like in the insert of fig.(3.26), where it can be observed that at higher sweep rate corresponds to higher magnetization.

According to eq.(3.3), measurements at given temperature and at different sweep rate can provide more voltage data points at low level range (10^{-4} - 10^{-2} μV/mm). Data obtained from magnetization measurements have been integrated with the characteristics obtained with transport current and are presented in fig.(3.27) with the respective power law predictions previously obtained by fitting data between 0.1 μV/mm and 1 μV/mm.

The magnetization data give a further evidence of the decrement in slope of the E-J characteristics with field. According to the new data point, data at 77 K shows an increased slope and indicate that the exponent n has been underestimated. On the other hand at higher field data indicate a non-accurate definition of I_C and seem to require a smaller power law exponent to allow power law fitting.

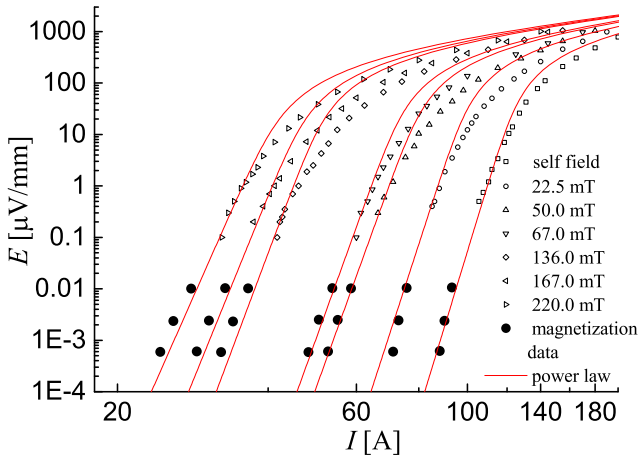

Figure 3.27: E-J characteristics measured in perpendicular field at 77 K and low voltage (10^{-4} - 10^{-2} μV/mm) magnetization data.

3.4.6 Power law exponent n-calculated from magnetization measurements

In order to calculate the n-number as a function of field, raw data have been interpolated with respect of a field vector with same step increment. The n-number can be calculated by inverting eq.(3.4) as in eq.(3.5).

$$n = \frac{\log \frac{(\mathrm{d}B/dt)_1}{(\mathrm{d}B/dt)_2}}{\log \frac{m_1}{m_2}} \tag{3.5}$$

where the numerator is simply given by the ratio between the imposed sweep rates. Two curves are obtained, one calculated between high sweep rates (195 Oe/sec - 45 Oe/sec) and the other one between low sweep rates (45 Oe/sec - 11 Oe/sec). Results are presented in fig.(3.28) where they have been compared with the n-number calculated from DC measurements.

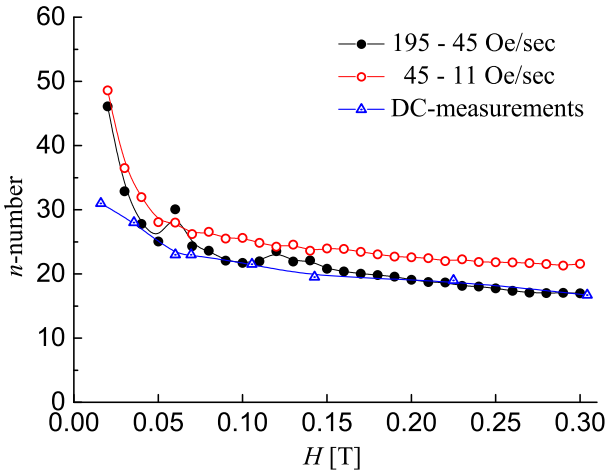

Figure 3.28: n-number dependence on field obtained from magnetization measurements. Comparison with the one obtained from DC measurements.

Smaller sweep rates, which in turn correspond to lower voltage level, predict higher n-number value. The n-number dependence on field obtained by DC measurements is observed to lie below the ones obtained from magnetization measurements in self field, whilst the n- number predicted by both method are quantitatively similar when an external field is applied.

3.5 Conclusion

E-J characteristics of YBCO tape have been collected in both nitrogen bath and cryogen-free conditions. A reproducible technique to reduce the sample cross section

without causing any damage, has been developed and verified. The E-J characteristics of four different YBCO samples with reduced cross section have been collected in a range of temperature between 15 K - 80 K in self field scenario. The main results obtained in the work described in this chapter are:

- The E-J characteristics of 2G conductors, differently from 1G ones, deviate from the power law behaviour in a range of temperatures and at low fields;
- The slope of the dissipation plotted as a function of the current carried by the superconductor shows a unexpected curvature which indicates a more complex flux pinning mechanism than 1G conductors;
- The E-J characteristics have been observed to scale universally at temperatures between 40 K - 80 K and between parallel and perpendicular external field measurements.

4

HTS pinning models and E-J characteristics of 2G YBCO Tapes

4.1 Objectives

The experimental E-J characteristics over a wide range of temperatures (15 K-80 K) have been measured on four different YBCO tapes and the results have been presented in Chapter (3). The experimental measurements evidenced a deviation of the transition characteristics from power-law behaviour in a variety of temperatures and fields, and the deviation has been observed to be consistent for different samples. This chapter focuses on understanding, from a physical point of view, the flux dynamic and the dissipation mechanism which takes place in HTS conductors and on finding a mathematical relation able to predict the E-J characteristic behaviour.

4.2 Dynamic pinning properties of HTS and E-J characteristics

4.2.1 HTS pinning models

The phase transition observed in HTS, and described in section (1.2.5), is the result of the combined action of thermal fluctuations as well as of the pinning offered by sites of different nature, which characterise HTS conductors. Whilst point-like defects

are in fact indubitably present in YBCO in the form of oxygen vacancies, numerous recent experiments have demonstrated the importance of the effect on pinning of twin boundaries and columnar defects [24, 34, 66].

The static and dynamic responses of flux lines to thermal fluctuations and to correlated and uncorrelated disorders, at both high and low temperatures, have been investigated by the two pinning models discussed in section (1.2.6):

- The classical collective pinning model, formulated by Larkin and Ovchinnicov [35], predicts that the action of the large density of point-like defects randomly distributed in the material dominates the depinning mechanism and it is the reason for the glassy behaviour observed in HTS. According to the model, a single pinning centre contributes to hold in place more vortex lines, and at the same time, many pinning centres are needed to hold in place a single vortex. The classic pinning model is the accepted flux pinning mechanism of vortex glass in single crystals and high quality thin films of YBCO;
- The Boson-glass model, formulated by Nelson and Vinokur [36], predicts that the pinning is dominated by the action of correlated disorders along the c-axis and it claims the existence of a Bose-glass phase where flux lines are localised in columnar pins.

A common feature of the two models is that the flux lines are considered flexible elements and, thus, the flux lattice is not expected to be perfectly periodic and rigid as Abrikosov predicted. According to the HTS pinning models:

- The flux lattice can deform under the action of the pinning force;
- The long range order is destroyed;
- The periodicity of the vortex configuration is maintained in a small coherence volume inside which the flux lines lattice can be considered reasonably undistorted.

4.2.2 E-J characteristics of HTS pinning models

Central in the theory of both the classical collective pinning model and the Boson-glass model is not only the determination of the static forces exerted by the different

pinning centres but also the investigation of the dynamic behaviour of the depinning phenomena. Relevant information on the flux dynamics can been extrapolated from the analysis of the measurable E-J characteristics.

The two HTS pinning models predict the same pinning energy dependence on current density, which is of the kind $E \propto \exp(-U(J))$, and thus the same E-J characteristic relation, given by eq.(4.1). However, the two models describe different depinning regimes characterised by different exponents μ and pinning potentials U.

$$\frac{E}{E_C} = \exp\left[\frac{U}{k_B T}\left[1 - \left(\frac{J_C}{J}\right)^{\mu}\right]\right] = \exp\left[u_0\left[1 - \left(\frac{J_C}{J}\right)^{\mu}\right]\right] \tag{4.1}$$

In the work presented in this chapter, the experimental transition characteristics presented in Chapter (3) have been interpreted in the frame of the HTS pinning models, in order to deduce quantitative information about the pinning centres which characterise the YBCO conductors and thus to identify which model better describes the physical depinning mechanism in these conductors.

Overall non-linearity of HTS pinning models.

The theoretical dependence of current on voltage, which is of practical use to predict the experimental transition characteristics, can be obtained by taking the inverse of eq.(4.1). Hence, the current carried by the superconductor J_S can be expressed as in eq.(4.2).

$$J_S = \frac{J_C}{\left[1 - \frac{1}{u_0}\ln\left(\frac{E}{E_C}\right)\right]^{1/\mu}} \tag{4.2}$$

A relation between HTS pinning model parameters and the engineering power-law exponent n_{J_C}, calculated at J_C, can be obtained by calculating the derivative of eq.(4.1), as follows:

$$\frac{\mathrm{d}E}{\mathrm{d}J} = E_C \exp\left[\frac{U}{k_B T}\left[1 - \left(\frac{J_C}{J}\right)^{\mu}\right]\right] \frac{U\,\mu}{k_B\,T}\left(\frac{J_C}{J}\right)^{\mu}\frac{1}{J} \tag{4.3}$$

and

$$n = \frac{\mathrm{d}E/E}{\mathrm{d}J/J} = \frac{\mathrm{dln}E}{\mathrm{dln}J} = \frac{U\,\mu}{k_B\,T}\left(\frac{J_C}{J}\right)^{\mu} \tag{4.4}$$

According to the power law model, the ratio $\frac{\mathrm{d}E/E}{\mathrm{d}J/J}$ corresponds, by definition, to the exponent n. Note that in a limited range of J the n-number is almost a constant, otherwise it changes continuously as J is increased.

The engineering power law exponent n_{J_C} in now obtained using eq.(4.5) and it is expressed as function of the HTS pinning model parameters.

$$n_{J_C} = \left.\frac{\mathrm{d}E/E}{\mathrm{d}J/J}\right|_{J_C} = \frac{\mu\,U}{k_B\,T} = \mu\,u_0 \tag{4.5}$$

In order to predict the E-J transition characteristics by using the relation provided by the HTS pinning models, the two variables introduced in eq.(4.2) have to be known: the dimensionless pinning potential u_0 and the exponent μ. The effect that the latter parameters have on the transition curves can be observed in fig.(4.1) where E-J characteristics, obtained for $\mu = 0.0$, $\mu = 1.0$ and $\mu = 2.0$, are presented in the usual ln$E$-ln$J$ graph.

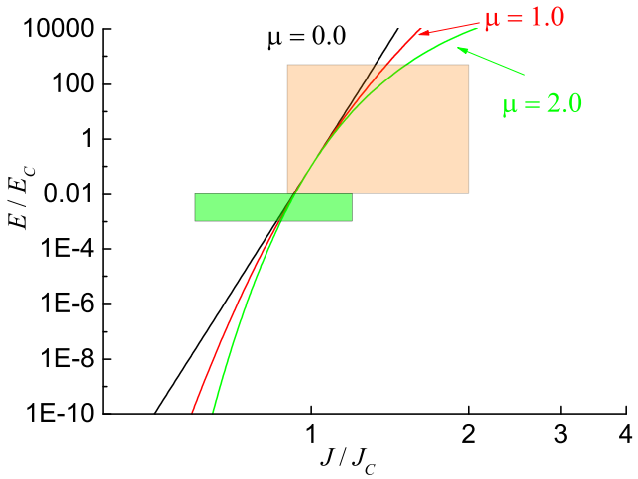

Figure 4.1: HTS pinning model predictions with power law exponent $n_{J_C} = 20$ and $\mu = 0.0$, $\mu = 1.0$ and $\mu = 2.0$. Orange area corresponds to data accessible with transient measurements, green area to the data accessible with magnetization measurements.

The E-J characteristics plotted in fig.(4.1) have been obtained by maintaining fixed $n_{J_C} = 20$ whilst varying the parameter μ. The region highlighted in orange corresponds to the range of voltage data accessible with transient measurements. Note that in a short window of J, despite the different μ the three E-J characteristics of fig.(4.1) are power law-like and collapse on the same curve. Depending on the exponent μ, the deviation from the power law is appreciable only at high voltage of the measured region. However, if a larger window of low voltage data were available, the exponent μ would be easier to define since the three curves separate from each other at low voltages. Magnetization measurements have been carried out and allowed to extend the measured data down to $10^{-3}E/E_C$, as shown by the green area in fig.(4.1). However, no clear distinction between curves of different μ can be made in this area, where E-J characteristics show a power-law like behaviour. Note that the power-law of constant exponent n is a limit case of eq.(4.4), with $\mu = 0.0$ and $U \to \infty$ with $n_{J_C} = \mu U/k_B T =$ finite. The latter case is represented by the black straight line in fig.(4.1).

4.2.3 Determination of the dynamic parameters of HTS pinning models

The temperature dependence of both the exponent μ and of the dimensionless pinning potential u_0 is unknown, thus the two parameters have to be determined. In order to independently determine these two HTS pinning parameters, a graphical method has been developed.

The E-J characteristic law eq.(4.1) provided by the model can be re-expressed as:

$$\log\left[1 - u_0^{-1} \cdot \ln\left(\frac{E}{E_C}\right)\right] = \mu \cdot \log\left(\frac{J_C}{J}\right) \tag{4.6}$$

According to eq.(4.6), a transition characteristic at given temperature is characterised by a constant slope μ when plotted in a $\log\left[1 - u_0 \cdot \ln(E/E_C)\right]$ versus $\log(J_C/J)$ graph. A set of E-J curves, characterised by the same ratio J/J_C but different parameters u_0, has been plotted in such a scaled graph and is presented in fig.(4.2a).

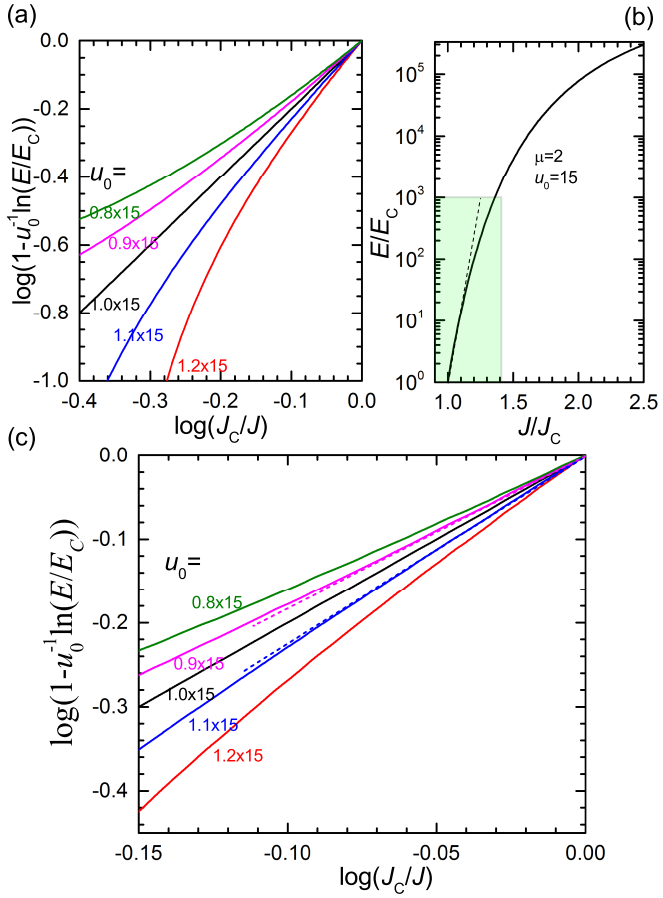

Figure 4.2: (a) Model predictions at given temperature with different u_0, plotted in a scaled graph $\log\left[1 - u_0 \cdot \ln(E/E_C)\right]$ versus $\log(J_C/J)$ and (b) corresponding predicted E-J characteristic curve. The green area indicates the range of measurements. (c) Model predictions at given temperature with different u_0 plotted in a scaled graph $\log\left[1 - u_0 \cdot \ln(E/E_C)\right]$ versus $\log(J_C/J)$, in the range of measurements.

It can be observed that, between the set of curves plotted in fig.(4.2a), only the one obtained by imposing the parameter $u_0 = 1 \times 15$ has a constant slope, as predicted by the model. Any curve obtained with $u_0 > 1 \times 15$ is characterised by a convex shape, whilst any curve obtained with $u_0 < 1 \times 15$ is characterised by a concave shape. Such a scaled graph allows the identification of the parameter u_0 which is required to predict a given transition curve. It also allows the exponent μ to manifest itself once a straight line is obtained. It can be observed as, for the curve in fig.(4.2a) with $u_0 > 1 \times 15$,

$\mu = 2$. Hence, by scaling the curves according to eq.(4.6) it is possible to decouple the HTS pinning parameters μ and u_0 and to determine them unequivocally.

The correspondent E-J characteristics prediction obtained with $u_0 = 1 \cdot 15$ and $\mu = 2$ is plotted in fig.(4.2b). The region corresponding to the range of voltage measured experimentally is highlighted in fig.(4.2b) by the green area and the scaled graph relative to this specific region is presented in fig.(4.2c). Despite the reduced sensitivity of u_0 in this region, a variation of $\sim 10\%$ still produces appreciable deviation, thus the graph provides a useful method to determine the two parameters.

As an example, experimental transition curves measured at 50 K are presented in fig.(4.3a) in the usual log$E$-logJ/J_C graph and compared with the curves predicted by the HTS pinning models, obtained for $u_0 = 12$, $u_0 = 14$, $u_0 = 15$ and $u_0 = 16$.

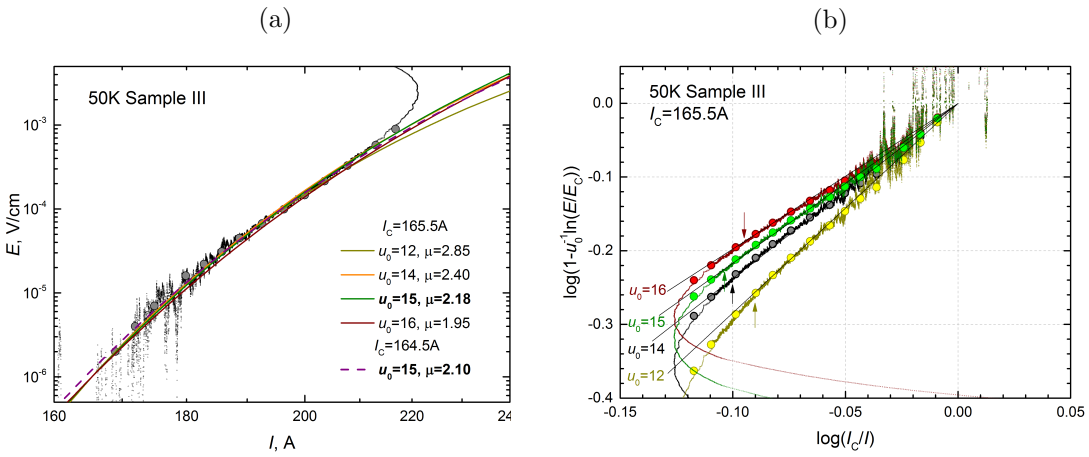

Figure 4.3: (a) E-J characteristics data at 50 K of Sample III and HTS pinning models predictions for different pinning potential $u_0 = 12$, $u_0 = 14$, $u_0 = 15$ and $u_0 = 16$. (b) Data and models prediction characteristics scaled in a graph $\log\left[1 - u_0 \cdot \ln(E/E_C)\right]$ versus $\log(J_C/J)$.

As is evident from fig.(4.3a), although the deviation from the power law ($\mu = 0$) can be accounted for the HTS pinning model relation, the identification of the dynamic depinning parameters cannot be done clearly only by fitting. This is because more than a couple of values for which the condition $U \cdot \mu \propto n_{J_C} = \text{constant}$ is verified, provide a good alignment with the experimental data.

E-J curves predicted by the HTS pinning model relation have been plotted for different values of u_0 and compared with the scaled experimental E-J characteristics at 50 K in fig.(4.3b), according to the scaling above described. On comparing the prediction curves of fig.(4.3b) with the experimental data, it can be observed that the fitting curve which best fits the data corresponds to $u_0 = 15$ and the parameter μ, which can be read from the graph in correspondence of $\log(I_C/I) = -0.10$, is $\mu = 2.10$. Note that data and predictions separate earlier when u_0 is underestimated ($u_0 = 12$) whereas data lie below the predicted curve when u_0 is overestimated ($u_0 = 16$).

Since the resolution of the current is within ± 1 A, errors in the measurement of the critical current might occur. The dependence of μ on the critical current has been investigated by applying the method described above for two critical current values, $I_C = 165.5$ A and $I_C = 164.5$ A. The resulting exponents μ, being $\mu = 2.18$ and $\mu = 2.1$ respectively, show slightly dependence on current, whilst the dimensionless parameter u_0 remains unchanged at $u_0 = 15$. Good estimation of the experimental data over three decades of voltage can be observed in fig.(4.3b), with $\mu = 2.1$. Because of the difficulty on accurately defining the exact point where the data are affected by heating, the exponent μ is accepted with an error margin, which in this specific case appears to be $\mu = 2.1 \pm 0.1$.

It is well know that E-J characteristics at temperatures below 50 K are harder to measure. Difficulties arise from:

- Increased noise level in the transient measurement due to a change in the power supply;
- Disagreement of DC measurements with transient data at low voltage level, whilst a good agreement is instead observed at a higher voltage level. The phenomena could be due the effect of heating during the voltage reading which makes an accurate prediction of I_C difficult;
- Heating effect due to the high operative current, which affects measurements after about two voltage decades. Thus the deviation from power-law behaviour of the characteristics at low temperatures is not appreciable.

It is therefore important to verify that the model also holds at low temperatures. As an example, the E-J characteristic at 20 K and the corresponding fitting curves obtained with $u_0 = 60$, $u_0 = 80$, and $u_0 = 100$ are presented in fig.(4.4a) in the usual log$E$-logJ/J_C graph and in fig.(4.4b) in a scaled graph $\log\left[1 - u_0 \cdot \ln(E/E_C)\right]$ versus $\log(J_C/J)$.

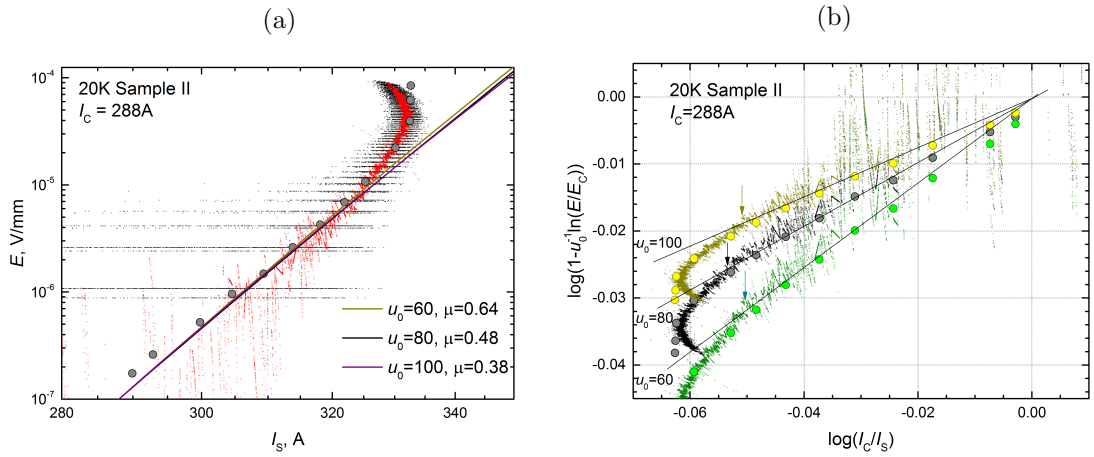

Figure 4.4: (a) E-J characteristics data at 20 K of Sample II and HTS pinning models predictions for different pinning potential $u_0 = 12$, $u_0 = 60$, $u_0 = 80$ and $u_0 = 100$. (b) Data and models predictions scaled in a graph $\log\left[1 - u_0 \cdot \ln(E/E_C)\right]$ versus $\log(J_C/J)$. Critical current $I_C = 288$ A.

The HTS pinning parameters which allow the latest departure from the predicted curve are $u_0 = 80$, and $\mu \sim 0.5$, which correspond to n_{J_C}=40, obtained with the critical current equal to $I_C = 288$ A. However, a good prediction of data with the HTS pinning model relation can be obtained only up to $\sim 20\mu$V/mm. Little differences on the departure of the model prediction from data, can be observed between curves obtained with $u_0 = 60$, $u_0 = 80$, and $u_0 = 100$ and the measured transition curve is so steep that it could be predicted by the simple power law equation. Fitting of the measured E-J characteristics at 20 K is possible for a wider window of values of the parameter μ than the one observed at 50 K, being $\mu = 0.5 \pm 0.5$. The latter observation suggests that the collective pinning could not be no more effective at these temperatures.

4.3 Experimental results analysed with the HTS pinning models

4.3.1 E-J characteristics at different temperatures

The experimental E-J characteristics measured in a range of temperatures and fields presented in Chapter (3) have been compared with the HTS pinning model predictions obtained according to eq.(4.2). Results are presented as a function of the current carried by the superconductor in fig.s(4.5a-d) for Sample I, Sample II, Sample III and Sample IV respectively. HTS pinning model prediction curves are plotted with dashed lines.

(a) (b)

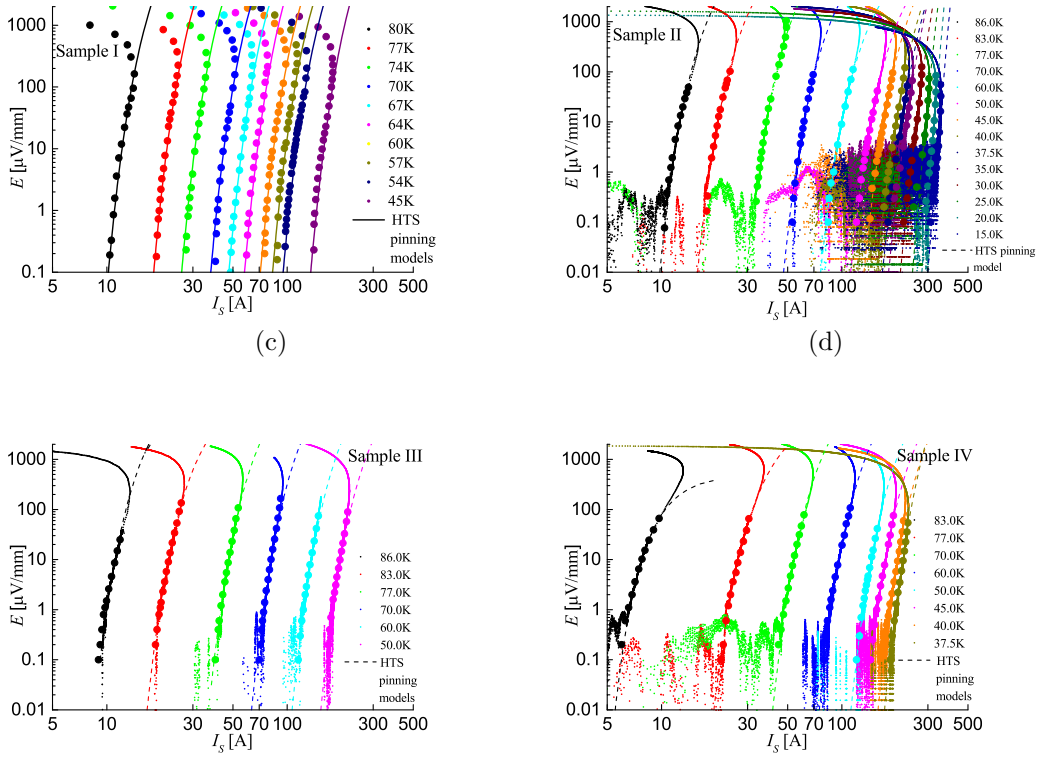

(c) (d)

Figure 4.5: Comparison between E-J characteristics predicted by HTS pinning model (dashed lines), and experimental data measured on (a) Sample I, (b) Sample II, (c) Sample III and (d) Sample IV, plotted as a function of the current carried by the superconductor.

The current-voltage relation provided by the HTS pinning models allow good fit-

ting of the all sets of E-J experimental data over three decades of voltage, for all the measured samples. At a high percentage of J/J_C the heating becomes dominant and E-J characteristics separate from the model predictions. The separation between data and model prediction takes place at lower voltage level as the temperature is lowered, due to the higher J.

The temperature dependence of the exponent μ and of the dimensionless pinning potential u_0, obtained from the HTS pinning model predictions, are presented in fig.s(4.6a-d) for Sample I, Sample II, Sample III and Sample IV, respectively.

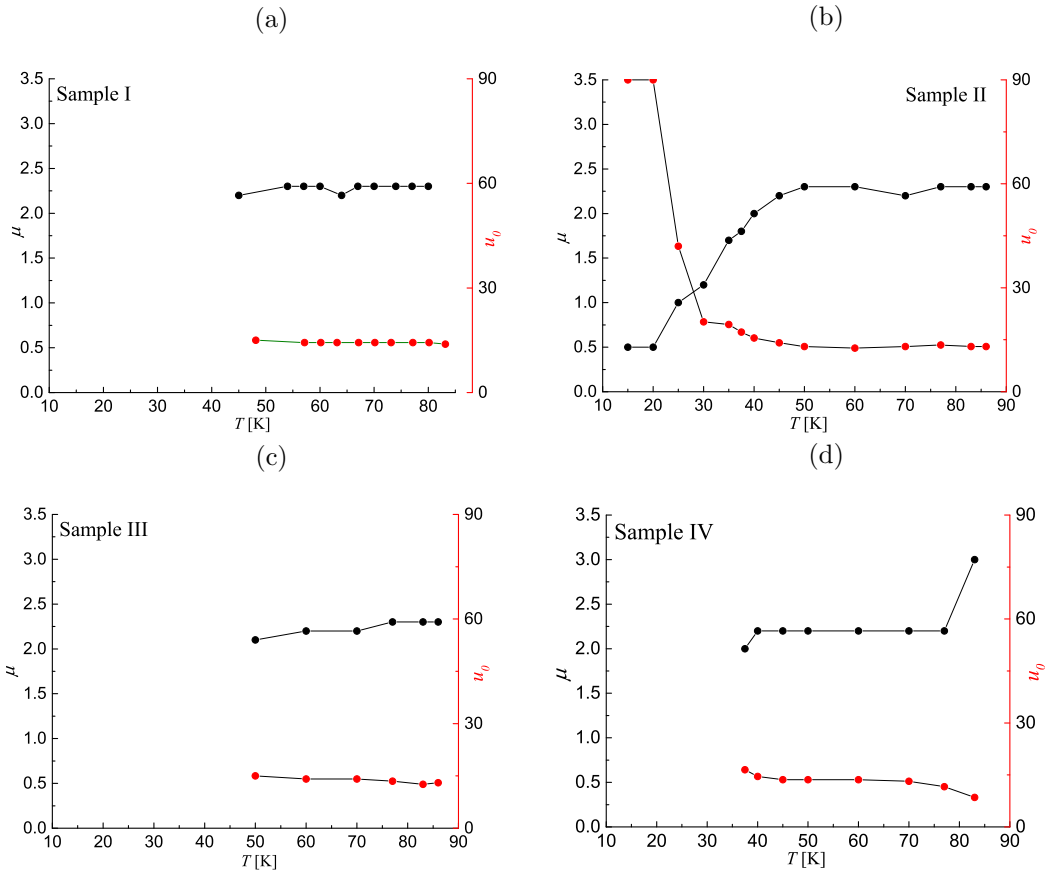

Figure 4.6: HTS pinning model parameters: the dimensionless pinning potential u_0 and the exponent μ against temperature obtained for (a) Sample I, (b) Sample II, (c) Sample III and (d) Sample IV.

Note that:

- The dimensionless pinning potential u_0 remains constant in the temperature range $45\,\mathrm{K} - 77\,\mathrm{K}$ for all measured samples, for Sample I $u_0 = 14.7 \pm 0.3$, for Sample II $u_0 = 13.6 \pm 0.5$, for Sample III $u_0 = 14.5 \pm 1.0$ and for Sample IV $u_0 = 13.4 \pm 0.2$;

- The dimensionless parameter u_0 increases at temperatures below $45\,\mathrm{K}$ and the increment changes abruptly below $35\,\mathrm{K}$ as shown in fig.(4.6b);

- The exponent μ remains almost constant in the temperature range $45\,\mathrm{K} - 77\,\mathrm{K}$ being $\mu = 2.25 \pm 0.05$, even for samples characterised by a greater variation in $n_{J_{C0}}$, which has been found to be $n_{J_{C0}} = 31 \pm 2$ for the four measured samples;

- Below $T = 45\,\mathrm{K}$, the exponent μ decreases as in fig.(4.6b). The temperature $T = 45\,\mathrm{K}$ might indicate a crossover temperature to a different dissipation regime.

- Below $T = 45\,\mathrm{K}$ the observed values of the exponent μ are similar to the ones predicted in the literature for YBCO epitaxial films, which lie in the range $0 < \mu < 1$ [28].

Results obtained on different samples are compared with one another in fig.(4.7) where the $n_{J_{C0}}$ axis is on the left (black axis and data), the exponent μ axis is on the right (red axis and data) and the dimensionless parameter u_0 axis is on the right, further distant from the graph (green dots). Note that despite the difference in the $n_{J_{C0}}$ observed in Sample I and Sample III when compared with Sample II and Sample IV, the HTS pinning exponents μ found for all the measured samples are quantitatively similar. Thus, it can be deduced that the depinning mechanism which takes place on different samples at the same temperature is similar.

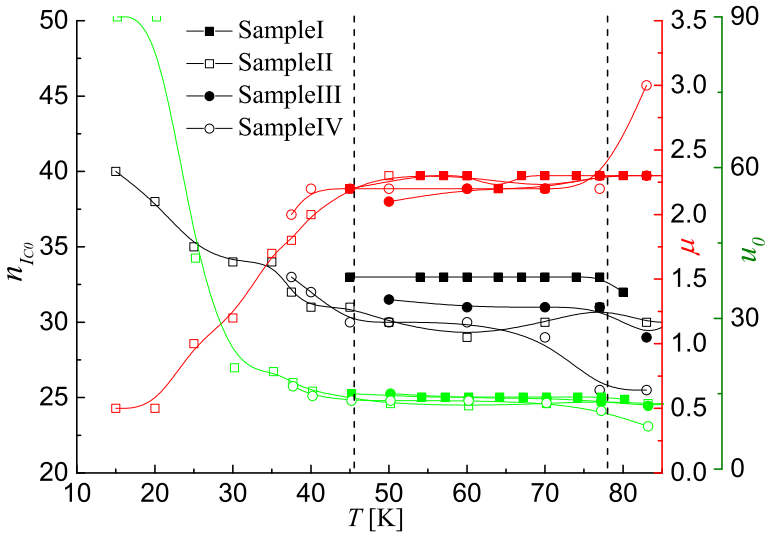

Figure 4.7: Dimensionless collective pinning potential u_0 and exponent μ against temperature of Sample I, Sample II, Sample III and Sample IV.

According to the HTS pinning parameters obtained for Sample II and Sample IV, which have been measured in a wider temperature window, a crossover temperature of $T = 45\,\mathrm{K}$ as indicated in fig.(4.7) by the dashed line, can be clearly seen. This crossover separates a high temperature region where both the exponent μ and the scaled pinning potential u_0 are observed to be constant, and a low temperature region where the exponent μ drops below 1, with a consequent steep increase in the scaled pinning potential.

In the high temperature region, the difference observed in n_{J_C} between tapes is attributed to a difference in the pinning potential u_0 since the exponent μ does not change in this temperature window. Note that although the power law exponent is expected to continuously change along the E-J characteristic (depending on the dissipation level at which is measured), the engineering n-number n_{J_C}, which is a useful parameter for magnet design, lies in the range 29 - 33 for temperatures above 45 K depending on the measured sample. For the protection of a magnet during quench events, a higher n-number is desirable as it increases the propagation velocity. According to the HTS pinning model theory, since the parameter μ chosen is already at its highest values, the pinning potential has to be increased in order to obtain a greater n_{J_C}.

Current-voltage characteristics of Sample I are presented in fig.(4.8a) in a scaled graph as a function of the the ratio I_S/I_C, where they are observed to collapse on the same curve. Since both the pinning potential u_0 and the parameter μ of Sample I are observed to be constant ($u_0 = 14.5 \pm 0.5$ and $\mu = 2.25 \pm 0.05$) in the measured temperature range as shown in fig.(4.7), all the E-J characteristics are evidently predicted by a single HTS pinning model curve, according to eq.(4.2).

(a) (b)

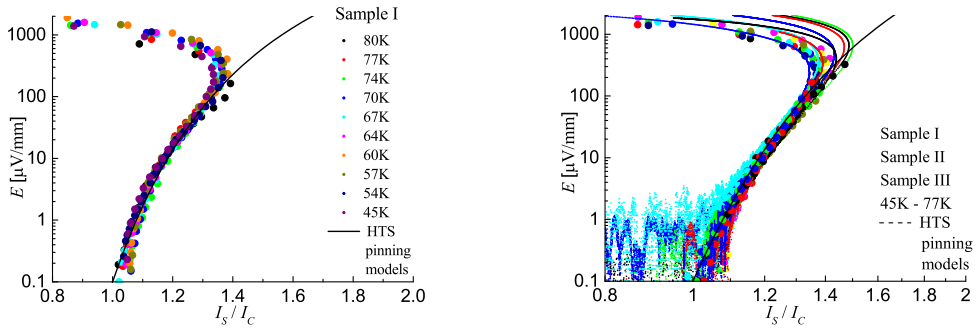

Figure 4.8: (a) Scaled E-J characteristics of Sample I and comparison with HTS pinning model curve, with $u_0 = 14.5 \pm 0.5$ and $\mu = 2.25 \pm 0.05$ (solid line). (b) Scaled E-J characteristics of Sample I, Sample II and Sample III and comparison with HTS pinning model curve, with $u_0 = 14.5 \pm 0.5$ and $\mu = 2.25 \pm 0.05$ (solid line).

The scaled characteristics of Samples I, II and III in the range of temperature $45\,\mathrm{K} - 77\,\mathrm{K}$, which present a slightly wider variation of $u_0 = 14 \pm 1.5$ whilst $\mu = 2.25 \pm 0.05$, when plotted together in fig.(4.8b) collapse on the same curve and can be all well represented by the HTS pinning model prediction (solid line) .

Measurements carried out on Sample II, in a wider range of temperatures, show a change in the pinning parameters below $T = 45\,\mathrm{K}$. Scaling I_S/I_C, all the E-J characteristics of Sample II below the crossover temperature and the respective HTS pinning model prediction have been plotted in fig.(4.9a). The black dotted line corresponds to the HTS pinning model prediction curve for E-J characteristics above $T = 45\,\mathrm{K}$, whilst the plain lines correspond to the model prediction at temperatures lower than $T = 45\,\mathrm{K}$. It can be observed as the change in shape, which reflects in the change in

μ, is not gradual, but rather drastic below $T = 45\,\mathrm{K}$.

(a) (b)

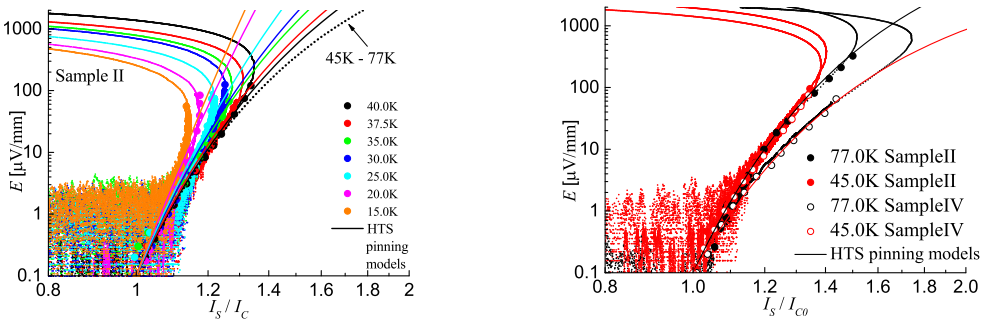

Figure 4.9: (a) Scaled E-J characteristics of Sample II in the range of temperature $15\,\mathrm{K} - 45\,\mathrm{K}$ and comparison with HTS pinning model curves and (b) scaled E-J characteristics of Sample II and Sample IV at $45\,\mathrm{K} - 77\,\mathrm{K}$ and comparison with HTS pinning model curves.

Differently from the other samples, Sample IV is characterised by smaller n_{J_C} above 70 K, as it can be observed in fig.(4.7). E-J characteristics of Sample IV at 45 K and at 77 K are presented in a scaled graph in fig.(4.9b) and compared with the HTS pinning model predictions. The difference in the behaviour of the E-J characteristic of Sample IV at 77 K compared to the other samples, which have been observed to have a similar behaviour in the range 45 K-77 K, is clear. This difference is possibly due to the fact that this sample is characterised by the lowest critical temperature transition, as discussed in Chapter (3).

4.4 The dynamic parameters and pinning of a single vortex and of vortex bundles

The change in μ obtained from experimental data is qualitatively predicted by both the classical pinning model and the Boson glass model as can be observed in the qualitative phase diagram of the two models in fig.(4.10a) and fig.(4.10b) respectively.

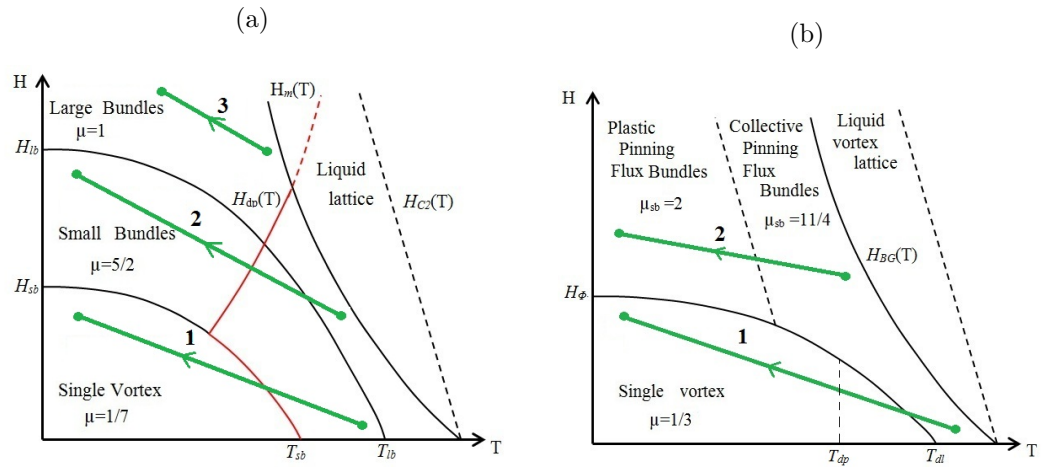

Figure 4.10: Qualitative phase diagrams of HTS in the presence of thermal fluctuations and (a) weak pinning centres and (b) strong pinning centres. Possible dynamic scenarios on reducing temperature at different field (solid green lines).

As it can be observed in fig.(4.10a) and in fig.(4.10b), both models predict a crossover temperature between a region characterised by $\mu > 1$, where the interaction between vortexes is relevant and the flux dynamic is determined by small flux bundles, and a region where μ is significantly $\mu < 1$ and the flux dynamic is dominated by pinning of single vortexes. Note that the predicted change in μ is not expected to be gradual but to be rather drastic at the crossover $H_{sb}(T)$ line. Also, both models predict a crossover temperature in the self field scenario, which is strongly influenced by thermal depinning.

According to results obtained from the experimental data, in order to go from $\mu > 1$ at high temperatures to a $\mu < 1$ at low temperatures, a field/temperature path shown by curve number 1 in both models must be followed. As H_{sb} and H_Φ are significantly greater than the self field values, path 1 is the one predicted to takes place in self-field measurements, whilst paths 2 and 3 are the expected path for measurements in presence of applied field.

According to the classic collective pinning model, the drastic change in μ observed on lowering the temperature can be sensibly interpreted as a passage from a small bundles regime to a single vortex regime which takes place at T_{sb} at zero field as shown in

fig.(4.10a). This would require that T_{sb} is above 20 K. The exponent μ has instead been observed to increase above > 2 at 83 K in Sample IV which is not predicted by any of the two models. Note that if further measurements were made in high fields, a opposite change in μ (curve 2) or no change at all (curve 3) would have been expected to be observed with reducing temperature.

According to the Boson glass model, on reducing the temperature in a self field scenario (curve 1 in fig(4.10b)), flux dynamics are initially dominated by collective movements of small vortex bundles with $\mu = 11/4$ ($T > T_{dl}$) and successively by single vortex lines regimes with $\mu = 1/3$ ($T < T_{dl}$). Note that measurements in fields higher than H_Φ (curve 2 in fig(4.10b)), does not allow access the single vortex regime and the μ would be expected to decrease (from $\mu = 11/4$ to $\mu = 2$) as the dynamic changes from the collective movement of flux bundles to a plastic regime [36].

4.4.1 Static properties of the HTS pinning models

The phase diagram and the measured exponent μ are not sufficient to establish which model best describes the flux dynamic in YBCO. Measurements have been therefore compared to theory in order to extract quantitative information about the single vortex flux dynamic and to understand which model better suits the experimental results obtained.

Depairing current

The depairing pinning current J_0 is a fundamental parameter which measures the strength of the pinning of the material when scaled with the critical current density $J_C(T)$. The depairing critical current density is a function of the thermodynamic critical field and it can be expressed as in eq.(4.7).

$$J_0(0) = 0.433 \frac{H_C(0)}{\lambda(0)} \tag{4.7}$$

Note that:

- The dependence on temperature of $\xi(T)$ and $\lambda(T)$ is expected to be of the kind $\xi(T) = \xi(0) \left[1 - \left(\frac{T}{T_C}\right)^2\right]^{-0.5}$ and $\lambda(T) = \lambda(0) \left[1 - \left(\frac{T}{T_C}\right)^2\right]^{-0.5}$ [20];

- In the limit of low temperature, typical values of coherence length $\xi(0)$ and penetration depth λ for YBCO are $\xi(0) = 14 \cdot 10^{-10}$ m and $\lambda(0) = 1400 \cdot 10^{-10}$ m;

- The thermodynamic field $H_C(T)$ is defined as $H_C(0) = 2.327 \cdot 10^8/(\xi(0)\,\lambda(0))$ and therefore is expected to have a temperature dependence of the kind:

$$H_C(T) \sim H_C(0) \left[1 - \left(\frac{T}{T_C}\right)^2\right] \tag{4.8}$$

Eq.(4.7) can therefore be modified to the form of eq.(4.9):

$$J_0(0) = J_0 \left[1 - \left(\frac{T}{T_C}\right)^2\right]^{1.5} \tag{4.9}$$

The thermodynamic field has been estimated to be $H_C(T) \sim 12000\,\mathrm{G}$ [5], and the deparing critical current density, according to eq.(4.9), has been found to be $J_0(0) \sim 3.7 \cdot 10^{12}\mathrm{A/m}^2$. Note that the $J_C(T)$ can be obtained from the measured critical current divided by the sample cross section of area $A = 2 \cdot 10^{-9}\,\mathrm{m}^2$.

The measurements presented in Chapter (3) are in a self field scenario and characterised by a crossover temperature $T = 45$ K below which μ drops below 1. According to both the classical collective pinning model and the Boson-glass model, the change in μ observed in the experimental data at temperatures $T > 45$ K, corresponds on passing from the small bundles into the single vortex regime, where values of μ are expected to lie in the range $0 < \mu < 1$. It should not be surprising that the exponent μ remains constant above $T = 45$ K for different samples, since HTS pinning models predict that even if the parameters J_C and n_{J_C} are slightly different the dynamic of vortex above the crossover temperature remains unvaried. Since both models predict the entrance into the single vortex regime, some quantitative estimation can be done.

4.4.2 Single vortex in Boson-glass model

According to the Boson-glass model, a sample is characterised by the presence of columnar defects of radius r_r, distanced from one another by a length d_r. The critical current density for a single vortex pinned by a single columnar defect is predicted to be of the same order of the depairing current density J_0 when $r_r > \xi$. Since the measured $J_C(T)$

is much smaller than the calculated J_0, it is realistic to be in case $r_r < \sqrt{2}\xi$ where the critical current density dependence on r_r and ξ is predicted to be the one of eq.(4.10).

$$J_C(T) = \frac{27\sqrt{2}}{64}\left(\frac{r_r}{\sqrt{2}\,\xi(T)}\right)^2 J_0(T) \qquad \text{with} \quad r_r < \sqrt{2}\xi \tag{4.10}$$

The measured critical current in the region where the single vortex regime is expected, have been used to estimate the defects dimensions according to eq.(4.10). The parameters $J_C(T)$, $\xi(T)$ and $J_0(T)$ needed for the analysis have been calculated and are listed in table(4.1). By using the value at $T = 15$ K, the radius of the columnar defects has been found to be $r_r \sim 7 \cdot 10^{-10}$ m.

T	$J_C(T)$	$\xi(T)$	$J_0(T)$
K	A/m^2	10^{-10} m	A/m^2
15	$\sim 15 \cdot 10^{10}$	~ 14	$\sim 3.5 \cdot 10^{12}$
45	$\sim 7 \cdot 10^{10}$	~ 16	$\sim 2.8 \cdot 10^{12}$

Table 4.1: YBCO critical current density $J_C(T)$, coherence length $\xi(T)$ and depairing current dependence on temperature $J_0(T)$.

4.4.3 Small bundles in Boson-glass model

According to the Boson-glass model, the crossover at zero field between single vortex regime to flux bundle depinning, takes place at the temperature T_{dl} (see fig.(4.10)) given by eq.(4.11).

$$T_{dl} \sim \widetilde{T_{dp}}(T_{dl}) \cdot \ln\left(\frac{d_r}{b_0}\right)^2 \tag{4.11}$$

where the parameter b_0 is defined as $b_0 = \max\left\{r_r, \sqrt{2}\,\xi\right\}$ and $\widetilde{T_{dp}}(T_{dl})$ is the thermal depinning energy calculated at the crossover temperature T_{dl}between the single vortex regime and the small bundles regime, as given by eq.(4.12).

$$\widetilde{T_{dp}}(T) \sim b_0\sqrt{\varepsilon_l \cdot \varepsilon_r(T)} \tag{4.12}$$

where $\varepsilon_r(T)$ is the pinning potential produced by a pinning defect and it can be calculated as follow:

$$\varepsilon_r(T) = \varepsilon_r \cdot \frac{\left(1 + \sqrt{\frac{T^2}{b_0 2_{\varepsilon_l \varepsilon_r}}}\right)}{2} \tag{4.13}$$

where $\varepsilon_r = \varepsilon_r(0)$ is the rod potential well given by eq.(4.14) and ε_l is the energy line tension given by $\varepsilon_l = \varepsilon_0 \cdot \lambda/\xi$.

$$\varepsilon_r = \varepsilon_0 \left(\frac{r_r}{2\,\xi(T)}\right)^2 = \left(\frac{\Phi}{4\pi\lambda}\right)^2 \left(\frac{r_r}{2\,\xi(0)}\right)^2 \sim 15 \cdot 10^{-14}\,\mathrm{N} \tag{4.14}$$

As it can be observed in fig.(4.10b), the Boson model predicts a change in regime in the single vortex phase at $T_{dp}(0)$ from pinning of a single vortex offered by a single rod to pinning of a single vortex due to action of many rods, whilst the crossover temperature from single vortex regime to collective pinning regime is expected to take place at T_{dl}. Since the crossover temperature is observed in the experimental data to be $T_{dl} = 45\,\mathrm{K}$, by using the parameters listed in table(4.1), according to eq.(4.15) T_{dp} can be estimated to be $T_{dp} \sim 18.6\,\mathrm{K}$.

$$T_{dp} = \widetilde{T_{dp}}(T_{dp}) \sim \left(\frac{3}{4}\right)^{0.5} b_0 \sqrt{\varepsilon_r \varepsilon_l} \tag{4.15}$$

In order for the condition $T_{dl} = 45$ K to be verified, the defects distance, calculated using eq.(4.11), is expected to be $d_r = 67 \cdot 10^{-10}$ m. Such defects dimensions suggest the presence of very dense twin boundaries which act as strong pinning centres.

Although the model offers a reasonable quantitative description of the system in the single vortex regime, a contradiction has been found on calculating the critical current in the collective pinning of vortex bundles, which is given by eq.(4.16).

$$J_C(T) = \left(\frac{\varepsilon_r}{\varepsilon_0}\right) \left(\frac{\xi(T)}{d_r}\right) \left(\frac{b_0}{d_r}\right)^2 \left(\frac{T_{dl}}{T}\right)^4 \cdot J_0(T) \tag{4.16}$$

The critical current is expected to sharply decrease with temperature because of the factor $(T_{dl}/T)^4$, a behaviour which has not been experimentally observed. At 45 K in fact, the critical current calculated according to eq.(4.16) is $J_C = 3.9 \cdot 10^7 \mathrm{A/m^2}$,a value extremely smaller than the measured one at the same temperature $\sim 7 \cdot 10^8$. Also, in order to predict a greater J_C, it should be verified that $r_r > \sqrt{2}\xi$ which is in contrast with the results obtained from the pinning of the single vortex analysis.

4.4.4 Single vortex in classic collective pinning model

According to the classic collective pinning scenario, the collective pinning length can be calculated as in eq.(4.17) and its dependence on temperature is plot in fig.(4.11).

$$L_C = \xi(T) \sqrt{\frac{J_0(T)}{J_C(T)}} \tag{4.17}$$

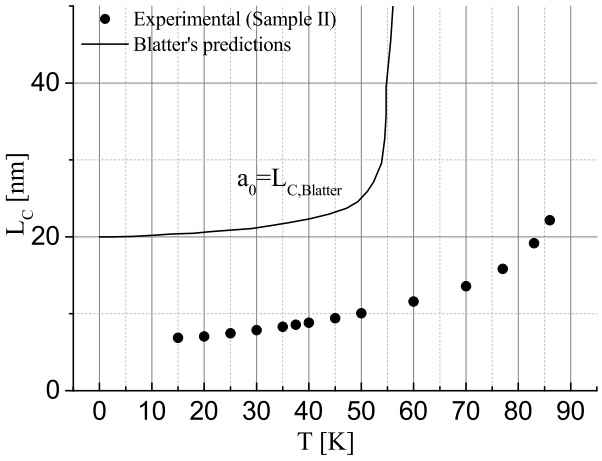

Figure 4.11: Collective pinning length L_C dependence on temperature. Comparison between experimental data of Sample II and Blatter's predictions.

As it can be observed in fig.(4.11), the length in which the flux lines are expected to deform is therefore of the order of nanometres, and decreases sharply at low temperatures ($L_C \sim 5 - 10$ nm between 10 K - 50 K, because of the effect of the increased critical transport current $I_C(T)$).

4.4.5 Small bundles in classic collective pinning model

Uncertainties on the validity of the classic collective pinning model arise at the crossover temperature. The classic collective pinning model predicts that the crossover between the collective pinning of single vortex lines to the collective pinning of flux bundles takes place when the condition $L_C = a_0$ is verified. In order to verify the latter condition, the field at the crossover temperature is expected to be:

$$B(T) = \frac{2\Phi}{\sqrt{3}\,\xi^2}\,\frac{J_C(T)}{J_0(T)} = 14.5\,H_{C2}\,\frac{J_C(T)}{J_0(T)} \tag{4.18}$$

Therefore, according to the value listed in table(4.1), at the temperature $T = 45\,\mathrm{K}$ it should be verified that $B \sim 30$ T, which is an unreasonably high value. Thus, the change from single vortex to small flux bundles cannot be quantitatively predicted from the classical collective pinning model because of the high critical current values measured which make L_C too small according to eq.(4.17) and not able to cross a_0 at any temperature. According to Blatter [5], the B_{sb} at 0 K is expected to be $B_{sb}(0) \sim 6$ T and $T_{sb} \sim 60$ K.

By using Blatter's field dependence on temperature $B_{sb} = B_{sb}(T)$, the expected collective pinning length $a_0 = L_{C,Blatter}$ that allows the passage to the small bundles dynamic, can be worked out and the result is plotted in fig.(4.11). $L_{C,Blatter}$ is observed to lie above the collective pinning length $L_{C,}$ obtained from experimental data in the measured temperatures.

Also, according to the collective pinning model, the ratio $J_C(45\,\mathrm{K})/J_0(45\,\mathrm{K}) \sim 0.028$ obtained from the experimental data corresponds, from eq.(4.18), to a field which is only a fraction of the thermodynamic one $\sim 0.4\,H_{C2}$. Therefore, according to the classic collective pinning model, the superconductor is already working close to its limit and very little improvement in J_C and in n_{J_C} can be expected to be achieved in these conductors.

In conclusion, although the change in the dynamic exponent μ observed from measurements is believed to show a transition from a single vortex to a small bundles dynamic as is predicted to happen by both the classic collective pinning model and the Boson-glass model, the measured critical current density and its dependence on temperature present inconsistencies with the model predictions provided by both models since they both predict a smaller current to the one measured in the small bundles regime:

- In the classic collective pinning model, reasonable self-field values require a larger collective pinning length L_C than the one obtained with measurements, and thus a smaller critical current density as in eq.(4.17).

- In the Boson glass model a much smaller reduction of current of the one experimentally observed is predicted by eq.(4.16). The dependence on temperature of the ratio $J_C(T)/J_0(T)$ calculated according to eq.(4.16) is presented in fig.(4.12) and compared with Blatter's prediction where it is clearly shown that the experimental data are ~ 5 greater than the values predicted by the model in the all measured range of temperatures.

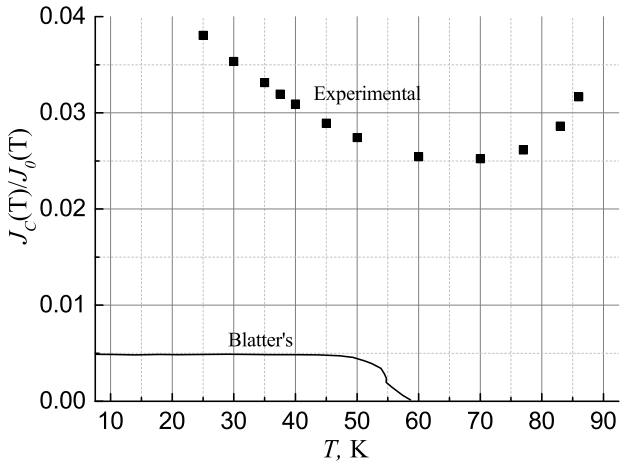

Figure 4.12: Scaled critical current with the deparing current $J_C(T)/J_0(T)$ versus temperature. Comparison between experimental data of Sample II and Blatter's predictions.

Two possible pictures are suggested in this work:

- Different criteria in the self field scenario: since the experimental data analysed are in the self-field scenario where the flux structure is rather complex and not uniform, the condition $L_C = a_0$ which determine the passage from a single vortex to a vortex bundles regime could not hold anymore. Blatter predicts, in fact, $B_{sb}(T_{sb}) = 0$ which implies that small bundle dynamics take place at any $T > T_{sb}$ even if no field is present and independently from the length L_C. However the problem of the small critical current predicted in the small bundles regime remains unsolved;

- Possibility of a mixed action of weak and strong pinning sites. At low temperatures weak pinning centres are strong enough to hold the single vortexes in place and the sample exhibits the glass behaviour, whilst at high temperatures, where thermal fluctuations are strong, weak pinning centres are not enough to hold the vortex in place and the correlated disorder becomes more important. The presence of strong pinning defects limits the delocalisation and wandering of the flux lines. In this scenario, further pinning is provided by the presence of weak pinning centres which further inhibit the delocalisation of flux bundles and allow the critical current density to remain high. Therefore, the coexistent weak pinning sites with strong pinning site can provide additional force to pin the lines as bundles, without suffering a reduction of the critical current density.

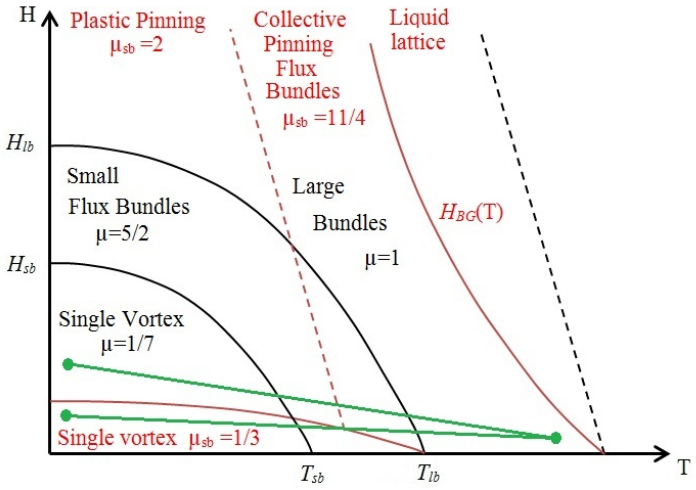

Figure 4.13: Qualitative phase diagram of HTS in presence of thermal fluctuation and weak pinning centres dominant action (solid black lines) and strong pinning centres dominant action (red solid lines). Possible dynamic scenarios in self field on reducing temperature (green solid lines).

According to the latter picture, the delocalization length l_{loc} in presence of flux bundles formed in presence of strong defects can be expressed as:

$$l_{loc} = d_r \ln \left(\frac{d_r}{b_0} \right)^2 \tag{4.19}$$

Since the crossover temperature is expected to be $T = 45$ K, l_{loc} is estimated to be $l_{loc} \sim 100 \cdot 10^{-10}$ m as it can be observed in fig.(4.11). According to eq.(4.19), the condition $l_{loc} \sim 100 \cdot 10^{-10}$ m is verified for $d_r \sim 68 \cdot 10^{-10}$ m, which is very similar to what predicted by single vortex analysis. By calculating eq.(4.17) at $L_C = l_{loc}$, it can be found $J_0/J_C \sim 0.026$ at 45 K, which is roughly the critical current density obtained by experimental measurements.

A qualitative diagram of the scenario expected is presented in fig.(4.13) where the black curves correspond to the classical collective pinning model scenario and the red lines to the Boson-glass model one. The possible mixed scenario here speculated is highlighted by the green line.

4.4.6 *E-J* characteristics in applied low fields

The collective pinning model has been applied to the *E-J* characteristics measured in a liquid nitrogen pool at 77 K with an external field of up to 300 mT in both perpendicular and parallel configuration. The data measured and relative collective pinning model predictions are presented in fig.(4.14a) and fig.(4.14b) for perpendicular and parallel field scenarios as a function of the current carried by the superconductors. A good agreement between the obtained curves through the collective pinning empirical formula and the experimental data can be observed also in applied field.

(c) (d)

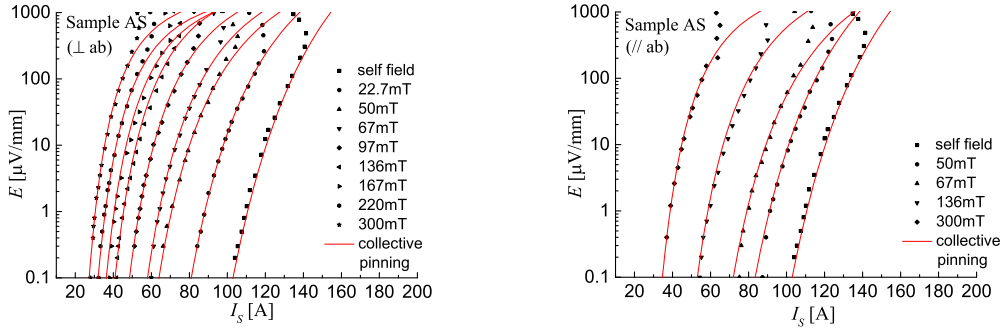

Figure 4.14: *E-J* characteristics measured in nitrogen bath presented as a function of the current carried by the superconductors (a) when an external perpendicular field is applied and (b) when an external parallel field is applied.

The analysis has also been extended to measurements collected in a perpendicular field scenario on the bridged tape, Sample V. Data and relative collective pinning model predictions are presented in fig.(4.15a) and in in fig.(4.15b) as a function of the total operative current and of the current carried by the superconductor respectively. Note that the current change on the x-axis is much less then the one observed on the uncut tape and the curves may look steeper as a result of the chosen scale.

(a) (b)

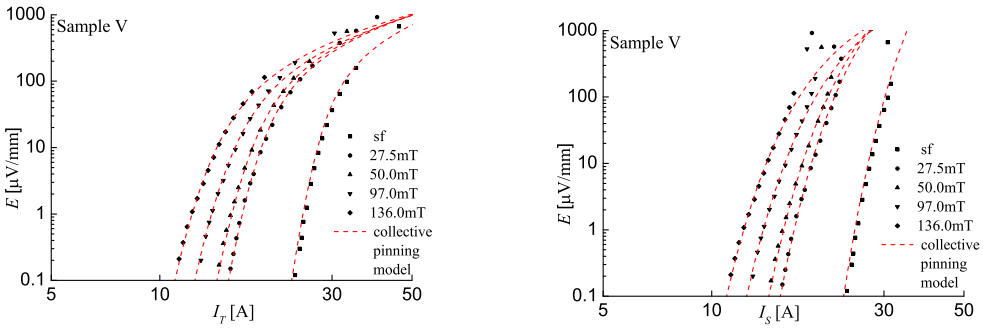

Figure 4.15: E-J characteristics and relative collective pinning model predictions of the 1 mm bridged tape Sample V, measured in low field in perpendicular configuration and plotted as a function of (a) the total operative current and of (b) the current carried by the superconductor.

The dependence on field of the pinning potential values obtained according to the collective pinning model analysis, namely the thermal excitation $u_0 = U_0/(k_B \cdot T)$ and the parameter μ, is shown in fig.(4.16a), where results are compared between parallel and perpendicular scenarios and in fig.(4.16b) where results are compared between Sample V and Sample AS, both exposed to a perpendicular field.

As it can be observed in fig.(4.16a), the exponent μ remains constant with decreasing field in both perpendicular and parallel field scenarios. On the other hand, the dimensionless parameter u_0 is found to decrease with field and, as a result, also the engineering n-number n_{J_C} decreases with field, in both perpendicular and parallel cases. All the parameters obtained are greater for measurements obtained with the applied field parallel to the ab plane. The u_0 curves in both perpendicular and parallel field tend to merge at high field, but more measurements at higher field would be required

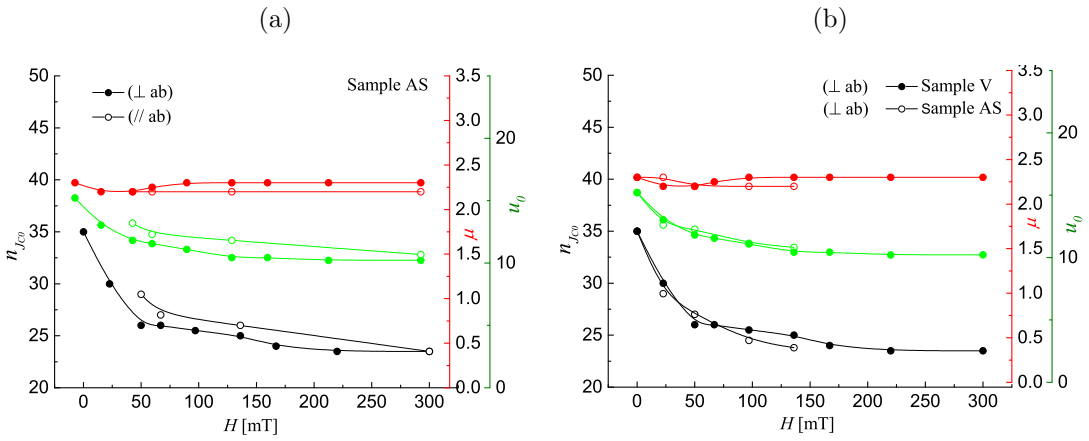

Figure 4.16: (a) Comparison of μ and u_0 dependence on field obtained in perpendicular and parallel field on Sample AS and (b) comparison of μ and u_0 dependence on field for bridged tape Sample AS and uncut tape Sample V, in perpendicular field.

to confirm this trend.

Concerning fig.(4.16b), it can be appreciated that both samples (cut and uncut), Sample V and Sample AS, present similar behaviour and that the field-dependent transient measurements collected on these samples can be described, according to the model, by the same collective pinning parameters.

4.4.7 Magnetization measurements and HTS pinning models

Magnetization measurements presented in section (3.3.3) allowed to extend the range of measurement down to $10^{-4}\mu$V/mm.

Thus the data obtained with magnetization measurements have been included in the DC measurements graph, as in fig.(4.17) and compared with the HTS pinning models predictions (red lines). A reasonable good agreement between the models and the predictions has been observed. The picture suggests the possibility of a change of regime in the presence of an external field applied, as the transport current is further increased.

In order to verify if the collective pinning model is able to predict the change from single vortex to small flux bundles regime in applied field, the critical current dependence

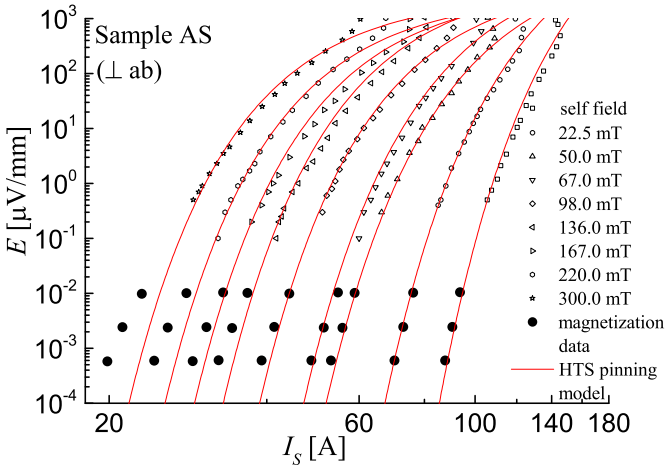

Figure 4.17: E-J characteristics measured in perpendicular field at 77 K and low voltage (10^{-4} -10^{-2} μV/mm) magnetization data, fitted by collective pinning model predictions (red lines).

on temperature in a 5 T field measured at the University of Houston [53] have been compared with the critical current dependence on temperature measured in self field. The two curves scaled with the critical current at 4.2 K, respectively $I_C \sim 340$ A in self field and $I_C \sim 90$ A at 5 T, are presented in fig.(4.18).

The critical current in the field of 5 T and in self field shows a similar dependence on temperature, disagreeing with the classic collective pinning model prediction given by eq.(4.16). On the other hand, since the ratio $J_{C,5T}/J_{C,sfield} \sim 0.2$, the factor J_C/J_0 of eq.(4.18) is smaller than in the self-field case and so is the field expected at the crossover between the two regimes ($B \sim 6.5$ T at 40 K). However, the condition $L_C > a_0$, associated with flux bundles regime cannot be verified since $L_C(40)\,\mathrm{K} \sim 19$ nm and $a_0(40\ \mathrm{K}) \sim 22$ nm. This is a further demonstration that the classic collective pinning model on its own is not able to quantitatively predict the passage from a single vortex to a small bundles regime, even when a reasonable high external field is applied and the flux is expected to penetrate the material more uniformly.

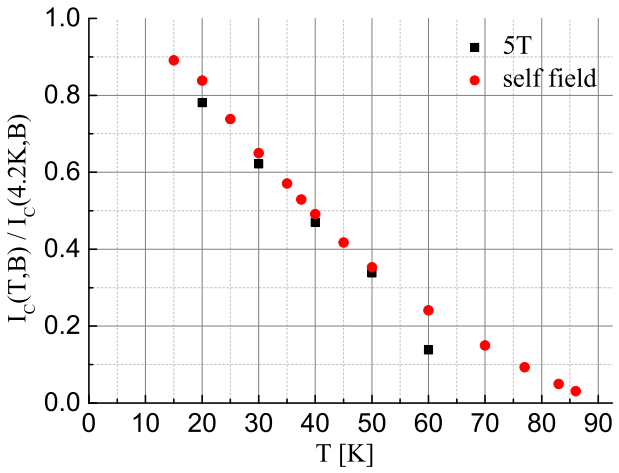

Figure 4.18: Critical current dependence on temperature measured in self field scenario and with 5 T field applied.

4.5 Conclusions

HTS pinning models allow the prediction of the E-J characteristics measured in a wide range of temperatures and fields on different samples. Thus, it can be claimed that the model proposed for YBCO single crystal well represents also the bi-axially textured film.

The exponent μ is observed to remain constant above $T = 45\,\mathrm{K}$ to the value $\mu = 2.2$ which, according to both the classical collective pinning model and the Boson model predictions, indicates that small vortex bundles are involved in the dissipation process. As the temperature is lowered below 45 K, the exponent μ is observed to decrease to values < 1 and, because of the smaller range of voltage data available, a good fitting of the experimental data is obtained even in the limit case of $\mu \longmapsto 0$, which corresponds to a simple power law model. The change in pinning parameters observed below $T = 45\,\mathrm{K}$ in the temperature range of 45 K-77 K, can be interpreted in the frame of change of regime from small vortex bundles to single vortex, which are qualitatively predicted by both the classical collective pinning model and the Boson-glass model. However, from quantitative analysis, the results obtained from both models are too week to justify the measured critical current in the expected small bundles region above $T = 45\,\mathrm{K}$. A

possible scenario suggested in this work is based on the combined action of weak pinning centres as well as strong pinning centres. According to this scenario, the presence of high density strong defects allows the pinning of flux bundles, which under the action of the thermal fluctuation partially wander away from the columnar pin. Extra pinning is then provided by weak pinning centres which act on the flux lines so that to obstacle the current reduction predicted by the Boson glass model in the presence of small bundles.

5

Flux pinning distribution and E-J characteristics of 2G YBCO Tapes

5.1 Motivation

The experimental E-J characteristics measured on different YBCO samples, presented in Chapter (3) showed deviation from power law behaviour in a variety of temperatures and fields. Such a deviation has been interpreted, as discussed in Chapter (4), in the frame of the HTS pinning models, according to which flux bundles are collectively pinned under the action of a multitude of correlated and uncorrelated defects present in the conductor. The HTS pinning model analysis qualitatively suggests that in presence of weak and strong pinning sites, the dynamic of flux lines in YBCO changes from the collective pinning of small flux bundles regime at high temperatures to the collective pinning of single vortex lines at low temperatures. Although the collective pinning behaviour is the believed mechanism responsible of the flux dynamic in YBCO tapes, the model introduces parameters related to the microscopic characteristics of the material and thus it does not allow easy comparison between different conductors quality and performances.

In this chapter, a macroscopic statistic model of more practical use, called *distribution model* is used to describe the non-linear E-J characteristics behaviour. According to the distribution model, the presence of pinning sites of different nature is associated to

a distribution of pinning potential and thus to a spatial distribution of critical current. In this chapter the model predictions are compared with the experimental results and the critical current distribution and the headline pinning range are investigated.

5.2 Theory of the distribution model

The concept of critical current, classically defined as the current at which dissipation starts and a measurable voltage is observed, is one of the fundamental parameter to describe the superconductor performances. However, dissipation is rather a gradual process which takes place as flux lines/bundles deform, dislocate until being completely depinned. Also, as explained in section (1.2.6), HTS conductors are characterised by complex crystalline structures and present high density of crystalline defects of different nature, which act differently on vortices.

The characteristic inhomogeneity of these conductors makes reasonable the assumption of:

- A wide distribution of pinning centres exerting different strength on vortices;
- A wide distribution of critical current density.

The distribution model was proposed by Kiss [67] and assumed a spatial distribution of a critical current, described in terms of a probability density function $P(J_C)$[68].

Since the critical current is not regarded any more as a uniform property, the flux motion cannot be considered uniform neither. Flux motion is instead predicted by the model to be a *percolative* motion as schematically represented in fig.(5.1). The unpinned flux bundles are thought as resistive clusters (represented in black spots) of different shape that form when a certain minimum current density J_{Cmin} is reached. Then the clusters grow percolatively as the current is further increased, until eventually completely cover the sample.

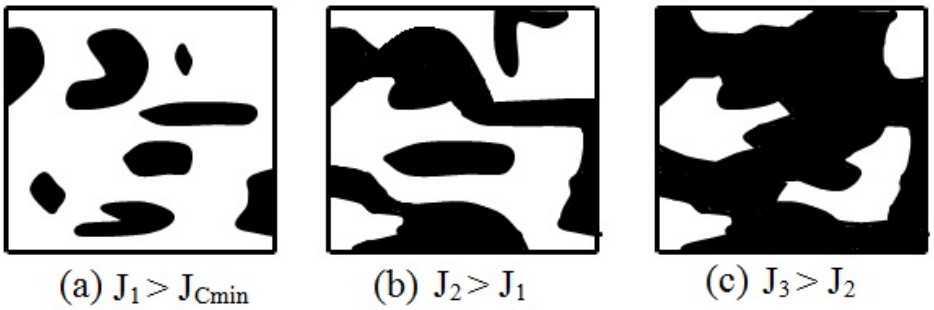

Figure 5.1: Schematic representation of the percolative motion of depinned flux bundles (black spots) following an increment in transport current above the minimum critical current density J_{Cmin} [69].

5.2.1 Analytical expression of the global E-J characteristic

According to the distribution model, the measured E-J characteristic is the results of the superimposition of elementary current-voltage characteristics of different domains, over the distribution of critical current density. Note that the model maintains the fundamental concept of critical current density both from a macroscopic and from a microscopical point of view:

- Macroscopically, the global critical current density corresponds to the minimum value of the distribution J_{Cmin};
- Microscopically, flux lines/bundles are predicted to experience a local drastic change from a pinned state to an unpinned state which takes place at a well defined local critical current value J_C. Therefore flux lines are assumed to experience an abruptive jump from the state of no flux flow to a fully flux flow regime at J_C.

The flux lines/bundles contribution to dissipation can be expressed as in eq.(5.1):

$$E_e(J_C, J) = \begin{cases} \rho_{ff} \cdot (J - J_C) & J > J_C \\ 0 & J < J_C \end{cases} \tag{5.1}$$

where ρ_{ff} is the flux flow resistivity and J_C is the local critical current value. According to eq.(5.1), if a transport current $J_C^{'} > J_{Cmin}$ is imposed, the flux bundles domains characterised by local critical current density $J_C < J_C^{'}$ are in flux flow regime

and contribute to dissipation, whilst the ones characterised by critical current density $J_C > J_C^{'}$ remain pinned and do not contribute to dissipation. Note that flux creep effects are disregarded since they have been observed to give a negligible contribute to the global dissipation characteristic [70].

For a given critical current distribution $P(J_C)$, the correspondent macroscopic E-J characteristic can be obtained by summing the contribution to dissipation of different domains, as in eq. (5.2).

$$E(J) = \int_{J_{Cmin}}^{J} P\left(J_C\right) \cdot E_e(J, J_C) \cdot \mathrm{d}J_C \tag{5.2}$$

Note as the assumption or either local zero dissipation or fully flux flow regime given by eq.(5.1) makes the integral of eq.(5.2) easier to solve when compared with the power law model one.

The depinning probability of flux bundles $P(J_C)$ which best predicts the experimental E-J characteristic of bulk and sputtered thin films in a range of temperatures and fields, has been found to be the Weibull distribution function given by eq.(5.3) [71, 72].

$$P(J_C) = \begin{cases} \frac{m}{J_0} \cdot \left(\frac{J_C - J_{Cmin}}{J_0}\right)^{m-1} \cdot \exp\left[-\left(\frac{J_C - J_{Cmin}}{J_0}\right)^{m}\right] & J_C > J_{Cmin} \\ 0 & J_c < J_{Cmin} \end{cases} \tag{5.3}$$

where the introduced parameter J_0 is called *pinning range* and is roughly equal to the width of the distribution, whilst m is the Weibull exponent parameter which affects the shape of the distribution. Note that the width of the probability distribution function is scaled by J_0, therefore if the current J_{Cmin} and J_0 are different but if the ratio J_{Cmin}/J_0 remains unchanged, the correspondent distribution is the same.

The macroscopic current-voltage law provided by the distribution model, can be obtained by substituting the definition of critical current distribution of eq.(5.3) into eq.(5.2). In the vicinity of the percolation threshold is verified $(J_C - J_{Cmin}) \to 0$, hence the exponential in eq.(5.3) can be approximated with a simple power law function and the analytical solution of the integral of eq.(5.2) is found to be the one of eq.(5.4):

$$E(J) = \frac{1}{J_0^m} \cdot \frac{\rho_{ff}}{m+1} \cdot (J - J_{Cmin})^{m+1} \qquad \text{with} \qquad J_{Cmin} > 0 \tag{5.4}$$

The current-voltage relation provided by the distribution model is very handy since it introduces parameters such as ρ_{ff}, J_{Cmin} and J_0 which are measurable quantities and, in contrast with current-voltage relation provided by the HTS pinning models, are not directly related to the microscopic characteristics of the material.

By imposing the engineering definition of critical current J_{C0}, according to which $E_C(J_{C0}) = 1\mu\text{V/cm}$, into eq.(5.4) it is possible to express J_0 as a function of ρ_{ff} and J_{Cmin}, as in eq.(5.5). Note the engineering current density is indicated as J_{C0} rather than J_C in order to be distinguished from the variable of the distribution function of eq.(5.3).

$$J_0 = \left(\frac{\rho_{ff} \cdot (J_{C0} - J_{Cmin})^{m+1}}{E_C \cdot (m+1)} \right)^{\frac{1}{m}} \tag{5.5}$$

The current-voltage relation can be therefore modified by a substituting into eq.(5.4) the definition of J_0 given by eq.(5.5), Hence, a simplified macroscopic E-J characteristic relation given by eq.(5.6), independent on both the flux flow resistivity and the pinning range J_0, can be obtained :

$$E(J) = E_C \cdot \left(\frac{J - J_{Cmin}}{J_{C0} - J_{Cmin}} \right)^{m+1} \tag{5.6}$$

Note that the only parameters introduced by the distribution model to characterise a typical E-J characteristic are the critical current J_{C0}, the percolation threshold J_{Cmin} and the exponent m.

Analogously to what done for the HTS models, a relation between the distribution model parameters and the local power law index $n_{J_{C0}}$ can be obtained by deriving the distribution model E-J characteristic law of eq.(5.6) and by calculating it at J_{C0} as in eq.(5.7).

$$n_{J_{C0}} = \frac{\mathrm{d}(\ln E)}{\mathrm{d}(\ln J)} \bigg|_{J=J_{C0}} = \frac{\mathrm{d}E/E}{\mathrm{d}J/J} \bigg|_{J=J_{C0}} = \frac{m+1}{1 - \frac{J_{Cmin}}{J_{C0}}} \tag{5.7}$$

Eq.(5.7) allows to express $n_{J_{C0}}$ as a function the minimum critical current value of the distribution J_{Cmin}, of the measured value of critical current J_{C0} and of the characteristic Weibull exponent m and the relation can be generalised for any current as in eq.(5.8).

Eq.(5.7) can be generalised as in

$$n(J) = \frac{m+1}{1-\frac{J_{Cmin}}{J}} \tag{5.8}$$

which, in the limit case of $J \to J_{Cmin}$ corresponds to the case of $n \to \infty$, whilst when $J \to \infty$, $n(J) \to m+1$.

Note that $n(J)$ continuously changes with current whilst the power law behaviour with constant n-number is met again in eq.(5.6) when $J_{Cmin} = 0$, which corresponds, according to eq.(5.8), to $n = m+1$. Differently from the power law model which predicts zero voltage only when $J = 0$, the distribution depinning model predicts zero voltage for all current below J_{cmin}.

As shown in Chapter (1), BSCCO tape transition characteristic can be well described by the power law model. Thus, from the distribution model point of view, it is expected to be characterised by weak pinning sites with $J_{Cmin} = 0$. On the other hand, the E-J characteristics of YBCO deviate from power law behaviour, hence, according to the depinning model, YBCO is characterised by pinning sites of better quality, all characterised by finite critical current, $J_{Cmin} > 0$.

5.2.2 E-J characteristic parameters obtained by a given distribution

According to the distribution model theory, a given critical current distribution is characterised by three parameters: J_{Cmin}, J_0 and m. Knowing these parameters, the engineering critical current J_{C0} can be expressed, according to eq.(5.5), as a function of J_{Cmin} and m:

$$J_{C0} = J_{Cmin} \cdot \left(\frac{J_0^m \cdot (m+1)}{\rho_{ff}} \right)^{\frac{1}{m+1}} \tag{5.9}$$

and the E-J characteristic can be obtained by substituting the engineering critical current J_{C0} of eq.(5.9) into eq.(5.6), so that the current-voltage relation assumes the form of eq.(5.4) and the power law exponent $n_{J_{C0}}$ can be calculated according to eq.(5.7).

5.2.3 Distribution parameters obtained by a given E-J characteristic

According to the distribution model theory, a given E-J characteristic is characterised by the parameters: $n_{J_{C0}}$, and J_{C0} and m. Knowing these parameters, the minimum

current threshold J_{Cmin} can be expressed, according to eq.(5.5), as a function of J_{C0}, $n_{J_{C0}}$ m:

$$J_{Cmin} = J_{C0} \cdot \left(\frac{n_{J_{C0}}}{n_{J_{C0}} - m - 1} \right) \tag{5.10}$$

The E-J characteristic law predicted by the model can be obtained by substituting J_{Cmin}, expressed as in eq.(5.10), into eq.(5.6), so that the current-voltage relation assumes the form of eq.(5.11).

$$E(J) = E_C \cdot \left[\frac{n_{J_{C0}}}{m+1} \cdot \left(\frac{J}{J_{C0}} - 1 \right) + 1 \right]^{m+1} \tag{5.11}$$

whilst the underline distribution can be obtained according to eq.(5.3), once calculated the pinning range J_0 according to eq.(5.5)

5.3 Distribution model parameters

The law proposed by the distribution model, given by eq.(5.6), provides information on three E-J characteristics parameters such as I_{C0}, I_{Cmin} and m, whilst no direct information about the pinning range I_0, and hence on the current distribution, is directly provided. In order to understand how a change in the observable parameters affect the current distribution associated to the transition characteristic, different possible scenarios have been investigated. In the different scenarios the observable parameters I_{C0}, $n_{I_{C0}}$ and m have been varied and the the relative parameters I_{Cmin} and I_0 have been consequently derived. Note that the absolute current values have been used instead of the critical current density ones, since this is the parameter actually measured during experiments and thus of practical use for performance comparison.

As an example, a reference E-J characteristic curve with $I_{C0} = 100$ A and $n_{I_{C0}} = 30$ and $m = 6$, which are typical parameter or YBCO tapes, has been produced and compared one to one with others distribution model curves, which parameters correspond to the following three cases:

- Scenario I: E-J characteristic prediction with smaller critical current I_{C0}, smaller n-number $n_{I_{C0}}$ and smaller exponent m than the reference case;

- Scenario II: E-J characteristic prediction with the same n-number $n_{I_{C0}}$ and exponent m of the reference case, but greater critical current I_{C0} than the reference case;

- Scenario III: E-J characteristic prediction with greater critical current I_{C0}, greater n-number $n_{I_{C0}}$ and greater exponent m than the reference case.

The parameters used in the reference case and in the different scenarios are listed in table (5.1). For each case the parameter in bolt are the one maintained equal to the reference case whilst in red are evidenced the parameters that have been changed and from which all the others have been calculated.

	I_{C0}[A]	$n_{I_{C0}}$	m	I_{Cmin}[A]	I_0[A]
Reference	100	30	6	76.6	273.3
Scenario I	20	18	3.5	15	248.1
Scenario II	200	**30**	**6**	153.3	613.5
Scenario III	300	40	8	240	414.3

Table 5.1: Percolation parameters of a case reference and of three possible scenarios called Scenario I, Scenario II and Scenario III.

5.3.1 Scenario I: reduced I_{C0} and wider distribution

The E-J characteristics obtained according to the distribution model parameters listed in table (5.1) for the reference case and for Scenario I, are plotted in fig.(5.2) where are labelled as curve (0) and curve (1) respectively. The parameters I_{Cmin} and I_0 have been calculated by using eq.(5.7) and eq.(5.5), and whilst a reduction of 80% is observed on I_{Cmin} with respect of the reference case, the pinning range I_0 remains almost unchanged (10% reduction of I_0).

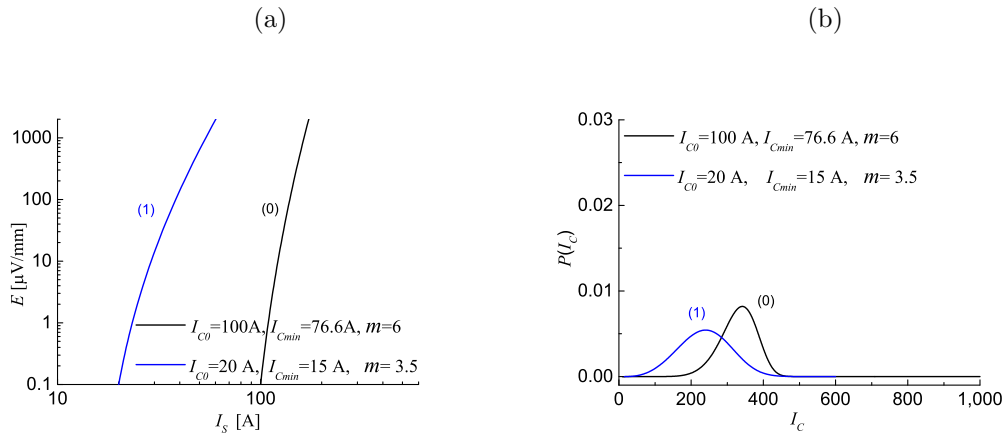

Figure 5.2: (a) E-J characteristics and (b) critical current distributions of a reference case with $I_{C0} = 100$ A, $n_{I_{C0}} = 30$ and $m = 6$ compared to Scenario I characterised by smaller critical current I_{C0}, smaller n-number $n_{I_{C0}}$ and smaller exponent m than a reference case.

Because of the smaller parameter I_{C0} imposed, the transition curve obtained for Scenario I, curve (1) of fig.(5.2a) lies on the left side of the reference characteristic, curve (0). The smaller $n_{I_{C0}}$ affects the slope of the curve at low voltage level, whilst the increased bending observed at high voltage is due to the small parameter m imposed. The critical current distributions associated with the two transition characteristics of fig.(5.2a) are presented in fig.(5.2b). The effect of the smaller parameter m reflects on a broader distribution, when plotted in a non scaled graph. The change in the shape of the bell can be attributed only to the parameter m, since in this scenario I_0 reduces less than 10% when compared to the change in m which is more than 40%, as it can be observed in table (5.1).

5.3.2 Scenario II: increased I_{C0} and same distribution

The E-J characteristics obtained according to the distribution model parameters listed in table (5.1) for the reference case and for Scenario II, are plotted in fig.(5.3a) and are respectively labelled as curve (0) and curve (2). The parameters I_{Cmin} and I_0 have been calculated according to eq.(5.7) and eq.(5.5) and, since both m and $n_{I_{C0}}$ are maintained constant, according to eq.(5.7) the ratio I_{Cmin}/I_{C0} is the same for the two cases.

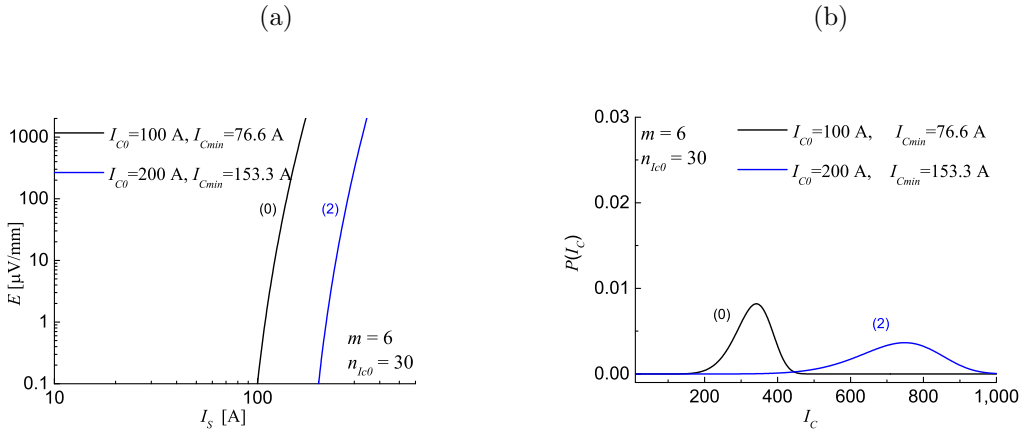

Figure 5.3: (a) E-J characteristics and (b) critical current distributions of a reference case with $I_{C0} = 100$ A, $n_{I_{C0}} = 30$ and $m = 6$ compared to Scenario II characterised by the same n-number $n_{I_{C0}}$ and exponent m of the reference case, but greater critical current I_{C0}.

Since both the exponent m and the n-number $n_{I_{C0}}$ are the same for the two characteristics of fig,(5.3a), the transition characteristic of Scenario II, curve (2), has the same shape of the one of the reference case, curve (0) but it is translated at higher critical current I_{C0}. The critical current distribution associated with the two transition characteristics of fig.(5.3a) are presented in fig.(5.3b). The effect of the increased pinning range I_0 which is about three times bigger than the one of the reference case, reflects on a broader distribution, when plotted in a non scaled graph.

5.3.3 Scenario III: increased I_{C0} and narrower distribution

The E-J characteristics obtained according to the distribution model parameters listed in table (5.1) for the reference case and for Scenario III, are plotted in fig.(5.4a). The transition characteristic of Scenario III, curve (3), is characterised by greater critical current I_{C0}, greater n-number $n_{I_{C0}}$ and greater exponent m than the reference case. The parameters I_{Cmin} and I_0 have been calculated according to eq.(5.7) and eq.(5.5) and they are both observed to increased although a larger increase is observed on I_{Cmin} which is three times bigger than the reference case differently from I_0 which is instead only 1.5 times bigger.

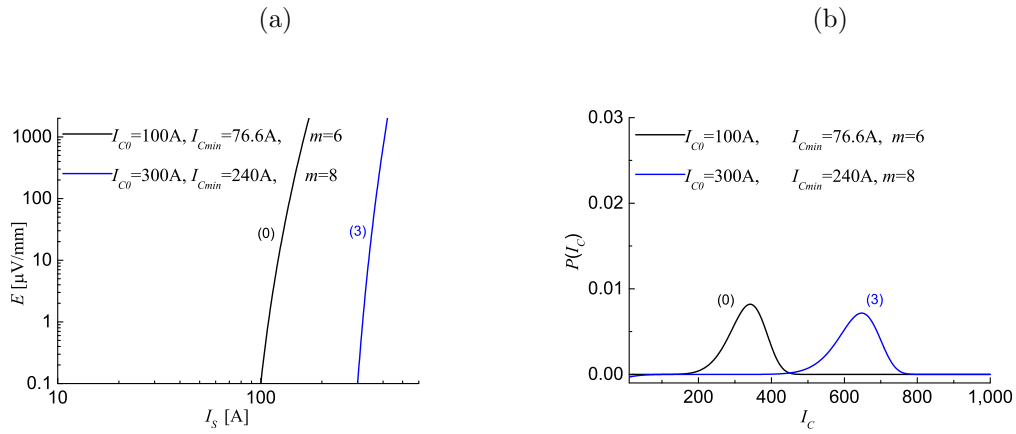

Figure 5.4: (a) E-J characteristics and (b) critical current distributions of a reference case with $I_{C0} = 100$ A, $n_{I_{C0}} = 30$ and $m = 6$ compared to Scenario III characterised by greater critical current I_{C0}, greater n-number $n_{I_{C0}}$ and greater exponent m than a reference case.

Because of the greater parameter I_{C0}, the transition characteristic (3) of fig.(5.4a) lies on the right of the current-voltage curve of the reference case (0). The critical current distribution associated with the two transition characteristics of fig.(5.4a) are presented in fig.(5.4b). It can be observed as, in a non scaled graph, the effect of broadening the bell due to the increased pinning range I_0 is mitigated by the increased exponent m.

However, since the depinning probability function of eq.(5.3) is scaled in term of I_0, the distributions obtained for Scenario I, scenario II and Scenario III can be compared one another and with the reference case when scaled in a graph as the one of fig.(5.5).

It is evident from fig.(5.5) how the effect of the reduced parameter m, which in Scenario I considerably changes whilst I_0 remains almost constant, actually corresponds to a broader distribution than the one of the reference case. The effect of an increment in I_0 as in Scenario III, although moderated by an increased m, produces a narrower distribution. The E-J characteristics with the same parameter m and the same ratio I_{Cmin}/I_0, as in Scenario II, are characterised by the same distributions, and in fact the distribution of Scenario II and of the reference case, plotted in a scaled graph, are observed to overlap.

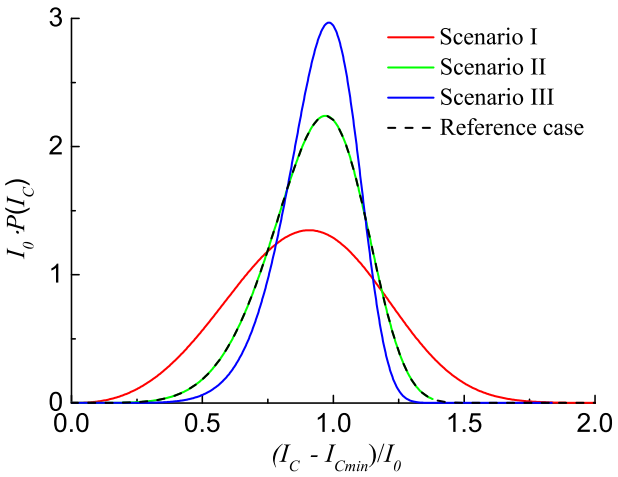

Figure 5.5: Scaled current distribution of Scenario I, Scenario II, Scenario III and reference case.

Note that, since a big m has as effect to narrower the distribution, in the limit of $m \to \infty$, the critical state is approached, the distribution looses meaning and the bell-curve is a step function typical of the critical state.

5.4 Applicability and methodology of pinning distribution analysis

5.4.1 Non-power law E-J characteristics of 2G YBCO can be described by the distribution model

In order to verify the applicability of the model to the experimental data, the procedure described in section (5.2.3) has been applied to the experimental data.

For given experimental transition characteristic, the current I_{C0} is calculated with the engineering criteria whilst the parameter $n_{I_{C0}}$ is obtained according to the power law analysis. Prediction curves are therefore obtained by varying the parameter m in eq.(5.11), until a good fitting of the data is achieved, and by calculating I_{Cmin} for each attempt according to eq.(5.10).

As an example, the E-J characteristic collected at 77 K have been fitted with the

distribution model law. Data and predictions curves obtained for $m = 4$, $m = 6$ and $m = 8$ are plotted in fig.(5.6) as a function of the current carried by the superconductor.

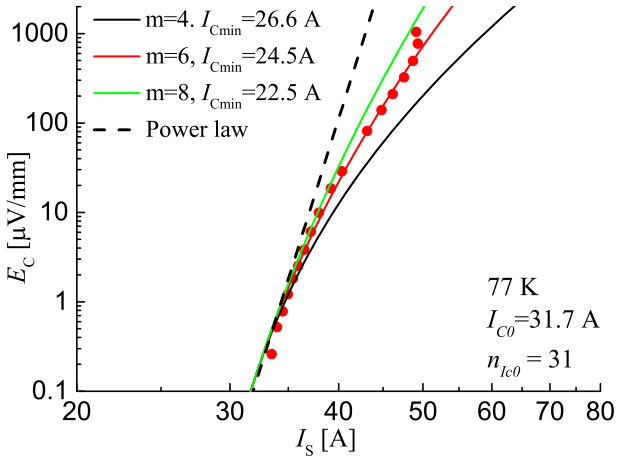

Figure 5.6: *E-J* characteristic of bridged 1mm 2G YBCO at 77 K plotted as a function of the current carried by the superconductor, compared with distribution model prediction obtained with $I_{C0} = 31.7$ A, $n_{I_{C0}} = 31$ and $m = 4$, $m = 6$ and $m = 8$. Comparison with power law predictions (dashed line).

As it can be observed in fig.(5.6), the distribution model curve obtained by imposing $m = 6$ successfully follows the *E-J* characteristic data, indicating that the deviation from power law (dashed lines) can be accounted from the distribution model. Note as $m = 4$ and $m = 8$ predict curves which deviate from the experimental data. The minimum current threshold I_{Cmin} is observed to reduce as the exponent m increases.

Although the model satisfactory predicts the experimental data, no information of the pinning range I_0, and thus on the distribution characteristic, are available. The analysis done so far is purely parametric, and the parameters set obtained (m and I_{Cmin}) do not correlate to the macroscopic depinning process, predicted to be dominated by full flux flow, to the distribution model. In order to obtain the pinning range I_0, the flux flow resistivity needs to be associated to the model and the information obtained on the pinning range will allow to define weather or which model should be applied. In order to achieve these information, and to verify if the underlying

distribution model parameters offer a reasonable physical description of the depinning phenomena, a preliminary investigation of the flux flow resistivity is required.

5.4.2 Deduction of the pinning distribution

According to eq.(5.12), in order to calculate the pinning range I_0:

- The level of dissipation given by ρ_{ff} has to be established;
- An estimation of the self field contribution B_{sf} has to be done.

Flux flow resistivity.

The distribution model assumes that flux lines which jump from a pinning centre to another, experience fully flux flow during the fly. According to the flux flow model the flux low resistivity can be expressed by using the Bardeen's relation [73], which predicts that at given temperature ρ_{ff} is proportional to the resistivity of the tape in the normal state ρ_n and inversely proportional to the upper critical field B_{C2}, as in eq.(5.12).

$$\rho_{ff}(T) = \rho_n(T) \cdot \frac{B}{B_{c2}} \tag{5.12}$$

The proportionality between the flux flow resistivity ρ_{ff} and the resistivity of the normal state ρ_n has been has been proved to hold for YBCO epitaxial films in the range of temperature 76.5 K - 85 K [74] and, in this work, its validity has been assumed to hold at lower temperatures.

The ρ_{ff} dependence on temperature can be obtained by re-expressing the upper critical field B_{C2} as in eq.(5.13). Note that the effect of self field has been taken into account by expressing the total field B as result of both action of the applied field B_{app} and of the self field B_{sf}.

$$\rho_{ff}(T) = \rho_n(T) \cdot \frac{B_{sf} + B_{app}}{B_{C2}\,(0) \cdot \left[1 - \left(\frac{T}{T_C}\right)^2\right]} \tag{5.13}$$

with $B_{C2}(0) = 100$ T and $T_C = 92$ K [2].

Concerning $\rho_n(T)$, experimental data of the normal resistivity dependence on temperature are available in literature. The resistivity of YBCO single crystal in the normal

state ρ_n and its dependence on temperature have been measured by Anderson [75] on YBCO single crystal, and the data obtained are shown in fig.(5.7).

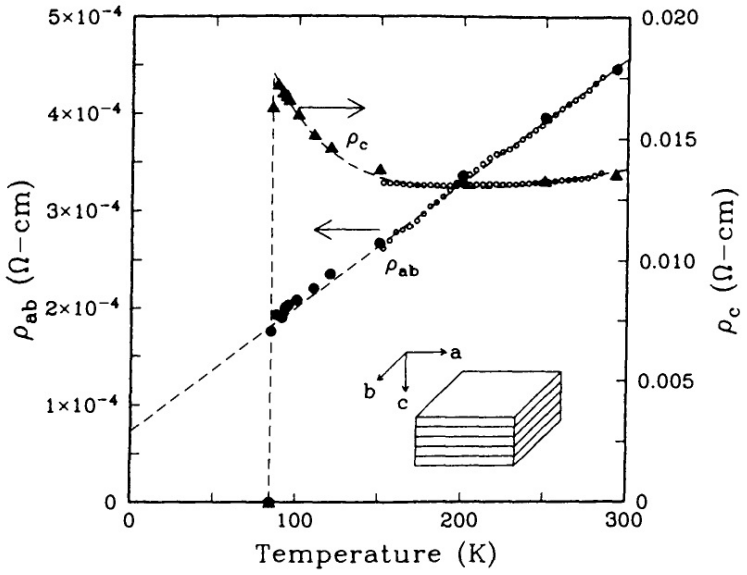

Figure 5.7: Resistivity of YBCO single crystal in the normal state dependence on temperature [75].

The normal resistivity has been measured in the range of temperature 77 K - 300 K where is shown linear dependence on temperature. Resistivity values below 77 K have been extrapolated.

Self-field estimation.

A proportional dependence of self-field on current as the one of eq.(5.14), has been considered:

$$\bar{B}_{sf} = \alpha \cdot I \tag{5.14}$$

where α is the proportionality coefficient between field and current.

The difficulty on determining α is due to the fact that this parameter has to account for the not uniform distribution of field in the conductor, which in particular for film conductors, is strongly non linear and diverges at the edges. Since the difficulty on

determining the coefficient α theoretically, the latter has been determined graphically, by using the available data collected in perpendicular applied field. By looking at the in field data, the contribution of the self field together with the contribution of the applied field allows to observe a smooth change of I_0 with field, as the flux flow resistivity ρ_{ff} changes from being dominated from the applied field to be dominated by the self field.

A set of coefficients α has been assumed in order to calculate, in sequence:

- The self field contribution $\bar{B}_{sf}$, according to eq.(5.14);
- The flux flow resistivity ρ_{ff}, according to eq.(5.13);
- The pinning range I_0, according to eq.(5.5).

The parameters I_{Cmin} and m needed to calculate the pinning range I_0 are obtained by fitting the E-J characteristics collected on Sample AS, in perpendicular applied field scenario, as shown in fig.(5.8a), and the parameters obtained by the distribution model fitting are shown in fig.(5.8b) as a function of temperature.

The pinning range I_0 obtained by varying the coefficient α, is then shown in fig.(5.8c) as a function of the total field B_{TOT}, where B_{TOT} is the sum of the contribution of the self field produced by the tape B_{sf} and of the field externally applied by the electromagnet. Note that the pinning range obtained according to the flux flow resistivity, calculated with Bardeen's law, is physically reasonable, being only few times bigger than the critical current I_{C0}. The latter confirms that the flux flow model correlates the macroscopic depinning process to the distribution model. Strong support to the model is given by the fact that ρ_{ff} has been calculated on an experimental base, by using the using the resistivity of the material in the normal state ρ_n.

It can be observed as the coefficient α which produce a smooth pinning range dependence on field is $\alpha = 45 \cdot 10^{-5}$ T/A which corresponds to $B_{sf}(77K) = 45$ mT.

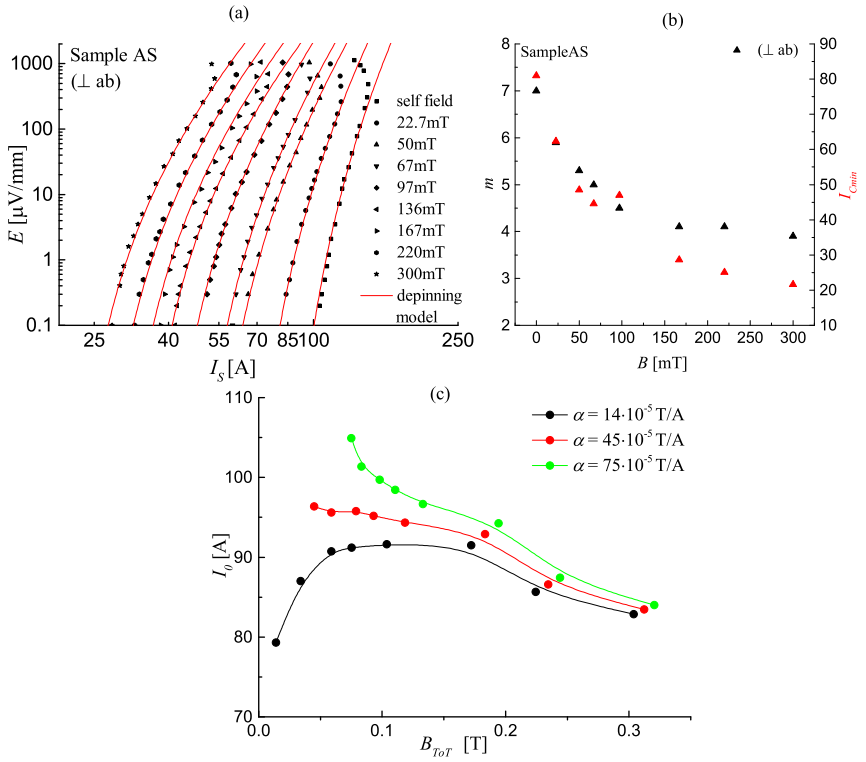

Figure 5.8: (a) Scaled E-J characteristics of Sample AS collected at 77 K with applied field perpendicular to the ab plane (self field - 300 mT). Comparison with distribution model predictions. (b) Parameters m and I_{Cmin} dependence on field obtained with distribution model analysis. (c) Pinning range I_0 dependence on total field B_{TOT}, for different coefficient α imposed, $\alpha = 14 \cdot 10^{-5}$ T/A, $\alpha = 45 \cdot 10^{-5}$ T/A and $\alpha = 75 \cdot 10^{-5}$ T/A.

Numerical estimation of the self-field. As further support to the results obtained by using the flux flow model and the distribution model parameters, the self field has been numerically calculated. The magnetic flux $\Phi(x)$ produced by the tape, according to the analysis carried out by Yang.Y. [76] on the tape geometry influence on the AC losses, can be calculated by using eq.(5.15).

$$\Phi(x) = \frac{\mu_0 \cdot I_{C0}}{\pi \cdot a} \cdot \left\{ \begin{array}{c} x \cdot \ln\left(\frac{\sqrt{a^2-x^2}}{\sqrt{a^2-a_0^2}-\sqrt{x^2-a_0^2}}\right) + \\ +a \cdot \ln\left(\frac{x\cdot\sqrt{a^2-a_0^2}-a\cdot\sqrt{x^2-a_0^2}}{a_0\cdot\sqrt{a^2-x^2}}\right) + \\ +\sqrt{a^2-a_0^2} \cdot \ln\left(\frac{x+\sqrt{x^2-a_0^2}}{a_0}\right) \end{array} \right\} \tag{5.15}$$

The equation is valid for Type II superconductors with rectangular cross-section where a_0 and a are respectively the limit of the field free region and the current reversal contour, as schematically represented in fig.(5.9). The coordinates origin are assumed to be in the centre of the tape cross section.

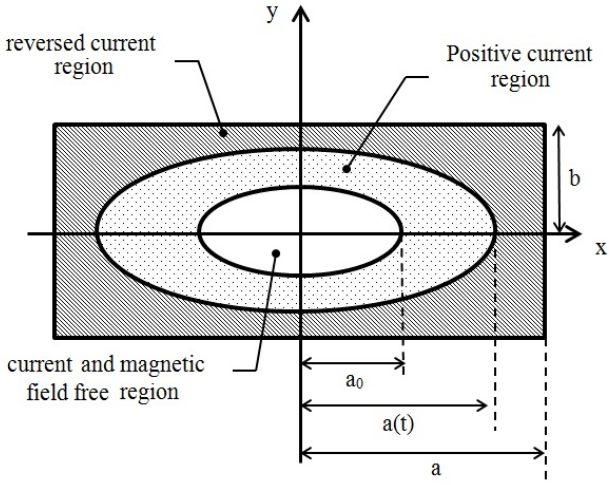

Figure 5.9: Current penetration profile for a rectangular cross-section of the superconductor of half height b and half width a, with a_0 the limit of the field free region and $a(t)$ the current reversal contour [77].

Eq.(5.15) has been adapted for a rectangular cross section where the internal free current and the field region are not present. Also, the reversed current region can be assumed negligible, so that the magnetic flux $\Phi(x)$ can be calculated numerically in the limit of $a_0 \to 0$ and $a(t) \to a$. The result of the limit is expressed in eq.(5.16).

$$\Phi(x) = \frac{\mu_0 \cdot I_{C0}}{\pi} \cdot \ln(2) \tag{5.16}$$

The averaged magnetic field can be calculated by simply dividing eq.(5.16) by half width a, thus it has been obtained $\overline{B} \sim 14$ mT, with $a = 2 \cdot 10^{-3}$ m and $I_{C0} = 100$ A.

The magnetic field numerically calculated is ~ 3 times smaller than the one obtained according to the flux flow model analysis. However, such a difference is considered reasonable, since, as mentioned, the field distribution along the x axis in tape of rectangular shape is not linear. The magnetic field is in fact observed to diverge $B \to \infty$ at the edges [78]. Thus, the contribution to flux flow mostly comes from the edges and the field average along the all width of the tape underestimates the actual self-field.

Summarising, it has been proved that the distribution depinning model, which is based on a statistical approach, does not just allow to predict the experimental data transition characteristics, but also allows to trace a critical current distribution with a physical foundation. The strength of the model is given by the fact that the pinning range I_0 is not calculated arbitrarily but based on the actual measured experimental data of ρ_n.

5.5 Experimental results analysed with the distribution model

5.5.1 E-J characteristics in self field, at different temperatures.

The E-J characteristics predicted by the distribution model, by following the methodology described in section (5.2.3), have been compared with the experimental E-J characteristics measured in a range of temperatures and fields presented in Chapter (3). Results are presented in fig.s(5.10a-d) for Sample I, Sample II, Sample III and Sample IV respectively as a function of the current carried by the superconductor. Depinning model predictions are plotted in dashed lines.

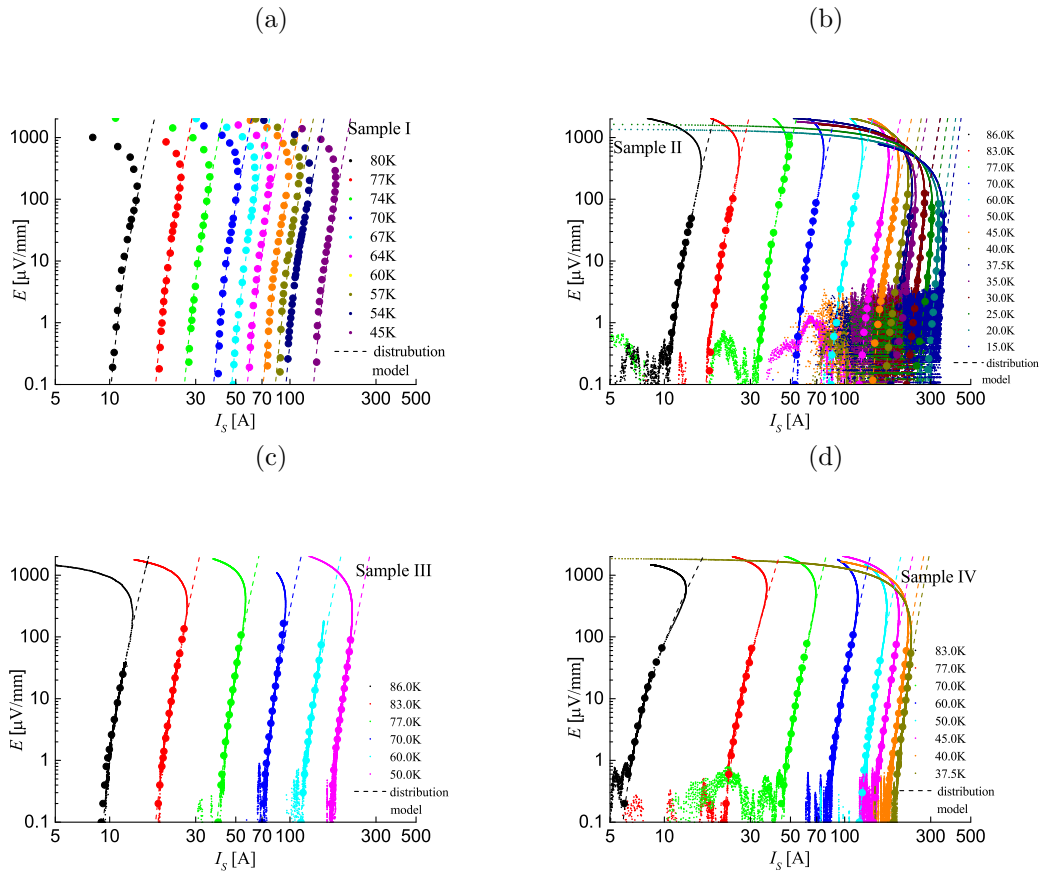

Figure 5.10: Comparison between E-J characteristics predicted by depinning model and experimental data measured on (a) Sample I (80 K - 45 K), (b) Sample II (80 K - 15 K), (c) Sample III (86 K - 50 K) and (d) Sample IV (37.5 K - 83 K), plotted as a function of the current carried by the superconductor.

The all set of E-J characteristics measured on different samples, can be satisfactory fitted by the distribution model law as clearly visible in fig.s(5.10a-d). At high temperatures, the distribution model consistently matches the E-J characteristics for more than three voltage decades.

The parameter m dependence on temperature obtained with the distribution model analysis is shown in fig.s(5.11a-d) for Sample I, Sample II, Sample III and Sample IV, respectively and it is compared with the parameter $n_{I_{C0}}$ dependence on temperature.

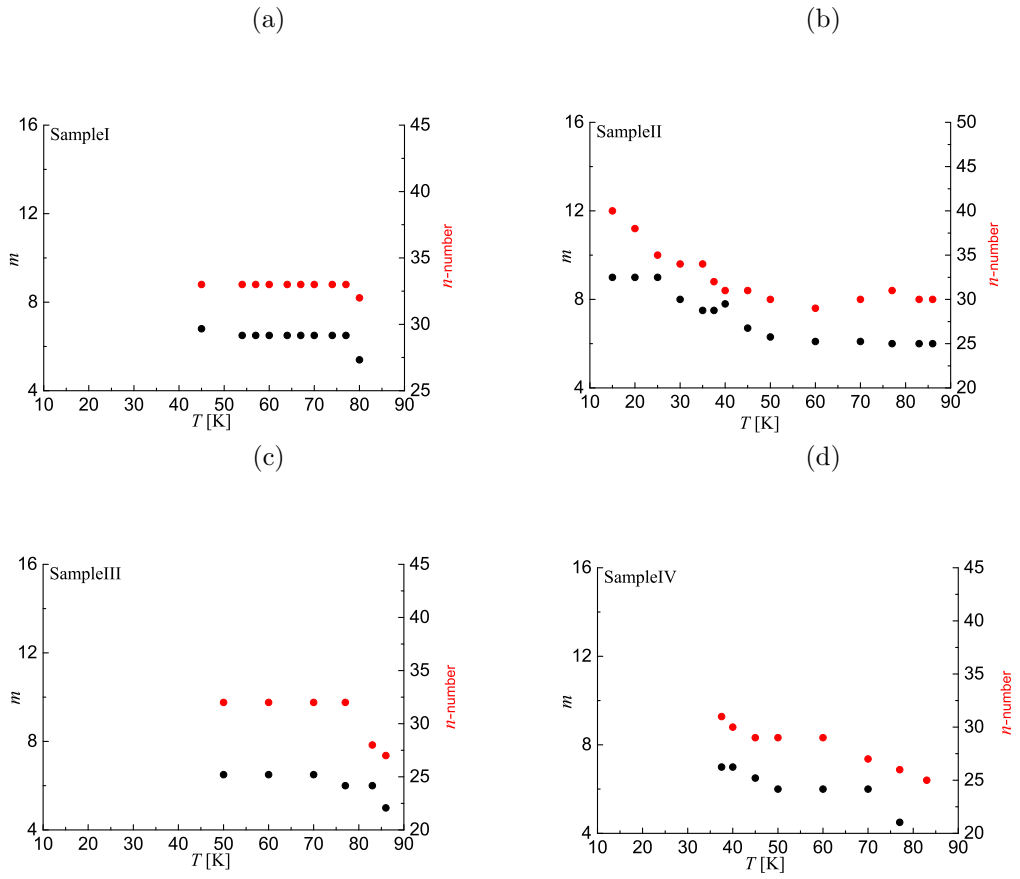

Figure 5.11: Weibull exponent m and power law exponent n dependence on temperature for (a) Sample I, (b) Sample II, (c) Sample III and (d) Sample IV.

It can be observed as the parameter m follows a qualitatively similar dependence on temperature of the one of the $n_{I_{C0}}$ and in particular:

- The parameter m of Sample I remains almost constant to the value $m = 6.5 \pm 0.1$ in the all measured set of temperatures whilst n-number is $n = 33 \pm 0.5$;

- The parameter m of Sample II remains constant to the value $m = 6.1 \pm 0.1$ in the range of temperature 50 K - 86 K where the correspondent n-number is $n = 30 \pm 1$, and then gradually increases as the temperature is further decreased;

- The parameter m of Sample III remains almost constant to the value $m = 6.1 \pm 0.1$ in the all measured set of temperatures and the n-number is $n = 30 \pm 1$;

- The parameter m of Sample IV remains almost constant to the value $m = 6.0 \pm 0.2$ in the range of temperature 50 K - 77 K where the correspondent n-number is $n = 30 \pm 1$, and then gradually increases as the temperature is further decreased. A particularly small value of m =2.9 has been observed at 83 K.

For a better comparison of the E-J characteristics at different temperatures and of the respective fitting curves, data of Sample I are presented in a scaled graph in fig.(5.12a), plotted as a function of the normalised current carried by the superconductor. As observed in Chapter (3), the E-J characteristics of Sample I are characterised by the same n_{I_C} and therefore, once opportunely scaled, collapse on the same curve. As a consequence, the scaled transition curves of fig.(5.12a) can be fitted by a single prediction curve characterised by the same parameter m. The distribution model transition curve which allows a good prediction of the E-J characteristics of Sample I is obtained for $m = 6$ and it is plotted with the plane line in fig.(5.12a).

(a) (b)

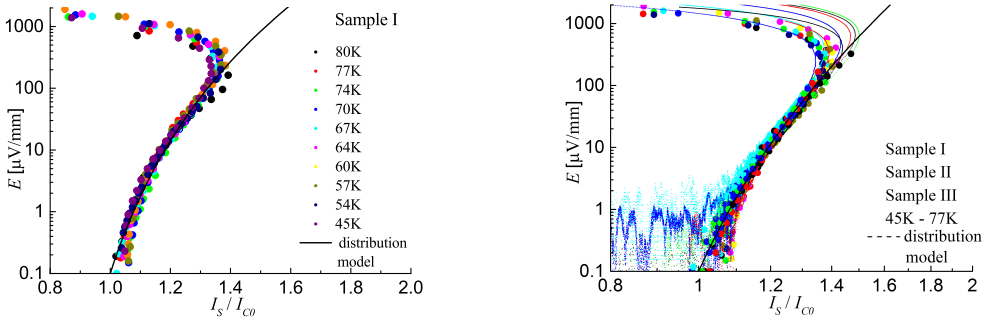

Figure 5.12: (a) Scaled E-J characteristics of Sample I and comparison with distribution model curve, with $m = 6$ (solid line). (b) Scaled E-J characteristics of Sample I, Sample II and Sample III and comparison with distribution model curve, with $m = 6$ (solid line).

Similarly to what observed in the HTS pinning model analysis, the distribution model prediction curve allows good prediction of the E-J characteristics of both Sample I, Sample II and Sample III in the range of temperatures 45 K - 77 K, region of temperatures where they are characterised by similar value of the parameter n_{J_C} and hence collapse on the same scaled curve. Scaled curves and the predicted curve (plain line) are shown in fig.(5.12b).

On the other hand, the E-J characteristics of Sample II show a drastic change in n-number at about $T = 45$ K , value after which both the n-number and the parameter m start decreasing, as shown in fig.(5.11b). A scaled graph of the E-J characteristics below this temperature and of the respective distribution model prediction is shown in fig.(5.13a). The dashed black line, corresponds to the distribution model prediction curve which well represent the E-J characteristics above 45 K, whilst the plain lines corresponds to the model prediction at temperatures lower than $T = 45$ K. The drastic change in shape observed below $T = 45$ K can be accounted by the model with an increasing m parameter.

(a) (b)

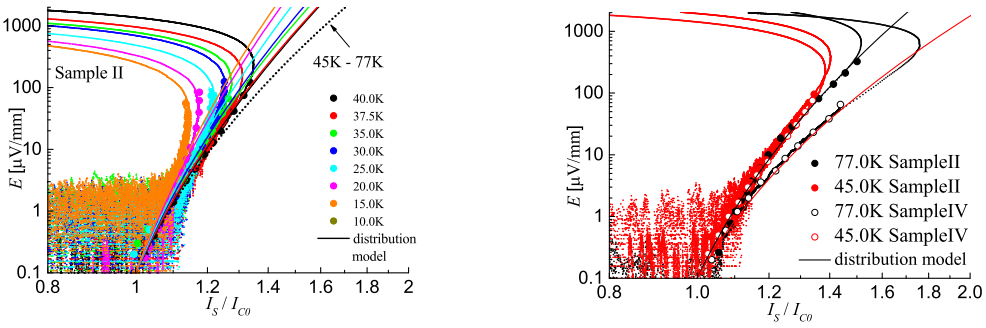

Figure 5.13: (a) Scaled E-J characteristics of Sample II in the range of temperature 15 K - 45 K and comparison with distribution model curves and (b) scaled E-J characteristics of Sample II and Sample IV at 45 K and 77 K and comparison with distribution model curves.

Differently from the other samples, Sample IV is characterised by smaller n-number above 70 K, as it can be observed in fig.(5.11d), and the latter has been attributed to the lower critical temperature observed in the transition measurements presented in Chapter (3). In order to evidence the difference observed between Sample IV and the other samples, the E-J characteristics of Sample IV and of Sample II at 45 K and at 77 K are presented in a scaled graph in fig.(5.13b) and compared with the distribution model predictions. The different behaviour of the E-J characteristic of Sample IV at 77 K from all the other samples is clearly observable in fig.(5.13b) and it can be accounted by a smaller $m = 4.7$. Further decrease in m is observed with increasing temperature.

5.5.2 Distribution parameters as a function of temperature

The dependence on temperature of the minimum current threshold I_{Cmin} and of the pinning range I_0 is shown in fig.s(5.14a-d) for Sample I, Sample II, Sample III, and Sample IV respectively, and is compared with the engineering critical current I_{C0}.

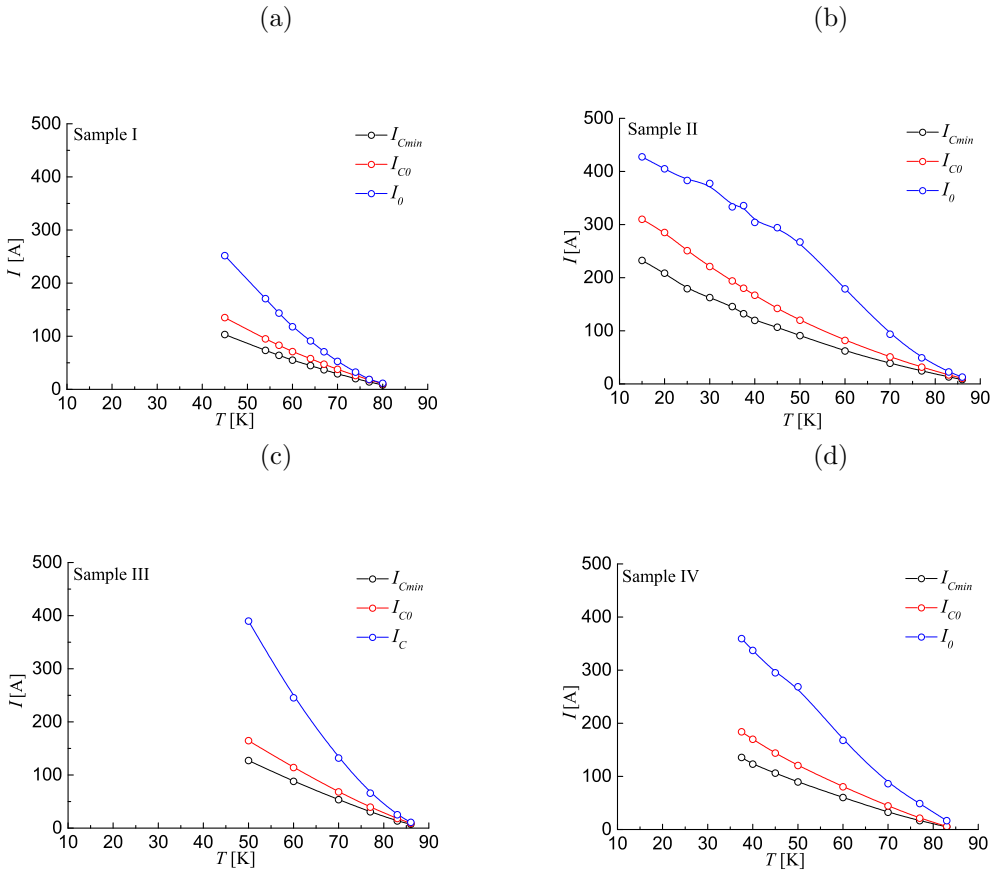

Figure 5.14: Minimum current threshold I_{Cmin}, engineering critical current I_{C0} and pinning range I_0 dependence on temperature for (a) Sample I, (b) Sample II, (c) Sample III and (d) Sample IV.

Similar distribution model parameters dependence on temperature has been observed for the samples measured and, in order to allow better comparison between different samples, I_{Cmin} and I_0 temperature dependence obtained for Sample I, Sample II, Sample III and Sample IV are plotted together in fig.(5.15a) and in fig.(5.15b) respectively. Note that Sample III, which is the sample thought to have a better stoichiometric oxygen content compared to the others, is the one that shows greater I_{Cmin}

and I_0.

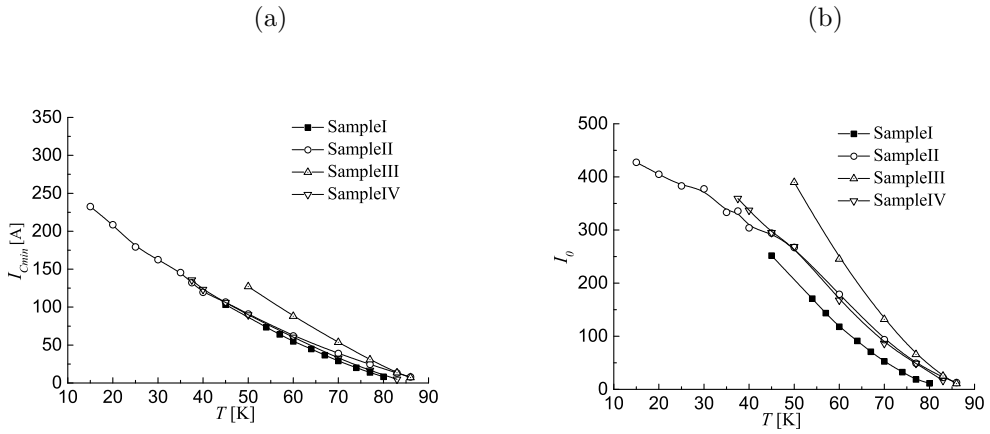

Figure 5.15: (a) Minimum current threshold I_{Cmin} and (b) pinning range I_0 dependence on temperature of Sample I, Sample II, Sample III and Sample IV.

5.5.3 Underlying distribution of 2G YBCO tape as a function of temperature

The probability distribution of critical current correspondent to the measured *E-J* characteristics of Sample II, which is the one measured in a wider range of temperatures, have been obtained according to eq.(5.3) The probability current distributions of Sample II are shows in fig.(5.16a) as a function of the current I_C and the probability current distributions of all samples are shown in fig.(5.16b) as a function of the scaled current $(I_C - I_{Cmin})/I_0$.

It can be seen in fig.(5.16) as, at high temperatures (45 K - 77 K), despite the parameter m remains unchanged, the distribution of critical current becomes wider as the temperature is lowered. According to the scenario described section (5.3.2), the latter is due to the increased pinning range I_0 with lowering the temperature.

At low temperatures (15 K - 40 K), the effect of m of narrowing the distribution curves is contrasted by the effect of the increased pinning range I_0 which acts opposite to it as discussed in section (5.3.3).

By scaling the distribution with respect of $(I_C - I_{Cmin})/I_0$, as done in fig.(5.16), a better comparison between different temperatures can be done and the effect of the

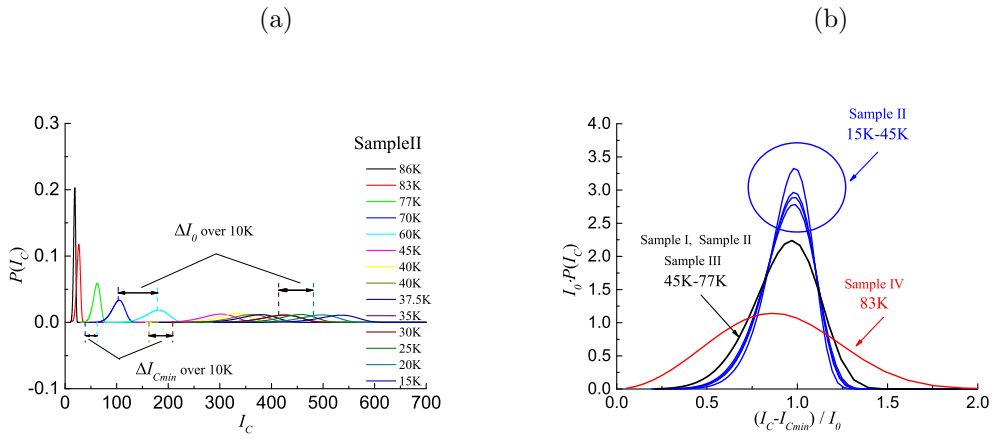

Figure 5.16: (a) Probability distribution function of Sample II plotted as a function of the current I_C and (b) probability distribution function of Sample I, Sample II and Sample III in the range of temperatures 45 K - 77 K, of Sample II in the range of temperatures 15 K - 40 K and of Sample IV 83 K plotted as a function of the scaled factor $(I_C - I_{Cmin})/I_0$.

different exponent m on the distribution can be better visualised. It can be observed that:

- The *E-J* characteristics of Sample I, Sample II and Sample III present $m = 6.3 \pm 0.3$ in the range of temperature $45\,\mathrm{K} - 77\,\mathrm{K}$, and are therefore characterised by the same distribution curve, as for scenario II presented in section (5.3.2). The distribution characteristic for this range of temperatures is plotted with the black line in fig.(5.16);

- The *E-J* characteristics of Sample II in the range of temperatures 15 K - 40 K are characterised by an increasing parameter m which, similar to Scenario III discussed in section(5.3.3) acts on narrowing the distribution as the temperature is lowered. The distribution characteristics for this range of temperatures are plotted in blue lines in fig.(5.16);

- The *E-J* characteristics of Sample IV are characterised by a small exponent m and therefore by a broader critical current distribution, as the one shown by the red dashed line in fig.(5.16) for the 83 K case where $m = 3$. The distribution characteristics for this range of temperatures are plotted in red lines in fig.(5.16).

Note that in fig.(5.16a) it is shown the variation of I_{Cmin} and of I_0 in 10 degrees at high (60 K - 70 K) and low (15 K - 25 K) temperatures to evidence the stronger variation of ΔI_{Cmin} with temperature when compared to ΔI_0.

5.5.4 *E*-*J* characteristic in applied field

The model has been applied also to the set of measurements collected in field. As shown in section (5.4), the distribution model allow to well predict *E*-*J* characteristics collected on Sample AS in a range of perpendicular applied fields. Measurements in field obtained by magnetization measurements have been included in the DC measurements graph as in fig.(5.17).

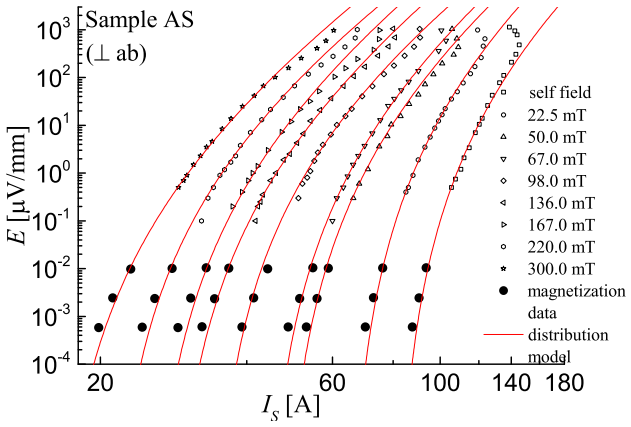

Figure 5.17: *E*-*J* characteristics measured in perpendicular field at 77 K and low voltage ($1{\cdot}10^{-4}$ - $1{\cdot}10^{-2}$ μV/mm) magnetization data, fitted by distribution model predictions (red lines).

Magnetization measurements allowed to obtain more points to complete the *E*-*J* characteristics at low voltage ($1{\cdot}10^{-4}$ - $1{\cdot}10^{-2}$ μV/mm), which further evidence the reduction of the n number with field, as in fig.(5.17). The distribution model consistently allows fitting of experimental data even at low range of voltage.

Note that the small power law exponent n obtained from measurements at low sweep rate and thus, at low voltage level presented in fig.(3.28) in Chapter (3), are in line

with the percolation model which predicts an exponent n continuously varying along the transition characteristic, according to eq.(5.8) .

The model predictions have been compared also to data collected on a tape with reduced cross section Sample V, as shown in fig.(5.18a) and on Sample AS in parallel field scenario as shown in fig.(5.18b). Data and model predictions are plotted as a function of the scaled current carried by the superconductors.

(a) (b)

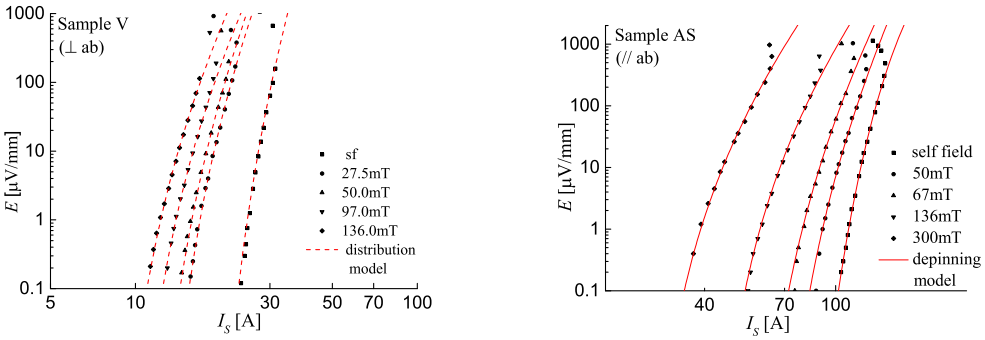

Figure 5.18: Scaled E-J characteristics collected at 77 K on (a) Sample V in a range of perpendicular to the ab plane applied field and on (b) Sample AS in a range of parallel to the ab plane applied fields (self field - 300 mT). Comparison with distribution model predictions.

The same current dependence on field can be observed in perpendicular field scenario for both Sample AS and Sample V: at 136 mT, for example, it can be observed, that the critical current is reduced of a factor of ∼2.4 for Sample AS and of ∼2.1 for Sample V, when compared with the critical current in self field. On the other hand, a smaller reduction can be observed in the parallel configuration, at 300 mT in fact the current has reduced of a factor smaller than 3, whilst in the perpendicular one is ∼ 4 times smaller than the current measured in self field.

Data in field have been compared with the distribution model predictions and the parameter m which allows good fitting of the data is presented as a function of the field applied in fig.(5.19) for Sample AS in both parallel and perpendicular field scenario,

and for Sample V. Comparison with the $n_{I_{C0}}$ dependence on field, which axis is on the right, is also included in the graphs.

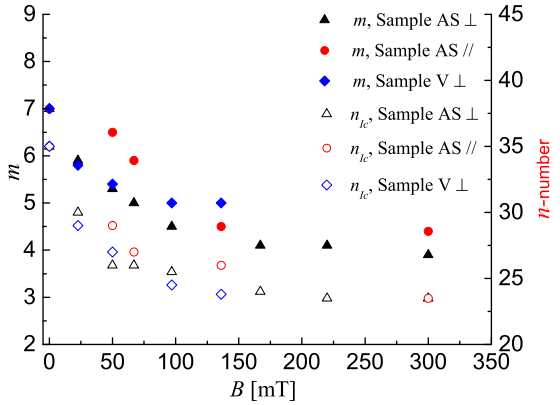

Figure 5.19: Weibull exponent m and apparent n-number dependence on fields for Sample AS measured in both perpendicular and parallel field scenario and for Sample V.

The parameter m is observed to have the same qualitative trend in both perpendicular and parallel field scenario. More important, the parameter m shows the same qualitative dependence on field than the apparent n-number and they are both observed to be bigger in the parallel applied field scenario rather than in the perpendicular one. Similar results for the Weibull exponent m have been obtained for bridged and unbridged sample.

5.5.5 Pinning distribution dependence on field

The distribution model parameters I_{Cmin}, I_{C0} and I_0, are plotted in fig.(5.20a) and fig.(5.20b) for perpendicular and parallel scenario respectively.

The effect that distribution parameters have on the current probability distribution function is shown in fig.(5.21), where the current distribution of four different fields (self field, 98 mT, 220 mT and 300 mT) measured on Sample AS in the perpendicular configuration, is presented. As it can be observed in fig.(5.21a), the distribution function obtained for different fields are presented as a function of $(I_C - I_{Cmin})$, where is further evidenced as the pinning range remains almost constant as the field is increased. On the other hand, m is seen to decrease as the field is increased.

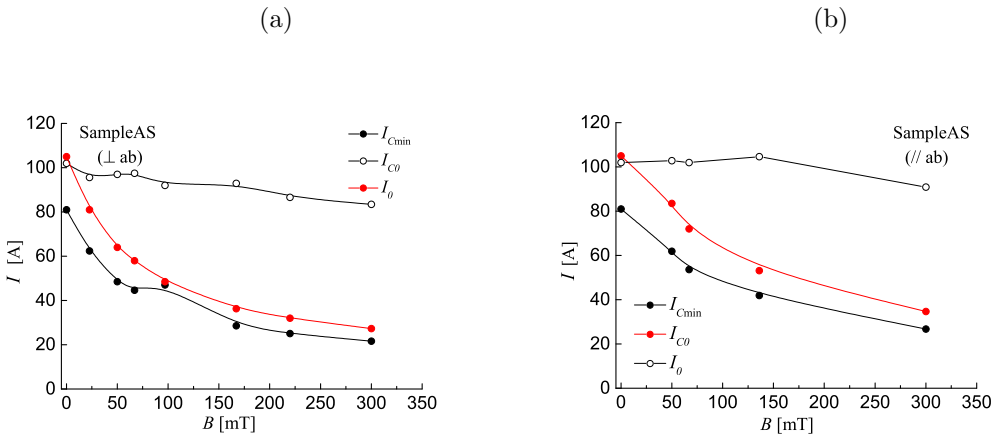

Figure 5.20: Minimum current threshold I_{Cmin}, engineering critical current I_{C0} and pinning range I_0 dependence on temperature of Sample AS in presence of (a) perpendicular and (b) parallel applied field.

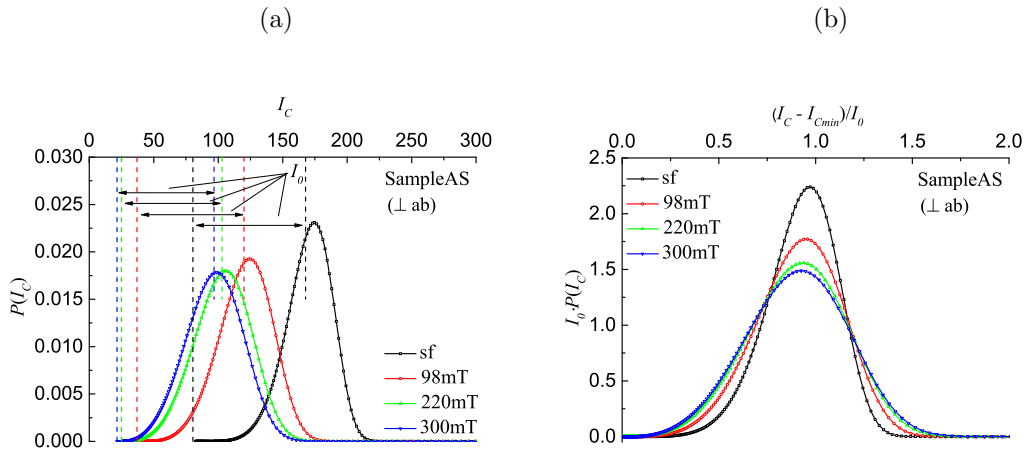

Figure 5.21: Current distribution of Sample AS in self field and at 98 mT, 220 mT and 300 mT perpendicular applied field plotted (a) as a function of I_C and (b) as a function of $(I_C - I_{Cmin})/I_0$.

Thus, the shape of the distribution curves in field is mostly determined by the parameter m and, by scaling the current distribution curves with respect of I_0 as in fig.(5.21b), a broader shape can be observed as the field is increased.

5.6 Discussion

5.6.1 Pinning distribution at different temperatures

The minimum current threshold I_{Cmin} and the engineering critical current I_{C0} present a qualitatively similar temperature dependence and this behaviour is confirmed for all sample measured. The similar trend agrees with eq.(5.7) since the ratio m/n is observed to be constant with temperature. The current I_{Cmin} is below the engineering critical current along the temperature range, suggesting that the dissipation starts at current smaller than the one measurable with transport measurements, due to the extended influence of the thermal activated flux flow. The classical definition of macroscopic critical current is therefore conserved by the model which individuate in the minimum current threshold I_{Cmin}, the current at which dissipation starts.

At temperature below 45 K, the pinning range I_0 is observed to saturate whilst a faster increment in I_{Cmin} is observed as shown in fig.(5.22) for Sample II, which is the sample measured in a wider range of temperatures.

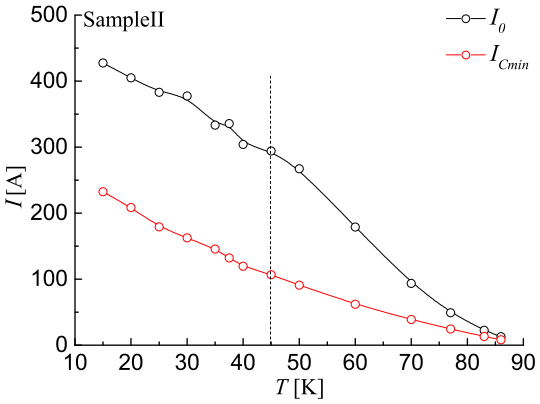

Figure 5.22: Pinning range I_0 and minimum current threshold I_{Cmin} of Sample II dependence on temperature.

The two parameters show different slope at low temperatures: the pinning range I_0 presents a convex shape whilst I_{Cmin} a concave one. The latter suggests the presence of both strong and weak pinning centres in the material. The first ones, not strongly

affected by temperature, allow a slow reduction of I_0, whilst the second ones, strongly affected by temperature, are the cause of the strong reduction observed in I_{Cmin}, as clear from fig.(5.22).

In terms of distributions, the saturation of I_0, in parallel with an increasing exponent m corresponds to bell curves which narrower as the temperature is lowered, due to the difference $I_0 - I_{Cmin}$, which is reducing with increasing temperature.

The peak of the distribution can be obtained deriving eq.(5.3) and imposing the condition:

$$\frac{\partial P(I_C)}{\partial I_C} = 0 \tag{5.17}$$

from which it is obtained:

$$\left(\frac{I_C - I_{Cmin}}{I_0}\right)_{max} = \left(\frac{m-1}{m}\right)^{1/m} \sim 1 \tag{5.18}$$

Hence the peak of the critical current distribution always takes place in correspondence of the unit in a scaled graph as the one of fig.(5.21b), and the pinning range I_0 corresponds to about the difference between the minimum and the maximum value in the distribution.

A mathematical definition of the pinning range I_0 is obtained by calculating the average current value of the distribution as in eq.(5.19).

$$\int_{I_{Cmin}}^{\infty} I_C \cdot P(I_C) \cdot dI_C = I_{Cmin} + \Gamma\left(\frac{m+1}{m}\right) \cdot I_0 \tag{5.19}$$

where the $\Gamma(\frac{m+1}{m}) \sim 0.9$ which in turn leads to

$$I_0 \sim \frac{\overline{I}_C - I_{Cmin}}{0.9} \tag{5.20}$$

which allows to calculate I_0 once known $\overline{I}_C$ and I_{Cmin}.

5.6.2 Pinning distribution at different fields

Whilst parameters such as m, I_{Cmin} and I_C have a sharp dependence on field, the pinning range I_0 remains steady in the range of field measured for both perpendicular and parallel field scenario as shown in fig.(5.20a) and fig.(5.20b).

In term of distribution, since the pinning range is steady with field whilst m is changing, the distribution curves are observed to broader similarly to scenario I in section (5.3.1). The pinning range of each field is evidenced in fig.(5.21) and indicates the difference between I_{Cmin} and almost the centre of the bell of the distribution. Since the I_0 is steady with field, the difference in shape of the distribution has to be attributed to the difference in the exponent m, as discussed in section (5.3.1).

The results obtained suggest that on increasing field, weaker pinning centres appear, resulting in a broader critical current distribution. On the other hand, it has been observed the presence of strong pinning centres are surprisingly not strongly affected by field, so that the dissipation is at the same level of I_0 as the field is increased. With further increment in field, the scaling current is expected to eventually drop down, thus further investigation is required.

The convex shape observed for I_0 agrees with the scaling law empirically predicted by the flux creep model for metallic superconductors [79], which defines the current I_0 as the depinning current at sufficiently low temperature and field where thermal activation is not significant. The pinning force per unit volume, in presence of the only self-field B_{sf} perpendicular to the current direction, can be calculated by taking into account the distribution of critical current $P(I_C)$ according to eq.(5.21),

$$F_P = \int_{I_{Cmin}}^{\infty} B_{sf} \cdot \frac{I_C}{A} \cdot P(I_C) \cdot dI_C = \int_{I_{Cmin}}^{\infty} \alpha \cdot \frac{I_C^2}{A} \cdot P(I_C) \cdot dI_C \tag{5.21}$$

where B_{sf} has been calculated as $B_{sf} = \alpha \cdot I_C$ and $P(I_C)$ is the probability distribution function of the critical current. The integral of eq.(5.21) has a numerical solution which has been calculated with Mathematica. The depinning current at the estimated self-field B_{sf} can be simply calculated as:

$$I_{\mathrm{dep}}(B_{sf}) = \frac{F_P \cdot A}{B_{sf}} = \frac{\int_{I_{Cmin}}^{\infty} \alpha \cdot I_C^2 \cdot P(I_C) \cdot \mathrm{d}I_C}{\int_{I_{Cmin}}^{\infty} \alpha \cdot I_C \cdot P(I_C) \cdot \mathrm{d}I_C} \tag{5.22}$$

where the self field B_{sf} in eq.(5.22) has been assumed proportional to the distribution averaged critical current I_C^{av}. As an example, the solution of eq.(5.22) for $m = 6$ has been calculated and it is given in eq.(5.23):

$$I_{\mathrm{dep}}(B_{sf}) \sim I_{Cmin} + 0.95 \cdot I_0 \tag{5.23}$$

where it can be observed that, as the term with I_0 dominates on I_{Cmin}, it results to be $I_{\rm dep} \propto I_0$. This proportionality can be observed in fig.(5.23) where the calculated $I_{\rm dep}$ has been compared with the depinning range I_0 of Sample II measured at different temperatures. Thus it has been shown as in presence of a current distribution, the depinning current is determined by the depinning range I_0 of a distribution rather than the critical current. Note that in the limit of no distribution ($I_0 = 0$) the depinning current is instead determined by I_{Cmin} as predicted by eq.(5.23).

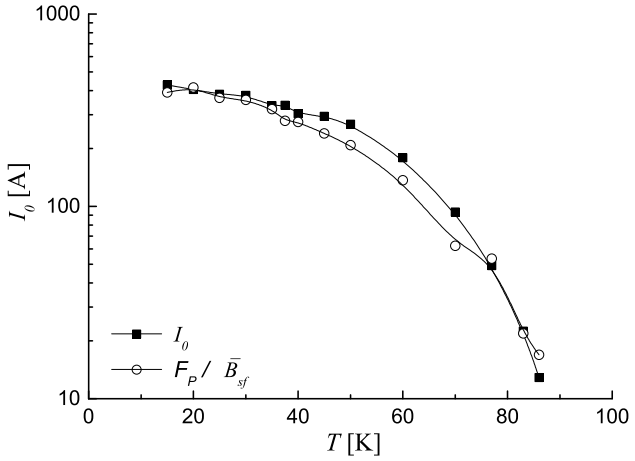

Figure 5.23: Scaling current I_0 and depinning current I_{dep} dependence on temperature obtained with $\overline{B}_{sf} = \alpha \cdot I_C^{av}$.

5.7 Conclusion

Transport measurements at different temperatures on 2G YBCO conductors revealed an underlining E-J characteristic described by inhomogeneous distribution of critical current. The model does not provide microscopic information about the depinning mechanism, which is still believed to be described by collective pinning of small flux bundles at temperature above $T = 45$ K and of single vortex at temperature below, but it is of practical utility since it introduces parameters that can be related to the tape performance such as I_{Cmin} and I_0 and permits comparisons between conductors with different critical current densities. The model agrees with the picture of both

action of strong a weak pinning centres which act differently on the critical current distribution. Strong pinning centres are not strongly dependent on field in the range $0 - 300\,\mathrm{mT}$ and temperature and therefore allow the pinning range to change smoothly with temperature and field, differently from I_{Cmin} which is associated to the presence of weak pinning centres that became quickly ineffective as either the temperature or the field is increased.

5. FLUX PINNING DISTRIBUTION AND E-J CHARACTERISTICS OF 2G YBCO TAPES

6

Quench investigation

6.1 Introduction

The progress in the performance and the commercial availability of second generation (2G) YBCO tapes has led to the availability of practical conductors suitable for medium/high field applications at intermediate temperature range. As described in section(1.4.2), is crucial to understand, for such applications, the rule played by the thermal stability during quench and how it is affected by the relevant thermal-electrical properties dependence on temperature. The current sharing regime can in fact potentially extend for about 100 K up to T_C, where the resistivity, heat capacity and thermal conductivity dependence on temperature are no negligible. Two parameters of the experimental setup can be changed to affect the dissipation level in the current sharing regime: the temperature and the current. Due to the difficulty of achieving measurements at high currents, previous work primarily investigated the MQE on its temperature dependence and to a lesser degree on the current dependence [46, 47, 51, 80, 81, 82]. Significant inconsistencies among previous publications have been observed, being for example the MQE results for the similar 2G conductor (Super Power 2G HTS with Cu/Cu stabiliser) for [47] and [82] different by 400%. Furthermore, the majority of the published work on HTS quench are observation based with limited effort of explanation. While experimental results are crucial ingredients for a better understanding of the HTS quench behaviour, it is important to find underlying mechanisms for the experimental observations.

The work presented in this chapter aims for a better understanding by focusing on the

MQE current and temperature dependence. Measurements collected on 2G YBCO tape 4 mm wide, in both self-field and in perpendicular applied field scenario (0.1 T) are presented. The field has been applied in order to reduce the critical current and obtain measurement at lower temperatures. Measurements at high current have also been performed with particular attention on the MQE behaviour at current at $j = I/I_C > 0.8$.

6.2 Thermal-electrical properties

The quench behaviour of HTS at low temperatures is fundamentally influenced by the no-linear thermal-electrical properties of these conductors over a wide temperature range where the current is shared between the quenched superconductor and the resistive matrix. As a precursor of the present study, the specific heat C_p, the thermal conductivity k, the and resistivity ρ, where measured between 2 K and 30 K, and their dependence on temperature is shown in fig.(6.1).

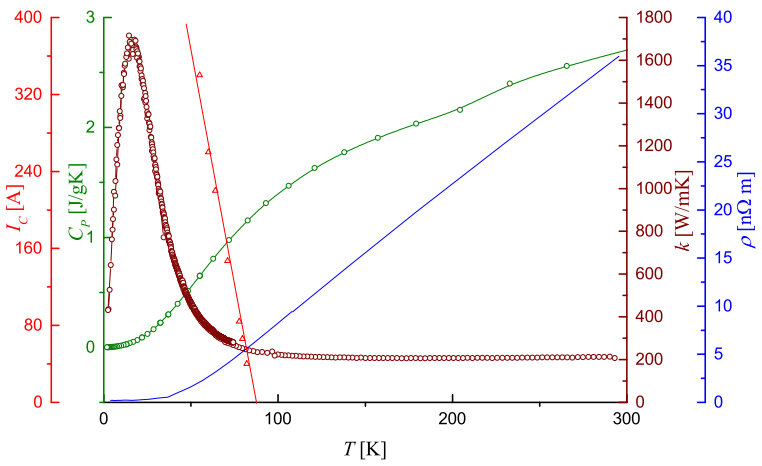

Figure 6.1: Specific heat C_p, thermal conductivity k and resistivity ρ, of 2G YBCO tape dependence on temperature.

- The normal resistivity below T_C was obtained with a sample specially processed at 600°C in vacuum, so that to disable the superconducting transition and it is

plotted with the solid blue line in fig.(6.1). The vertical dashed line represents the superconducting transition that occurs at $\sim$ 88 K. Below 30 K the sample shows a residual resistivity of 0.22 nΩm. The measured resistivity is mainly attributed to the 20 μm Cu layer covering the YBCO film.

- The specific heat, plotted as a green line in fig.(6.1), exhibits a linear trend a low temperature ($<$ 6 K) mainly due to the presence of Ni in the Hastelloy substrate;
- The thermal conduction is almost totally carried by the Cu layer, and the thermal conductivity represented with a dark red line in fig.(6.1), presents a large peak at 13 K, confirming its high purity.

6.3 Critical current

The critical current of the YBCO tape measured in adiabatic conditions is plotted as a function of temperature in fig.(6.2), for self-field (black dots) and in-field of 0.1 T (red dots) scenario. In both cases a linear decrement of critical current with temperature is observable and the critical current in the in-field scenario is $\sim$ 2.5 times smaller than in self-field one.

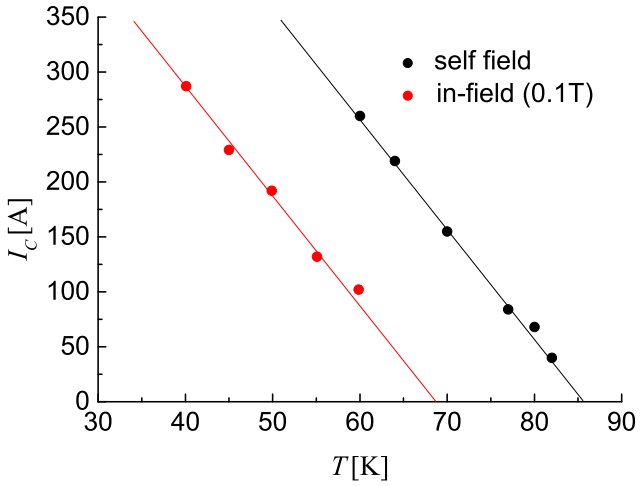

Figure 6.2: The temperature dependent critical current in self-field (black dots) and in-field at 0.1 T (red dots).

6.4 Quench measurement protocol

Quench measurements were carried out injecting a predetermined percentage of the I_C in the tape: supplying a current smaller than the critical value ensures the tape is in equilibrium before the quench is initiated.

In order to initiate a quench, a short heat pulse is discharged from a miniature heater, creating a localised thermal disturbance in the conductor. The time evolution voltages and temperature along the conductor are monitored by thermocouples and voltage taps connected to the data logger. The electrical and thermal potential are recorded simultaneously at 10 kHz. Once the sample recovers the superconducting state, the procedure is repeated increasing the amplitude of the heat pulse until quench in the sample is observed. The amount of energy injected into the sample to instigate a quench event is gradually controlled by increasing the voltage on the power supply. When a quench event is recorded, the sample is left to cool down for few minutes before repeating the next measurement in order to restore the initial temperature along the all sample length.

The minimum energy needed to quench the tape is determined by repeating the experiment with the voltage of the heater setted just below the previous voltage value which caused the quench event. The voltage has been incremented with fine steps ($\sim 0.005\,\mathrm{V}$) to define well the actual quench voltage.

The HTS sample has been protected from burning out during tests by a quench protection system which allows to cut off the current source when the voltage across the sample exceeds a maximum level (typically 10 - 100 mV) [41].

6.5 Quench initiation

6.5.1 Typical recovery and quench event

Hot spots are generated on the sample following the deposition of the heat pulses. The minimal amount energy required to quench a sample, which operates at a certain temperature and transport current, is determined by measuring the temporal evolution of the hot spot. The energy injected into the heater is therefore gradually increased till

an irreversible quench is detected. Temperature and voltage evolution with time are recorded in different positions along the sample by a set of thermocouples and voltage taps as shown in the sample set up of fig.(2.2). In order to measure, the minimum quench energy (MQE), several heat pulses are deposited with a value in between from the last recovery event and the last quench event.

Temporal evolution of voltage and temperature.

As an example, the temporal evolution of temperature and voltage following the generation of an hot spot on the sample, measured at the operative temperature of 66 K and with the sample carrying 210 A (95 % of the critical current of the sample at that temperature), are presented in fig.(6.3) and in fig.(6.4) respectively. The temperature trace is measured with a thermocouple adjacent to the sample heater labelled T_0 and the voltage response with the corresponding voltage taps near the heater location V_0.

In fig.(6.3) the temperature response to four different pulses of increased entity is presented and the consequent recovery and quench events associated can be easily identified.

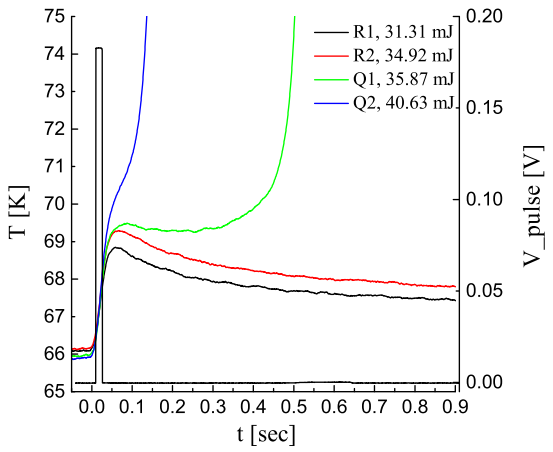

Figure 6.3: Temperature T_0 as a function of time following different applied heat pulses of 15 ms. Starting conditions: operative temperature 66 K, operative current 210 A.

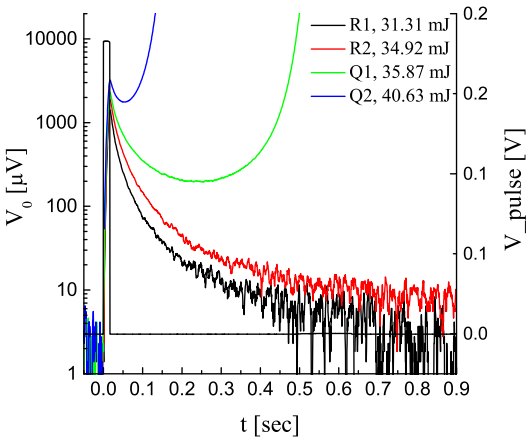

Figure 6.4: Voltage V_0 evolution as a function of time following different applied heat pulses of 15 ms. Starting conditions: operative temperature 66 K, operative current 210 A.

- Recovery: the temperature evolution as well as the voltage evolution in two recovery cases, indicated as R1 and R2, are shown in fig.(6.3) and in fig.(6.4) respectively, with the black line for case R1 and the red line for case R2. The two recovery events have been generated by depositing 31.31 mJ in the recovery case R1 and 34.92 mJ in the recovery case R2. In both cases, a peak of voltage is developed across the hot spot and is followed by an increment in temperature with a peak of about $\sim$ 4 K, as it can be observed in fig.(6.3). The increased energy deposited in the recovery case R2 corresponds to a higher peak in temperature as well as in voltage than the recovery case R1. However, in those cases the energy deposited on the sample is enough to let a small zone surrounding the heater transient to the normal state, but the heat generated in such a resistive zone, is contrasted by the cooling power of the system and is not enough to let all tape quench. Thus even if a peak on voltage is recorded across the heater, both voltage and temperature recover to the initial value;

- Quench: the temperature evolution as well as the voltage evolution in two irreversible quench cases are shown in fig.(6.3) and in fig.(6.4) respectively, with

the green line for the quench case Q1 and the blue line for the quench case Q2. The two quench cases correspond to the applied heat pules of 35.87 mJ (quench) and 40.63 mJ (overheated quench) respectively. In both cases the temperature and the voltage increase irreversibly with time. However the causes of quench are different: in the quench case Q2, the quench event is principally due to the external disturbance applied, which entity is big enough to make both voltage and temperature sharply increase. In the other case, instead, the quench event is takes place because of the heat generated in the normal zone surrounding the heater. When the minimal quench energy is applied in fact, both voltage and temperature profiles, show an initial peak due to the external pulse applied on the sample, after which, as the deposited heat is conducted away, decrease and flatten. A plateau in both temperature and voltage occurs as the disturbance spreads out along the tape in quasi steady-state, where the heat generated by the normal zone is balanced out by the system cooling power. When the heat generated by the normal zone dominates, both voltage and temperature are observed to increase again rapidly.

When comparing fig.(6.3) and fig.(6.4) a delay between the peak in temperature and the voltage profile is observed. The temperature peak is reached when the voltage across the hot spot has already disappeared. This increment is due to the diffusion of the energy stored in the hot spot.

Spatial evolution of temperature and voltage.

The voltage spatial evolution after pulse deposition is shown in both case of recovery R1 (top graph) and quench Q1 (bottom graph) in fig.(6.5). In case of insufficient energy to quench the sample (top graph), the voltage rises in the zone nearby the heat deposition affecting V_0 and V_1 which quickly recover to the initial value. The voltage taps located further than V_1 are not affected by the local disturbance. In both cases of quench (bottom graph) and recovery (top graph), the initial energy deposited produces a local peak in V_0 and V_1 after which the two voltage profile flatten to a value different from the initial one and greater than zero.

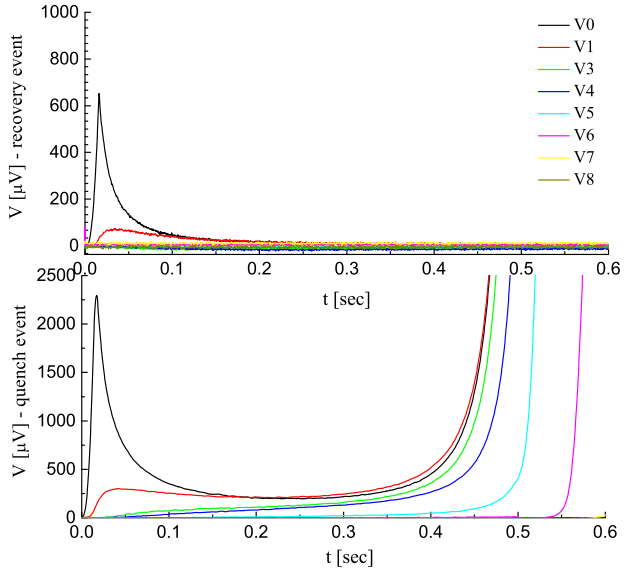

Figure 6.5: Voltage spatial evolution after pulse deposition, in case of recovery R1 (top graph) and quench Q1 (bottom graph) measured at 66 K with operative current 95% I_C.

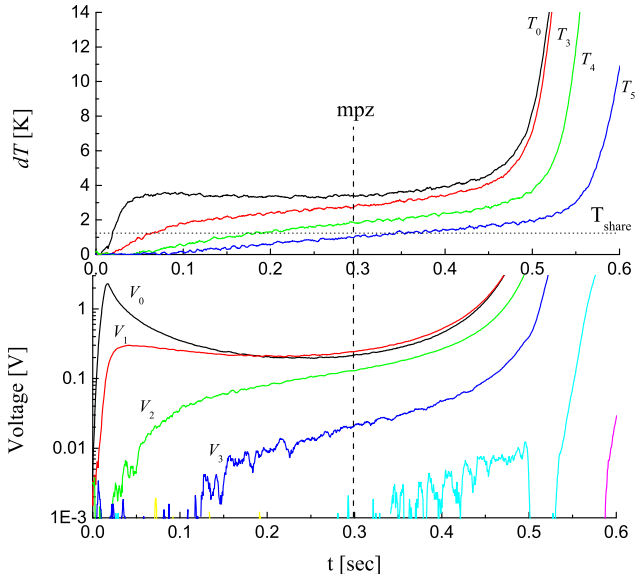

Figure 6.6: Normal zone extension measured by spatially distributed voltage taps and thermocouples. Operative temperature 66 K, operative current 210 A (95 % of I_C), MQE of 35 mJ.

The heat generated in the normal zone formed in the region of the hot spot, leads to the thermal runaway and, as the normal zone propagates, all the voltage taps further located measure in sequence an increment in voltage. As evidenced in the bottom graph of fig.(6.6) in fact, V_0 rapidly rises to a peak and, after a plateau of about 0.3 sec, it starts to rise again due to the contribution of heat generation by the transport current in the normal zone, and the dissipation spreads to V_4 followed by rapid thermal quench propagating to V_5 after about 0.6 s.

6.6 MQE, $NZPV$ and l_{MPZ}

Three important parameters already introduced in Chapter (1) allow to investigate the thermal material of the conductor: the MQE, the $NZPV$ and the l_{MPZ}. Information about these quantities can be obtained by a measured quench event as explained below.

Minimum quench energy.

The heat generated in the heater is given by eq.(6.1)

$$MQE = I \times V_h \cdot t \tag{6.1}$$

where V_h is the pulse voltage across the heater, I is the current and t is the length of the pulse. Because the resistance of the heater is a function of temperature, a direct measurements of the current by imposing the voltage is not possible. An additional constant resistance R_{ref}, maintained at room temperature, has been put in series with the heater R_h, and the voltage V_{ref} developed across it has been measured in order to calculate the operative current as V_{ref}/R_{ref}. The additional resistance $R_{ref} = 0.35\,\Omega$ is offered by a constantan wire. Because of $R_{ref} \ll R_h$, V_{ref} is small and the voltage developed across the heater V_h in eq.(6.1), can be approximate with the total pulse voltage V_0 and assumes the form of eq.(6.2)

$$MQE = \frac{V_{ref}}{R_{ref}} \cdot V_0 \cdot t \tag{6.2}$$

Since the recorded voltage pulse is not a perfect step function, a more accurate calculation can been done when considering the area of the square pulse as in eq.(6.3):

$$MQE = \int_0^{t_p} \frac{V_{ref}}{R_{ref}} \cdot V_0 \cdot dt = \frac{V_0}{R_{ref}} \cdot \int_0^{t_p} V_{ref} \cdot dt \tag{6.3}$$

Normal zone propagation velocity.

Assuming that the MPZ has a uniform propagation velocity, the $NZPV$ can be obtained from the measured spatial distribution of the voltage taps, in the region where they sharply increase with time. The first voltage taps pair and the end-end voltage taps are normally not used since the first one is too close to the heater and maybe still affected by the heat deposited whilst the other one does not measure a significant voltage increment, because of the protections intervention, which prevents the quench to propagate to the end of the sample. Once selected a good pair of voltage taps distanced Δs, it is possible to calculate the time window in which both voltage taps reach the same voltage value and the minimum zone propagation velocity can be calculated as Δs/Δt.

Minimum propagation zone.

The evolution of the normal zone can be described with spatial and temporal dimensions. The l_{MPZ} is defined as the length of the conductor which is above the current sharing temperature T_{CS} before a quench event is triggered. With respect to time, the l_{MPZ} is defined at the point where the heat generation and the cooling power are nearest to an equilibrium state.

As an example the minimum propagation zone MPZ has been graphically estimated for the quench event measured at 66 K and with the operative current of 210 A (95 $\%I_C$) by looking at both the voltage and the spatial heat diffusion along the sample during a quench event, as the one shown in fig.(6.6).

Since the current dependence on temperature is known, the current sharing temperature T_{CS} correspondent to 95 % of the operative current can be calculated. In the case here presented, it results to be 0.6 degree above the operative temperature. Therefore,

by looking at the time just before the run away of V_0 (vertical dot line in fig.(6.6)) it is possible to identify which thermocouples read a temperature above T_{CS}. In this particular case the MPZ has been found to end just before the T_5 location which corresponds to about 25 mm.

6.7 Results and discussion

6.7.1 MQE temperature dependence

The minimum quench energy dependence on temperature, at different percentage of the critical current ($I/I_C > 0.8$), has been investigated. Measurements have been carried out in self-field in the range of temperatures 60 K- 79 K. In order to overcome the limit in current of the system, a perpendicular field of 0.1 T has been applied allowing measurements in a lower temperatures range of 42 K - 62 K. The MQE obtained at different temperatures when applying high percentages of the critical current ($80\%I_C - 99\%I_C$), are plotted as a function of temperature in fig.(6.7a) for the self-field case and in fig.(6.7b) for the in-field case at 0.1 T.

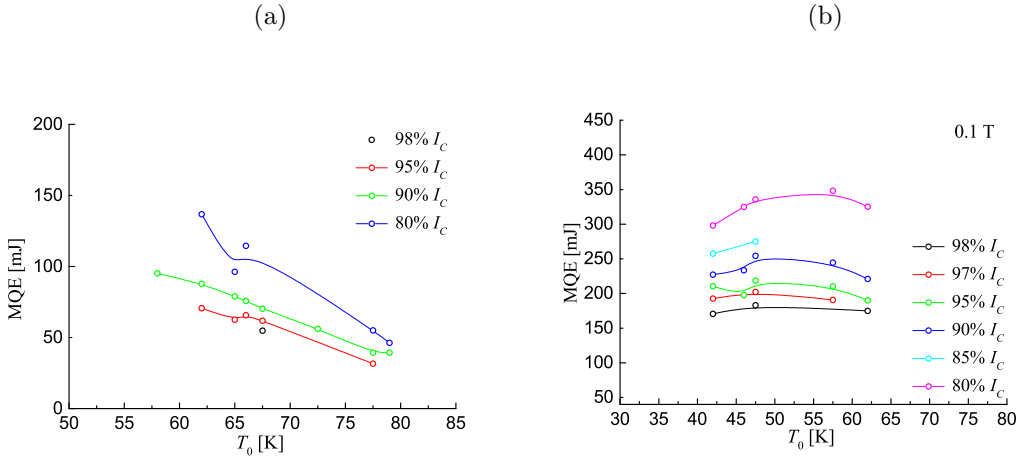

Figure 6.7: Minimum quench energy dependence on temperature (a) in self-field and (b) with 0.1 T perpendicular field applied.

It can be observed that:

- The MQE needed to initiate a quench increases as the operative current is reduced, in both the self-field and the in-field measurement;

- As effect of the reduced I_C at 0.1 T, the MQE measured in field is more than two times bigger than the one measured in self-field, i.e. at T=62 K, the MQE is $\sim$ 87 mJ in self-field and $\sim$220 mJ at 0.1 T;

- The measured MQE in self-field surprisingly increases with reducing temperature. This trend slows down at 0.1 T where the temperature is further reduced.

A particular attention has been put on quench measurements dependence on the operative current.

6.7.2 MQE dependence on current

The minimum quench energy plotted as a function of the scaled current $(1-j)$ where $j = I/I_C$, is presented in fig.(6.8a) and in fig.(6.8b) for the self-field and the in-field case respectively. The current has been normalised by using the $I_C(T)$ dependence on temperature presented in fig.(6.2).

(a) (b)

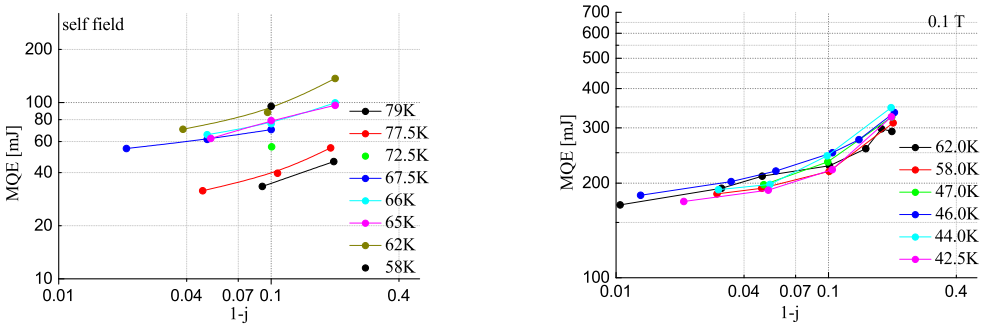

Figure 6.8: Experimental MQE as a function of the scaled current $(1-j)$ measured in (a) self-field and (b) in perpendicular applied field scenario of 0.1 T.

The MQE data obtained show a surprisingly slow reduction with current in both measurements in self-field and in-field at $I/I_C > 0.9$. Such a behaviour is in agreement with recent results obtained on different tapes and coils which such as on BSCCO 2212 coil at different applied fields (15 T, 18 T, 20 T) in liquid helium, which results are

plotted in fig.(6.9). The respective expected prediction are plotted in dashed lines [83] in the same figure.

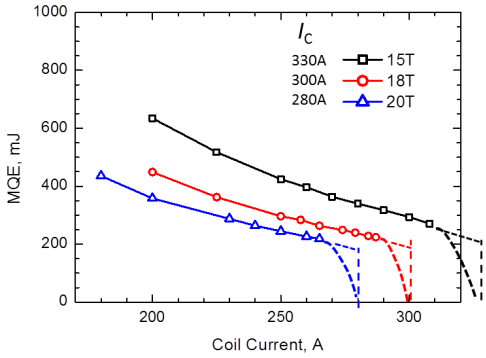

Figure 6.9: MQE dependence on current measured on BSCCO 2212 coil at different applied fields (15 T, 18 T, 20 T) [83].

A similar non-vanishing behaviour of MQE with current has been observed in numerous measurements on LTS such as on multi-filamentary MgB_2 and MgB_2 pancake [84, 85], NbTi Rutherford cable [86] and NbTi solenoid [87].

The following work is an attempt to explain two distinct HTS quench features:

- The observed increase of MQE with reducing temperature;
- The apparent non-vanishing MQE in the vicinity of J_C opposite to the one found in LTS superconductor.

For the former, it is important to find out the turning point temperature where rapid reduction of c_P eventually halts the MQE increase. For the latter, it is important to firstly, examine the MQE-current scaling in detail to identify the systematic difference from LTS, and secondly, to attempt a plausible explanation. In order to address both objectives, a semi-quantitative analysis of $MQE(I,T)$ by extending the established quench theory for the critical state to power law superconductors has been suggested.

6.7.3 MQE for Critical State Superconductors

The current dependence of the critical state MQE has been obtained previously [87] and here is presented a simplified version without the need of solving the differential

equations [87].

The one dimensional heat diffusion equation with heat generation is given by eq.(6.4).

$$c_p \frac{\partial T}{\partial t} = \frac{\partial}{\partial x}\left(k \cdot \frac{\partial T}{\partial x}\right) + J \cdot E(T, J) \tag{6.4}$$

Note that in eq.(6.4) the filling factor λ has been removed since the definitions presented are consistently changed based on the engineering current density $J = I/A$ where A is the total cross section of the tape, therefore the critical current density is now defined as $J_e = I_C/A$ and the overall thermal-electrical properties (k,c_p, ρ_n) are defined for the conductor composite as a whole, as found by direct measurements presented in fig.(6.1).

Eq.(6.4) can be transformed with dimensionless time and coordinates by scaling the length with the classic formula of the minimum propagation zone l_{MPZ} in critical state given by eq.(6.5) and the time with the time constant of the heat diffusion in the normal zone t_0 defined as in eq.(6.6) within l_{MPZ}.

$$l_{MPZ} = \frac{\pi}{2} \cdot \left[\frac{k(T_0)(T_C - T_0)}{\rho_n \cdot j \cdot J_e^2(T_0)}\right]^{0.5} \tag{6.5}$$

$$t_0 = \frac{d \cdot c_P(T_0) \cdot l_{MPZ}^2}{k(T_0)} \tag{6.6}$$

where d is the density of the matrix.

Therefore, by introducing the dimensionless length ξ,

$$\xi = \frac{x}{l_{MPZ}} \tag{6.7}$$

the dimensionless time τ,

$$\tau = \frac{t}{t_0} \tag{6.8}$$

together with a dimensionless current j

$$j = \frac{I}{I_e} \tag{6.9}$$

and a dimensionless temperature u

$$u = \frac{\Theta}{1 - j} \tag{6.10}$$

with

$$\Theta = \frac{T - T_0}{T_C - T_0} \tag{6.11}$$

the non-dimensional 1d quench equation of the critical state is reduced to the dimensionless form of eq.(6.12):

$$\frac{\partial u}{\partial \tau} = \frac{\partial}{\partial \xi}\left(\frac{\partial u}{\partial \xi}\right) + \left(\frac{\pi}{2}\right)^2 \frac{E(u,j)}{(1-j)\rho_n J_e(T_0)} \tag{6.12}$$

where the dimensionless heat generation is given by:

$$G(u,j) = \frac{E(u,j)}{(1-j)\rho_n J_e(T_0)} \tag{6.13}$$

Assuming a linear critical current density $J_e(T)$, the dimensionless critical current can be expressed as in eq.(6.14).

$$J_e(T) = J_e(T_0) \cdot \frac{T_C - T}{T_C - T_0} = J_e(T_0) \cdot (1 - \Theta) = J_e(T_0) \cdot (1 - u \cdot (1 - j)) \tag{6.14}$$

It follows that the current sharing voltage in critical state is a linear function of the temperature rise as shown in eq.(6.15) where it has been expressed as a function of u and and j.

$$E(u,j) = \rho_n \left(J - J_e(T)\right) = \rho_n J_e(T_0)(1-j)(u-1) \tag{6.15}$$

Thus the non-dimensional 1d quench equation assumes the form of eq.(6.16).

$$\frac{\partial u}{\partial \tau} = \frac{\partial}{\partial \xi}\left(\frac{\partial u}{\partial \xi}\right) + \left(\frac{\pi}{2}\right)^2 \cdot (u-1) \cdot H(u-1) \tag{6.16}$$

where $H(x)$ is the Heaviside function defined as:

$$H(x) = \begin{cases} 0, & x \leq 1 \\ 1, & x > 0 \end{cases} \tag{6.17}$$

By introducing eq.(6.15) into eq.(6.13), it can be found that the heat generation of critical state current sharing $G(u, j, n = \infty)$ is simply $u-1$, independent of transport current j, as shown by the black dashed line in fig.(6.10). Note that $G(u, j, n = \infty)$ vanishes at the current sharing temperature T_{cs}, correspondent to $u = 1$, where $J_e(T_{cs}) = J$. Since (a) the existence of the MQE is preserved under linear transformations and (b) all parameters have been eliminated from the above dimensionless quench equation for the critical state, its dimensionless MQE has to be a pure number ($\eta_{MQE,cs}$), independent of current and thermal-electric properties.

The dimensionless MQE $\eta_{MQE,cs}$ can be found using Wilson's method [41] by solving the stationary equation:

$$\frac{d^2u}{d\xi^2} + \left(\frac{\pi}{2}\right)^2 \cdot (u-1) \cdot H(u-1) = 0 \tag{6.18}$$

with boundary condition $u(0) = u_0$ and $u(L) = 0$ and minimising the enthalpy

$$\eta(u_0) = \int_0^{L(u_0} u(\xi) d\xi \tag{6.19}$$

The above eq.(6.18) is easily solved and the minimization of $\eta(u_0)$ leads:

$$\eta_{MQE,cs} = 1 + \frac{2\sqrt{2}}{\pi} \sim 1.9 \tag{6.20}$$

The corresponding dimensioned energy MQE, cs in the real world dimensions of space and time is expressed in eq.(6.21), where $Q_0(T_0)$ is a prefactor independent on current.

$$MQE, cs(j) = \eta_{MQE,cs} \cdot l_{MPZ} \cdot A \cdot d \cdot c_P(T_0) \cdot (T_C - T_0)(1-j) = Q_0(T_0) \cdot (1-j) \cdot j^{-0.5} \tag{6.21}$$

According to eq.(6.21) the critical state MQE, cs scales with $1-j$ which approaches to zero rapidly as $J \to J_e$. This prediction is in contrast with the not vanishing MQE in the close vicinity of J_e experimentally observed on HTS conductors.

6.7.4 MQE in Power Law Superconductors

As shown extensively in the previous chapters, the current-voltage characteristics (CVC) of high temperature superconductors exhibits a strong non-linear behaviour which is significantly different from the critical state.

$$E = E_C \cdot \left(\frac{I}{I_C}\right)^n \tag{6.22}$$

According to the current sharing model described in section (1.4.1), the total current density can be expressed as in eq.(1.20), which in dimensionless coordinates assumes the form of eq.(6.23).

$$(1 - (1-j)u) \left(\frac{E(u,j)}{E_0}\right)^{\frac{1}{n}} + \frac{E(u,j)}{J_e(T_0)\rho_n} = j \tag{6.23}$$

By introducing eq.(6.23) into eq.(6.13) non-linear heat generation $G(u, j, n)$ can be obtained as follow:

$$G(u, j, n) = (u - 1) - \left(\frac{1}{1-j} - u\right) \cdot \left(\left(\frac{E(u, j)}{E_0}\right)^{\frac{1}{n}} - 1\right) \tag{6.24}$$

Thus, for quench behaviour dominated by the heat generation in the current sharing regime, the power-law CVC leads to a lower heat generation than the critical state as shown by the solid lines in fig.(6.10), obtained for $j = 0.9$ and $n = 20$ and assuming different matrix resistivity ρ_n values. Note that for $n \to \infty$, eq.(6.24) reduces to the critical state dimensionless heat generation $u - 1$.

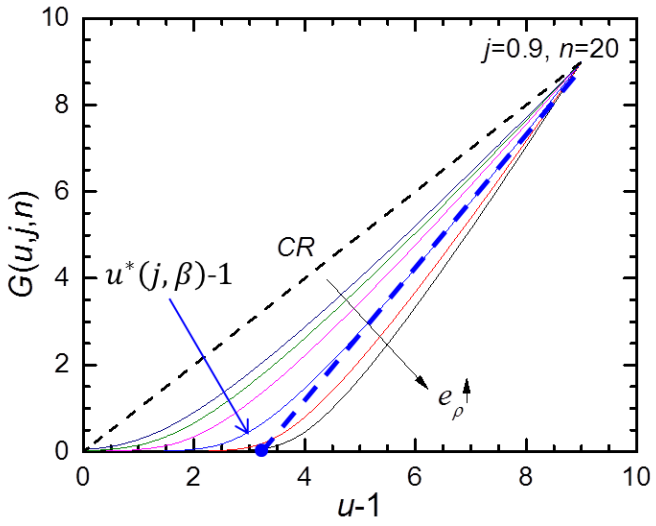

Figure 6.10: Dimensionless heat generation as a function of u, for the critical state (black dashed line) and in power-law (solid lines) for $j = 0.9$ and $n = 20$ with different e_ρ.

Due to the lack of a closed form expression of the power-law current sharing equation, it is difficult to elucidate an explicit $MQE - j$ scaling. However, as shown in fig.(6.10), the dimensionless heat generation term $G(u, j, n)$ for power-law superconductors can be approximated by a linearisation (blue dashed line in fig.(6.10)) of conveniently single Newton-Raphson iteration.

A new dimensionless parameter β is defined as a function of the exponent n and of

the matrix resistivity ρ_n where $e_\rho = J_e(T_0) \cdot \rho_n / E_0$ represents the normal conductor dissipation:

$$\beta^2 = \frac{(j \cdot e_\rho)^{1/n}}{1 + \frac{1}{n \cdot j} \cdot (j \cdot e_\rho)^{1/n}} \tag{6.25}$$

The approximated straight line in fig.(6.10) is $(u - u^*(j,\beta)) \cdot \beta^2$, where $u^*(j,\beta)$, defined as

$$u^*(j,\beta) = \frac{(1 - j \cdot \beta^{-2})}{(1-j)} \tag{6.26}$$

is the effective current sharing temperature. Note that is higher than the current sharing temperature for the critical state case. As an example $e_\rho = 25000$, $\beta = 1.23$ and $u^* = 4.05$ for typical 2G HTS at 77 K with $J_C = 3 \cdot 10^8$ Am^2, $\rho_n = 8 \cdot 10^{-9}$ Ωm, $n = 20$ and $j = 0.9$.

The non-dimensional 1d quench equation in the approximated power law case, assumes the form of eq.(6.27),

$$\frac{\partial u}{\partial \tau} = \frac{\partial}{\partial \xi}\left(\frac{\partial u}{\partial \xi}\right) + \left(\frac{\pi}{2}\right)^2 \cdot (u - u^*) \cdot \beta^2 \tag{6.27}$$

By further scaling the dimensionless temperature u by $u^*(j,\beta)$, and the dimensionless length ξ by β^{-1} and introducing the dimensionless parameters $\nu = \frac{u}{u^*(j,\beta)}$ and $\zeta = \beta \cdot \xi$, the approximated power-law quench equation becomes identical to that of the critical state, as shown by eq.(6.16).

$$\frac{\partial \nu}{\partial s} = \frac{\partial}{\partial \zeta} \cdot \left(\frac{\partial \nu}{\partial \zeta}\right) + \left(\frac{\pi}{2}\right)^2 \cdot (\nu - 1) \tag{6.28}$$

which analogously to the critical state dimensionless quench equation has a minimum $\eta_{MQE,PL}$ which is a pure number and can be calculated as:

$$\eta_{MQE,PL}(j,\beta) = u^*(j,\beta) \cdot \beta^{-1} \cdot \eta_{MQE,cs} \tag{6.29}$$

Similarly to what has been done for the critical state case, the dimensioned MQE of power-law superconductors is obtained as in eq.(6.30).

$$MQE = Q_0(T) \cdot \beta^{-1} \cdot \left(1 - \frac{j}{\beta^2} \cdot\right) \cdot j^{-0.5} \tag{6.30}$$

It is clear that the (1-j) factor in eq.(6.21) is replaced by $(1 - j \cdot \beta^{-2})$, thus the MQE reduces significantly slower at high j. Note that in presence of a non linear dissipation,

it is expected a higher MQE, since the predicted heat generation is smaller than the one predicted by the critical state. Similar results would have been obtained by using the HTS pinning models dissipation law or the distribution model dissipation law. The choice of the power law relation is mainly dictated by practical reason, because of the simplicity of the power-law relation and its validity in the proximity of I_C.

The approximated power-law model allows the non vanishing experimental MQE with current as it can be observed in fig.(6.11), where the model predictions obtained for different e_ρ and scaled with $MQE(j = 0.5)$ are plotted as a function of $(1 - j)$ and compared with the critical state prediction (dashed line).

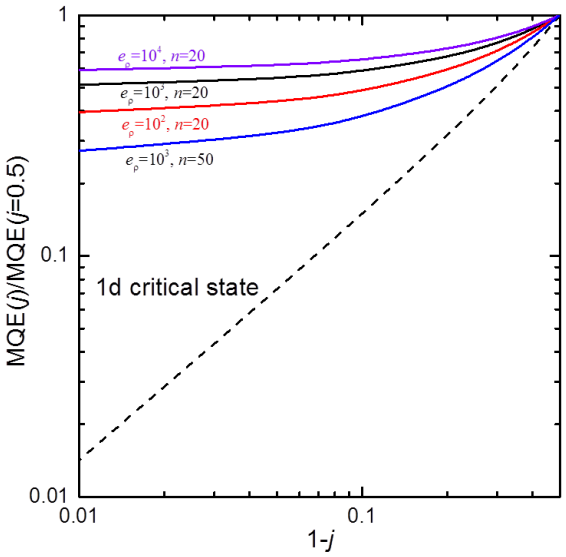

Figure 6.11: MQE dependence on current in the approximate power law case for different e_ρ (solid lines). Comparison with the critical state case (dashed line).

6.7.5 Application of the Critical State model and Power-law approximated model to data

Experimental data collected in self-field and at 0.1 T have been compared with the MQE predicted by both the critical state model and the power-law approximated model, according to eq.(6.21) and eq.(6.30) respectively. It is possible to normalise for comparison the predictions and the experimental data with the measured/calculate

MQE at $j = 0.9$, since $MQE = 0.1 \cdot Q_0$, which corresponds to $j \sim 0.86$. Fig.(6.12a) and in fig.(6.12b) show the normalised critical state (dashed line) and the power law (solid line) MQE in self-field and at 0.1 T respectively.

(a) (b)

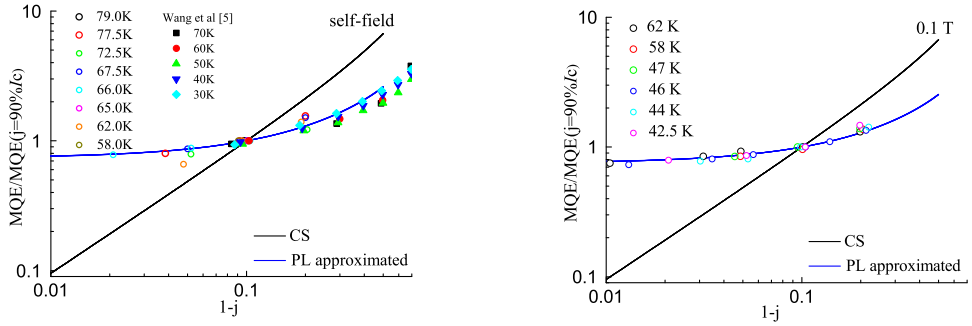

Figure 6.12: (a) Experimental MQE and approximate power law predictions, scaled versus $(1 - j)$ in self field and (b) in perpendicular applied field scenario.Measurement from Wang et al are also included in (a).

The normalized power-law with a $(1 - j \cdot \beta^{-2}) \cdot j^{-0.5}$ dependence, clearly agrees with the experimental results whilst a strong deviation of the critical state (dashed line), characterised by a $(1 - j) \cdot j^{-0.5}$ current dependence, is observed in both self-field and applied field. Furthermore, the experimental data of Wang et al [81] (solid symbols in Fig. 5(a)) on a similar 2G conductor (SuperPower YBCO 2G HTS with Cu/Cu stabilisation) also exhibit a current dependence consistent with that given by the approximated power-law.

The experimental data temperature dependence in self-field and with 0.1 T presented in fig.(6.13a) and fig.(6.13b) respectively, is compared to the analytical MQE. A temperature dependence similar to the one of the experimental data is predicted by the prefactor $Q_0(T_0)$. To better highlight the similarity with the experimental findings, the power-law analytical MQE has been scaled with a factor 2.5 (green lines). The predicted decreasing trend of the MQE with reducing temperature, observed below 35 K, is strongly dominated by the heat capacity cubic power dependence on temperature and by the decreasing thermal conductivity. Such a trend is reversed at temperature

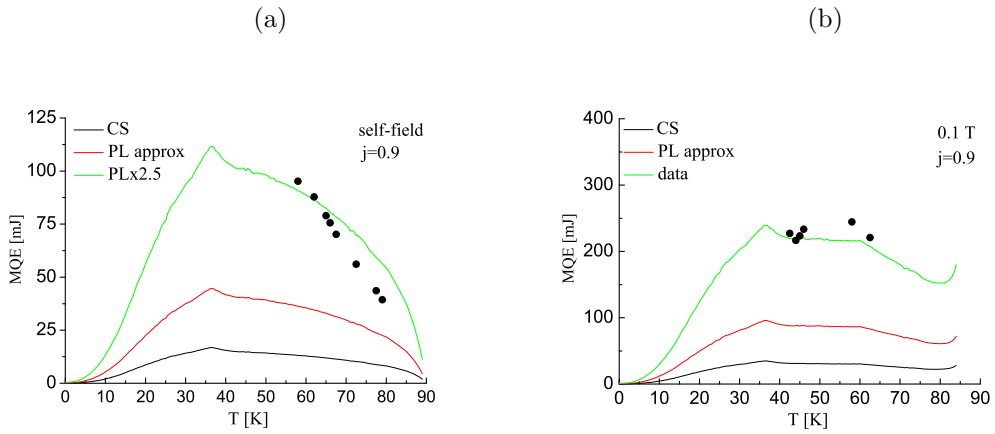

Figure 6.13: Experimental MQE, critical state predictions (black line), approximated power-law prediction (red line) and scaled (x2.5) approximated power-law (green line) at $j = 0.9$, plotted versus temperature in (a) self-field and (b) in perpendicular applied field scenario.

above 35 K due to the increase in thermal conductivity and to the large temperature margin. Note that the MQE plateau observed in the range 35 K - 60 K at 0.1 T is the result of a faster increase in current which occurs in field at ∼70 K. It is unlikely that the observed similarity in temperature dependence in accidental, however the factor 2.5x between data and predictions is yet to be understood as it cannot be accounted by the temperature dependence of c_P within the normal zone, which has been considered in calculation although is not taken into account in Q_0. A possible explanation for the difference observed between the data and the model is the additional conduction and the thermal mass offered by the instrumentation wires, which would affect $Q_0(T)$ and thus the absolute value of MQE but not its current dependence. The latter will be confirmed by removing all the instrumentation wires for temperature/voltage profiles in future work. It would be also very interesting to measure the predicted decrease of MQE with temperature below 35 K and therefore further work at low temperature will be carried out.

7

Conclusion and further work

7.1 Conclusion

The aim of this work was to investigate and understand the nature of the depinning mechanisms in 2G superconductors at low fields. The investigation has been carried out by measuring the E-J characteristics in a wide range of temperatures, in both self-field and in perpendicular applied field scenarios.

First of all, in order to carry out the measurement presented in this thesis, practical problem related to the high currents involved at intermediate temperature and thermal stability issues had to been solved.

In order to overcome these practical problems, an experimental dual mode cryostat able to deliver up to 600 A and to work in a wide range of temperatures (15 K-90 K) and fields (0 K-5 T), was successfully assembled and tested. An custom-built platform for measurements and a thermal and electrical link between the cryocooler and the platform were also designed and manufactured. A strategy to carry out measurements upon 2G tapes at very low temperatures, which would otherwise have a projected current at 10 K of $\sim$ 10000 A, was developed. The method consisted of reducing the tape cross section by using a very novel technique for milling small bridges (or grooves) directly into the tape structure. The technique was tested in order to ensure that no damage to the tape was induced, and the tape with reduced cross-section was proven to be representative of the standard one: the critical current was in fact observed to reduce linearly with the bridge width and the E-J characteristics of the sample as provided were un-affected by the bridge width. The temperature gradient above the measured

region was successfully limited by reducing the length of the sample measured. For this purpose, a specific sample holder with a 1 mm gap between the current junctions, was designed and optimised. The latter solution allowed the reduction of the self heating effect during measurements. The effect of self-heating on measuring was also reduced by using a measurement protocol based on a combination of both DC measurements and short current pulses. In conclusion, the manufactured set-up and the developed methodology allowed to extend E-J characteristics measurement to a broader temperature window not yet available in literature, and to collect reliable data over two voltage decades.

Surprisingly, the measurement collected in a short-length set-up have been found to be markedly different from those collected in the common liquid measurements set-up: the non-linear behaviour of the E-J characteristics was found to strongly differ from power law behaviour conventionally used to describe dissipation in HTS. The deviation from the power law was observed to be consistent in a large range of temperatures (15 K - 84 K) and fields (self-field to 300 mT) and the power-law exponent n, calculated in the range of voltage 0.1-1 μV/mm, was found to remain unexpectedly steady in the range of temperatures 45 K-77 K being $n = 30 \pm 1$ for all samples measured. An increment in the exponent n was instead observed with further decreasing temperature, and $n = 40$ at at the lowest temperature measured $T = 15$ K. The deviation from the power law indicated a more complex flux pinning mechanism than 1G conductors which has been interpreted, in this work, with both a microscopic approach based on HTS pinning models and with a macroscopic approach, based on the distribution model of pinning strengths and currents in the material.

The collected data were analysed in the frame of the HTS pinning models according to which the dissipation mechanism is strongly affected by the nature of the flux pinning centres in the material. Two different HTS pinning models, one valid for materials characterised by the presence of weak pinning centres (classic collective pinning model) and the other one for materials characterised by correlated defects which act as strong pinning centres (Boson model), developed 15 years ago, were applied and compared to the experimental results. Although starting from different assumptions, the two models propose the same mathematical E-J relation. However, most published E-J data were

at high temperatures where the melting of the vortex glass was the main focus and the models have never been compared with experimental data in a wide range of temperatures and in self- field, where change in dynamics from pinning of a single vortex to pinning of a bundle is expected. The HTS pinning model law was therefore used to predict the current-voltage characteristics at different temperatures and then compared with data. A good agreement between predictions and the experimental E-J characteristics has been observed. The parameter μ provided by the models is an indication of the type of collective pinning which dominates at given conditions, and it can suggest either pinning of a single vortex or of small/medium/big bundles. A constant exponent μ has been measured in the range of temperatures 45 K - 77 K being $\mu = 2.25 \pm 0.5$, whilst it has been observed that $0 < \mu < 1$ for temperatures below 45 K. Both models predict a change in flux regime at the cross over temperature of 45 K from collective pinning of flux bundles to pinning of a single vortex. However, no single model of the two can explain data from a static analysis point of view. According to the classic collective pinning model, in fact, the calculated collective length is too small and would imply unreasonable high self-field as well as smaller critical current densities than the measured ones. On the other hand the Boson model predicts a smaller reduction of the critical current with temperature than the one experimentally observed. Also, the measurements in field showed that the classic pinning model is not able to predict the passage from the collective bundles regime to the single vortex regime, even when reasonable field is applied ($\sim$ 5T). It has been speculated in this thesis, that there is the possibility of a complementary action of strong and weak pinning centres, which are both present in the tape.

Although is believed that the different nature of pinning centres dominates the depinning mechanism in YBCO, and that the HTS pinning models are able to describe the non linear E-J characteristics behaviour typical of this conductor, the parameters introduced do not allow for easy comparison between conductors performances. Hence, the attention has been focused on a macroscopic distribution model, based on the assumption of a distribution of pinning centres of different strength, and hence on a distribution of critical current density in the tape. The distribution model introduces the parameters I_{Cmin} which is the current at which the dissipation starts, the exponent m, which determines the shape of the distribution, and the pinning range I_0, which is

a parameter related to the pinning strength of the material. The parameter I_{Cmin} has been observed to have the same temperature dependence as the critical current density I_{C0}. A weaker dependence on temperature has been instead observed for I_0, further suggesting a coexistence of weak and strong pinning centres. The pinning range I_0 in fact, remains almost constant in the range of fields analysed, indicating the presence of strong pinning centres that are strongly resistant, not just to temperature but also to the applied field.

Quench measurements on 4 mm wide 2G YBCO tape, in both self-field and in-field scenarios (0.1 T) were collected, with particular attention on the MQE behaviour at current $j = I/I_C > 0.8$, where measurements where not available yet. The strongly non-linear E-J characteristics behaviour observed in the previous analysis, suggested that a power-law heat generation could explain the MQE dependence at high currents. A surprisingly non-vanishing behaviour of the MQE with current, as the critical current is approached, has been observed experimentally. Such experimental observation was in contrast with the critical state heat generation predictions. An approximated power-law heat generation, which corresponds on a scaled graph to a critical state heat generation with higher critical temperature, has been found to be able to explain the slower reduction of MQE observed at high currents. A good agreement between the approximated power-law model and the experimental results has been found in both self-field and in-field scenarios.

7.2 Further work

Using the information gained from these experiments, the natural progression should be to attempt E-J characteristic at high fields. Measurement at fixed temperatures (below 45 K) and increasing fields, should in fact allow the passage from collective pinning of a single vortex to collective pinning of bundles to be clearly distinguished, providing further support to the HTS pinning models and clarifying which pinning defects (correlated or uncorrelated) are dominating in the depinning mechanism of flux lines in 2G YBCO conductors.

With regard to the quench measurement, although the model proposed allowed the prediction of the MQE dependence on current, the absolute value of the predicted

MQE has been observed to be much smaller than the measured one (a factor of ~ 2.5). It is believed that this disagreement is mainly due to the experimental set-up used. Although it is very useful to measure the spatial/temporal evolution of quench along the tape, the instrumentation could affect measurements. By looking at the quench equation provided by the model in fact, it is evident how a difference in the thermal conductivity k could affect the absolute value of the MQE, without affecting the current dependence. In order to verify if this is the cause of the problem, the system should be re-tested with the minimum instrumentation (voltage taps/thermocouples) possible.

References

[1] Vladimir Z. Kresin and Stuart A. Wolf. *Fundamentals of Superconductivity*. Plenum Press, New York, 1990. 5

[2] Charles P. Poole, Horacio A. Farach, and Richard J. Creswick. *Superconductivity*. Academic Press, 1995. 8, 9, 10, 13, 14, 138, 197

[3] Charles Kittel. *Introduction to Solid State Physics*. John Wiley and Sons Inc, 1986. 8

[4] Teruo Matsushita. *Flux Pinning in Superconductors*. Springer, 2007. 9

[5] G. Blatter, M. V. Feigel'man, V. B. Geshkenbein, A. I. Larkin, and V. M. Vinokur. **Vortices in High-Temperature Superconductors**. *Rev. Mod. Phys.*, **66**:1125–1388, Oct 1994. 10, 29, 30, 31, 112, 116

[6] C.P. Bean. **Magnetization of High-Field Superconductors**. *Rev. Mod Phys.*, **36**:31, 1962. 11

[7] Y. B. Kim, C.F. Hempstead, and A.R. Strnad. **Magnetization and Critical Supercurrents**. *Phys. Rev.*, **129**:528, 1963. 11

[8] Seizaburo Iwasa. *Case Studies in Superconducting Magnets, Design and Operational Issues*. Plenum Press, New York and London, 1994. 14, 33, 197

[9] D. Dimos and P. Chaudhari. **Superconducting transport properties of grain boundaries in $\mathcal{Y}\mathcal{B}a_2Cu_3O_7$ bycristals**. *Physical Review B*, **41**:4038–1049, 1989. 15

[10] Nabatame T., S. Koike, O. B. Hyun, I. Hirabayashi, H. Suhara, and K. Nakamura. **Transport superconducting properties of grain boundaries in $Tl_1Ba_2Ca_2Cu_3O_x$ thin films**. *Appl. Phys. Lett.*, **65**:776, 1994. 15

[11] Peter J. Lee. *Engineering Superconductivity*. Wiley-Interscience, 2001. 15

[12] R. N. Bhattacharya and M. P. Paranthaman. *High Temperature Superconductors*. Wiley-VCH, 2010. 15

[13] Guy Deutscher. *New Superconductor: from Granular to High Tc*. World Scientific Publishing Company, 2006. 16

REFERENCES

[14] M. Parans Paranthaman and T. Izumi. **High-performance YBCO-coated conductor wires**. *MRS bulletin*, 2004. 16

[15] Thomas P Sheahen. *Introduction to High Temperature Superconductors*. Novel Research Laboratory, Whasington DC, 1993. 17, 19

[16] F. J. Owens and C.P. Jr Poole. *The New Superconductors*. Stuart Wolf, 2002. 17, 19

[17] G. W. Crabtree and D. R. Nelson. **Vortex Physics in High Temperature Superconductors**. *Physics Today*, **50**:38, 1997. 20

[18] H. Safar, P. L. Gammel, D. A. Huse, D. J. Bishop, J. P. Rice, and D. M. Ginsberg. **Experimental evidence for a first-order vortex-lattice-melting transition in untwinned, single crystal $\mathcal{Y}\mathcal{B}a_2Cu_3O_7$**. *Phys. Rev. Lett.*, **69**:824–827, 1992. 21, 25

[19] D. A. Huse, M. P. A. Fisher, and D. S. Fisher. **Are superconductors really superconducting?** *Nature Publishing Group*, **358**:553–559, August 1992. 21

[20] Michael Tinkham. *Introduction to Superconductivity*. Dover Publications,Inc., 1996. 22, 24, 28, 111, 198

[21] P.W. Anderson. **Theory of Flux Creep in Hard Superconductors**. *Physical Review Letters*, **9**(7):309, 1962. 22

[22] D. Dew-Hughes. **Model for flux creep in high T_C superconductors**. *Cryogenics*, **28**:674, 1988. 23

[23] W. K. Kwok, S. Fleshler, U. Welp, J. Vinokur, M. Downey, G. W. Crabtree, and M. M. Miller. **Vortex Lattice Melting in Untwinned and Twinned Single Crystals of $YBa_2Cu_3O_{7-\delta}$**. *Phisical Review Letters*, **69**(23):3370–3373, December 1992. 24, 198

[24] M. Charalambous, J. Chaussy, and P. Lejay. **Evidence of the resistivity along the c-axis for a transition within the vortex state for H$\|$ ab in single crystal $YBa_2Cu_3O_7$**. *Phisical Review B*, **45**(9):5091–5094, March 1992. 24, 96

[25] Anant Narlikar. *Studies of High Temperatures Superconductors (Advances in Research and Applications)*, **49** of *HTS Film and More on Vortex Studies*. Nova Science Publisher,Inc., 2005. 24

[26] Y. Iye, T. Tamegai, H. Takeya, and H. takei. **The Anisotropic Upper Critical Field of Single Crystal $YBa_2Cu_3O_x$**. *Japanese Journal of Applied Physics*, **26**(6):L1057–L1059, June 1987. 25

[27] Matthew P. A Fisher. **Vortex-glass superconductivity: A possible new phase in bulk high-T_C oxides**. *Phys. Rev. Lett.*, **62**:1415–1418, Mar 1989. 25

[28] R. H. Koch, V. Foglietti, W. J. Gallagher, G. Koren, A. Gupta, and M. P. A. Fischer. **Experimental Evidence for Vortex-Glass superconductivity in Y-Ba-Cu-O**. *Phisical Review Letters*, **63**(14):1511–1514, June 1989. 25, 26, 106, 198

[29] P. L. Gammel, L. F. Schneemeyer, and D. J. Bishop. **SQUID picovoltometry of $YBa_2Cu_3O_7$ single crystals: Evidence for a finite-temperature phase transition in the high-field**. *Phisical Review Letters*, **63**:953–956, Feb 1991. 25

[30] T. K. Worthington, E. C. Olsson, S. Nichols, T. M. Shaw, and D. R. Clarke. **Observation of a vortex-glass phase in polycristalline $\mathcal{Y}\mathcal{B}a_2Cu_3O_{7-x}$ in a magnetic field**. *Physical Review B*, **43**:10538–10543, 1991. 25

[31] E. Nazarova, K. Nenkov, K. BuchKov, and A. Zahariev. **Scaling Behaviour of Current-Voltage characteristics of $\mathcal{Y}\mathcal{B}a_2Cu_3O_{7-x}$ Polycristalline sample**. *The Open Superocnductivity Journal*, **3**:1–6, 2011. 25

[32] Alan T. Dorsey. **Linear and nonlinear conductivity of a superconductor near T_C**. *Phys. Rev. B*, **43**:7575–7585, 1992. 25

[33] R. H. Koch, V. Foglietti, W. J. Gallagher, G. Koren, A. Gupta, and M. P. A. Fischer. **Koch, Foglietti, and Fisher reply**. *Phisical Review Letters*, **64**(21):2586, May 1990. 25, 26, 198

[34] L. Civale. **Vortex pinning and creep in high-temperature superconductors with columnar defects**. *Supercond. Sci. Technol.*, **10**:A11, 1997. 27, 96

[35] A. I. Larkin and Yu. N. Ovchinnikov. **Pinning in Type II Superconductors**. *Journal of Low Temperature Physics*, **34**(3-4):409, 1979. 27, 28, 96

[36] David R. Nelson and V.M. Vinokur. **Boson localization and correlated pinning of superconducting vortex arrays**. *Physical review B*, **48**(17):13060–, November 1993. 30, 96, 111

[37] A. Rimikis, R. Kirmich, and Th. Schneider. **Investigation of n-number of composite superconductors**. *IEEE transaction of applied superconductivity*, **10**:1239–1242, 2000. 34

[38] Carlos Yujiro Shigue, Tatiane Tobias Da Cruz, Jerika Suely Lamas, Carlos Alberto Baldan, and Ernesto Rupper Filho. **Analysis of the E-J curve of HTS tapes under DC and AC magnetic field at 77K**. *IEEE Transactions on Applied Superconductivity*, **19 N.3**, June 2009. 34, 88

[39] E. Martinez, E.A. Young, M. Bianchetti, O. Monuz, S.I Schlachter, and Y. Yang. **Quench onset and propagation in Cu-stabilized monofilament $\mathcal{M}gB_2$ conductors**. *Superconductor Science and Technology*, **21**:1–8, 2008. 34

[40] Xiaorong Wang, A. R. Caruso, M. Breschi, Guomin Zhang, U.P. Trociewitz, H. W. Weijers, and J. Schwartz. **Normal zone initiation and propagation in Y-Ba-Cu-O coated conductors with Cu stabilizer**. *Applied Superconductivity, IEEE Transactions on*, **15**:2586 – 2589, 2005. 34

[41] Martin N. Wilson. *Superconducting Magnets*. Oxford Science Publication, 1987. 34, 36, 38, 41, 43, 164, 176

[42] Y. Fukumoto, Q. Li, Y.L. Wang, M. Suenaga, and P. Haldar. **Very low level residual resistivity in silver-sheathed (Bi,Pb)2Sr2Ca2Cu3O10 tapes**. *Applied Physics Letters*, **66**:1827–1829, April 1995. 35

[43] Arup K. Ghosh. **V-I transition and n-value of multifilamentary LTS and HTS wires and cables**. *Physica. C. Superconductivity and its applications*, **401**, 2004. 35

[44] R. H. Bellis and Y. Iwasa. **Quench propagation in High T_C superconductors**. *Cryogenics 1994*, **34**:129–144, 1993. 38

[45] S. B. Kim, A. Ishiyama, H. Okada, and S. Nomura. **Normal-zone Propagation properties in Bi-2223/Ag superconducting multifilamnet tapes**. *Cryogenics*, **8**:823–831, 1998. 40

[46] A. Ishiyama, M. Yanai, T. Morisaki, H. Ueda, Y. Shiohara, T. Izumi, Y. Iijima, and T. Saitoh. **Normal Transition and Propagation Characteristics of YBCO tape**. *Applied Superconductivity, IEEE Transactions on*, **15**:1659 – 1662, 2005. 40, 161

[47] X. Wang, U. P. Trociewitz, and J. Schwartz. **Near-adiabatic quench experiments on short $\mathcal{Y}\mathcal{B}a_2Cu_3O_{7-\delta}$ coated conductors**. *Journal of Applied Physics*, **101**:053904–1 – 053904–10, 2007. 40, 161

[48] A. Stenvall, A. Korpela, R. Mikkonen, and G. Grasso. **Stability considerations of multifilamentary $\mathcal{M}gB_2$ tape**. *Superconductor Science and Technology*, **19**:184–188, 2005. 40

[49] E. Martinez, F. Lera, M. Martinez-Lopez, Y. Yang, S. I. Schlachter, P. Lezza, and P. Kovac. **Quench development and propagation in metal/$\mathcal{M}gB_2$ conductors**. *Superconductor Science and Technology*, **19**:143–150, 2006. 40

[50] Y. Iwasa. **HTS magnets: stability; protection; cryogenics; economics; current stability/protection activities at FMBL**. *Cryogenics*, **43**:303–316, 2003. 41

[51] E. A. Young, C. M. Friend, and Yifeng Yang. **Quench Characteristics of a Stabilizer-Free 2G HTS Conductor**. *Applied Superconductivity, IEEE Transactions*, **19**:2500 – 2503, June 2009. 41, 161

[52] **SyPerPower Inc.** `http://www.superpower-inc.com`. 2013. 46, 198

[53] D.W. Hazelton. **Advances in 2G HTS Conductor for High Field Applications**. *Low Temperature High Field Superconductor Workshop (LTHFSW)*, November 5, 2013, St. Petersburg, FL, USA. 46, 122

[54] Y. Xie, A. Knoll, Y. Chen, Y. Li, X. Xiong, Y. Qiao, P. Hou, J. Reeves, T. Salagaj, K. Lenseth, L. Civale, B. Maiorov, Y. Iwasa, V. Solovyov, M. Suenaga, N. Cheggour, C. Clickner, J.W. Ekin, C. Weber, and V. Selvamanickam. **"Progress in scale-up of second-generation high-temperature superconductors at SuperPower Inc**. *Physica C: Superconductivity*, **426431**:849 – 85, March 2005. 46

[55] Y. Chen, X. Xiong, Y.Y. Xie, J.L. Reeves, X. Zhang, Y. Qiao, K.P. Lenseth, R.M. Schmidt, A. Rar, D.W. Hazelton, and K. Tekletsadik. **"Recent Progress in Second-Generation HTS Conductor Scale-Up at SuperPower**. *Applied Superconductivity, IEEE Transactions on*, **17**:3231 – 3234, June 2007. 46

[56] **Coolpower Cold-head Operating Manual**. *Coolpower models 4.2GM 445, 130, 065 and 150*, Leybold cryogenics. 51

[57] E.A. Young, W.O.S. Bailey, M.K. Al-Mosawi, C. Beduz, Y. Yang, S. Chappel, and A. Twin. **A Dual Operational Refrigerator/Flow Cryostat with Wide Bore Medium Field Magnet for Application Demonstration**. *Physics Procedia*, **36**:1346–1347, 2012. 52, 209

[58] National Institute of Standard NST and Technology. **Thermophysical Properties of Fluid Systems**. `http://webbook.nist.gov/chemistry/fluid/`. 59, 62

[59] W. Bailey, E. A. Young, Y. Yang, and C. Beduz. **Boiling heat transfer to a liquid nitrogen pool from Ag sheathed BiPb2223 tapes carrying over-current**. *Supercond. Sci. Technol.*, **19**:276, 2006. 62

[60] David J. Griffiths. *Introduction to Electrodynamics*. Prentice Hall, 1989. 73

[61] T. K. Worthington, W. J. Gallagher, and T. R. Dinger. **Anisotropic nature of High-Temperature Superconductivity in Single-Crystal $\mathcal{Y}\mathcal{B}a_2Cu_3O_{7-x}$**. *Physical Review Letters*, **59**:1160–1163, 1987. 85

[62] B. Roas and L. Schultz. **Anisotropy of the Critical Current Density in Epitexial $\mathcal{Y}\mathcal{B}a_2Cu_3O_x$ Films**. *Physical Review Letters*, **64**:479–482, 1990. 85

[63] H. Safar, J. Y. Coulter, M. P. Maley, S. Foltyn, P. Arendt, X. D. Wu, and J. O. Willis. **Anisotropy and Lorentz-force dependence of the critical currents in $\mathcal{Y}\mathcal{B}a_2Cu_3O_{x-\delta}$ thick films deposited on nickel-alloy substrates**. *Phys. Rev. B*, **52**:R9875–R9878, Oct 1995. 86

[64] Ho Kim, Jung, Jun Hyung Lim, Junho Joo, Seyong Choi, Wansoo Nah, Hong-Soo Ha, Chan Park, Hiroaki Kumakura, Akiyoshi Matsumoto, Michinaka Sugano, and Tsukasa Kiyoshi. **Magnetic field dependence on Y-123 coated conductor and Bi-2223 tape at 4.2K**. *Physica C*, **426-431**:1103–1107, March 2005. 88

[65] G.Ravi Kumar and P. Chaddah. **Magnetization Curves and Bean's Model in High-T_C Superconductors**. *Journal of Superconductivity*, **2**:247, September 1989. 91

[66] W. K. Kwok, U. Welp, G. W. Crabtree, K. G. Vandervoort, R. Hulscher, and J. Z. Liu. **Direct observation of dissipative flux motion and pinning by twin boundaries in $YBa_2Cu_3O_{7-\delta}$ single crystals**. *Phys. Rev. Lett.*, **64**:996, 1990. 96

[67] T. Kiss, T. Nakamura, M. Takeo, K. Kuroda, Y. Matsumoto, and F. Irie. **Flux Creep Characteristics in the Presence of a Pinning Distribution for Superconducting Thin Film**. *IEEE Transactions on Applied Superconductivity*, **5, N.2**, June 1995. 126

[68] K. Yamafuji and T. Kiss. **A new interpretation of the glass liquid transition of pinned fluxoids in high T_C superconductors**. *Physica C: Superconductivity*, **258**(3-4):197–212, February 1996. 126

[69] T. Kiss, S. Nishimura, M. Inoue, H. Okamoto, M Kanazawa, T. Matsushita, and Y. Sumiyoshi. **E-J characteristics of Bi2223/Ag tapes as a function of temperature, magnetic field and angle**. *Advances in Cryogenic Engineering*, **614**:1091, May 2002. 127, 203

[70] K. Yamafuji and T. Kiss. **Current-voltage characteristic near the glass liquid transition in high T_C superconductors**. *Physica C: Superconductivity*, **290**(1-2):9–22, October 1997. 128

[71] T. Kiss, T. Nakamura, K. Kuroda, M Takeo, F. Irie, and K. Yamafujy. **Pin fluctuation and the scaling of transport characteristic in superconductors**. *Czechoslovak Journal of Physics Supplement*, **46**(3):1071–1972, May 2002. 128

[72] F. Irie, Y. Tsujioka, and T. Chiba. **Characteristics of Critical Current Distribution for Oxide Superconductors Estimated from V-I Characteristics Using Weibull Function**. *Supercond. Aci. Technol.*, **5**:379–382, 1992. 128

[73] John Bardeen and M.J. Stephen. **Theory of the Motion of Vortices in Superconductors**. *Physical Review*, **140, N.4A**:A1197, 1963. 138

[74] Milind N. Kunchur, David K. Christen, and Julia M. Phillips. **Observation of Free Flux Flow at High Dissipation Levels in $YBa_2Cu_3O_{7-\delta}$ Epitexial Films**. *Physical Review Letters*, **70**:998–1001, February 1993. 138

[75] P.W. Anderson. **Theory of Superconductivity in the High-T_C Cuprates**. *Princeton Series in Physics*, June 2003. 139, 204

[76] Y. Yang, T. Hughes, C. Beduz, D.M. Spiller, R.G. Scurlock, and W.T. Norris. **The influence of geometry on self-field AC losses of Ag sheathed PbBi2223 tapes**. *Physica C: Superconductivity*, **256**(3-4):378, June 1996. 141

[77] T.J.S. Hughes. *Self field AC losses in Ag-sheated PbBi2223*. PhD thesis, School of Engineering Science, Faculty of Engineering, April 1997. 142, 204

[78] W. T. Norris. **Calculation of hysteresis losses in hard superconductors carrying ac: isolated conductors and edges of thin sheets**. *J. Phys. D: Applied Physics*, **3**(4):489–507, 1970. 143

[79] N. Ihara and T. Matsushita. **Effect of flux creep on irreversibility lines in superconductors**. *Physica C*, **257**:223–231, August 1995. 157

[80] E.A. Young, S. Chappell, I. Falorio, and Yifeng Y. **Quench Characteristics of a Cu-Stabilizd 2G HTS Conductor**. *IEEE Trans. App. Supercond.*, **21**:3062 – 3065, June 2011. 161

[81] X. Wang, U.P. Trociewitz, and J. Schwartz. **Self field quench behaviour of $\mathcal{Y}\mathcal{B}a_2Cu_3O_{7-\delta}$ coated conductors with different stabilizer**. *Supercond. Sci.*, **22**:1, 2009. 161, 180

[82] J. Pelegrin, E. Martinez, L.A. Angurel, Y.Y. Xie, and V. Selvamanickam. **Numerical and Experimental Analysis of Normal Zone Propagation on 2G YBCO Wires**. *IEEE Transaction on Applied Superconductivity*, **21**:3041, 2011. 161

[83] Yang Y, Young E.A., Falorio I., Bailey W.O.S., Friend C.M., Twin A., and Chappell S.P.G. **Quench Characteristics of Bi2212 Solenoid Insert Coils in Background Field up to 20 T**. *Applied Superconductivity*, **21**(2), 2011. 173, 206

[84] X. Wang, S.V.P.S.S. Pamidi, U.P. Trociewitz, and J. Schwartz. **Self field quench behaviour of multifilamentary $\mathcal{M}gB_2$ wires in liquid helium**. *Cryogenics*, **48**:467–477, 2008. 173

[85] Pelegrn J, Romano G., Martnez E., Angurel L. A., Navarro R., Ferdeghini C., Brisigotti S., Grasso G., and Nardelli D. **Experimental and numerical analysis of quench propagation on MgB2 tapes and pancake coils**. *Superconductors Science and Technology*, **26**(4), 2013. 173

[86] Shirshov L., Bogdanov I., Kozub S., Shcherbakov P., Slabodchikov P., Tkachenko L., and V. Zubko. **Stability Study of High-Current Superconducting Cables For Accelerator Magnets**. *Proceedings of RuPAC, Accelerators and Cryogenics*, **10**:192, 2008. 173

[87] L. Dresner. **Quench energies of potted magnets**. *Magnetic IEEE Transactions*, **21**(2):392 – 395, March 1985. 173, 174

List of Figures

1.1 Schematic representation of the magnetic behaviour of a perfect conductor and of a superconductor once cooled down when applying field before and after cooling. 4
1.2 Schematic phase diagram of a superconductor (a) Type I and (b) Type II. 6
1.3 Increment of the number of superconducting electrons n_s and decay of the magnetic field from the surface of the superconductor and respective characteristic lengths λ_L and ξ for (a) Type I superconductors and (b) Type II superconductors [2]. 8
1.4 Schematic representation of the magnetic field around an individual vortex [2]. 9
1.5 Arrangement of vortex of super-currents penetrated in the material. Lorentz force direction in presence of current. 9
1.6 Distribution of (a) $B(x)$ and of (b) $J_C(x)$ within an infinite slab superconductor according to Bean's model (plain lines) and to Kim's model (dashed lines). 12
1.7 Magnetic field (top graphs) and current profile (bottom graphs) with increasing field applied according to Bean's model [2]. 13
1.8 Magnetic field (top graphs) and current profile (bottom graphs) with decreasing field applied according to Bean's model [2]. 14
1.9 Magnetization curve obtained for an entire, positive, sweep magnetization $0 \rightarrow B_{C2} \rightarrow 0$ according to Bean's model (plain line) and in a realistic case (dashed line). [8]. 14
1.10 Schematic representation of $YBa_2C_3O_7$ unit cell. 17
1.11 Schematic representation of Bi-2223 unit cell. 18

1.12 Mean field phase diagram of low temperatures (black lines) and high temperatures (red lines) Type II superconductors. 19
1.13 Phase diagram of (a) clean and (b) dirty high temperatures superconductors. 20
1.14 Schematic sketch of displacement of (a) a single vortex line and of (b) a vortex bundle in glass state in presence of thermal fluctuations. 23
1.15 (a) Resistance of an untwinned $YBa_2Cu_3O_{7-\delta}$ crystal in magnetic fields of 0, 0.1, 0.5, 1, 1.5, 2, 3, 4, 5, 6, 7 and 8 T for $H \parallel c$ [23]. (b) Resistance dependence on temperature of a twinned YBCO crystal for several value of the magnetic field.[20]. 24
1.16 (a) *E-J* curves and (b) the scaling ($\nu = 1, 7, z = 4.8$) of epitaxial YBCO thin film at constant temperature (interval of 0.1 K) and magnetic field 4 T applied parallel to the *c*- axis [28, 33]. 26
1.17 Phase diagram of High Temperatures Superconductors in presence of thermal fluctuation and weak pinning centres according to classical collective pinning model. 29
1.18 Phase diagram of High Temperatures superconductors in presence of thermal fluctuation and strong pinning centres (Boson-glass model). . . 31
1.19 *E-J* characteristic predicted by critical state model (black plain line) and by power law model (red dashed line). 32
1.20 Current sharing model for HTS superconductors. 34
1.21 *E-J* characteristic of Bi-2223 high strength reinforced tape in liquid nitrogen bath at 77 K and in self field scenario. 36
1.22 Critical current versus temperature. General slope for LTS and HTS. . . 37
1.23 Schematic representation of heat generation in a normal zone according to (a) critical state model and (b) power law model. 39
1.24 One dimensional distribution of the normal zone. 41

2.1 Layers structure of the YBCO tape produced by Superpower [52]. . . . 46
2.2 Instrumentation of 2G YBCO sample for quench measurements. 47
2.3 Sample set-up for transient characteristic measurements. 49
2.4 Picture of the experimental apparatus for quasi-adiabatic measurement. 50

2.5 Schematic representation of the platform for dry operational mode measurement. 53
2.6 Platform for wet operational mode measurements. 54
2.7 Thermal and electrical flexible links. 56
2.8 Schematic design of the cryostat used for measurement in liquid nitrogen pool 58

3.1 Schematic experimental set-up for *E-J* characteristic of YBCO in liquid nitrogen pool scenario. 63
3.2 *E-J* characteristics of long length sample measured in liquid nitrogen bath, presented as a function of (a) the total operative current and (b) as a function of the superconducting current (plain line). Comparison with power law fitting. 63
3.3 Short sample experimental set up for *E-J* characteristics of YBCO tape in liquid nitrogen pool scenario. 64
3.4 *E-J* characteristics of short sample set-up with taps distanced 1 mm measured in liquid nitrogen bath and presented as a function of (a) the operative current and (b) of the superconducting current. 65
3.5 Experimental set-up for *E-J* characteristics of YBCO tape in free-cryogen scenario. 66
3.6 Enlargement of a milled narrow bridge of YBCO tape. 67
3.7 Critical current dependence on the tape cross section, measured at 77 K in liquid nitrogen bath. 68
3.8 Current-voltage characteristic of 4 mm width sample (Sample AS) and 1 mm bridged sample (Sample I) at 77 K. 68
3.9 (a) Current ramp up at 1.2 I_C and at 3.0 I_C at 77 K. (b) Transient characteristics correspondent to different current ramp up at 77 K. . . . 70
3.10 Schematic representation of the sample geometry for magnetization measurements. 73
3.11 (a) Superconducting transition measured on Sample II, Sample III and Sample IV, recorded during cooling down by imposing a constant transport current of $I = 1\,\mathrm{A}$. (b) Resistivity dependence on temperature of a cooked YBCO tape at 600°. 75

3.12 Critical current dependence on temperature, measured on Sample I, Sample II, Sample III and Sample IV. 76

3.13 *E-J* characteristics at 77 K, 74 K, 70 K and 67 K of Sample AS in self field measured in liquid nitrogen bath, and relative power law predictions, presented as a function of (a) the operative current current and (b) of the current carried by the superconductor. 77

3.14 *E-J* characteristics at 77 K, 74 K, 70 K and 67 K of Sample AS in self field measured in nitrogen bath, and relative power law predictions, presented as a function of the normalised superconducting current. . . . 79

3.15 *E-J* characteristics measured on (a) Sample I in the range of temperatures 45 K - 80 K, (b) on Sample II in the range of temperatures 15 K - 80 K, (c) on Sample III in the range of temperatures 50 K - 86 K (c) and (d) on Sample IV in the range of temperatures 37.5 K - 83 K plotted as a function of the operative current. Deviation from power law is confirmed for all samples, across the all range of temperature. 80

3.16 Scaled *E-J* characteristics of (a) Sample I, (b) Sample II, (c) Sample III and (d) Sample IV plotted as a function of the superconducting current. Deviation from power law is highlighted with the dashed lines. 81

3.17 Scaled *E-J* characteristics of (a) Sample I, (b) Sample II, (c) Sample III and (d) Sample IV plotted as a function of the normalised superconducting current. Deviation from power law is highlighted with the dashed lines. 82

3.18 (a) Scaled *E-J* characteristics plotted as a function of the scaled superconducting current of Sample I, Sample II, Sample II and Sample III in the range $45\,\mathrm{K} - 77\,\mathrm{K}$. (b) *E-J* characteristics comparison of Sample II and Sample IV at 45 K and 77 K. 83

3.19 Exponent n dependence on temperature for Sample I, Sample II, Sample III and Sample IV. 85

3.20 Critical current dependence on field in perpendicular and parallel configurations. 86

3.21 *E-J* characteristics of YBCO 4 mm wide measured in low fields in the range 0 - 0.3 T in perpendicular and parallel configurations respectively, plotted as a function of (a and c) the total current and (b-d) of the current carried by the superconductor. 87
3.22 *E-J* characteristics of YBCO 4 mm wide measured in low fields in the range 0 - 0.3 T in (a) perpendicular and (b) parallel configurations, presented as a function of the scaled current carried by the superconductor. 88
3.23 *E-J* characteristics of YBCO 4 mm wide measured in low fields in the range 0-0.3 mT in (a) perpendicular and (b) parallel configurations, presented as a function of the scaled current carried by the superconductor. 89
3.24 (a) Power exponent n and (b) critical current per unit width dependence on the applied perpendicular field for "as provided" sample (Sample AS), and samples with reduced cross section respectively of 1 mm, 2 mm and 3 mm. 90
3.25 *E-J* characteristics measured in low perpendicular fields on Sample V, at 77 K. 90
3.26 Magnetization curves at 77 K up to 4 T for three different sweep rates: 195 Oe/sec, 45 Oe/sec and 11Oe/sec. 91
3.27 *E-J* characteristics measured in perpendicular field at 77 K and low voltage (10^{-4} - 10^{-2} μV/mm) magnetization data. 92
3.28 n-number dependence on field obtained from magnetization measurements. Comparison with the one obtained from DC measurements. . . . 93

4.1 HTS pinning model predictions with power law exponent $n_{J_C} = 20$ and $\mu = 0.0$, $\mu = 1.0$ and $\mu = 2.0$. Orange area corresponds to data accessible with transient measurements, green area to the data accessible with magnetization measurements. 98
4.2 (a) Model predictions at given temperature with different u_0, plotted in a scaled graph $\log[1 - u_0 \cdot \ln(E/E_C)]$ versus $\log(J_C/J)$ and (b) corresponding predicted *E-J* characteristic curve. The green area indicates the range of measurements. (c) Model predictions at given temperature with different u_0 plotted in a scaled graph $\log[1 - u_0 \cdot \ln(E/E_C)]$ versus $\log(J_C/J)$, in the range of measurements. 100

4.3 (a) E-J characteristics data at 50 K of Sample III and HTS pinning models predictions for different pinning potential $u_0 = 12$, $u_0 = 14$, $u_0 = 15$ and $u_0 = 16$. (b) Data and models prediction characteristics scaled in a graph $\log[1 - u_0 \cdot \ln(E/E_C)]$ versus $\log(J_C/J)$. 101

4.4 (a) E-J characteristics data at 20 K of Sample II and HTS pinning models predictions for different pinning potential $u_0 = 12$, $u_0 = 60$, $u_0 = 80$ and $u_0 = 100$. (b) Data and models predictions scaled in a graph $\log[1 - u_0 \cdot \ln(E/E_C)]$ versus $\log(J_C/J)$. Critical current $I_C = 288$ A. . 103

4.5 Comparison between E-J characteristics predicted by HTS pinning model (dashed lines), and experimental data measured on (a) Sample I, (b) Sample II, (c) Sample III and (d) Sample IV, plotted as a function of the current carried by the superconductor. 104

4.6 HTS pinning model parameters: the dimensionless pinning potential u_0 and the exponent μ against temperature obtained for (a) Sample I, (b) Sample II, (c) Sample III and (d) Sample IV. 105

4.7 Dimensionless collective pinning potential u_0 and exponent μ against temperature of Sample I, Sample II, Sample III and Sample IV. 107

4.8 (a) Scaled E-J characteristics of Sample I and comparison with HTS pinning model curve, with $u_0 = 14.5 \pm 0.5$ and $\mu = 2.25 \pm 0.05$ (solid line). (b) Scaled E-J characteristics of Sample I, Sample II and Sample III and comparison with HTS pinning model curve, with $u_0 = 14.5 \pm 0.5$ and $\mu = 2.25 \pm 0.05$ (solid line). 108

4.9 (a) Scaled E-J characteristics of Sample II in the range of temperature 15 K − 45 K and comparison with HTS pinning model curves and (b) scaled E-J characteristics of Sample II and Sample IV at 45 K − 77 K and comparison with HTS pinning model curves. 109

4.10 Qualitative phase diagrams of HTS in the presence of thermal fluctuations and (a) weak pinning centres and (b) strong pinning centres. Possible dynamic scenarios on reducing temperature at different field (solid green lines). 110

4.11 Collective pinning length L_C dependence on temperature. Comparison between experimental data of Sample II and Blatter's predictions. . . . 115

4.12 Scaled critical current with the deparing current $J_C(T)/J_0(T)$ versus temperature. Comparison between experimental data of Sample II and Blatter's predictions. 117

4.13 Qualitative phase diagram of HTS in presence of thermal fluctuation and weak pinning centres dominant action (solid black lines) and strong pinning centres dominant action (red solid lines). Possible dynamic scenarios in self field on reducing temperature (green solid lines). 118

4.14 *E-J* characteristics measured in nitrogen bath presented as a function of the current carried by the superconductors (a) when an external perpendicular field is applied and (b) when an external parallel field is applied. 119

4.15 *E-J* characteristics and relative collective pinning model predictions of the 1 mm bridged tape Sample V, measured in low field in perpendicular configuration and plotted as a function of (a) the total operative current and of (b) the current carried by the superconductor. 120

4.16 (a) Comparison of μ and u_0 dependence on field obtained in perpendicular and parallel field on Sample AS and (b) comparison of μ and u_0 dependence on field for bridged tape Sample AS and uncut tape Sample V, in perpendicular field. 121

4.17 *E-J* characteristics measured in perpendicular field at 77 K and low voltage (10^{-4} -10^{-2} μV/mm) magnetization data, fitted by collective pinning model predictions (red lines). 122

4.18 Critical current dependence on temperature measured in self field scenario and with 5 T field applied. 123

5.1 Schematic representation of the percolative motion of depinned flux bundles (black spots) following an increment in transport current above the minimum critical current density J_{Cmin} [69]. 127

5.2 (a) *E-J* characteristics and (b) critical current distributions of a reference case with $I_{C0} = 100$ A, $n_{I_{C0}} = 30$ and $m = 6$ compared to Scenario I characterised by smaller critical current I_{C0}, smaller n-number $n_{I_{C0}}$ and smaller exponent m than a reference case. 133

5.3 (a) E-J characteristics and (b) critical current distributions of a reference case with I_{C0} = 100 A, $n_{I_{C0}}$ = 30 and m = 6 compared to Scenario II characterised by the same n-number $n_{I_{C0}}$ and exponent m of the reference case, but greater critical current I_{C0}. 134

5.4 (a) E-J characteristics and (b) critical current distributions of a reference case with I_{C0} = 100 A, $n_{I_{C0}}$ = 30 and m = 6 compared to Scenario III characterised by greater critical current I_{C0}, greater n-number $n_{I_{C0}}$ and greater exponent m than a reference case. 135

5.5 Scaled current distribution of Scenario I, Scenario II, Scenario III and reference case. 136

5.6 E-J characteristic of bridged 1mm 2G YBCO at 77 K plotted as a function of the current carried by the superconductor, compared with distribution model prediction obtained with I_{C0} = 31.7 A, $n_{I_{C0}}$ = 31 and m = 4, m = 6 and m = 8. Comparison with power law predictions (dashed line). 137

5.7 Resistivity of YBCO single crystal in the normal state dependence on temperature [75]. 139

5.8 (a) Scaled E-J characteristics of Sample AS collected at 77 K with applied field perpendicular to the ab plane (self field - 300 mT). Comparison with distribution model predictions. (b) Parameters m and I_{Cmin} dependence on field obtained with distribution model analysis. (c) Pinning range I_0 dependence on total field B_{TOT}, for different coefficient α imposed, $\alpha = 14 \cdot 10^{-5}$ T/A, $\alpha = 45 \cdot 10^{-5}$ T/A and $\alpha = 75 \cdot 10^{-5}$ T/A. 141

5.9 Current penetration profile for a rectangular cross-section of the superconductor of half height b and half width a, with a_0 the limit of the field free region and $a(t)$ the current reversal contour [77]. 142

5.10 Comparison between E-J characteristics predicted by depinning model and experimental data measured on (a) Sample I (80 K - 45 K), (b) Sample II (80 K - 15 K), (c) Sample III (86 K - 50 K) and (d) Sample IV (37.5 K - 83 K), plotted as a function of the current carried by the superconductor. 144

5.11 Weibull exponent m and power law exponent n dependence on temperature for (a) Sample I, (b) Sample II, (c) Sample III and (d) Sample IV. 145

5.12 (a) Scaled E-J characteristics of Sample I and comparison with distribution model curve, with $m = 6$ (solid line). (b) Scaled E-J characteristics of Sample I, Sample II and Sample III and comparison with distribution model curve, with $m = 6$ (solid line). 146

5.13 (a) Scaled E-J characteristics of Sample II in the range of temperature 15 K - 45 K and comparison with distribution model curves and (b) scaled E-J characteristics of Sample II and Sample IV at 45 K and 77 K and comparison with distribution model curves. 147

5.14 Minimum current threshold I_{Cmin}, engineering critical current I_{C0} and pinning range I_0 dependence on temperature for (a) Sample I, (b) Sample II, (c) Sample III and (d) Sample IV. 148

5.15 (a) Minimum current threshold I_{Cmin} and (b) pinning range I_0 dependence on temperature of Sample I, Sample II, Sample III and Sample IV. 149

5.16 (a) Probability distribution function of Sample II plotted as a function of the current I_C and (b) probability distribution function of Sample I, Sample II and Sample III in the range of temperatures 45 K - 77 K, of Sample II in the range of temperatures 15 K - 40 K and of Sample IV 83 K plotted as a function of the scaled factor $(I_C - I_{Cmin})/I_0$. 150

5.17 E-J characteristics measured in perpendicular field at 77 K and low voltage ($1{\cdot}10^{-4}$ - $1{\cdot}10^{-2}$ μV/mm) magnetization data, fitted by distribution model predictions (red lines). 151

5.18 Scaled E-J characteristics collected at 77 K on (a) Sample V in a range of perpendicular to the ab plane applied field and on (b) Sample AS in a range of parallel to the ab plane applied fields (self field - 300 mT). Comparison with distribution model predictions. 152

5.19 Weibull exponent m and apparent n-number dependence on fields for Sample AS measured in both perpendicular and parallel field scenario and for Sample V. 153

5.20 Minimum current threshold I_{Cmin}, engineering critical current I_{C0} and pinning range I_0 dependence on temperature of Sample AS in presence of (a) perpendicular and (b) parallel applied field. 154
5.21 Current distribution of Sample AS in self field and at 98 mT, 220 mT and 300 mT perpendicular applied field plotted (a) as a function of I_C and (b) as a function of $(I_C - I_{Cmin})/I_0$. 154
5.22 Pinning range I_0 and minimum current threshold I_{Cmin} of Sample II dependence on temperature. 155
5.23 Scaling current I_0 and depinning current I_{dep} dependence on temperature obtained with $\overline{B}_{sf} = \alpha \cdot I_C^{av}$. 158

6.1 Specific heat C_p, thermal conductivity k and resistivity ρ, of 2G YBCO tape dependence on temperature. 162
6.2 The temperature dependent critical current in self-field (black dots) and in-field at 0.1 T (red dots). 163
6.3 Temperature T_0 as a function of time following different applied heat pulses of 15 ms. Starting conditions: operative temperature 66 K, operative current 210 A. 165
6.4 Voltage V_0 evolution as a function of time following different applied heat pulses of 15 ms. Starting conditions: operative temperature 66 K, operative current 210 A. 166
6.5 Voltage spatial evolution after pulse deposition, in case of recovery R1 (top graph) and quench Q1 (bottom graph) measured at 66 K with operative current 95% I_C. 168
6.6 Normal zone extension measured by spatially distributed voltage taps and thermocouples. Operative temperature 66 K, operative current 210 A (95 % of I_C), MQE of 35 mJ. 168
6.7 Minimum quench energy dependence on temperature (a) in self-field and (b) with 0.1 T perpendicular field applied. 171
6.8 Experimental MQE as a function of the scaled current $(1-j)$ measured in (a) self-field and (b) in perpendicular applied field scenario of 0.1 T. . 172
6.9 MQE dependence on current measured on BSCCO 2212 coil at different applied fields (15 T, 18 T, 20 T) [83]. 173

6.10 Dimensionless heat generation as a function of u, for the critical state (black dashed line) and in power-law (solid lines) for $j = 0.9$ and $n = 20$ with different e_ρ. 177
6.11 MQE dependence on current in the approximate power law case for different e_ρ (solid lines). Comparison with the critical state case (dashed line). 179
6.12 (a) Experimental MQE and approximate power law predictions, scaled versus $(1 - j)$ in self field and (b) in perpendicular applied field scenario.Measurement from Wang et al are also included in (a). 180
6.13 Experimental MQE, critical state predictions (black line), approximated power-law prediction (red line) and scaled (x2.5) approximated power-law (green line) at $j = 0.9$, plotted versus temperature in (a) self-field and (b) in perpendicular applied field scenario. 181

LIST OF FIGURES

List of Tables

1.1 Comparison between LTS and HTS characteristic parameters. 42

2.1 Data for different operative configurations of the measurement facility [57]. 52

3.1 Critical current and n-number values as a function of temperature, obtained according to power law model. 78

3.2 Critical current and n-number values as a function of temperature, obtained according to power law model for Sample II at temperatures below 45 K. 84

4.1 YBCO critical current density $J_C(T)$, coherence length $\xi(T)$ and depairing current dependence on temperature $J_0(T)$. 113

5.1 Percolation parameters of a case reference and of three possible scenarios called Scenario I, Scenario II and Scenario III. 132